

FEDERAL UNIVERSITY OF MINAS GERAIS
School of Engineering
Graduate Program in Mechanical Engineering

Luiz Henrique Jorge Machado

**EXPERIMENTAL THERMODYNAMIC AND ROTORDYNAMIC ANALYSES
OF AUTOMOTIVE TURBOCHARGERS USING FLUID FILM BEARINGS
WITH DIFFERENT GROOVE SHAPES**

Belo Horizonte
2022

Luiz Henrique Jorge Machado

Experimental thermodynamic and rotordynamic analyses of automotive turbochargers using fluid film bearings with different groove shapes

Doctoral Dissertation – Final Version

Doctoral dissertation presented to the Graduate Program in Mechanical Engineering from Federal University of Minas Gerais as a partial requirement for obtaining the Doctor degree in Mechanical Engineering.

Advisor: Prof. Marco Túlio Corrêa de Faria, Ph.D.

Co-advisor: Prof. Dr. Fabrício José Pacheco Pujatti

Area of Concentration: Design and Systems

Belo Horizonte
2022

M149e

Machado, Luiz Henrique Jorge.

Experimental thermodynamic and rotordynamic analyses of automotive turbochargers using fluid film bearings with different groove shapes [recurso eletrônico] / Luiz Henrique Jorge Machado. - 2022.
1 recurso online (268 f. : il., color.) : pdf.

Orientador: Marco Tulio Correa de Faria.

Coorientador: Fabrício José Pacheco Pujatti.

Tese (doutorado) - Universidade Federal de Minas Gerais, Escola de Engenharia.

Apêndices: f. 231-268.

Bibliografia: f. 203-230.

Exigências do sistema: Adobe Acrobat Reader.

1. Engenharia mecânica - Teses. 2. Turbocompressores - Teses.
3. Emissão acústica - Teses. 4. Mancais - Indústria - Teses. 5. Estudos experimentais - Teses. I. Faria, Marco Tulio Correa de. II. Pujatti, Fabrício José Pacheco. III. Universidade Federal de Minas Gerais. Escola de Engenharia. IV. Título.

CDU: 621 (043)



UNIVERSIDADE FEDERAL DE MINAS GERAIS
ESCOLA DE ENGENHARIA
PROGRAMA DE PÓS-GRADUAÇÃO EM ENGENHARIA MECÂNICA

FOLHA DE APROVAÇÃO

**"EXPERIMENTAL THERMODYNAMIC AND ROTORDYNAMIC ANALYSES OF AUTOMOTIVE TURBOCHARGERS
USING FLUID FILM BEARINGS WITH DIFFERENT GROOVE SHAPES"**

LUIZ HENRIQUE JORGE MACHADO

Tese submetida à Banca Examinadora designada pelo Colegiado do Programa de Pós-Graduação em Engenharia Mecânica da Universidade Federal de Minas Gerais, constituída pelos Professores: Dr. Marco Tulio Corrêa de Faria (Orientador - Departamento de Engenharia Mecânica/UFMG), Dr. Fabrício José Pacheco Pujatti (Coorientador - Departamento de Engenharia Mecânica/UFMG), Dr. Eduardo Bauzer Medeiros (Departamento de Engenharia de Produção/UFMG), Dr. Ramon Molina Valle (Universidade Federal de Minas Gerais), Dr. Domingos Alves Rade (Instituto Tecnológico de Aeronáutica/ITA) e Dr. Michel Fillon (Diretor do Centre National de la Recherche Scientifique (CNRS), França), como parte dos requisitos necessários à obtenção do título de **"Doutor em Engenharia Mecânica"**, na área de concentração de "Energia e Sustentabilidade".

Tese aprovada no dia 10 de junho de 2022.



Documento assinado eletronicamente por **Marco Tulio Correa de Faria, Professor do Magistério Superior**, em 15/06/2022, às 15:07, conforme horário oficial de Brasília, com fundamento no art. 5º do [Decreto nº 10.543, de 13 de novembro de 2020](#).



Documento assinado eletronicamente por **Michel Fillon, Usuário Externo**, em 16/06/2022, às 08:02, conforme horário oficial de Brasília, com fundamento no art. 5º do [Decreto nº 10.543, de 13 de novembro de 2020](#).



Documento assinado eletronicamente por **Domingos Alves Rade, Usuário Externo**, em 16/06/2022, às 12:46, conforme horário oficial de Brasília, com fundamento no art. 5º do [Decreto nº 10.543, de 13 de novembro de 2020](#).



Documento assinado eletronicamente por **Fabrício Jose Pacheco Pujatti, Professor do Magistério Superior**, em 20/06/2022, às 08:12, conforme horário oficial de Brasília, com fundamento no art. 5º do [Decreto nº 10.543, de 13 de novembro de 2020](#).



Documento assinado eletronicamente por **Eduardo Bauzer Medeiros, Membro de comissão**, em 20/06/2022, às 09:46, conforme horário oficial de Brasília, com fundamento no art. 5º do [Decreto nº 10.543, de 13 de novembro de 2020](#).

Documento assinado eletronicamente por **Ramon Molina Valle, Professor Magistério Superior - Voluntário**, em 20/06/2022, às 15:54, conforme horário oficial de Brasília, com fundamento no art. 5º do [Decreto nº 10.543, de 13 de novembro de 2020](#).



A autenticidade deste documento pode ser conferida no site https://sei.ufmg.br/sei/controlador_externo.php?acao=documento_conferir&id_orgao_acesso_externo=0, informando o código verificador **1525832** e o código CRC **F944240F**.

To my father, Carlos Roberto.

ACKNOWLEDGMENT

The author is sincerely grateful to his academic advisor Prof. Marco Faria for their knowledge and support for more than 15 years, since the first works in the Rotor Dynamics Group, and for his important experience in academia. The author also is immensely grateful to Prof. Fabrício Pujatti, co-advisor, who helped him to return to the academy, start the doctoral programs and to become a substitute Professor.

The author is thankful to the committee members: Prof. Eduardo Bauzer, former coordinator of the Aerospace Engineering course and who helped the author during his Professor time; Prof. Ramon Molina, former Mobility Technology Center coordinator, who supported in several important moments during the doctorate; Prof. Domingos Rade, who promptly accepted the invitation as a member of the committee board, and Prof. Michel Fillon, with their valuable help and attention in the last months of this work.

There are contributions in this work that were invaluable at important moments: Prof. Oscar Sandoval, for dedication several times to all experimental tests and data analysis. B.S. Eng. José Pereira, also for all time of data collection, tech data reports, and the commitment in this project during years. Prof. Bryan Caetano, B.S. Eng. Victor Hanriot and B.S. Eng. Victoria Santos for their help with tests, software and figures supports.

The contributions of Biagio Turbos and Motoliga were fundamental for the accomplishment of this work: To engineers Miguel Dell'Agli for believing in this project to improve Brazilian industry, with engineer Massimo Ambivero. To the various technicians and engineers, and especially to the technician Emerson Gazato who provided accurate information for the best production of the bearings. To the engineer Hélio Gonçalves who always support the university and allowed the use of the Motoliga structure for the precision EDM machining process. To the technician Geraldo Costa who produced the micrometric details of the bearings.

The author also thanks researcher Mr. Marco Luzio and engineer Dr. Noushin Mokhtari the time spent with their expertise in the acoustic emission data analysis.

The author is greatly thankful to his wife, Prof. Juliana Basílio, for her tireless dedication in recent years to give the author all the family support to continue this work. To his mother Celina, father Carlos and aunt Célia for the support and guidance during his education. To his sister, Prof. Carla Machado, as a prime example of a researcher and professor. And to the great and complete inspiration of the author's life, his daughter Yasmin.

The author appreciated the contributions of The Coordination of Superior Level Staff Improvement of Brazil (CAPES) and The National Council for Scientific and Technological Development of Brazil (CNPq) for the fundamental financial support during this graduate time and investments at CTM LabTurbo.

Resumo

Este trabalho apresenta um estudo experimental da influência do perfil da ranhura axial de mancais radiais hidrodinâmicos semiflutuantes sobre o comportamento dinâmico e termodinâmico em pequenos turbocompressores utilizados nas indústrias automotiva e aeronáutica. Uma bancada de ensaios a quente utilizando gás GLP para testes de turbocompressores capaz de representar diferentes condições de velocidade e vazão mássica é utilizada para o desenvolvimento desse estudo. Sete diferentes turbocompressores com mancais semiflutuantes de diferentes perfis de ranhura axial são selecionados para a avaliação da resposta dinâmica e termodinâmica em diferentes condições de operação, inclusive pré-*surge* e *surge*. Cada mancal semiflutuante possui em seu corpo interno duas áreas de apoio do eixo e uma para o fluxo livre do lubrificante e são fabricados por processos de usinagem convencional diretamente pelo fabricante do turbocompressor. É utilizado o processo de eletroerosão de precisão (EDM) para a fabricação exclusiva das ranhuras, sendo elas: triangular, meia elipse, quarto de elipse, quarto de elipse invertido, retangular, trapezoidal e circular (ou "meia lua"). A análise comparativa do comportamento termodinâmico é efetuada por meio de ensaios de desempenho e eficiência dos compressores e dos conjuntos turbina-rotor em velocidade e vazão mássica constantes. Sensores de temperatura, pressão e fluxo mássico de ar e de gás são instalados em diversos pontos à montante e à jusante do compressor e da turbina. Para o estudo de dinâmica de rotores, espectros de frequência e diagramas das órbitas de precessão do munhão são obtidos a partir da medição das vibrações em diferentes velocidades estacionárias e fluxos de ar constantes de operação. Diagramas em cascata (*waterfall plots*) são realizados em aceleração e desaceleração dos turbocompressores. Acelerômetros e sensores de proximidade sem contato são utilizados para captar os sinais desejados de vibração sobre os turbocompressores sob diferentes condições de operação do turbocompressor. As respostas síncronas e subsíncronas também são obtidas e analisadas para cada turbocompressor para a faixa de velocidades de rotação de, aproximadamente, 0 a 145.000 rpm. Sinais de emissão acústica são captadas nas condições de velocidades e fluxos constante. Diversos tratamentos nesses dados são realizados, com diferentes filtros eletrônicos e análise estatística. São realizadas correlações dos dados de emissão acústica com a mudança apenas da velocidade de operação, apenas do fluxo de massa de ar do compressor, com a situação pré-*surge* e *surge*. Uma avaliação preliminar das dimensões das ranhuras dos mancais analisados é efetuada por meio de análise metrológica dimensional antes dos testes para certificar que a quantidade de lubrificante e a área efetiva de contato rotor-mancal estão dentro do determinado em projeto. Os resultados experimentais obtidos permitem a confecção de importantes mapas de desempenho termodinâmico e curvas da resposta dinâmica dos sete turbocompressores analisados, fornecendo subsídios relevantes para a seleção do perfil da ranhura axial do mancal flutuante mais apropriado para uma dada condição de operação do turbocompressor. Adicionalmente, é possível apresentar que os dados de emissão acústica utilizando filtro passa-banda entre 50 e 100 kHz com análise de curtose apresentam fortes características para detecção da situação de pré-*surge* em pequenos turbocompressores.

Palavras-chave: Turbocompressores. Análise experimental. Mancal de anel flutuante. Ranhura axial. Emissão acústica.

Abstract

This work presents an experimental study of the influence of the axial groove shape of semi-floating ring bearings on the dynamic and thermodynamic behavior of small turbochargers used in the automotive and aeronautical industries. A hot flow test bench using LPG gas for turbocharger tests at different speed and mass flow conditions is used for the development of this study. Seven different turbochargers with semi-floating ring bearings with different axial groove shapes are selected for the evaluation of dynamic and thermodynamic response under different operating conditions, including pre-surge and surge. Each semi-floating ring bearing has in its internal part two end areas to bear the rotor and one middle area for the free flow of the lubricant. The bearings are manufactured by conventional machining processes directly by the turbocharger manufacturer. The electrical discharge machining (EDM) process is used for the exclusive manufacture of grooves, which are: triangular, half-ellipse, quarter-ellipse, quarter-ellipse inverted, rectangular, trapezoidal and circle (or half-moon). The comparative analysis of the thermodynamic behavior is carried out through performance and efficiency tests of compressors and turbine-rotor assemblies at constant speed and mass flow. Temperature, pressure and air and gas mass flow transducers are installed at various points upstream and downstream of the compressor and turbine in the test bench. For the study of rotor dynamics, frequency spectra and diagrams of the journal precession orbits are obtained from the measurement of vibrations at different stationary speeds and constant operating airflows. Waterfall plots are performed on acceleration and deceleration of turbochargers. Accelerometers and displacement transducers (proximity probes) are used to pick up the vibration signals on turbochargers under different turbocharger operating conditions. Synchronous and subsynchronous responses are also obtained and analyzed for each turbocharger for the range of rotational speeds from approximately 0 to 145,000 rpm. Acoustic emission signals are captured under steady-state speed and flows. Several treatments are performed on these data, with different electronic filters and statistical analysis. Correlations are made of the acoustic emission data with the change only in the operating speed, only in the mass flow of air from the compressor, with the pre-surge and surge condition. A preliminary evaluation of the dimensions of the grooves of the analyzed bearings is carried out by means of dimensional metrological analysis before the tests to certify that the amount of lubricant and the effective area of rotor-bearing contact are within the determined in the design. The experimental results obtained allow the creation of important thermodynamic performance maps and dynamic response curves of the seven turbochargers analyzed, providing relevant subsidies for the selection of the most appropriate axial groove shape of the floating ring bearing for a given turbocharger operating condition. Additionally, it is possible to show that acoustic emission data using a bandpass filter between 50 and 100 kHz with kurtosis analysis have strong characteristics for detecting the pre-surge condition in small turbochargers.

Key-words: Turbocharger. Experimental analysis. Floating ring bearing. Axial groove. Acoustic emission.

LIST OF FIGURES

Figure 1 – Turbocharger diagram. (ALSAEED, 2005).....	26
Figure 2 – Turbocharger compressor flow map with the (a) surge line and (b) choke line (WESTFALL, 2015).....	28
Figure 3 – Schematic figures of numerical groove shapes models of (a) Sharma and Tomar (2021), (b) Sahu and Sharma (2019), (c) Kumar and Sharma (2019), (d) Jin <i>et al.</i> (2021).....	30
Figure 4 – Turbocharger used in the (a) Lycoming TIO-540-AE2A engine (LYCOMING, 2006) and (b) Rotax 914 F/UL (ROTAX, 2019).....	35
Figure 5 – Schematic drawing of a turborcharger rotor-bearing system. (CHATZISAVVAS <i>et al.</i> , 2015).....	36
Figure 6 – (a) Rotating Floating Ring Bearing (HATAKENAKA <i>et al.</i> , 2002), and schematic figure of a (b) RFRB and a (c) SFRB.....	39
Figure 7 – The fluid film bearings with oil whirl. (EHRICH, 2004).	44
Figure 8 – Schematic diagram of dynamic sliding multi-region method under Alford’s force for centrifugal compressor (LI <i>et al.</i> , 2021).	46
Figure 9 – Orbit map for a TC (SINGH and GUPTA, 2020).....	47
Figure 10 – The Waterfall plot for a turbocharger (HOLMES <i>et al.</i> , 2004).....	48
Figure 11 – 3D Waterfall diagram for a turbocharger (HUNG-NGUYEN SCHÄFER, 2015).....	49
Figure 12 – (a) Curve of a 2D waterfall spectrum with synchronous and subsynchronous vibrations in a TC FRB and (b) schematic drawing of the outer and inner films of a FRB. (CHANDRASEKARAN <i>et al.</i> , 2021).....	51
Figure 13 – The split in two subsynchronous due the Alford’s force and reduced damping observed in a waterfall diagram. (GOODING <i>et al.</i> , 2020).	52
Figure 14 – Rolls-Royce Power Gearbox monitoring method (NOWOISKY <i>et al.</i> , 2020)	55
Figure 15 – Sensor instrumentation for the Rolls-Royce power gearbox test rig. Font: NOWOISKY <i>et al.</i> (2020).....	57
Figure 16 – Test set up for cavitation analysis using AE sensor (sensor ‘i’ in the Figure) (MOUSMOULIS <i>et al.</i> , 2019).....	57
Figure 17 – Configuration of the LABTURBO-CTM (UFMG) hot-flow workbench used in this work. (Updated from SANDOVAL, 2019)	60
Figure 18 – The LABTURBO-CTM (UFMG) hot-flow workbench.....	61
Figure 19 – Schematic drawing of the Biagio Turbos TC AUT1000 (BIAGIO, 2021).....	63
Figure 20 – Journal bearing lateral view: (a) external; (b) internal.....	64

Figure 21 – Journal bearing front view: (a) bearing; (b) original triangular axial groove detail	65
Figure 22 – Groove perimeter projection and area.....	67
Figure 23 – The cold balancing machine (a) with the protection cover, and (b) detail of rotor-bearing assembly coupled to the machine.	71
Figure 24 – The seven rotor-bearing sets after balancing	72
Figure 25 – (a) New turbine and compressor housing and (b) miscellaneous parts and final packaging.....	73
Figure 26 – Workbench with the AUT1000 compressor and turbine housing and without the rotor-bearing set.....	73
Figure 27 – Schematic drawing of the LABTURBO/CTM UFMG air line	75
Figure 28 – ATLAS COPCO GA55VSD AFF compressor configuration installed.....	75
Figure 29 – Schematic drawing of the LABTURBO/CTM UFMG fuel line	76
Figure 30 – Tubular combustion chamber (dimensions in millimeters)	76
Figure 31 – Combustion chamber	77
Figure 32 – Schematic drawing of the LABTURBO/CTM UFMG compressing line	77
Figure 33 – Schematic drawing of the LABTURBO/CTM UFMG lubrication system ...	78
Figure 34 – Lubrication system.....	79
Figure 35 – Compressor inlet and outlet line schematic illustrating location and position of pressure and temperature transducers.....	81
Figure 36 – Area at the shaft end for measuring rotational speed.....	82
Figure 37 – Rotating speed measurement by optical sensor	83
Figure 38 – Turbocharger assembly on the workbench. X-axis, Y-axis and Z-axis positions indicate the mounting location of the accelerometers.	86
Figure 39 – Turbocharger extended axle with installed proximity probe	88
Figure 40 – Turbocharger compressor housing modified to install the proximity probes	88
Figure 41 – AE set mounted on compressor housing.....	89
Figure 42 – Compressed air inlet control valve	91
Figure 43 – Layout of the combustion ignition system.....	91
Figure 44 – Thermal insulation of components.....	95
Figure 45 – TD data acquisition system	96
Figure 46 – RD data acquisition systems	98
Figure 47 – Command center and TD data monitoring and recording set.....	99
Figure 48 – Fluid pressure and temperature supervision interface.....	99
Figure 49 – Fluid pressure and temperature supervision interface.....	100
Figure 50 – Fluid pressure and temperature supervision interface.....	100

Figure 51 – The National Instruments DAQ set.....	101
Figure 52 – RD accelerometer and acoustic emission data monitoring and recording interface.	101
Figure 53 – Examples of turbocharger compressor (a) performance and (b) efficiency maps (Font: DHINAGARAN <i>et al.</i> , 2017) and turbine (c) performance and (d) efficiency maps (Font: HUNG-NGUYEN SCHÄFER, 2015).	103
Figure 54 – Turbocharger frequency spectrum (SINGH and GUPTA, 2020)	104
Figure 55 – Turbocharger waterfall during acceleration and deceleration (KIRK and ALSAEED, 2011).....	105
Figure 56 – Turbocharger orbit rotor obtained (SINGH and GUPTA, 2020).....	106
Figure 57 – AE sensor signal in a cavitation test and a zoom (windowing) into one of the peaks (YLÖNEN <i>et al.</i> , 2020).....	108
Figure 58 – (a) Measurement of graphite to calibrate and (b) a PA6 adaptive base to use on the compressor housing with the automatic pencil.....	109
Figure 59 – (a) Performance and (b) Efficiency maps for the turbocharger supported on bearings with triangular shape grooves	113
Figure 60 – (a) Performance and (b) Efficiency maps for the turbocharger supported on bearings with half-ellipse shape grooves.....	114
Figure 61 – (a) Performance and (b) Efficiency maps for the turbocharger supported on bearings with quarter-ellipse shape grooves.....	114
Figure 62 – (a) Performance and (b) Efficiency maps for the turbocharger supported on bearings with inverted quarter-ellipse shape grooves.....	115
Figure 63 – (a) Performance and (b) Efficiency maps for the turbocharger supported on bearings with rectangular shape grooves.....	115
Figure 64 – (a) Performance and (b) Efficiency maps for the turbocharger supported on bearings with trapezoidal shape grooves	116
Figure 65 – (a) Performance and (b) Efficiency maps for the turbocharger supported on bearings with half-moon shape grooves	116
Figure 66 – Turbine (a) performance and (b) efficiency maps for the turbocharger supported on bearings with triangular shape grooves	121
Figure 67 – Turbine (a) performance and (b) efficiency maps for the turbocharger supported on bearings with half-ellipse shape grooves	121
Figure 68 – Turbine (a) performance and (b) efficiency maps for the turbocharger supported on bearings with quarter-ellipse shape grooves.....	122
Figure 69 – Turbine (a) performance and (b) efficiency maps for the turbocharger supported on bearings with inverted quarter-ellipse shape grooves.....	122

Figure 70 – Turbine (a) performance and (b) efficiency maps for the turbocharger supported on bearings with rectangular shape grooves	123
Figure 71 – Turbine (a) performance and (b) efficiency maps for the turbocharger supported on bearings with trapezoidal shape grooves	123
Figure 72 – Turbine (a) performance and (b) efficiency maps for the turbocharger supported on bearings with half-moon shape grooves	124
Figure 73 – Criteria score for the compressor maximum compression.....	129
Figure 74 – Criteria score for the compressor corrected mass flow at maximum compression.....	130
Figure 75 – Criteria score for the turbine maximum expansion.....	130
Figure 76 – Criteria score for the turbine corrected mass flow at maximum expansion.	131
Figure 77 – Criteria score for the maximum compressor efficiency.....	133
Figure 78 – Criteria score for the minimum compressor efficiency	134
Figure 79 – Criteria score for the maximum turbine efficiency.....	134
Figure 80 – Criteria score for the minimum turbine efficiency.....	135
Figure 81 – Synchronous curves for the turbocharger TC 1 with bearings with triangular axial grooves at the initial and last balancing conditions	139
Figure 82 – Synchronous curves for the turbocharger TC 2 with bearings with half-ellipse axial grooves at the initial and last balancing conditions	139
Figure 83 – Synchronous curves for the turbocharger TC 3 with bearings with quarter-ellipse axial grooves at the initial and last balancing conditions.....	140
Figure 84 – Synchronous curves for the turbocharger TC 4 with bearings with inverted quarter-ellipse axial grooves at the initial and last balancing conditions	140
Figure 85 – Synchronous curves for the turbocharger TC 5 with bearings with rectangular axial grooves at the initial and last balancing conditions	141
Figure 86 – Synchronous curves for the turbocharger TC 6 with bearings with trapezoidal axial grooves at the initial and last balancing conditions	141
Figure 87 – Synchronous curves for the turbocharger TC 7 with bearings with half-moon axial grooves at the initial and last balancing conditions	142
Figure 88 – Maximum amplitude of synchronous response for TCs 1 to 4 using efficiency map.	147
Figure 89 – Maximum amplitude of synchronous response for TCs 5 to 7 using the efficiency map.	148
Figure 90 – Maximum amplitude of subsynchronous response for TCs 1 to 4 using the efficiency map	152

Figure 91 – Maximum amplitude of subsynchronous response for TCs 5 to 7 using the efficiency map	153
Figure 92 – Example of orbit graph with 0.1 mm x 0.1 mm area	157
Figure 93 – Rotor orbits of the TC1 supported on bearings with triangular axial grooves and indication of the measurement points on the efficiency map.	158
Figure 94 – Rotor orbits of the TC2 supported on bearings with half-ellipse axial grooves and indication of the measurement points on the efficiency map.	160
Figure 95 – Rotor orbits of the TC3 supported on bearings with quarter-ellipse axial grooves and indication of the measurement points on the efficiency map.....	162
Figure 96 – Rotor orbits of the TC4 supported on bearings with inverted-quarter-ellipse axial grooves and indication of the measurement points on the efficiency map.....	163
Figure 97 – Orbit of the TC 4 rotor for speed line 2 with 78% of valve closing indicating the occurrence of light shaft rub condition.....	164
Figure 98 – The inner oil whirl at 0.25 x subsynchronous vibration at TC4 in speed line 1	165
Figure 99 – Rotor orbits of the TC5 supported on bearings with rectangular axial grooves and indication of the measurement points on the efficiency map.	166
Figure 100 – Rotor orbits of the TC6 supported on bearings with trapezoidal axial grooves and indication of the measurement points on the efficiency map.	168
Figure 101 – Rotor orbits of the TC7 supported on bearings with half-moon axial grooves and indication of the measurement points on the efficiency map.	169
Figure 102 – Cascade diagram of TC 1 mounted with SFRB using triangular axial groove	175
Figure 103 – Cascade diagram of TC 2 mounted with SFRB using half-ellipse axial groove	176
Figure 104 – Cascade diagram of TC 3 mounted with SFRB using quarter-ellipse axial groove.....	177
Figure 105 – Cascade diagram of TC 4 mounted with SFRB using inverted quarter-ellipse axial groove	178
Figure 106 – Cascade diagram of TC 5 mounted with SFRB using rectangular axial groove	179
Figure 107 – Cascade diagram of TC 6 mounted with SFRB using trapezoidal axial groove	180
Figure 108 – Cascade diagram of TC 7 mounted with SFRB using circular axial groove	181

Figure 109 – EA measured data treated by (a) Wavelet Transform and (b) Band-pass Filter	187
Figure 110 – The 4,200 new EA data obtained from the Wavelet Transforms and Band-pass Filters of 30 measured data from each TC.....	188
Figure 111 – Windowing of speed line 105 krpm of TC 1 @ 0% V.C.....	189
Figure 112 – Information from windowing of speed line 105 krpm of TC 1 @ 0% V.C.	190
Figure 113 – The 7 statistic function for each 4 characteristic of the 4,200 new treated EA data	191
Figure 114 – Kurtosis of RMS from each rotation in different valve closing position with a band-pass filter of 50 to 100 kHz for each TC at 67 krpm (speed line 1)	192
Figure 115 – Kurtosis of RMS from each rotation in different valve closing position with a band-pass filter of 50 to 100 kHz for each TC at 89 krpm (speed line 2)	193
Figure 116 – Kurtosis of RMS from each rotation in different valve closing position with a band-pass filter of 50 to 100 kHz for each TC at 105 krpm (speed line 3)	193
Figure 117 – Kurtosis of RMS from each rotation in different valve closing position with a band-pass filter of 50 to 100 kHz for each TC at 121 krpm (speed line 4)	194
Figure 118 – Kurtosis of RMS from each rotation in different valve closing position with a band-pass filter of 50 to 100 kHz for each TC at 135 krpm (speed line 5)	194
Figure 119 – (a) The fluid film journal bearing lateral view and (b) the isometric view.	231
Figure 120 – cast bronze journal (a) before and (b) during the machining process.....	232
Figure 121 – Metrology verification of final AUT1000 journal bearing: (a) Full length of double bearing; and (b) Bearing internal diameter.....	232
Figure 122 – Tolerances verified in AUT1000 journal bearing production.....	233
Figure 123 – (a) Journal bearings without axial grooves and (b) wire EDM machining manufacturing the different axial grooves shapes	234
Figure 124 – On-time wire EDM machining during the process of axial groove production.	235
Figure 125 – Rotor-bearing at start (a) and at the end (b) of the assembly process.....	237
Figure 126 – Dimensions to be verified in AUT1000 journal bearing production	239
Figure 127 – Model TM-505 Measuring Microscope (MITUTOYO, 2019).....	240
Figure 128 – Micrometric Head 164-162 (MITUTOYO, 2019).....	241
Figure 129 – Schematic drawing with the reference number of each groove.....	243
Figure 130 – Frequency spectra for the x axis (horizontal radial) for TC 1.....	254
Figure 131 – Frequency spectra for the y axis (vertical radial) for TC 1	254

Figure 132 – Frequency spectra for the z axis (axial) for TC 1	255
Figure 133 – Frequency spectra for the x axis (horizontal radial) for TC 2.....	255
Figure 134 – Frequency spectra for the y axis (vertical radial) for TC 2.....	256
Figure 135 – Frequency spectra for the z axis (axial) for TC 2	256
Figure 136 – Frequency spectra for the x axis (horizontal radial) for TC 3.....	257
Figure 137 – Frequency spectra for the y axis (vertical radial) for TC 3.....	257
Figure 138 – Frequency spectra for the z axis (axial) for TC 3	258
Figure 139 – Frequency spectra for the x axis (horizontal radial) for TC 4.....	258
Figure 140 – Frequency spectra for the y axis (vertical radial) for TC 4.....	259
Figure 141 – Frequency spectra for the z axis (axial) for TC 4	259
Figure 142 – Frequency spectra for the x axis (horizontal radial) for TC 5.....	260
Figure 143 – Frequency spectra for the y axis (vertical radial) for TC 5.....	260
Figure 144 – Frequency spectra for the z axis (axial) for TC 5	261
Figure 145 – Frequency spectra for the x axis (horizontal radial) for TC 6.....	261
Figure 146 – Frequency spectra for the y axis (vertical radial) for TC 6.....	262
Figure 147 – Frequency spectra for the z axis (axial) for TC 6	262
Figure 148 – Frequency spectra for the x axis (horizontal radial) for TC 7.....	263
Figure 149 – Frequency spectra for the y axis (vertical radial) for TC 7.....	263
Figure 150 – Frequency spectra for the z axis (axial) for TC 7	264
Figure 151 – Kurtosis of filtered AE data from TC 1 speed lines 1 to 5.....	265
Figure 152 – Kurtosis of filtered AE data from TC 2 speed lines 1 to 5.....	266
Figure 153 – Kurtosis of filtered AE data from TC 3 speed lines 1 to 5.....	266
Figure 154 – Kurtosis of filtered AE data from TC 4 speed lines 1 to 5.....	267
Figure 155 – Kurtosis of filtered AE data from TC 5 speed lines 1 to 5.....	267
Figure 156 – Kurtosis of filtered AE data from TC 6 speed lines 1 to 5.....	268
Figure 157 – Kurtosis of filtered AE data from TC 7 speed lines 1 to 5.....	268

LIST OF TABLES

Table 1 – Technical data of the Biagio AUT1000 Turbocharger (BIAGIO, 2021).....	62
Table 2 – Main reasons for groove shapes choice.....	66
Table 3 – Groove shape and design descriptions assumptions.....	68
Table 4 – Grooves proportional drawing in bearing and enlarged.....	69
Table 5 – Balancing TC machine characteristics	72
Table 6 – Technical data of the pressure transducers.....	80
Table 7 – Technical data of the temperature transducers	80
Table 8 – Turbine-type flowrate Transducer Technical Data. Font: Sandoval (2019).	81
Table 9 – Technical data of the rotary speed sensor and signal converter system.....	83
Table 10 – Technical data of the accelerometer.....	85
Table 11 – Technical data of the frequency analyzer.....	85
Table 12 – Technical Data of the Displacement Sensor.....	87
Table 13 – Technical data of the AE sensor.....	90
Table 14 – Technical data of the DAQ for AE sensor	90
Table 15 – Technical data of the flame programmer	92
Table 16 – Steps for the standard operating temperature stabilization of the centrifugal compressor.....	93
Table 17 – Test Points for the AUT1000 Biagio Centrifugal Compressor	94
Table 18 – Uncertainties considered for evaluating the results of this work	110
Table 19 – Test Points for the Centrifugal Compressor of the Turbocharger	112
Table 20 – Comparative thermodynamic performance characteristics of the turbochargers supported on bearings with different axial grooves.....	118
Table 21 – Comparison between compressor isoentropic efficiency data	119
Table 22 – Comparative values of turbine mass flow for the turbochargers supported on bearings with different axial grooves.	125
Table 23 – Comparative values of turbine efficiency for the turbochargers supported on bearings with different axial grooves.	127
Table 24 – MCDM matrix for Compressor and Turbine Performance	132
Table 25 – MCDM matrix for Compressor Maximum and Minimum Efficiency.....	136
Table 26 – MCDM matrix for Turbine Maximum and Minimum Efficiency	136
Table 27 – MCDM matrix for Compressor and Turbine Efficiency.....	137
Table 28 – Ranking of turbochargers based on the thermodynamic analysis	137
Table 29 – 1 st and 2 nd critical speeds for each TC.....	143
Table 30 – Relationship between Speed lines and Critical Speeds.....	143

Table 31 – Amplitude of synchronous response for TCs 1 to 4.....	145
Table 32 – Amplitude of synchronous response for TCs 5 to 7.....	146
Table 33 – Amplitude of subsynchronous response for TCs 1 to 4.....	150
Table 34 – Amplitude of subsynchronous response for TCs 5 to 7.....	151
Table 35 – Pugh scores for imbalance and fluid film instability response (Synchronous and subsynchronous vibrations).....	154
Table 36 – Number of orbit events for each TC.....	171
Table 37 – Pugh scores based on for orbit response rank for the TCs.....	172
Table 38 – Number of orbit events for each TC.....	184
Table 39 – Pugh scores for waterfall response rank for TCs.....	185
Table 40 – Final RD score & rank.....	186
Table 41 – Number of shaft revolutions and points per revolution.....	189
Table 42 – Kurtosis of RMS from each rotation in valve closing positions 4, 5 and 6 with a band-pass filter of 50 to 100 kHz for each TC at 67 krpm (speed line 1).....	195
Table 43 – Kurtosis of RMS from each rotation in valve closing positions 4, 5 and 6 with a band-pass filter of 50 to 100 kHz for each TC at 89 krpm (speed line 2).....	195
Table 44 – Kurtosis of RMS from each rotation in valve closing positions 4, 5 and 6 with a band-pass filter of 50 to 100 kHz for each TC at 105 krpm (speed line 3).....	196
Table 45 – Kurtosis of RMS from each rotation in valve closing positions 4, 5 and 6 with a band-pass filter of 50 to 100 kHz for each TC at 121 krpm (speed line 4).....	196
Table 46 – Kurtosis of RMS from each rotation in valve closing positions 4, 5 and 6 with a band-pass filter of 50 to 100 kHz for each TC at 135 krpm (speed line 5).....	197
Table 47 – Final classification of bearing grooves.....	198
Table 48 – Dimensions and tolerances for AUT1000 journal bearing.....	233
Table 49 – Final grooves of journal bearings and zoom at grooves.....	235
Table 50 – Geometric measures and tolerances of each bearing produced and verified by MGFC Ltd. (all measures in mm) – green (approved) and red (not approved).....	239
Table 51 – Main characteristics of the Measuring Microscope (MITUTOYO, 2019). ..	240
Table 52 – Characteristics of the microscope slide table used (MITUTOYO, 2019)....	241
Table 53 – Characteristics of the ocular and objective lens used (MITUTOYO, 2019).	241
Table 54 – Characteristics of Digital Micrometric Heads (MITUTOYO, 2019).....	242
Table 55 – Reference points and details for the metrological analysis.....	242
Table 56 – Theoretical and manufactures measures for TC 1 (triangular groove).	244
Table 57 – Theoretical and manufactures measures for TC 2 (half-ellipse groove).	244
Table 58 – Theoretical and manufactures measures for TC 3 (quarter-ellipse groove)..	244

Table 59 – Theoretical and manufactures measures for TC 4 (inverted quarter groove).	245
.....	245
Table 60 – Theoretical and manufactures measures for TC 5 (rectangular groove).	245
Table 61 – Theoretical and manufactures measures for TC 6 (trapezoidal groove).	246
Table 62 – Theoretical and manufactures measures for TC 7 (half-circle groove).	246
Table 63 – Uncertainty sources and random effects.	247
Table 64 – Values for the coverage factor ($k_{95\%}$) for a 95% confidence level as a function of the number of effective degrees of freedom (ν_{ef}).	249
Table 65 – Geometric Parameters of each groove for TC 1 (triangular groove).	249
Table 66 – Geometric Parameters of each groove for TC 2 (half-ellipse groove).	249
Table 67 – Geometric Parameters of each groove for TC 3 (quarter-ellipse groove).	250
Table 68 – Geometric Parameters of each groove for TC 4 (inverted quarter-ellipse groove).	250
.....	250
Table 69 – Geometric Parameters of each groove for TC 5 (rectangular groove).	251
Table 70 – Geometric Parameters of each groove for TC 6 (trapezoidal groove).	251
Table 71 – Geometric Parameters of each groove for TC 7 (half-circle groove).	252

NOMENCLATURE

Symbol	Description
1x	Synchronous vibration
AE	Acoustic Emission
API	American Petroleum Institute
BE	Burst Energy
C	Counts of threshold crossings
C_1	Inner film clearance
C_2	Outer film clearance
$C_{p,ex}$	Specific heat of exhaust gas [J/kg·K]
CAD	Computer-aided design
CTC	Count of Threshold Crossing
DAQ	Data acquisition system
E	Burst Energy [dB·s]
FFB	Fluid film bearing
FRB	Floating ring bearing
G	Gravity acceleration
GFB	Gas foil bearing
ICE	Internal Combustion Engine
LPG	Liquefied petroleum gas
\dot{m}_T	Turbine mass flow rate [kg/s]
MA	Maximum Amplitude
MCDM	Multiple-criteria decision-making
M.P.	Measurement Point
P_1	Compressor inlet pressure [Pa]
P_2	Compressor discharge pressure [Pa]
P_3	Turbine inlet pressure [Pa]
P_4	Turbine discharge pressure [Pa]
RFRB	Rotating floating ring bearing
RD	Rotordynamic
RMS	Root mean square
SAE	Society of Automotive Engineers
SFD	Squeeze film damper
SFRB	Semi floating ring bearing
SL	Speed Lines [krpm]
Sub1	1 st Subsynchronous frequency
Sub2	2 nd Subsynchronous frequency
Sub3	3 rd Subsynchronous frequency
T_1	Compressor inlet temperature [K]
T_2	Compressor discharge temperature [K]
T_3	Turbine inlet temperature [K]
TC	Turbocharger
TD	Thermodynamic
U_{max}	Maximum Amplitude [dB]
U_t	Threshold line [dB]
V.C.	Valve Closing Positions [%]

WMD	Wide mesh bearing damper
\dot{W}_C	Compressor Power [W]
ζ	Temperature change dimensionless parameter
η_C	Compressor Efficiency
η_T	Turbine Efficiency
η_{TC}	Overall Efficiency
γ_a	Ratio of specific heats for air
γ_{ex}	Ratio of specific heats for exhaust gas
Ψ	Thermal stability criterion

TABLE OF CONTENTS

1.	INTRODUCTION	25
1.1.	RELEVANCE	28
1.2.	AIM	32
1.3.	DISSERTATION TEXT STRUCTURE.....	33
2.	LITERATURE REVIEW	34
2.1.	AUTOMOTIVE AND AERONAUTICAL TURBOCHARGER.....	35
2.2.	ROTORDYNAMICS OF TURBOCHARGER	36
2.2.1.	Turbocharger oil bearings.....	37
2.2.2.	Axial grooves for oil bearings	41
2.2.3.	Turbocharger Stability	42
2.3.	TC ROTORDYNAMICS ANALYSIS	46
2.4.	TURBOCHARGER TEST RIG	56
2.5.	COMPARISON AND RANKING METHODOLOGIES	58
3.	METHODOLOGY	59
3.1.	TURBOCHARGER TEST WORKBENCH (OVERVIEW).....	59
3.2.	TURBOCHARGERS	62
3.3.	FLUID FILM JOURNAL BEARINGS	63
3.3.1.	Original journal bearing.....	64
3.3.2.	Modified journal bearings.....	65
3.3.3.	Axial grooves shapes and dimensions	67
3.4.	TURBOCHARGERS ASSEMBLIES.....	71
3.5.	WORKBENCH (SYSTEMS AND INSTRUMENTATION).....	74
3.5.1.	Turbine Power System.....	74
3.5.2.	Combustion chamber	76
3.5.3.	Compression Line.....	77
3.5.4.	Lubrication System.....	78
3.5.5.	The control room	79
3.5.6.	Pressure measurements	79

3.5.7. Temperature measurements	80
3.5.8. Air flow measurements in the centrifugal compressor	81
3.5.9. Turbocharger rotating speed measurement.....	82
3.5.10. Rotordynamic test apparatus	83
3.5.11. Accelerometers and frequency analyzer	84
3.5.12. Proximity probes and drivers	86
3.5.13. Acoustic emission sensor	89
3.5.14. Control and monitoring systems	90
3.6. THERMODYNAMIC AND ROTORDYNAMIC DATA ACQUISITION DEVICES	92
3.6.1. Standards and Procedures	92
3.6.2. TD data acquisition device	95
3.6.3. RD data acquisition device	97
3.6.4. TC command center + TD and Proximity probe data recorder	98
3.6.5. DAQ sets for accelerometer and AE data recording	101
3.7. THERMODYNAMIC AND ROTORDYNAMIC DATA ACQUISITION PROCEDURE	102
3.7.1. Turbocharger Thermodynamic Maps and Graphs	102
3.7.2. Turbocharger Rotordynamic Graphs	104
3.8. UNCERTAINTY PROPAGATION ANALYSIS.....	108
4. RESULTS AND DISCUSSION.....	111
4.1. TD MAP AND GRAPHS	111
4.1.1. Centrifugal compressor performance and efficiency.....	111
4.1.2. Combined Turbine performance and efficiency	120
4.1.3. Overall TC performance and efficiency – TD classification.....	127
4.1.4. Turbocharger Thermodynamic rank	137
4.2. RD GRAPHS AND RESULTS.....	138
4.2.1. Preliminary rotor-bearing balancing and synchronous responses	138
4.2.2. Frequency spectrum.....	143

4.2.3. Rotor whirling orbit	156
4.2.4. Waterfall Diagrams.....	172
4.2.5. Turbocharger rotordynamic rank.....	185
4.3. ACOUSTIC EMISIONS TESTS	186
4.4. FINAL REMARKS.....	198
5. CONCLUSION	200
6. REFERENCES	203
APPENDIX A – Original and brand new fluid film bearings technical details of manufacturing and assembly.....	231
APPENDIX B – Metrological analysis of the brand new journal bearings	238
B.1. Metrological analysis of bearings externally and internally.....	238
B.2. Experimental apparatus for metrological groove analysis.....	240
APPENDIX C – Steady-state frequency spectra	253
APPENDIX D – Kurtosis graphs for each turbocharger	265

1. INTRODUCTION

Turbochargers have been used to increase the maximum power that can be obtained from a given internal combustion engine (ICE) by increasing the air density before entering the engine (HEYWOOD, 2015).

Lee *et al.* (2015) state that with the oil crisis in 1970s gave diesel engines a higher economic status than gasoline engines and encouraged their distribution in the market. This happened due to their higher economic efficiency and specific power with the introduction of the turbocharging technology. Moreover, there is a current worldwide trend of turbocharging as a solution for the downsizing of vehicle engines to respond to the energy crisis and to the stricter regulations for exhaust gas. In order to improve the specific power and increase fuel efficiency, the use of turbochargers (TCs) has encountered an increasing demand.

The main reasons for the reduction of emissions by downsizing are the reduction of the number and/or size of the cylinders, the generation of less friction during the work of the reciprocating engine and the reduction of the overall weight of the vehicle due to a smaller engine, leading to a decrease in frictional forces (GOLLOCH, 2006). Miller (2008) mentions that turbocharger (TC) is the most important additional component currently available for internal combustion engines.

Moreover, electric motors and battery-powered systems with power-to-weight ratio, as well as volume-to-weight ratio, low maintenance costs and longer product life for transport systems are not yet well developed in the automotive and small aircraft segment. Some recent work on the use of biofuels, such as ethanol, have become a target for several engine manufacturers and governments that want to minimize vehicle emissions and increase sustainability (ARAÚJO *et al.*, 2017). The idea of using these biofuels in hybrid, and fuel cell is increasingly present while other technologies remain incipient (DAVIS and INAJIMA, 2021). Therefore, further research on the behavior of turbochargers is necessary.

Turbochargers not only present a feasible solution to reduce vehicle gas emissions but also consist of a great business potential, since the market for turbochargers is expected to grow by US\$ 1.22 billion over the period 2021-2025 (TECHNAVIO, 2021). A recent study shows that for the next 10 years (2021-2031) an additional demand for turbocharged ICEs is expected due to increasing emission regulations in Europe and Asia, where hybrid vehicles are expected to be fitted with a TC or multiple TCs systems, which in turn is estimated to propel the industrial turbochargers market (TMR, 2021).

Since the TC is a turbine-driven compressor, when exhaust gas flows through the turbine wheels, the compressor wheel is rotated by the turbine, and the external air is compressed and sent to the combustion chamber. Figure 1 shows the main components of a TC: two halves are joined together by a shaft. On one side, hot exhaust gases spin the turbine that is connected to a compressor, which takes air in and compresses it into the engine. This compression gives to the engine extra power, increasing its efficiency. In fact, an increase of the amount of air entering the combustion chamber induces an increase in the amount of fuel available for increasing the power.

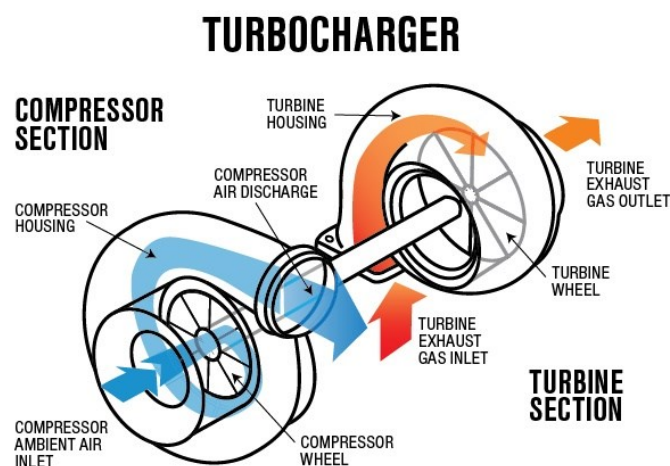


Figure 1 – Turbocharger diagram. (ALSAEED, 2005).

One of the main elements of turbomachinery, like turbochargers, are the bearings, which are essential for the development of efficient and safe industrial rotating machines. Commercial vehicle turbochargers are generally supported by fluid film bearings. The main reasons for the intensive use of fluid film bearings in turbomachinery and industrial rotating machines are their low cost, large load capacity, longevity and good damping capacity.

In the literature there is a variety of works on the thermodynamic analysis of turbochargers (TCs) focused on the improvement of their efficiency and performance. There are also works on the evaluation of the rotating system dynamic response, but few focusing on bearings and their role on the behavior of TCs. It is rare to find experimental works that evaluate jointly thermodynamic and rotordynamic characteristics of TCs.

To increase the ability to predict rotordynamic phenomena in industrial rotating machines, experimental procedures have been developed for analysis, design and monitoring of rotating machines and bearings (SCHLEGEL, 1984). These techniques in

rotordynamics are highly dependent on intensive experiments. Furthermore, the experimental results provide useful information to validate the computational procedures available for analyzing rotor-bearings systems.

The trend towards increasing the power/weight ratio of turbomachinery (downsizing and increased power requirement with new energy sources) results in faster and more flexible rotors. Increasing the machine speed, reducing the size of the rotating parts, increasing the number of stages, and reducing the clearance between the rotating and stationary parts are some ways used to increase this ratio (GADANGI, 1995), which also generate a larger potential for vibration problems. With respect to this matter, fluid film bearings are vital components for attenuating excessive vibrations in rotating machinery. Zeidan (1989) indicates that the major consideration in the design of most high-speed rotating machines is the reduction of shaft vibration amplitudes and the transmission of forces to the support system. Therefore, the support system should deserve special attention in the analysis and design of these machines.

Proper selection and design of bearings can greatly contribute to the reduction of synchronous vibration and to the stability of high-speed rotating machines. Technical information about the behavior of bearings with different characteristics are essential for the proper selection of efficient, safe and lower cost support systems for turbomachinery.

Improvements on the mechanical design and dynamic efficiency of TCs are also important. Schweizer (2009) analyzes various instability conditions of journal bearings under different TC operating conditions, but without discussing the influence of the bearing design on the dynamic response of TCs. San Andrés and Kerth (2004) present that the commercial automotive TCs generally use floating ring bearings (FRBs) due to their low cost and reduced power losses. However, fluid film instabilities can affect this type of rotor/bearing system, although reaching limit cycles that enable the entire operation of TC. Serrano *et al.* (2013(a)) add that mechanical losses in the rotor-bearing assembly are today one of the largest sources of real power dissipation in TCs, emphasizing the importance to the bearing configuration in the TC design.

Additionally, turbomachines such as turbochargers can be subjected to the surge, which is the breakdown of steady flow in the compressor that occurs at a low flow rate, as well as the choke, which is the condition that occurs in the compressor when it operates at very high mass flow rate, and the flow through the compressor can't be further increased. Figure 2 shows the (a) surge lines and the (b) choke lines in a typical turbocharger compressor flow map.

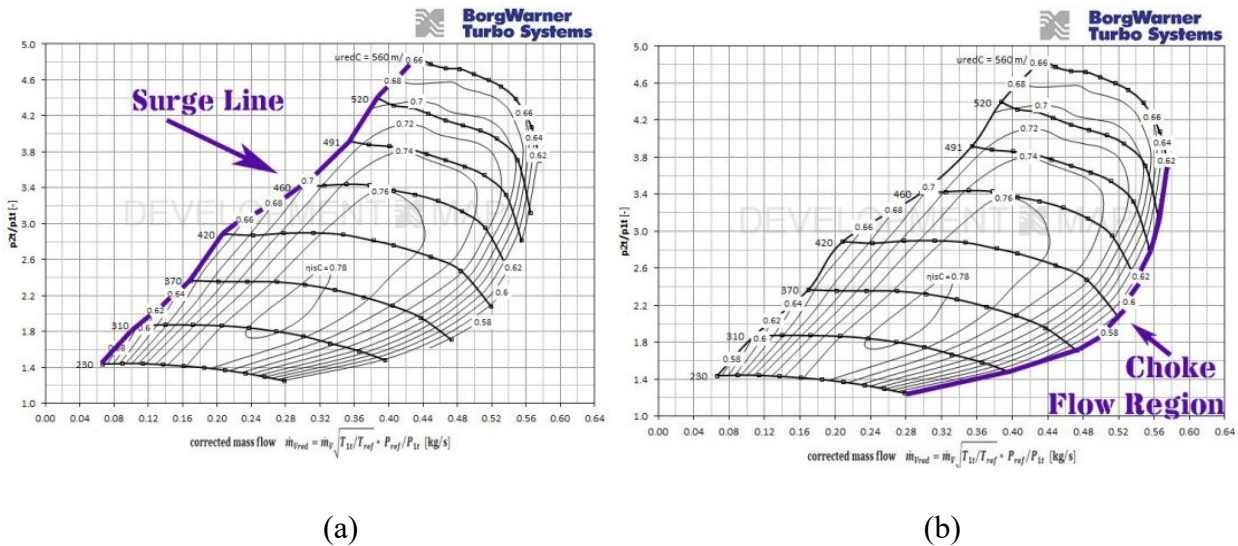


Figure 2 – Turbocharger compressor flow map with the (a) surge line and (b) choke line (WESTFALL, 2015).

Surge is critical to TCs since it can damage the bearing and, in some cases, results in mechanical failure of the rotor compressor and other components. Thus, the early detection of surge onset (pre-surge conditions) provides important information to the turbocharger compressor for safe and effective operation at different speeds and air mass flow rates.

1.1. RELEVANCE

Technological advances in materials, manufacturing and design of fluid film journal bearings have allowed to enlarge the operating limits of temperature, pressure, flow and speed of bearings used in turbochargers. Several improvements in the design of FRBs for TCs are an important research area in rotordynamics. Nowadays, there are some research works focused on the analysis of high-speed turbochargers supported on FRBs and on other bearing types. An important parameter in the bearing design for TCs, which has not received much attention in the technical literature, is the lubricant axial feed grooves introduced into FRBs. The influence of the lubricant grooves on the dynamic behavior of the bearings and their role in providing damping and stiffness to TC rotor is still an open subject for investigation. It is possible to observe that there is some work on the quantity, angular positioning, width and length of axial grooves in FRB bearings. However, there is no study on the influence of the FRB groove shape on the performance and behavior of turbochargers.

The influence of the bearing behavior, under several rotating speed ranges and load conditions, on the dynamic response of TCs is rarely found in the vast technical literature of rotordynamics. Besides the analysis of the bearing behavior, a reliable TC design requires a thermodynamic analysis to assess the influence of the rotating speed, pressure and temperature variations on the machine dynamic response (SANDOVAL *et al.*, 2018). A recent study describing a theoretical model to analyze the thermodynamic and rotordynamic behaviors of TCs has been presented by Lee *et al.* (2015). This study shows measurements of the dynamic rotor performance characteristics of a TC supported by gas foil bearings (GFBs) as well as a comparison with turbocharger supported by oil floating ring bearings (FRBs) and fluid film bearings (FFBs), but without any experimental analysis of the difference between the bearings.

The discussion of the use of theoretical and experimental methodologies that have been employed to analyze the dynamic behavior of turbomachinery has been widely presented in the scientific community for decades, and bearings have a fundamental role in this area.

Dimond *et al.* (2009) present a review of the relative strengths and weaknesses of bearing measurements methods. The authors present those theoretical models can present errors ranging from 5% to 400%, and indicate that experimental validation of bearing models is vital to consolidate numerical models. Several papers are dedicated to present experimental methodologies to study the dynamic behavior of turbomachinery with sliding bearing, such as magnetic bearing (JARROUX *et al.*, 2021), foil bearing (XU *et al.*, 2018), tilting pad bearing (CIULLI *et al.*, 2021) and rolling bearing (FONSECA *et al.*, 2018). FRBs are also experimentally studied, but mainly in thermal (DOUSTI and ALLAIRE, 2019) and tribology (MA *et al.*, 2021) aspects.

In the last years, the experimental dynamic behavior analysis of turbomachinery supported by FRBs indicates the importance of the axial groove shapes on the analysis of this type of bearing. Xie and Zhu (2022) show in a new study that FRBs experimental data obtained following international standards provide subsidies to develop more accurate numerical models. Figure 3 shows schematic figures of different groove shapes used in numerical models' studies. The role of axial grooves has been the focus of several experimental studies dealing with different bearing designs, such as textured micro grooves (WANG *et al.*, 2020; GONG *et al.*, 2019; JIN *et al.*, 2021; XIE *et al.*, 2021; XIE *et al.*, 2022), herringbone (LIU and CHEN, 2022) and partial radial groove (SHINDE and PAWAR, 2021).

The most of these recent works show that the groove shape has been subjugated in the mathematical models in the past. The current studies shows that the axial grooves need to be modeled considering the radial and axial oil flow with different pressures in each area element of the groove (using computational fluid dynamics and finite element method, for example), as well as the heat transfer through the oil, air, and groove walls.

However, experimental studies that associate the thermal and dynamic behavior of automotive turbochargers with different axial groove shapes of journal bearing are almost inexistent in the literature and become important to provide reliable subsidies for the various mathematical models that have been developed in recent years that involve the axial grooves shapes of fluid film bearings.

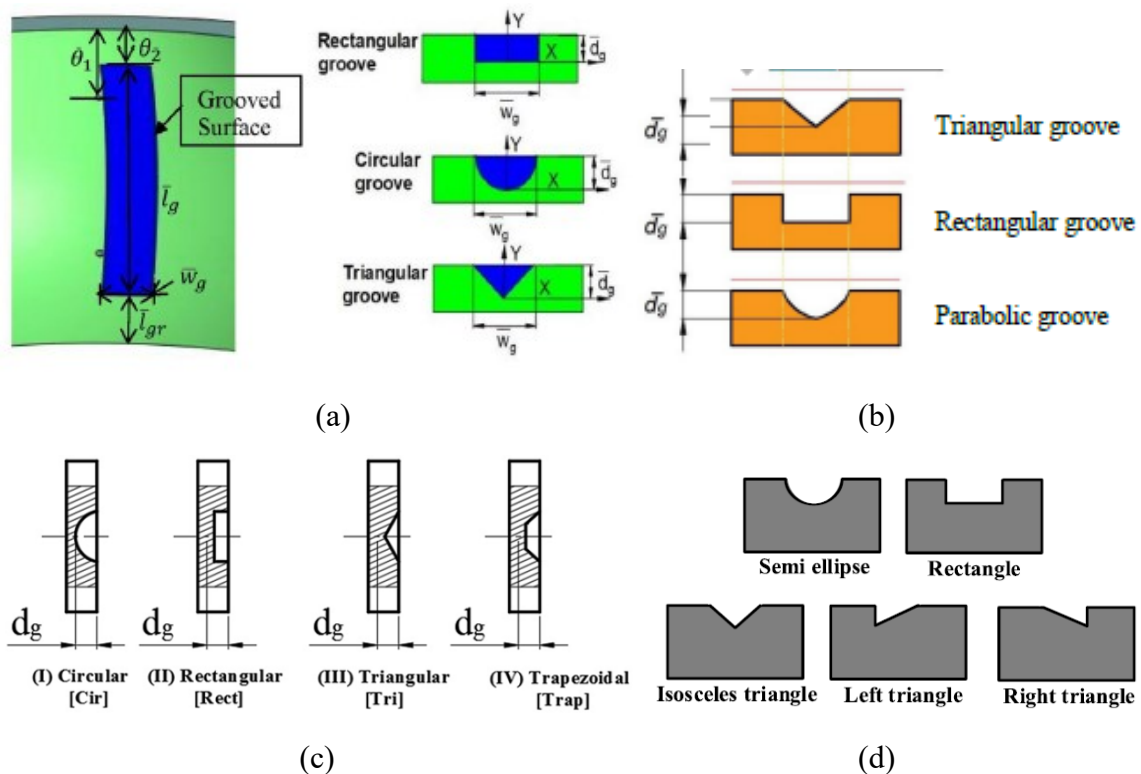


Figure 3 – Schematic figures of numerical groove shapes models of (a) Sharma and Tomar (2021), (b) Sahu and Sharma (2019), (c) Kumar and Sharma (2019), (d) Jin *et al.* (2021).

Another observation by Dimond *et al.* (2009) is given about the experimental methodology in the analysis of bearings. Most of the experiments did not include comprehensive uncertainty analysis as part of the reported results, making it difficult to analyze the potential data obtained by several studies.

Additionally, it is known that acoustic emission (AE) analysis is an important tool to detect incipient failure in rotating machinery caused by cavitation (MOUSMOULIS *et al.*, 2019), blade condition (ZHANG *et al.*, 2022), cracked shafts (FARIA and

PIMENTEL JR., 2019), corrosion in valves (ALI *et al.*, 2019) shaft-bearing friction analysis (MOKHTARI *et al.*, 2020; TIAN *et al.*, 2019), shaft-to-seal rubbing (LEAHY *et al.*, 2006) as for starved fluid film bearings (PODDAR and TANDON, 2020). Likewise, there are no studies that analyze several TC experimental parameters using acoustic emission and their potential gains in an earlier and quality prediction of operation and failure characteristics, such as pre-surge. Pre-surge condition has been studied using experimental pressure data and time-consuming data analysis methods (KOZHUKHOV *et al.*, 2020; KITAMURA *et al.*, 2018; XUE and WANG, 2019), temperature abrupt rise-turn (LIU and ZHENG, 2013) and some works with vibration and sound pressure data together (GAO *et al.*, 2017), without great effectiveness in the detection of pre-surge on different TC operating conditions. The AE data could employ to improve the analysis of the pre-surge phenomenon using correlation.

In an attempt of enlarging the knowledge about the thermal and dynamic behaviors of high-speed turbomachinery supported by floating ring bearings with different axial grooves shapes, this study aims at presenting an experimental investigation of automotive TCs that can bring technical data for their design for the automotive and aeronautical industries. Thermal analyses are carried out by turbocharger air/gas inlet and outlet mass flows, as well as pressures and temperatures are monitored to obtain thermal performance and efficiency. The dynamic response of the TCs is evaluated by measuring the vibration levels using accelerometer and proximity probes, as well as the use of acoustic emission transducer.

The innovative aspects of the current work and the differences from previous works are:

1. The use of a turbocharger hot test bench using LPG (liquefied petroleum gas), allowing to obtain a hot flow to the turbine, like the real condition, without pulsations and vibrations, compared to most benches with cold air or hot air using ICEs.
2. The monitoring system includes analysis of behavior and performance variables together, not covered in other studies, both for the process and machine. The thermodynamic analysis is performed mostly on the process performed by the test bench, while the dynamic analysis is performed on the turbocharger.
3. As the groove shapes present simple geometric changes, phenomena and/or specific behaviors of turbochargers can be better observed using the combined analysis of the thermal and dynamic behavior of the system. The instrumentation used brings a comparative advantage by allowing thermal and dynamic data to be obtained under the

same operating conditions at the same time, making the comparison of each TC more robust and assertive.

4. There is no study on the influence of the axial groove geometry of floating ring bearings on the behavior of turbochargers.

5. The acoustic emission data can enlarge the understanding of the turbocharger behavior at several situations, such as speed variations in the same conditions of air flow in the compressor, as well as the opposite: variations of airflow at the same speeds. Additionally, new analysis of pre-surge and surge conditions.

The results rendered in this work may bring new insights into the mechanical behavior of automotive TCs and provide some guidance to the design of more efficient, safer, and less expensive bearings for their supporting systems.

A positive aspect of the experimental results is related to the use of a TC hot flow bench following international standards.

1.2. AIM

The main goal of this work is to investigate experimentally the thermodynamic and rotordynamic behavior of high speed TCs supported by floating ring journal bearings with different axial groove shapes. In this investigation, the methodology combines the procedures used for thermal and dynamic analysis of rotating systems. The experimental responses of the TCs are captured by temperature, pressure and flow meter transducers for thermodynamic (TD) analysis and by accelerometers and proximity probes for rotordynamic (RD) analysis and an overall correlation analysis between TD and RD data with acoustic emission transducers to allow a rating of the quality of each groove shape. Also, a statistical analysis of threshold and filtered acoustic emission data is implemented to permit early detection of the surge condition.

Some objectives of this work are described in the following items:

- Study the rotordynamic behavior of turbochargers with different FRBs axial grooves using accelerometers to obtain frequency spectra and waterfall plots, using proximity probes to get orbit plots and correlating them with the performance and efficiency flow maps from thermodynamic analysis.
- Analyze data obtained by acoustic pressure transducers to correlate with important parameters of flow and vibration stabilities.

- Discuss about an accurate and robust experimental methodology to develop reliable bearings and mathematical models in various TC operating regimes.
- Correlate the features of AE signals and the different conditions of speed, valve closing, pre-surge and surge of the TCs obtained during the tests.

1.3. DISSERTATION TEXT STRUCTURE

The chapters of this doctorate dissertation are described below.

Chapter 1 – Introduction: Describes the motivation and the dissertation purpose.

Chapter 2 – Literature Review: Describes the most important works related to this dissertation.

Chapter 3 – Experimental Methodology: Provides all parameters and properties of the turbocharger test rig, the turbocharger used and the journal bearings, as well as the method of manufacturing the bearings studied. This chapter also includes all analyses applied to the FRB in this study and the instrumentation used to obtain the thermodynamic and rotordynamic data throughout the TC operating regime.

Chapter 4 – Results: Presents all the results and discussion with the main bibliographies, comparing the results and analyzing the best grooves shapes for each operating regime, as well as the results of the acoustic emission sensor

Chapter 5 – Conclusion: Provides conclusions about the behavior of each groove shape and its impacts. It also discusses how pre-surge detection methodology using AE sensors can help further advances in the industry.

Bibliography – A list of all papers, books and related works cited in this dissertation.

Appendix A – Presents the technical details of manufacturing and assembly of the journal bearings

Appendix B – Shows the metrological analysis of the bearings.

Appendix C – Complements the work with the frequency spectra data.

Appendix D – Indicates the thresholds, filters and results obtained statistically with the acoustic emission transducer.

2. LITERATURE REVIEW

Most of the turbocharger (TC) analyses in the technical literature are focused on the compressor maps (or flow maps) that consist in calculating the pressure ratio and mass flow rate for a specific engine. Surge and choke lines are obtained, which are very important to evaluate the region of flow instability. These lines are important to obtain the efficiency islands, which can depict the point where the maximum turbocharger efficiency is attained (the best mass flow rate and boost pressure required to meet the higher power to the internal combustion engine (ICE)). On the other hand, the dynamic analysis of rotor-bearing system of high-speed turbomachinery, such as automotive turbochargers, allows to obtain more efficient and safer designs that can achieve a best cost-benefit relation between efficiency and performance with low levels of vibration and noise. Therefore, there is a gap in the literature where the dynamic effects of the rotor-bearing systems are rarely analyzed in relation to the operating ranges of the TCs, which causes difficulties in the joint analysis of thermodynamic and rotordynamic effects to classify specific design parts, such as the bearings.

Additionally, many researchers in academia and industries have incessantly searched for solutions to predict reliably the pre-surge condition in TCs, since the entry of the turbocharger in the surge zone presents intense shock waves that can result in a severe damage.

This chapter presents an introduction to the main characteristics of turbochargers used in industry, mainly in the automotive and aeronautical industries. A description of some important studies on the rotordynamics of turbocharger, involving stability and instability conditions, is discussed with recent publications about the behavior of turbocharger oil bearings and their main sources of instability are presented, discussing aspects associated with mechanical losses, oil whirl and oil whip, and aerodynamic forces. A discussion about the use of axial grooves in journal bearings to improve rotordynamic response is also undertaken. The main instrumentation used in turbocharger testing benches to obtain efficiency and performance thermodynamic data as well as the rotordynamic responses are presented. Furthermore, a section is included to describe some research works that show the application of the acoustic emission (AE) analysis in the analysis of rotating machines. Finally, an analysis of methodologies for classifying experimental results is presented.

2.1. AUTOMOTIVE AND AERONAUTICAL TURBOCHARGER

The TCs used in transportation industry are different from the turbomachines used in industries of oil and gas, mining, chemical, power plant, and others. TCs are lighter, smaller and work with exhaust gas from engines at speeds between 150,000 and 350,000 rpm, while industrial turbomachines have higher power and larger sizes and usually operate between 3,000 and 20,000 rpm at nominal conditions (NGUYEN-SCHÄFER, 2015).

In automotive and aircraft industries, the TCs used in ICEs are mostly of small/medium sizes, while in naval and locomotive turbochargers are comparatively larger. The former TCs have high shaft speed and the journal tends to operate at centered position. Therefore, the TC analysis requires a specific approach, mainly in the choice of rotor-bearing system.

The production of turbochargers with high reliability is strongly needed in the aircraft industry (SANCHEZ, 2019) and the bearing designs are a crucial part of this.

Nowadays, turbochargers are studied for other applications in transportation industry, besides automobiles, such as in aircraft (HASSAN, 2007; PIANCASTELLI *et al.*, 2012; MANSOURI and OMMI, 2019; MCGOWAN *et al.*, 2019; SUN *et al.*, 2021), in marine (GUAN *et al.*, 2015; KIM *et al.*, 2017; VARBANETS and KARIANSKIY, 2012, WEN *et al.*, 2012; LU *et al.*, 2022; PÍŠTĚK *et al.*, 2021) and locomotives (MENON *et al.*, 2007; YANG *et al.*, 2016, YU *et al.*, 2015, YU *et al.*, 2011). Figure 4 shows a Lycoming TIO-540-AE2A 350 HP engine and a Rotax 914 F/UL, both with an assembled turbocharger, used in several light aircraft and light helicopters.

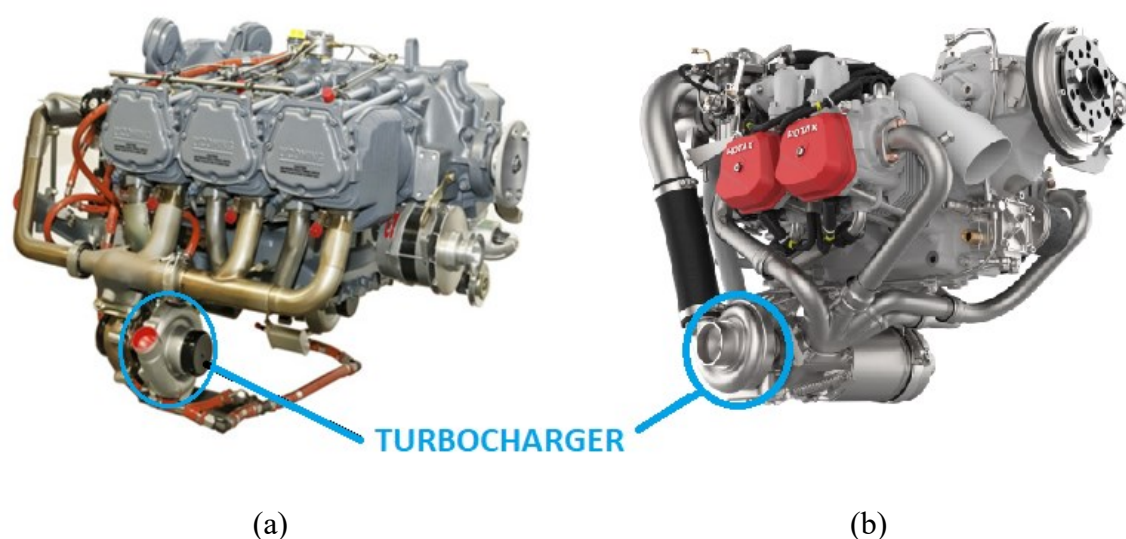


Figure 4 – Turbocharger used in the (a) Lycoming TIO-540-AE2A engine (LYCOMING, 2006) and (b) Rotax 914 F/UL (ROTAX, 2019)

Perge *et al.* (2018) point out that, in the past, automotive turbochargers could only be found in Diesel engines, but more recently they are also being increasingly used in Otto engines. Lee *et al.* (2019) present the importance of turbocharger with hydrogen-fueled ICEs. Studies of hybrid cars using turbochargers (JAIN *et al.*, 2016; URBÁNSKI and PRZYBYLA, 2022), hydrogen fueled engines with turbochargers (JILAKARA *et al.*, 2015; LEE *et al.*, 2019; LUO *et al.*, 2019) and turbocharged fuel cell systems (KERVIEL *et al.*, 2018; ROUSHENAS *et al.*, 2020; FILSINGER *et al.*, 2021; MANTELLI *et al.*, 2021) have shown important results in the use of TCs in recent years as well.

There is a permanent effort to optimize the components of car engines, and the turbochargers have received great attention from the automotive industries. The design must not only improve the thermodynamic performance and efficiency of turbine and compressor, but also try to reduce the mechanical losses of the rotor-bearing assembly and to avoid the dynamic instability arising from the bearing system due to various natural sources of turbomachinery. Ozaki *et al.* (2021) present important information on the need to develop the technology of turbochargers for next-generation engines.

2.2. ROTORDYNAMICS OF TURBOCHARGER

Schweizer (2010) and Kirk and Alsaeed (2011) described a typical turbocharger rotor-bearing system, which consists of a turbine wheel, a compressor wheel, a shaft, and bearings, as it is shown in Figure 5.

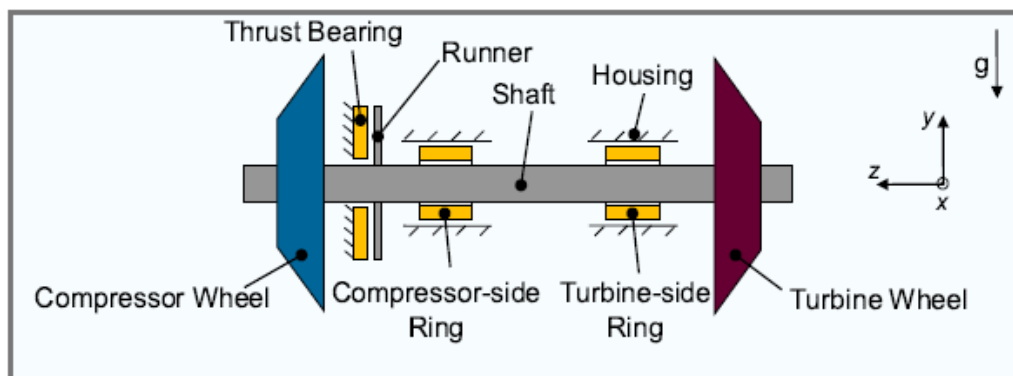


Figure 5 – Schematic drawing of a turbocharger rotor-bearing system.
(CHATZISAVVAS *et al.*, 2015)

Tian *et al.* (2012) indicate that the design of rotor-bearing system in TC must receive extra attention due the possibility of excessive vibration levels from the TC plus from the ICEs.

Engineering targets of more efficient and low cost turbochargers lead to redesign of the compressor and turbine stages to obtain better flow capacity (ALSAEED, 2005). Furthermore, more efficient rotor-bearing systems are crucial to achieve these goals. As presented, turbochargers are manufactured with fluid film bearings to provide damping to the system with low cost and easy manufacture. However, they are known for their instabilities generated by hydrodynamic action of the thin fluid film. Hydrodynamic instability is associated with cross-coupled stiffness, which usually occurs in fixed geometry bearings, as FRBs.

2.2.1. Turbocharger oil bearings

Fluid film bearings are frequently used in TCs because to their capability of generating viscous damping to the rotating system and the possibility of cooling. A thin oil film separates the rotating shaft from the steady bearing, generating a fluid film reaction viscous force capable of supporting the rotor.

The bearing instability due to the hydrodynamic action of the fluid film bearing in different types of turbomachinery has motivated the development of different bearing designs to increase the stable operating speed range of high-speed turbomachines. Allaire and Flack (1981) classify the main journal bearings used in high-speed turbomachines as (i) Fixed Pad Non-Preloaded Journal Bearings; (ii) Fixed Pad Preloaded Journal Bearings; (iii) Fixed Pad Journal Bearings with Steps, Dams, or Pockets; and (iv) Non-Fixed Pad Journal Bearings.

The first indicated above, fixed pad non-preloaded journal bearings, has as main advantages the low in cost and ease to manufacture. The main types of this bearing are plain bearings and floating bush bearings (or floating ring bearings, FRBs), both with or without axial grooves (ALLAIRE and FLACK, 1981).

Some large turbochargers (e.g., diesel locomotive TCs) use fixed pad preloaded journal bearings (or non-cylindrical journal bearings), normally 3 lobe or offset-half bearings, mounted in a squeeze-film damper, that can provide additional external damping to the rotating system, improving the rotor stability conditions.

High-speed and small TCs, for automotive and aeronautical applications, are usually supported by floating ring bearing (FRB), which consist of a freely rotating journal

bearing bushing with separated oil films between the bushing and both the shaft and the center housing. Depending on the size and load other bearing designs can be applied using a non-rotating bearing ring. Peng *et al.* (2021) and Smolik *et al.* (2020) show that studies of FRBs are more often in the rotordynamic analysis of TCs because of their better dynamic characteristics compared to other types of bearings. San Andres *et al.* (2007) explained that due to low production costs, TC assemblies are supported on floating ring bearings (FRBs), even though subsynchronous motions of significant amplitudes occur over a wide speed range. Despite of this, the subsynchronous whirl motions generally reach a limit cycle enabling continuous operation.

Pettinato and DeChoudhury (2003) discussed the redesign of a high-speed turbocharger for improved bearing life and mechanical operation. The original bearing is a three-axial-groove cylindrical journal bearing and the new is a three-lobe journal bearing. These modifications resulted in reduced oil leakage across end seals, reduced coke buildup at the turbine, increased thrust load capacity, and improved the rotordynamic response. However, this study considered the limit speed of 20 krpm. The use of FRBs has been demonstrated to be the best solution for high-speed turbochargers, where recent studies show experimental tests of non-cylindrical shapes in FRBs (ZHANG *et al.*, 2019(a); ZHANG *et al.*, 2019(b); ZHANG *et al.*, 2020), as well as numerical improvement studies of the finite element model (FEM) focused on FRBs. (BIN *et al.*, 2018; BIN *et al.*, 2021).

The FRBs have different designs. According to Nguyen-Schäfer (2015), most of the oil-lubricated journal bearings used in TCs possesses a ring with two motions: the rotation and floating in the both inner and outer oil films, as it can be seen in Figure 6(a). This type of bearing is called rotating floating ring bearing (RFRB). Some designs have another type of bearing called semi-floating ring bearing (SFRB). In SFRB, the bearing ring does not rotate in the bearing housing. The major differences between RFRB and SFRB are their assembling procedures and their ring motions. The ring in RFRB can rotate freely, as indicated in Figure 6(b), while in SFRB it cannot rotate because of a locking pin, as shown in Figure 6(c).

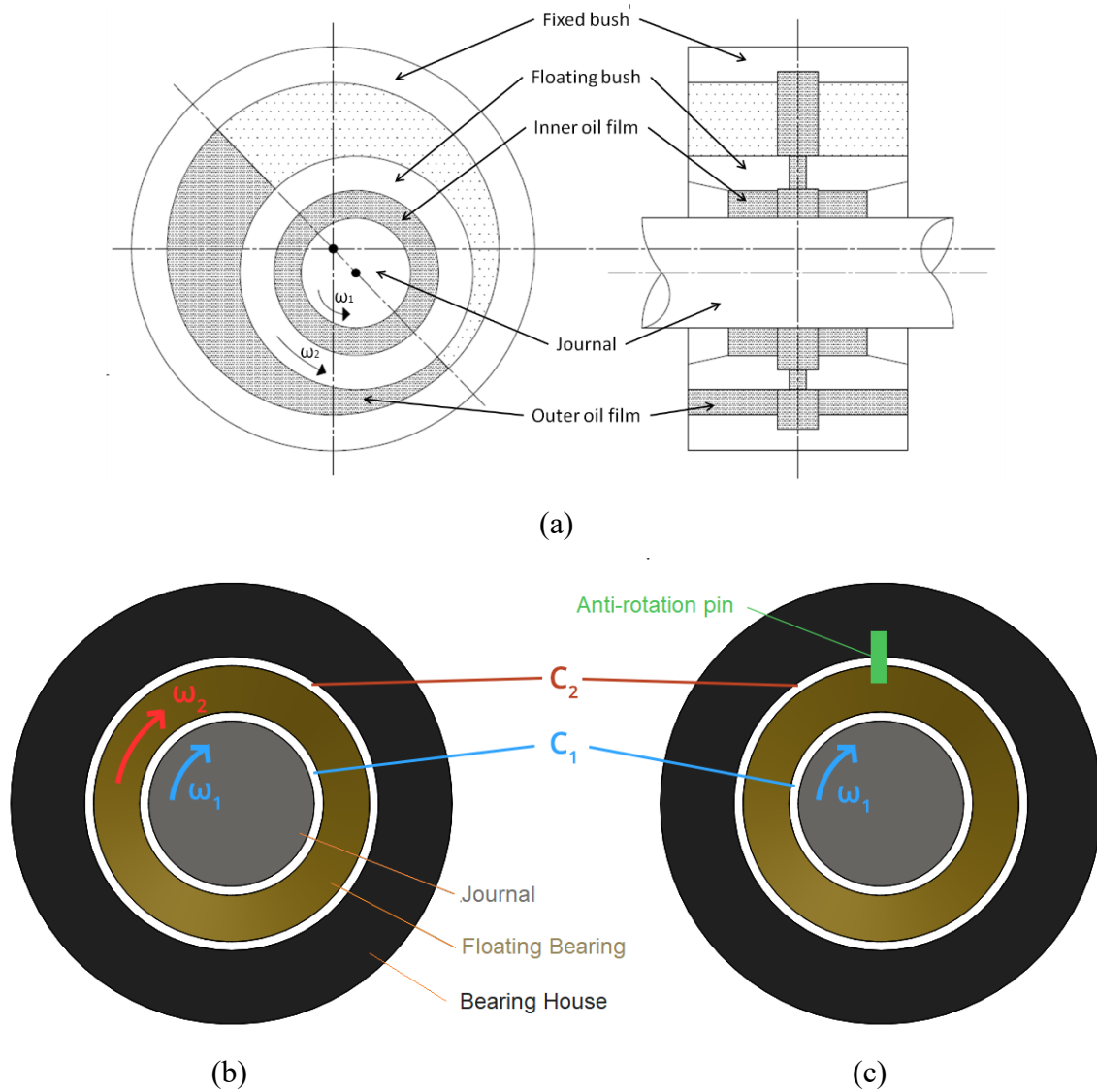


Figure 6 – (a) Rotating Floating Ring Bearing (HATAKENAKA *et al.*, 2002), and schematic figure of a (b) RFRB and a (c) SFRB

Therefore, the outer oil film of SFRB just acts as a squeeze film damper (SFD). Liang *et al.* (2016) described that RFRBs and SFRBs are utilized to decrease the vibrations by providing damping with a simple, light and affordable structure. The rings of RFRB and SFRB are set between the shaft and housing, covering loosely the journal. Two oil films are formed when the rotor rotates, and the oil film between the journal and ring is called inner film with a clearance named C_1 , while the other oil film between the ring and housing is called outer film with a clearance named C_2 . A part of vibration energy of the shaft is transferred across the inner film to the ring and dissipated by whirling motion of the outer oil film. Therefore, the outer clearance C_2 affects operating life and reliability of the rotor-bearings and needs to be paid more attention during the design process.

Comparatively, RFRB has smaller friction than SRFB, especially in TCs at low-end torque (TCs that provides more than 90% of torque at engine speeds, normally, below 3,000 rpm), improving the dynamic behavior of TC at low rotor speed. Many studies are focused on the analysis and estimation of the power losses, oil temperature problems and heat fluxes by the bearing friction. (GIAKOUMIS, 2010; SERRANO *et al.*, 2013 (b); SERRANO *et al.*, 2015; DELIGANT *et al.*, 2012; BONTEMPO *et al.*, 2015; RAKOPOULOS *et al.*, 2005; SERRANO *et al.*, 2013 (a); SERRANO *et al.*, 2007; LÜDDECKE *et al.*, 2012; SUNIL, 2012; SERRANO *et al.*, 2010; AGHAALI *et al.*, 2015; PAYRI *et al.*, 2010; KAUFMANN, 2014; ZEH *et al.*, 2020; ALAVIYOUN and ZIABASHARHAGH, 2020; ALEXANDER and PORPATHAM, 2021; SERRANO *et al.*, 2020). The common conclusion is that the determination of the bearing friction losses is fundamental in the evaluation of the mechanical losses in TCs.

Perge *et al.* (2018) stated that the TC bearing friction mostly affects the “low speed” operation of the turbocharger and is therefore relevant for the transient response and part of the load emissions of modern combustion engines. A detailed analysis of the mechanical losses occurring in the bearing system of automotive turbochargers is presented in their study.

However, SFRB provides a better performance than RFRB in stability and vibration attenuation at super high rotor speed (TIAN *et al.*, 2012), but the outer film of SFBR cannot support static load without whirling motion of the ring (BONELLO *et al.* 2002).

In the automotive industry, the RFRBs and SFRBs have become the main bearing systems for turbochargers, mainly for small/medium engines. According to Alsaeed (2005) these bearings are the best choice for the damping characteristics since they stabilize the rotor introducing external damping without the need of larger bearing housings, while the conventional geometry-fixed journal bearings provide poor stable conditions in high-speed turbomachines. Tian *et al.* (2016) states that SFRB is the mostly used radial bearing type due to the current difficulty of designs that effectively attenuate rotor instability. Kirk (2014) demonstrated that the evaluation of the SRFBs gave no indication that the RFRBs provided a smaller power loss, indicating that SFRBs are good design option for this service. Additionally, he concluded that oil flow is also a critical issue for future design considerations of oil floating bearings and a zero subsynchronous excitation may not be possible.

Lopez Hidalgo (2014) explains that the rolling bearings for TCs have the advantage of a shorter response time (turbolag or low-end torque) during the acceleration of the TC. When a TC rotor with rolling bearings is working at low speed, the coefficient of friction is smaller than a TC with floating bearings. However, at high speeds and due to the increase in oil temperature and decrease in viscosity, the difference in friction between rolling bearings and floating bearings is not significant. Additionally, the floating bearing supply damping for the system, to reduce the rotor instability, and rolling bearings have several disadvantages as compared to the floating bearings, like larger wear, higher manufacturing costs and more noise generation. In particular, floating ring oil bearings (FRBs) undergo high vibration attenuation and achieve high-speed stability due to the pair of fluid films inside and outside the floating ring (LEE *et al.* 2015).

2.2.2. Axial grooves for oil bearings

Axial grooves in fluid film bearings are of fundamental importance for the distribution of lubricant and hydrodynamic pressure, improving the lubricant capability of carrying the heat and the pressure shape which can generate an increase in the stiffness and damping for the rotating system.

There are studies for several conditions of axial groove use, such as location (ROY and MAJUMDAR, 2005; KINI *et al.*, 2009; ROY and KAKOTY, 2013), length and width ratio (DWIVEDI and PATHAK, 2021), quantity of grooves (PAI and PAI, 2008; BRITO *et al.*, 2012), surface texture (GUO, 2017; LI *et al.*, 2019; RAO *et al.*, 2020), radial angle difference (KADAM and BANWAIT, 2018), straight, small and large-angle chevron (XIANG *et al.*, 2019; WANG *et al.*, 2020), constant versus convergent widths (LIU and CHEN, 2022) among other factors of the axial grooves used in bearings. For the analysis of the effect of grooves, most existing computational fluid film bearing design simulation tools are inadequate to assess this problem as they fail to realistically incorporate lubricant feed conditions such as feeding pressure, and the actual geometry and location of feeding grooves. The lack of mass conservative algorithms might not be much of a problem in conditions where the pressure build-up region is far from the groove regions. However, when grooves start to interfere with the pressure profile, those models will be inadequate as they will not provide a rigorous treatment of groove mixing and other phenomena taking place at the vicinity of grooves. (BRITO *et al.*, 2016).

Brito *et al.* (2016) also describe that one of the greatest difficulties during axial groove design is to obtain the adequate values for the number, geometry, location, among

other factors related to the oil feed grooves, often considering heterogeneous working conditions (e.g., groove positioning in relation to the load line that change several times during the machine operation). The existence of multiple locations along the fluid film bearing surface may be desirable to provide uniform cooling and lubricant distribution, thus avoiding the lack of harmful lubricant. On the other hand, grooves can interfere with hydrodynamic pressure generation if the zone of high hydrodynamic pressure increase zone is too close to the lubricant feed grooves and they start to act as pressure reducers rather than pressure sources.

Examples of such complex phenomena are the mixing of hot lubricant coming from upstream of the groove with fresh lubricant (KOSASIH and TIEU, 2004; JEDDI *et al.* 2005) and the occurrence of reverse flow of lubricant re-entering the groove from downstream or the backflow of groove lubricant flowing upstream in the direction opposite to the journal rotation (GROPER and ETSION, 2002; PINKUS, 1990).

Several studies have been helping the design of axial grooves, such the analysis under different operating conditions (CHATTERTON *et al.*, 2017), such as variable loads (BRITO *et al.*, 2016) and oil type (MCCARTHY *et al.*, 2009), as well as in the manufacturing characteristic of the rotor and bearing, such as roughness (ROY *et al.*, 2021) and use of nanoparticles in the bearings (YATHISH *et al.*, 2014), obtaining results in the field of thermodynamics (SINGH *et al.*, 2008) and rotordynamics (BRITO *et al.*, 2007).

However, there is currently a trend in works focusing on using bearings with axial grooves considering different types of fluids (GONG *et al.*, 2019; DAS and ROY, 2018; MALLYA *et al.*, 2017), including with nanoparticles (ABASS and MUNEER, 2018; SHOOROKI *et al.*, 2021), biolubricants (ZULKHANAFI *et al.*, 2020) and water (FENG *et al.*, 2019), and systems that allow axial displacement (degree of freedom) for better rotordynamic response (XIANG *et al.*, 2019), as well as experimental studies with the variation of groove conditions in bearings are rare and there is no discussion about, for example, the influence of groove shapes on the thermodynamic and rotordynamic response.

2.2.3. Turbocharger Stability

The floating ring bearings (FRB) present a large speed range of stable operation and advantageous manufacturing costs from most of the available fluid film bearings in the market (ALSAEED, 2005). But FRBs can also generate subsynchronous vibrations in the rotating system (GUNTER and CHEN, 2005; HOLMES *et al.*, 2004; HATAKENAKA *et al.*, 2002). Ryu and Ashton (2016) concluded that the FRBs are prone to show a complex

rotordynamic behavior with large amplitude subsynchronous motions over a wide speed range. Nonetheless, the subsynchronous whirl motions reach a limit cycle, thereby providing cost-effective solutions. Then, the rotordynamic stability analysis of turbochargers becomes a vital part of the design process.

In the FRBs, the inner oil film has the function to carry the rotor and provides enough stiffness and damping for the system; and the outer oil film provides a high value for the damping coefficient to the rotor to reduce its whirl amplitude at critical speeds and attenuate some vibration noise, mainly from rotor unbalance and oil whirl. Thus, these bearings allow very high rotational speeds, but can induce self-excited shaft vibrations (BERNHAUSER *et al.*, 2017). These self-excited whirl motions caused by the fluid film bearings are generally associated with “oil whirl” and “oil whip” (VANCE, 1988). Oil whirl is probably the most common cause of subsynchronous instability in hydrodynamic journal bearings. Boyaci *et al.* (2007) explained that the “oil whip” phenomenon in FRB occurs in a different form compared to that observed in cylindrical journal bearing. The rotor at the stability limit starts either oscillating with about half of the FRB speed or the half of the FRB speed plus the half of the journal speed. The work shown that the reason is some parameters of the rotor- system and a rotor-floating ring bearing model presented with the indicated characteristics applying the nonlinear equations of motion to verify the start of the instability.

There are two main vibration sources in turbochargers (and in all other turbomachinery): first, the rotor mass imbalance, and, second, the rotordynamic instability and self excited vibration (EHRICH, 2004). The majority of automotive turbochargers with oil-film bearings exhibits strong sub-harmonic vibration. According to Holt *et al.* (2005) the increase in the lubricant feeding pressure in the bearing would lead to synchronous motions of larger amplitudes, although it would delay the onset of one of the whirl motions, and also showed that low oil temperature would decrease the amplitudes of both synchronous and subsynchronous motions. The subsynchronous vibrations cause noise, large rotor whirl amplitude and rub in rotor-stator and rotor-bearing assemblies. Studies like that of Kirk and Alsaeed (2011) presented that the bearing fluid-film instability is the main source of the vibration in automotive TCs. In their study, the high-speed diesel engine turbocharger present subsynchronous vibrations for a wide speed range. The nonlinear forces inside the bearings are causing the rotor to whirl in a limit cycle. The study had shown a new method for improving the dynamic stability by inducing the turbocharger rotor unbalance in order to suppress the subsynchronous vibration.

Rotor unbalance can be reduced by balancing the rotor and/or by straightening the shafts that have been bowed by thermal effects (ALSAEED, 2005). Correcting balancing masses can be used to reduce the rotor synchronous response, but the self excited vibrations can occur at critical operating conditions and have not always simple remedy (ALSAEED, 2005). The mechanism of self-excitation can be categorized as whipping and whirling, parametric instabilities, stick-slip rubs and chatter and instabilities in forced vibrations (EHRICH, 2004). Another important instability is the aerodynamic force in centrifugal compressors (VANCE, 1988).

According to Alsaeed (2005), whirling and whipping are the subsynchronous instabilities in turbochargers and some known sources are the internal rotor damping (hysteretic damping), fluid-film journal bearings, and aerodynamic cross-coupling.

The turbochargers with rotating floating ring bearings (RFRB) or semi-rotating floating bearings (SRFB) normally use engine oil that circulates in the bearing clearance with an average velocity of about one-half the shaft speed. It is well known that oil whirl is a half-frequency phenomenon that can progress giving rise to unstable subsynchronous whirling motion, which is associated with the oil whip (VANCE, 1988).

Figure 7 shows the tangential force component developed from the bearing thin fluid film that induces the forward whirl of the rotor. Instability occurs when such a force exceeds the inherent stabilizing damping forces.

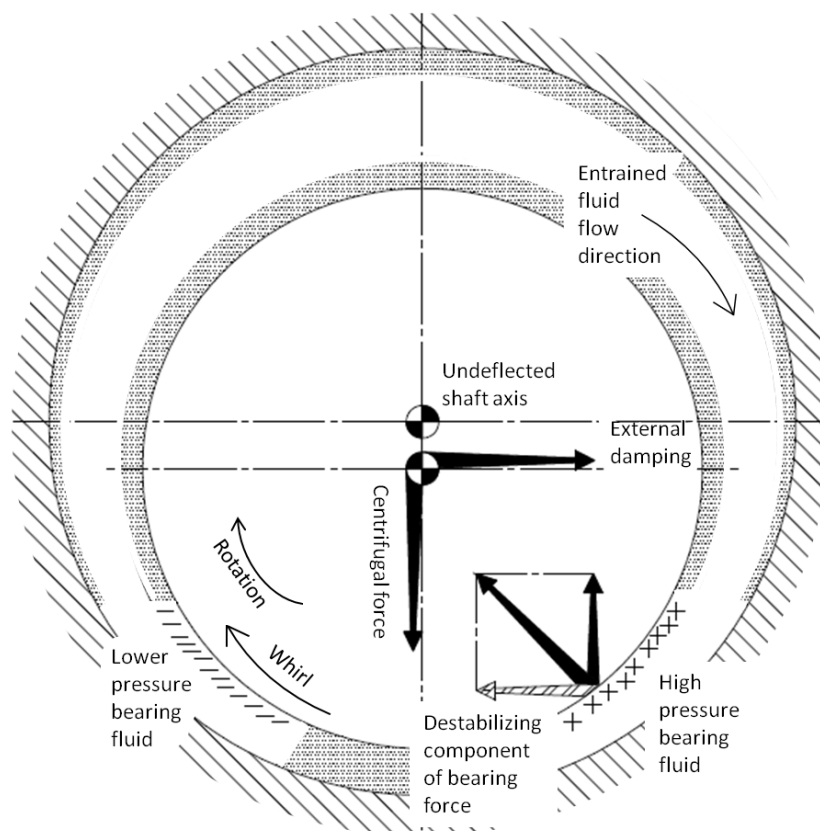


Figure 7 – The fluid film bearings with oil whirl. (EHRICH, 2004).

Fan *et al.* (2011) show that the oil whip induces other self-excited vibration and causes a self-excited reverse shaft whirling rub, known as dry-whip, which is a secondary phenomenon resulting from the oil whip. The coexistence of oil whip and dry whip in journal bearings has been experimentally observed (ROBBERSMYR *et al.*, 2014).

According to the work of Nguyen-Schäfer (2015), the turbocharger shaft rotates initially at centered position, at very small journal bearing eccentricity, because of the rotor small weight. As the rotating speed increases, the journal tends to touch the bearing housing (high unbalance force). When the critical speed is reached, the journal tends to return to the bearing center (there is a self-centering effect for the shaft at supercritical speeds).

On the other hand, shafts of industrial turbomachines usually start to rotate at of-centered position, in which the journal bearing eccentricity is not so small, due the large rotor weight. Even with the increase of the speed, the journal maintains its of-centered position near to the equilibrium position. Consequently, it has been observed that the whirling orbits of industrial turbomachines are frequently more stable and smaller than the turbocharger orbits, which makes orbit analysis a fundamental need.

In addition, Nguyen-Schäfer (2015) show that the large vibration levels at the rotor critical speeds and at the instability speed range are the two important issues in the rotordynamic analysis of automotive turbochargers

In TCs, the fluid film instability happens more often than in other turbomachines. To improve the understanding about this instability, all the rotating parts of TCs must be considered at the beginning of the rotordynamic analysis (NGUYEN-SCHÄFER, 2015).

Another important stability analysis factor to be considered is the aerodynamic influence of the compressor. In propellers, compressors, turbines and other turbomachines, destabilizing aerodynamic forces can occur due to the tip clearance variation around the circumference of the compressor blades.

These forces are known as Alford's force (ALFORD, 1965). Alford's force has been recognized as highly influential in axial compressors for nearly 50 years (EHRICH, 1972; WACHEL, 1975; VANCE, 1988), but must be considered also in the stability analysis of radial centrifugal flow machines in various applications, such as turbomachines in oil industries (API, 2014; API, 1996; NICHOLAS and KOCUR, 2005). API 617 Standard (API, 2014) and Evans and Fulton (2010) recommends that stability analysis shall

be performed on all centrifugal axial compressors and/or radial flow rotors except those rotors whose maximum continuous speed is below the first critical speed.

Li *et al.* (2021) state that there are two interface zones in centrifugal impeller that can be applied to centrifugal compressors as well: A, the boundary layer region, and B, the air domain of the impeller (Figure 8). It is further stated that the leading edge of the blade in a centrifugal compressor is the main force part, and the Alford effect is significant, while the torque of the eccentric flow field has little effect on the blade outlet.

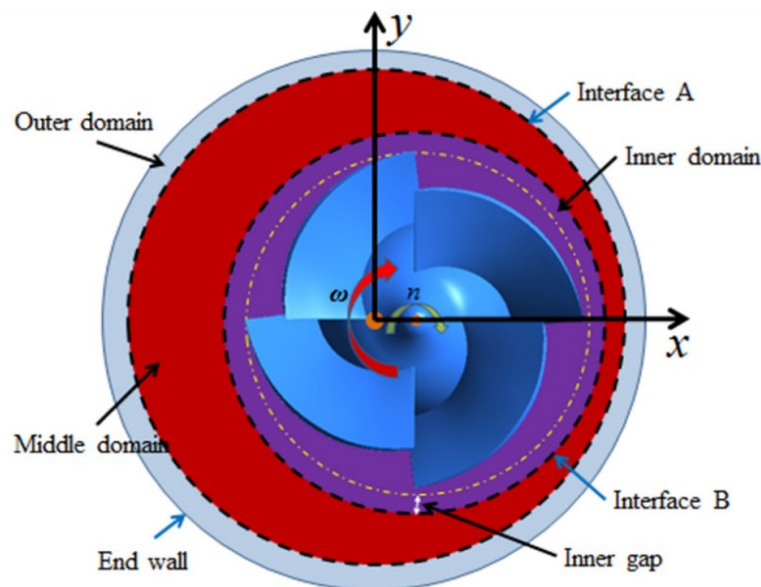


Figure 8 – Schematic diagram of dynamic sliding multi-region method under Alford's force for centrifugal compressor (LI *et al.*, 2021).

Several works show the effects of Alford's force on turbomachinery and emphasize the importance of their consideration in the rotor design (KIM *et al.*, 2003). Gunter (2020) shows that Alford's forces acting on the compressor and turbine of a TC have impact in the prediction of the rotordynamic response, which can lead to high amplitude subsynchronous conical whirl motion. Storace *et al.* (2011) indicate that the Alford's force drives backward rotor whirl over most of the compressor operating range, being an important source of instability to be analyzed experimentally.

2.3. TC ROTORDYNAMICS ANALYSIS

The steady-state turbocharger tests are an important way to obtain thermodynamic data from turbochargers (HEUER *et al.*, 2005), while it has been demonstrated that the survey of these data in a transient regime (pulsating flow) does not bring significant gains in the analysis of mass flow and efficiency (i.e., in TD analysis)

(IWASAKI *et al.*, 1994). Accelerometers and frequency spectra to analyze the rotordynamic response in turbochargers at steady-state are widely used (SCHWEIZER and SIEVERT, 2009; YING *et al.*, 2009; HOLT *et al.*, 2005; FIGURELLA *et al.*, 2014).

However, transient analysis for RD is always required. Vance (1988) shows that in the vibration transient analysis of rotating machines, it is very usual to obtain cascade diagrams, or waterfalls, during the machine run-up or coast-down. Vance (1988) also states that coast-down vibratory response is more suitable because it is carried out by turning off power, avoiding disturbances in the energy supply to the system.

Another important tool for analyzing the steady-state rotor response is the orbit analysis. Nguyen-Schäfer (2015) states that the use of displacement transducers (proximity probes) in turbochargers for orbit measurement allows visualizing the synchronous response (orbit amplitude), and instabilities such as (i) permanence in the rotor whirling orbit limit cycle, ie, without orbit "escapes"; (ii) inner and outer loops, which indicate backward and forward whirl, as well as (iii) shaft rubs with shapes called babana shape and (iv) when there is high radial load generated by cross-coupled stiffness of the bearing, in so-called lying eight shape. The use of orbits to verify the rotordynamic response at steady-state conditions in TCs has been performed in several studies (LEE and HONG, 2017; PENG *et al.*, 2021; CAO *et al.*, 2017) and the use of frequency spectra plus orbit analysis has become more frequent in TCs analysis (SINGH and GUPTA, 2020) as presented in Figure 9.

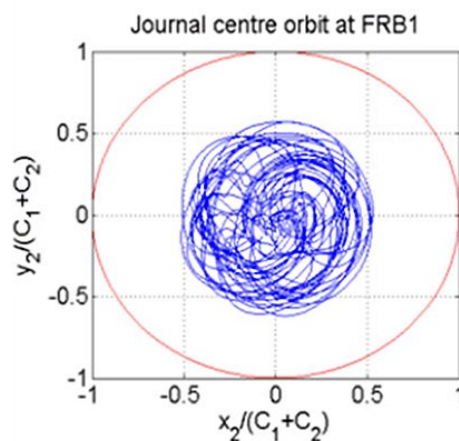


Figure 9 – Orbit map for a TC (SINGH and GUPTA, 2020).

Holmes *et al.* (2004) indicate the importance to employ the waterfall plot in the vibration analysis of turbochargers due to the non-linear nature of the fluid film bearings. The authors show that a typical automotive turbocharger with floating ring bearings present high subsynchronous vibration amplitudes, indicating that the oil whirl instability starts at

a very low speed. They state the vibration tests at transient conditions are important to observe the instability in turbochargers, which is performed using the Waterfall plot (Figure 10).

In the analysis of Figure 10, Holmes *et al.* (2004) show that the first low frequency oil whirl mode dominates over a large speed range and is a rigid body mode of conical shape with the turbine and compressor wheels moving out of phase. Above 40,000 rpm, a second whirling mode starts. Both turbine and compressor wheels are whirling forward in phase at the second natural frequency. A second oil-whirl mode stops around 55,000 rpm which is explained by the starts of the turbocharger third mode, slight increasing the bearing load. Above 70,000 rpm, the oil-whirl second mode limit the cycle motion.

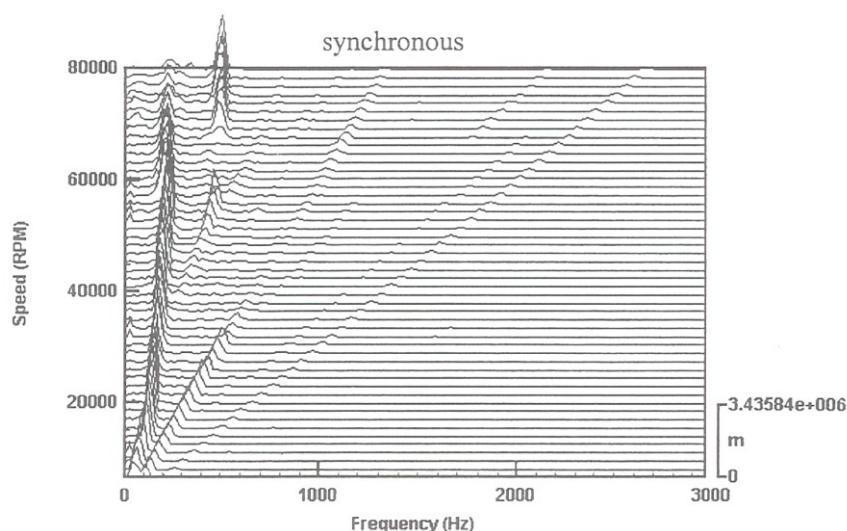


Figure 10 – The Waterfall plot for a turbocharger (HOLMES *et al.*, 2004).

Another important analysis using waterfall in TCs with FRBs occurs in the field of inner and outer oil whirals. Tian *et al.* (2012) analyze the dynamic behavior of rotor-bearings system in fuction of the FRB outer clearance. Through run-up and coast-down vibration tests, it is observed nonlinear frequency jumps of critical limit cycle oscillations.

Figure 11 presents the usual form of presentation of the waterfall plots for turbochargers in a 3D format to analyze the inner and outer oil whirl as well.

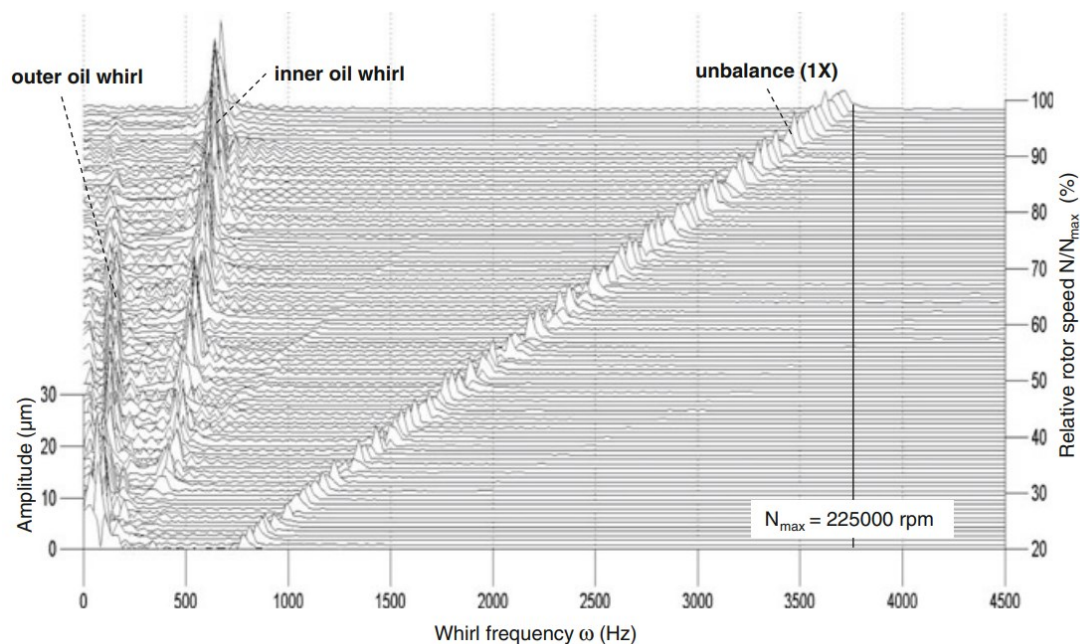


Figure 11 – 3D Waterfall diagram for a turbocharger (HUNG-NGUYEN SCHÄFER, 2015).

Schweizer (2009) explains that both inner and outer oil films of FRBs can become unstable and exhibit oil whirl/whip instabilities and in another work Schweizer (2010) indicates that the dynamics of the system is dominated by the nonlinear behavior of the full-floating ring bearings. In both papers, the author uses the waterfall 2D and 3D to analyze the bifurcation, which is the study of different conditions to start the instabilities in TC bearings.

This bifurcation is associated with a strong instability, which, in many times, resulted in the rotor destruction. This fatal instability is called Total Instability. It is shown that Total Instability is caused by synchronization of two limit cycles, namely synchronization of the inner and outer oil whirl/whip. Total Instability is of practical interest and observed in real technical rotor systems, and frequently leads to complete rotor damage (SCHWEIZER, 2010).

To determine the existence and the approximate size of stable and unstable limit cycles in the neighbourhood of the stability critical speed depending on the bearing design parameters, the Hopf bifurcation is used (AMAMOU and CHOUCANE, 2011). A Hopf bifurcation is explained by Strogatz (2018) as a critical point where any system switches from stability to instability and a periodic solution arises, i.e., it is a local bifurcation where any dynamical system fixed point starts to be instable.

The Hopf bifurcation theory is used in some studies to analyze dynamic response of rotating systems supported on oil lubricated bearings and verify the conditions

for instability (BOYACI *et al.*, 2007; AMAMOU and CHOUCANE, 2011; BROWN *et al.*, 2000; INOUE and ISHIDA, 2006; SCHWEIZER, 2009; TIAN *et al.*, 2013). Singh and Gupta (2020) and Amamou (2022) show several numerical studies to try to detect the instability in order to enlarge the understanding about procedures that can be used in controlling vibrations in turbochargers.

Holt *et al.* (2003(a)) explain that current automotive turbochargers with floating ring bearings (FRB) and RFRBs are less used than SFRBs due to the vibratory response, but SFRBs often exhibit subsynchronous instabilities reaching limit cycles. They also have shown that the subsynchronous whirling frequencies of a TC do not lock (whip) at the system natural frequencies but continuously track the rotor speed. Waterfall plots, subsynchronous whirling curves and temperature analysis are performed to show this finding. Moreover, Holt *et al.* (2003(b)) compare the experimental data about instability with the nonlinear rotordynamic predictions. The predictions evidence two unstable whirl ratios at approximately half ring speed and half ring speed plus half journal speed. The transient nonlinear responses reveal the importance of rotor imbalance in suppressing the subsynchronous instabilities at large rotor speeds.

If the inner oil films become unstable (inner oil whirl/whip), the stable outer oil films act like an “external” damper so that the inner oil whirl/whip may be passed through it. On the other hand, the oil whirl/whip of the outer oil films is damped by the inner fluid films. Due to the mutual damping between the inner and outer oil films, the inner and outer bearing eccentricities remain well below in the oil whirl/whip region

Simulations and measurements from Schweizer (2010) showed that normally two rotor modes are excited in the turbo-charged system analyzed: the gyroscopic conical forward mode and the gyroscopic cylindrical forward mode. The oil whirl/whip frequencies of the inner and outer oil films excite these two modes. For San Andrés *et al.* (2012), it is usual as well to obtain two typical subsynchronous responses associated with the cylindrical and conical whirling mode shapes in rotors supported by SFRBs.

In the same way, Schweizer and Sievert (2009) observed four main frequencies of FRBs including a synchronous and three subsynchronous vibrations. Run-up spectra of the rotor exhibited three characteristic subsynchronous frequencies:

- 1st Subsynchronous (Sub1) - oil whirl/whip frequency ω_{Sub1} of inner oil film excites the gyroscopic conical forward mode;
- 2nd Subsynchronous (Sub2) - oil whirl/whip frequency ω_{Sub2} of inner oil film excites the gyroscopic cylindrical forward mode;

- 3rd Subsynchronous (Sub3) - oil whirl/whip frequency ω_{Sub3} of outer oil film excites the gyroscopic conical forward mode.

Figure 12 shows the subsynchronous vibrations in FRBs observed by Schweizer (2010).

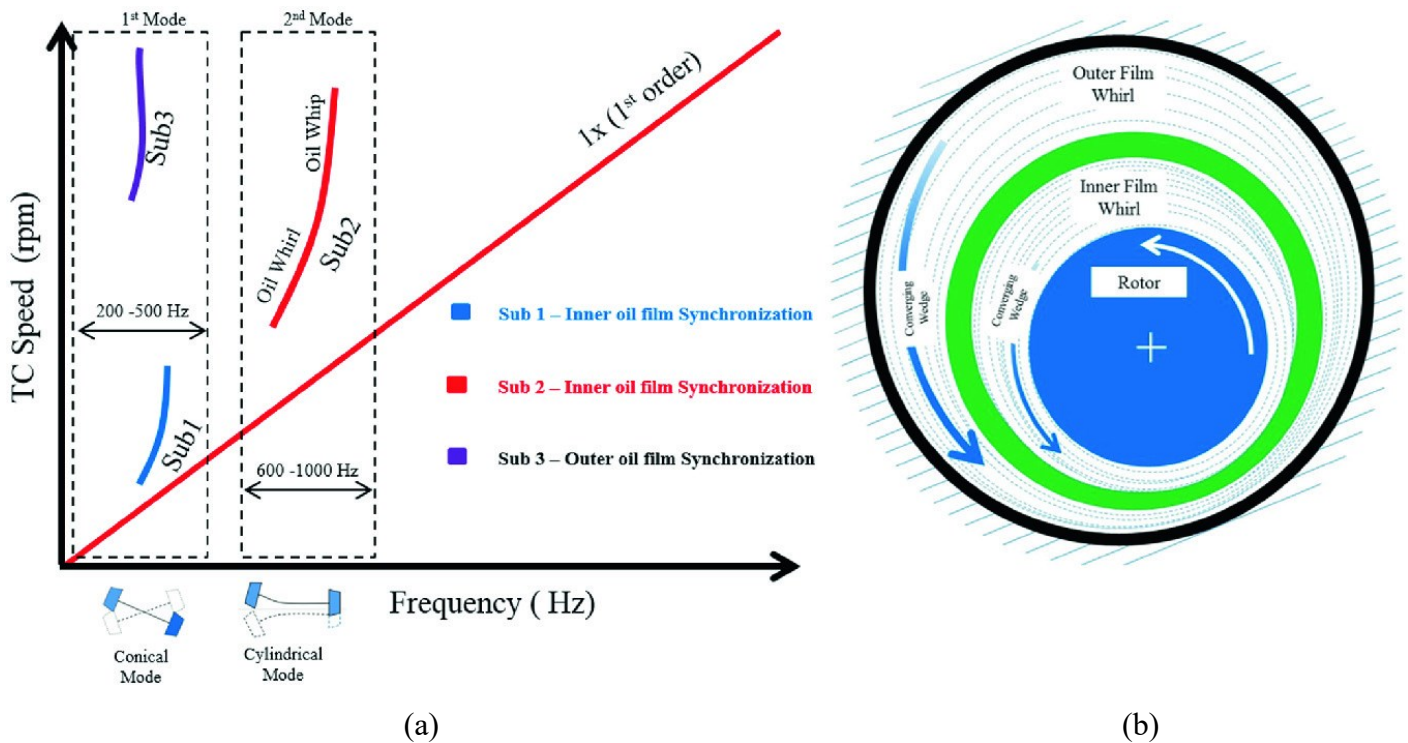


Figure 12 – (a) Curve of a 2D waterfall spectrum with synchronous and subsynchronous vibrations in a TC FRB and (b) schematic drawing of the outer and inner films of a FRB. (CHANDRASEKARAN *et al.*, 2021).

The Alford's force is another instability that must be analyzed in TCs with FRBs. Wohrab (1983) concludes with experimental results that flow-conditioned forces have direct influence on rotor-bearing behavior and the bearing design must consider these aerodynamic forces.

Gooding *et al.* (2020) present that the Alford's force can be detected in waterfall and orbit graphs in an experimental apparatus. The Alford's force in compressors with fluid film bearings can be observed by a split of two subsynchronous parallel lines that occurs when the damping is insufficient to prevent the action of aerodynamic forces, as shown in Figure 13.

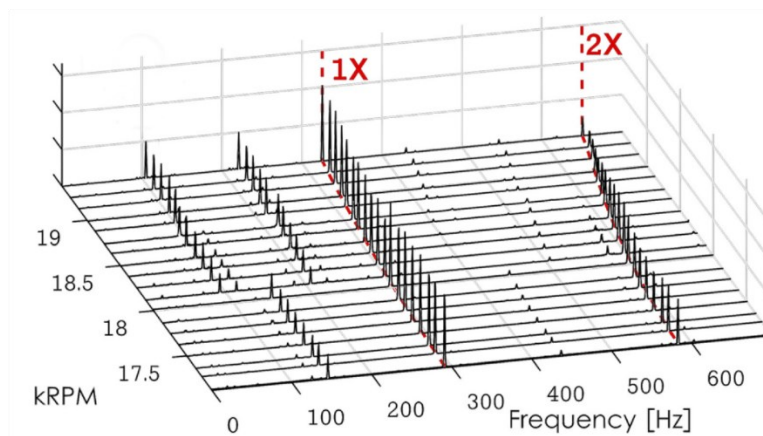


Figure 13 – The split in two subsynchronous due the Alford's force and reduced damping observed in a waterfall diagram. (GOODING *et al.*, 2020).

Acoustic Emission Measurements for Turbochargers

In the literature review performed for this work, it has been not found publicatitons dealing with the vibratory analysis of automotive turbochargers employing acoustic emission (AE) analysis. On the other hand, noise measurements to analyze the dynamic behavior of turbochargers have been described in many works, in which measurements of the air pressure are performed by microphones, using different frequency bands between 1 and 40 kHz (HUNG-NGUYEN SCHÄFER, 2013; TENG and HOMCO, 2009; RAVAGLIOLI *et al.*, 2015; SHARMA *et al.*, 2019; SANDOVAL, 2019; DOLATABADI *et al.*, 2020) obtaining generalized information about TD and RD responses.

Other works also try to obtain specific information about the acoustic pressure surge condition (LIU and ZHENG, 2013; MARELLI *et al.*, 2018; SHARMA *et al.*, 2018; GALINDO *et al.*, 2017; KABRAL and ÅBOM, 2018; BANERJEE *et al.*, 2022), but without obtaining expressive results in conditions of pre-surge.

One of the greatest difficulties in using AE is the sensor mounting. The removal of air from the interface between the measurement surface and the AE sensor is crucial (THEOBALD *et al.*, 2008). Rigid bases and the installation of the sensor to the bases using thermogreases are important also to guarantee the transmission of the wave propagation energy, even at high temperatures.

Another important point in using AE signals is the threshold analysis, which is necessary to estimate the range of frequency to perform the AE measurements (UNNPÓRSSON, 2013). The initial calibration of the AE transducer requires special attention and can be performed using the break of a hard graphite lead on the measurement

surface to estimate the AE acquisition threshold (BOCZAR and LORENC, 2006; SAUSE, 2011; BABAK *et al.*, 2006).

The use of AE is widely used in rotating machinery condition monitoring and faults diagnosis. The sources of AE generation in rotating machinery are from the interaction of two media in relative motion such as impacts, friction, turbulence, cavitations, leakage, etc. (AL-OBAIDI *et al.*, 2012). The influence of size and depth of fractures in the shaft (PIMENTEL-JUNIOR *et al.*, 2016; SAWICKI *et al.*, 2009) is well determined by the use of AE. The use of AE to detect shaft-to-seal and seal to blade-tip rubbing in turbomachines have been investigated (LEAHY *et al.*, 2006; MBA and HALL, 2002; ABDELRHMAN *et al.*, 2014) where it is concluded that AE technology could be used as a tool for detecting seal and blade rubbing. In a similar way, analysis of sliding contact in machine elements (BORGHESANI *et al.*, 2018) can be detected using AE technology. The failure detection in rolling bearings (ROGERS, 1979; GAO *et al.*, 2017) is another important capability of early problem detection. Al-Dossary *et al.* (2006) and Al-Dossary *et al.* (2009) concluded that the geometric defect size in rolling bearings could be determined from the AE waveform. The developments in application of AE to gear defect diagnosis have been reviewed by Toutountzakis *et al.* (2005). They concluded that AE techniques used in gear defect detection is fraught with difficulties. Eftekharnejad and Mba (2009) presented an experimental investigation for the assessment of the effectiveness of AE in identifying induced defects on helical gears and that there is a direct relationship between AE and volume of removed material. In these works, the main form of treatment uses Wavelet transforms of different types (highlighting the Daubechies Wavelets). Most of these studies show that AE measurements are more sensitive than vibration measurements.

In turbomachines, one of the main uses of AE is in the analysis of cavitation of propellers, compressors, turbines and hydraulic pumps. Several works involve the detection/measurement of vortex cavitation due to tip clearance of propellers (LEE *et al.*, 2018; HAN *et al.*, 2018), modification of the flow of hydraulic pumps (MOUSMOULIS *et al.*, 2019), rotor wear (LINHARES *et al.*, 2011) and the influence of corrosion propagation over time in the mass flow (ALI *et al.*, 2019). In these cases, in addition to the wavelet transform, some bandpass filters also show good results. The importance to use large frequency range in the evaluation of the dynamic of turbomachines is due to AE be very sensitive to incipient defects (SIKORSKA and MBA, 2008) detecting transient elastic waves produced by a rapid release of energy from a localized source (VAHAVIOLOS, 1999)

Iga *et al.* (2011) explain that cavitation is a phase change phenomenon from liquid to gas that occurs in low-pressure regions of high-speed fluid machinery. Surge, as explained before, is an insufficient suction mass flow. However, both are turbomachine phenomena and generators of instabilities in the system. The use of AE transducers to analyze cavitation is already recognized as an important methodology to prevent turbomachines from entering into cavitation, for example, in liquid-propelled rockets (JOLLY, 1988; ALHASHAN *et al.*, 2016). One typical flow instability is the cavitation surge (FURUKAWA *et al.*, 2002), which is system instability accompanied by a pulsation phenomenon in the duct system. The cavitation are obtained for propellers in pumps at 60 to 120 kHz (RUS *et al.*, 2007) and even for the analysis of cavitation in tree plants at 100 to 200 kHz (VERGEYNST *et al.*, 2016). For journal bearings, cavitation is observed in frequencies between 175 and 230 kHz (PODDAR and TANDON, 2020).

The use of AE is important to detect certain types of failures in equipment that use rolling and plain bearings (AL-GHAMD and MBA, 2006), especially in extremely slow rotational speeds (MBA *et al.*, 1999(a); MBA *et al.*, 1999(b); JAMALUDIN *et al.*, 2001), when an early failure detection is desired (YOSHIOKA and FUJIWARA, 1982; YOSHIOKA and FUJIWARA, 1984) and to monitor split bearings with seeded defects on the inner and outer races (MORHAIN and MBA, 2003).

Current and relevant works to analyze friction and wear for journal bearings based on Acoustic Emission signals are those published by Mokhtari (MOKHTARI and GÜHMANN, 2018; BOTE-GARCIA *et al.*, 2020; MOKHTARI, 2020; MOKHTARI *et al.*, 2020). In these works, the types of interaction between fluid film bearing and rotor are studied at three friction states: dry (boundary), mixed, and fluid friction. The main contribution of these works for this study is given by the treatment and analysis of AE data, considering filtering methodologies (using bandpass filters) and types of statistical analysis using windowing signals and types of signal measurements. Most works that use AE for rotating machines have the limitation of analyzing through windowing, i.e., the AE data is segmented in such a way that only one rotation is obtained, and its characteristic analyzed or by using some statistic function on selected frequency ranges.

This methodology is the same used for monitoring the useful life of aerospace power gearbox drivetrain by Rolls-Royce (NOWOISKY *et al.*, 2020) and will be the basis for processing the data in this work together with the cavitation studies described above (similar as MOUSMOULIS *et al.*, 2019). Figure 14 shows the AE monitoring method for Rolls-Royce power gearbox analysis.

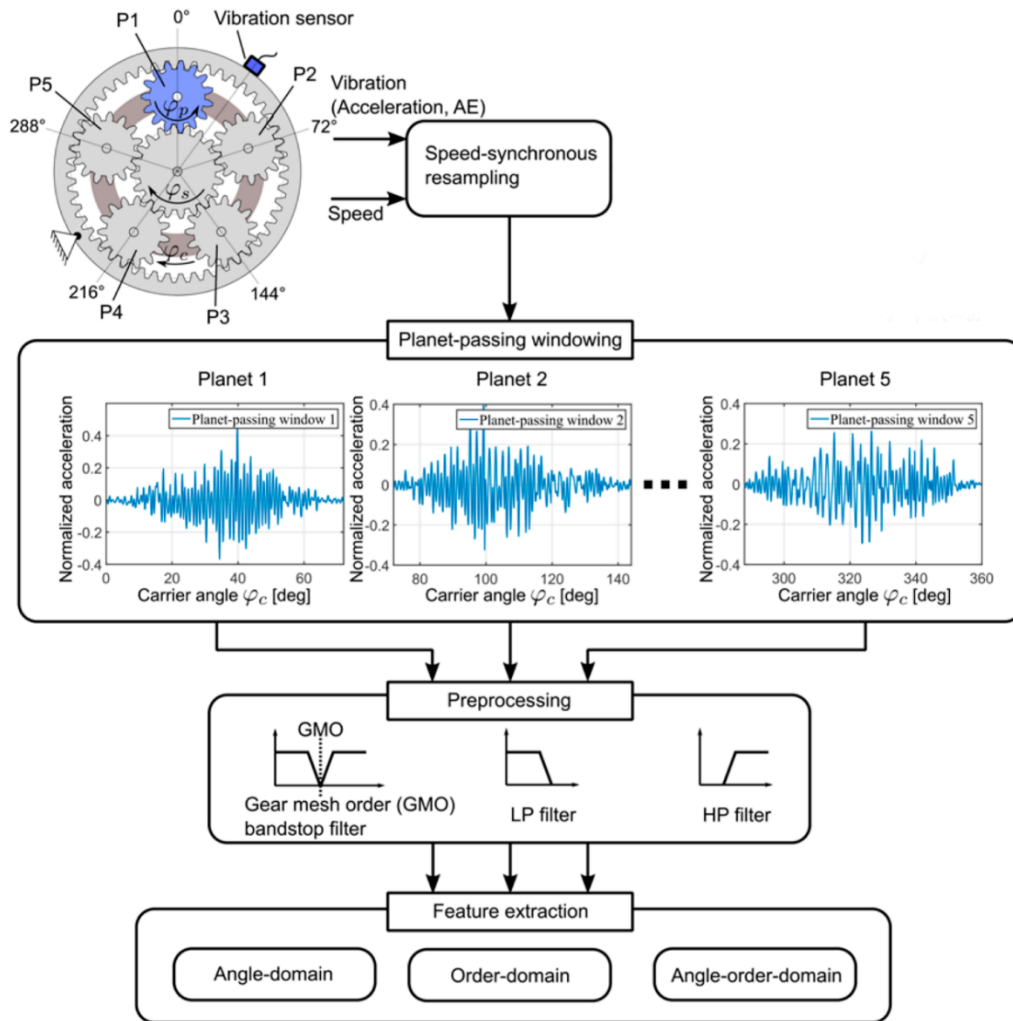


Figure 14 – Rolls-Royce Power Gearbox monitoring method (NOWOISKY *et al.*, 2020)

The method presented by Nowoisky *et al.* (2020) aims to detect locally distributed failures on the planet gears and the sun gear. The main idea to use AE are to monitor (i) the vibrations of the meshing tooth of each planet gear separately to detect anomalies in the vibration patterns when faulty teeth are in contact and (ii) the wear of hydrodynamic journal bearings during several conditions. Raw AE signals are obtained and in the preprocessing step, various filters such as low-pass filters, gear mesh band-stop filters for revealing the vibration sidebands, and high-pass filters are applied to the window-shaped vibration signals to feed the feature extraction methods. Afterwards, features are extracted from the time-domain AE signal (e.g.: root mean square (RMS), kurtosis, crest factor, in this case, the time-domain has been replaced by angle-domain to make it easier to find faults) and from the specif gear order-domain of the AE signal. In addition to the method presented, non-resampled vibration signals are also windowed in the time-domain and used for preprocessing and feature extraction to allow a detection of abnormal vibration characteristics in the vibration signals that occur throughout the gear train due to gear failures.

2.4. TURBOCHARGER TEST RIG

The literature presents a large number of Turbocharger On-engine Experimental Tests. One of these is the vibrational tests done by Kirk *et al.* (2010). Also, Nossier *et al.* (2016) introduced an experimental-based approach to measure the shaft/bearing clearance of turbocharger without disassembling it.

Few works use benches with hot air flow generated externally without the influence of a Diesel or Otto cycle engine. Noteworthy are the benches presented by Galindo *et al.* (2006) and Serrano *et al.* (2010) at CMT-Motores Térmicos (Universitat Politècnica de Valencia, Spain) and Sandoval (2019) at CTM (Universidade Federal de Minas Gerais, Brazil). The advantages of external hot air TC test rig are, mainly, the simulation of the real temperature conditions of the air mass that enters into the turbine housing (in the real case, from the exhaust gases of the ICEs), as well as the absence of the use of ICEs to simulate the gases under these conditions. Without the ICEs, it is possible to more precisely vary the input of hot gases into the turbine sub-system (flow, temperature, pressure of the gases without the influence of other intrinsic parameters of ICEs, as pulsation), obtaining better TD analyses, and not generating excessive vibrations that are normal in any reciprocating engine. , which negatively influence the DR analyses.

Rubio and San Andrés (2006) study indicated that the design of fluid film bearings remained a more empirical one and test rigs to obtain correct parameters of fluid film bearings are strongly important.

Lopez Hidalgo (2014) tested TCs with RFRB and SFRB in different failure conditions, as low oil-pressure or no-oil condition, presenting a rotordynamics analysis methodology for experimental tests and important new results that has not been previously obtained via numerical simulations.

Ryu and Yi (2018) presented measurements of static load characteristics on the wire mesh bearing dampers (WMDs) for application into small automotive TCs. No dynamic analysis is performed. Measurements of stiffness and damping parameters of a wire mesh dampers for SFRBs in automotive turbochargers are performed to evaluate the role of the new SFRB, which has been developed for improving the rotordynamic and vibration performance of automotive TCs at extreme operation conditions, such as high temperature, severe external force excitation, and large rotor imbalance. According to the authors, the new bearing design replaces outer oil films, i.e., squeeze film dampers (SFDs), in TC SFRBs with WMDs. This new bearing is intended to be an inexpensive and simple

alternative to SFDs, with consistent and superior damping capability, as well as predictable forced performance.

For AE tests of rotordynamic response, Nowoisky *et al.*, 2020 used a test rig shown in Figure 15 with the AE sensor mounted on the bearing cap to obtain information of gear wear, pitting, and gear teeth cracks, and different bearing conditions like low speeds, overload, start/stop cycles, insufficient oil supply or oil contamination.

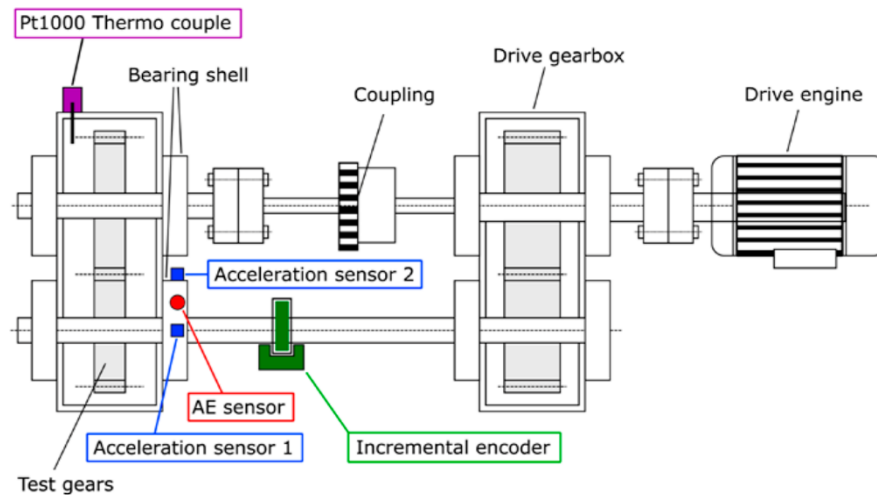


Figure 15 – Sensor instrumentation for the Rolls-Royce power gearbox test rig. Font: NOWOISKY *et al.* (2020)

Mousmoulis *et al.* (2019) explain in their studies the best set up of AE sensor to be performed on turbomachines. The AE sensor in the axial axis of a centrifugal pump is used to obtain cavitation characteristics, as shown in Figure 16.

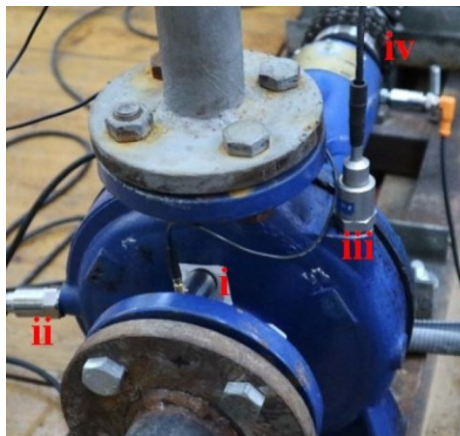


Figure 16 – Test set up for cavitation analysis using AE sensor (sensor 'i' in the Figure) (MOUSMOULIS *et al.*, 2019).

2.5. COMPARISON AND RANKING METHODOLOGIES

Several classifications and rankings through qualitative analyses have appeared on numerous publications. An example is Boyce (2010) who compares and classifies different types of bearings based on important parameters used in academia and industry and these are ranked in the order of growing stability. For different types of journal bearings, the RD analysis consider load capacity, suitable direction of rotation, resistance to half-speed whirl, and stiffness and damping. In thrust bearings, the same parameters of load capacity and suitable direction of rotation of the journal bearing are observed, but new classifications are performed considering tolerance of changing load/speed, tolerance of misalignment and space requirement.

One of the methods of classification of experimental data for an easier comparison and classification is the multiple-criteria decision-making (MCDM). MCDM is a technique that combines alternative's performance across numerous, contradicting, qualitative and/or quantitative criteria and results in a solution requiring a consensus (SEYDEL, 2006; KOLIOS *et al.*, 2016).

To facilitate a technique to rank the TCs in this work, the decision matrix using the Pugh method (PUGH, 1981; PUGH, 1996; OKUDAN and THAID, 2008) based on MCDM. The Pugh method is considered to allow a list of various results and their importance to provide a single higher rank. In recent years, several works that need to compare different data use the original or modified Pugh method, as in rotordynamics (Malkawi *et al.*, 2019), for turbochargers (Galindo *et al.*, 2017) and experimental works (Gürbüz and Gönülaçar, 2022). In this work, the TC rank is based on a Modified Pugh Weighted Matrix considering (i) most preferred concept; (ii) target requirements; and (iii) sensitivity analysis (TAKAI and ISHII, 2004). For the 7 TCs, a finer five- to nine-point scale is chosen for each case (SUBEDI, 2020). The Pugh weighted decision matrix presents better ratings in project engineering decisions (DE ANDRADE *et al.*, 2020).

3. METHODOLOGY

This chapter describes the experimental test apparatus employed to obtain thermodynamic (TD) and rotordynamic (RD) characteristics of turbochargers (TCs) with the components of the hot tub with tubular combustion chamber, including the data acquisition system, the transducers, the actuators and the all main components of the instrumentation system.

In addition, the turbochargers (TCs) parameters with different axial grooves shapes and the rotor-bearings assemblies used are shown, as well as the methodology to obtain TD signals (temperatures, pressures, flows) and RD signals (frequency spectrum, waterfalls, orbit plots and acoustic emission), besides presenting the operating conditions associated with pressure variation and the performance flow maps and graphs of TCs.

Although the focus of this work is the rotordynamic (RD) analysis, it is important that the thermodynamic (TD) analysis be carried out in parallel to verify the influence of bearing modification on the main design parameters evaluated in turbochargers.

A propagation analysis of measurement uncertainties is also presented to estimate the reliability in the measurements performed on the test apparatus.

3.1. TURBOCHARGER TEST WORKBENCH (OVERVIEW)

The design of the turbocharger test workbench used in this work meets the requirements of the standards currently established by the international institutions (SAE, 2022; SAE, 2011; SAE, 1995). The workbench operates in several different working regimes with adequate thermodynamic properties, simulating the exhaust gases of an internal combustion engine. The apparatus has interconnected instruments and devices for the measurement of independent variables in order to obtain performance maps and graphs throughout the working regime, as well as dynamic response graphs of the TC.

The hot-flow turbocharger test workbench redesigned and built in this work uses the configuration established by Venson (2007) and updated by Sandoval (2019): it is characterized by a hot-flow workbench with a tubular combustion chamber designed to work with gaseous fuels with several instruments for characterization of thermodynamic maps and rotordynamics analysis.

Figure 17 illustrates the basic configuration that is adopted and built in the automotive turbocharger testing laboratory of the Centro de Tecnologia da Mobilidade (CTM) at the Universidade Federal de Minas Gerais (UFMG), Brazil.

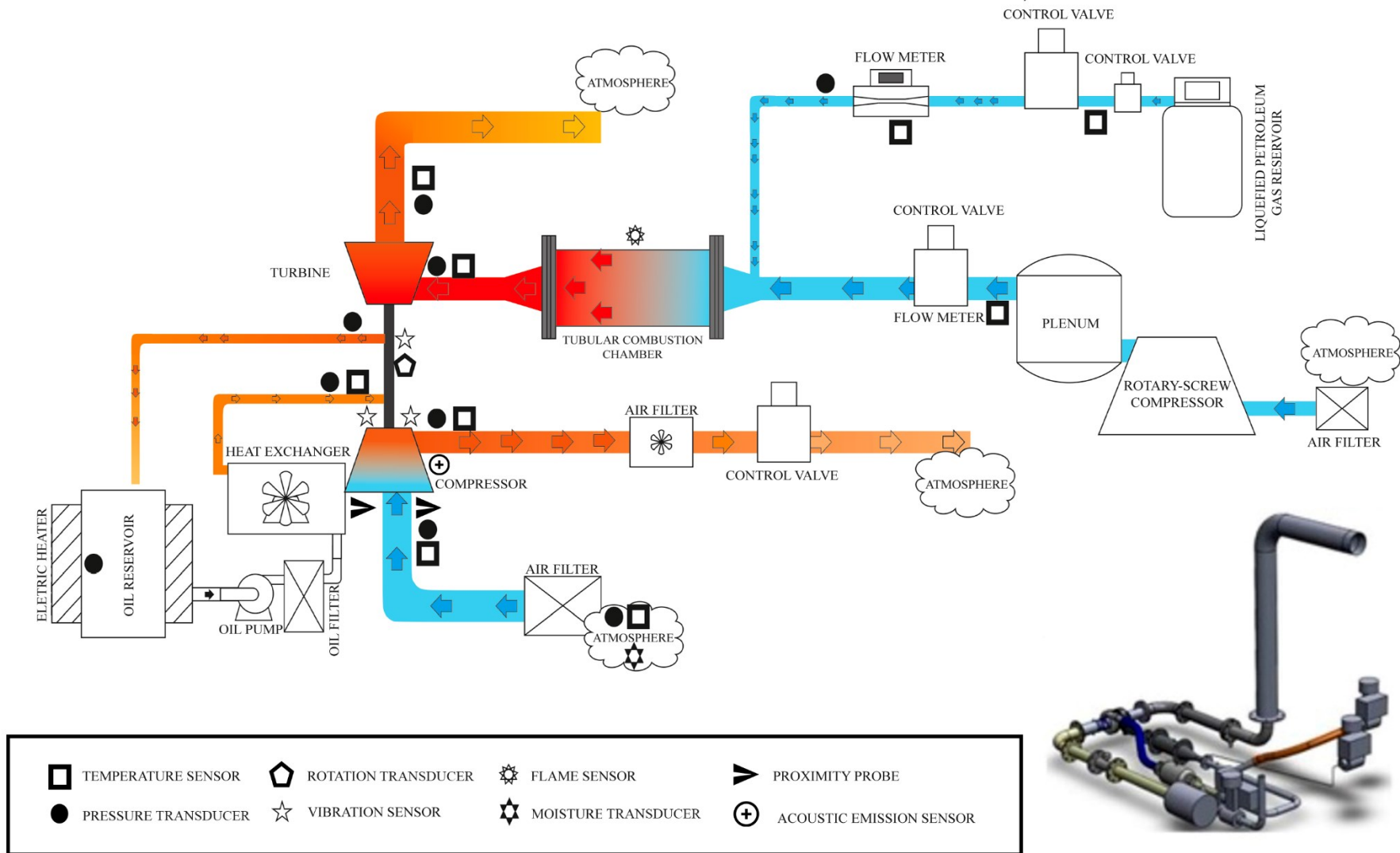


Figure 17 – Configuration of the LABTURBO-CTM (UFMG) hot-flow workbench used in this work. (Updated from SANDOVAL, 2019)

According to the results obtained by Sandoval (2019), the workbench and all its auxiliary systems proved to be robust enough. The TD measuring uncertainties of the instruments do not significantly influence the results and, therefore, this instrumentation is adequate for the development of the tests. Figure 18 presents the test bench overview.



Figure 18 – The LABTURBO-CTM (UFMG) hot-flow workbench

The fundamental variables to obtain the flow maps and thermodynamic graphics are selected according to SAE J1826 (SAE, 2022) and SAE J1723 (SAE, 1995) standards, respecting the distances and angles in which the pressure transducers, temperature sensors and flow meters are installed for each outputs and inputs of the turbocharger.

To improve the understanding of the workbench, a specific description of the components used can be divided into nine sets:

1. The turbocharger and components used (compressor, turbine, shaft, housing, journal bearing, thrust bearing).
2. air line components (volumetric compressors, air reservoir, air flow control valve);
3. fuel line components (fuel gas tank, safety valve, gas control valve);
4. compression line components (air filter and reservoir, compressor flow control valve);
5. components of the lubrication system (motor pump, oil filter, oil cooler, oil tank, oil heater);
6. components of the tubular combustion chamber;

7. control room components (control center, control panel, electrical panel);
8. TD data monitoring and recording devices (transducers, boards, drivers); and
9. RD data monitoring and recording devices (transducers, boards, drivers).

The validation of the thermodynamic map construction algorithm in this work is presented in Sandoval (2019).

Sections 3.2 to 3.6 describe each set described here.

3.2. TURBOCHARGERS

The experimental tests used a set of seven automotive turbochargers from Biagio Turbos Brazil, the AUT1000. This turbocharger model is used by the availability and interest of the MGFC Ltd. (Biagio Turbos brand owner) in this research. Table 1 shows the main geometric characteristics of the TC used.

Table 1 – Technical data of the Biagio AUT1000 Turbocharger (BIAGIO, 2021)

Data	Turbocharger
Manufacturer	MGFC Ltd. (Biagio Turbos)
Model	AUT1000
Type of ICE used and manufacturer	<i>Fully Integrated Robotised Engine (FIRE)</i> , 1.0 liter (999 cc), Fiat Powertrain Technologies ¹
Part number	5827109101
Compressor Area/Radius	0.48
Compressor Wheel Diameter	49 [mm]
Compressor Inducer Diameter	32.5 [mm]
Compressor Blades	6 full + 6 splitter
Compressor Housing Blades	N / A
Turbine Area/Radius	0.35
Turbine Wheel Diameter	45.5 [mm]
Turbine Inducer Diameter	35.5 [mm]
Turbine Blades	10 full
Turbine Housing Blades	N / A
Shaft diameter at bearing assembly	8 ± 0.002 [mm]
Weight	9 [kg]

¹ The Brazilian FIRE 1.0 liter engine did not come from the factory with the turbocharging system. The turbocharger can be installed by the user in a specialized mechanic workshop.

These TCs have been selected because of the feasibility of using bearings with different geometries in order to permit evaluate thermohydro- and rotor-dynamic behavior of the rotating machine running on different supporting systems. Figure 19 shows the AUT1000 automotive turbocharger model used for the tests in this work.

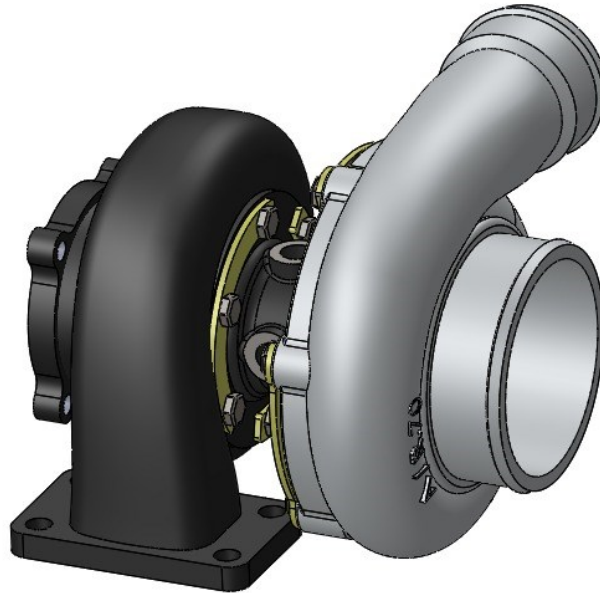


Figure 19 – Schematic drawing of the Biagio Turbos TC AUT1000 (BIAGIO, 2021).

The difference among the TCs selected in this work is only the fluid film journal bearing, which has different axial grooves shapes. All the other components, such as thrust bearing, shaft, volutes, blades, internal lubrication system and others are the same Part Numbers.

The TCs are tested and balanced at the MGFC facilities before they are assembled in the testing bench, and the details will be presented later in Section 3.4.

3.3. FLUID FILM JOURNAL BEARINGS

The AUT1000 fluid film journal bearings have been designed to work as double support in a one bearing component. The double bearing is a semi-floating type (SRFB) with five internal axial grooves. Two circumferential and two axial external grooves help the lubricant distribution outside and to inside the bearing by a lubricant provider hole.

3.3.1. Original journal bearing

In the original version, this bearing uses a triangular shape for the internal axial grooves (the interaction area of rotor-bearing assembly).

Figure 20 presents the side view of the semi floating journal bearing in the (a) external view and in the (b) internal view (b). In the external side view, it is possible to verify that the bearing has one hole for feeding and recirculating the oil into the bearing internal cavity, as well as having external cavities to recirculate the oil and create the external fluid film that provides additional stiffness and damping in FRBs. For the internal side view, it is possible to observe a central internal cavity with a larger diameter than the shaft where the oil supply and recirculation hole is connecting the internal and external cavities. The internal cavities on the left and right ends are used as a double support for the shaft: both internal cavities works as a double bearing system. The advantage of this manufacturing configuration is the reduction of the total cost of the bearings and larger control in the assembly, mainly in relation to the parallelism between the two bearings.

The Figure 21 illustrate a journal bearing schematic drawing.

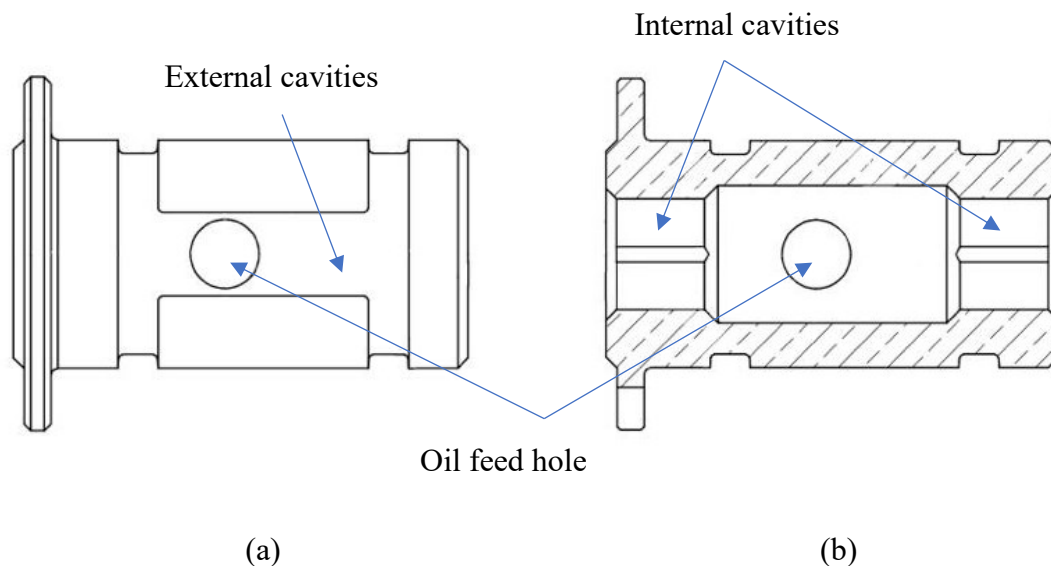


Figure 20 – Journal bearing lateral view: (a) external; (b) internal

Figure 21 shows (a) the front view of the bearing and (b) the groove detail. The standard bearing has five axial grooves and it is maintained for the current work. The grooves in the drawing present the triangular shape detail.

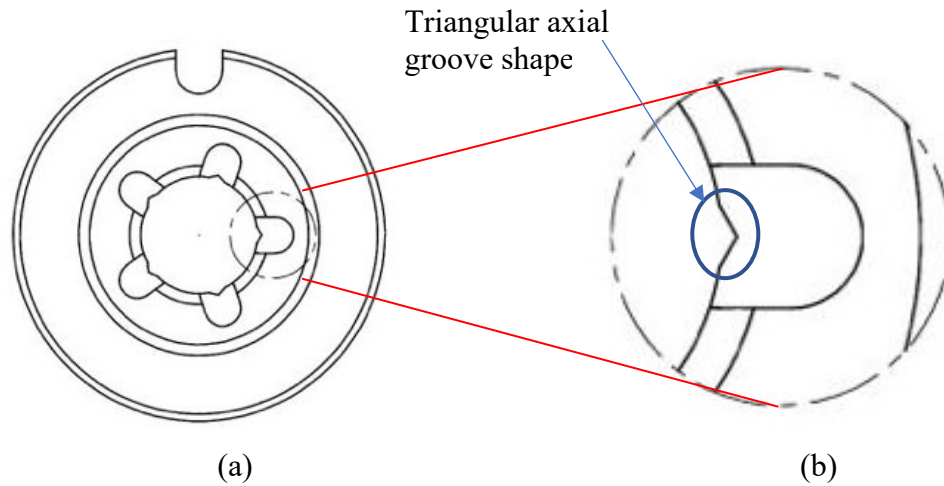


Figure 21 – Journal bearing front view: (a) bearing; (b) original triangular axial groove detail

The Appendix A presents technical details about manufacturing and assembly of the original journal bearings used in the BIAGIO AUT1000.

3.3.2. Modified journal bearings

The brand new journal bearings from AUT1000 are produced with the same original journal bearings process explained in Section 3.5, except for the final triangular axial broaching.

To produce new axial grooves shapes, the wire EDM (Electrical Discharge Machining) is choosed instead of broaching. This choice is made due to the lower cost of producing several different grooves shapes, as well as the fact that there is no need to modify all the calibration of CNC machines and to manufacture new broaching bars with each shape, which would also demand high cost and time for production. Moreover, the wire EDM used in this work achieves accuracies of ± 0.0025 mm, instead of CNC machining at MGFC Ltd. broaching with a ± 0.005 mm accuracy. However, the roughness of grooves with broaching would be smaller.

Seven original bearings are chosen to produce the axial grooves in the wire EDM machining. Appendix A show manufacturing details of grooves using EDM.

Table 2 presents the main reasons for choosing each type of axial groove shape based on several shapes used in different types of grooved bearings.

Table 2 – Main reasons for groove shapes choice

Groove shape	Reason for groove shape choice
Half-ellipse	2 nd shorter height with a smooth shape across the entire width and used in numerical groove analysis (JIN <i>et al.</i> , 2021; DAI <i>et al.</i> , 2022; SAHU and SHARMA, 2019) and in schematic figures (ZEIDAN and PAQUETTE, 1994; BROWN, 1997; KHONSARI and BOOSER, 2006; SHOUP and LAWRENCE, 2016). Also called arc shape (DAI <i>et al.</i> , 2022) and parabolic (SAHU and SHARMA, 2019).
Quarter-ellipse	Shape in order to simulate conditions similar to pressure dam journal bearings. Based on orthogonal triangle grooves (XIANG <i>et al.</i> , 2020; KUMAR <i>et al.</i> , 2019; JIN <i>et al.</i> , 2021) and quarter circles (KUMAR <i>et al.</i> , 2019).
Inverted quarter-ellipse	A confirmation of the pressure dam effect and orthogonal triangle/quarter circles grooves, when positioning it inverted, in the counter-rotation of the shaft. The inverted position is also tested by Xiang <i>et al.</i> (2020), Jin <i>et al.</i> (2021) and Kumar <i>et al.</i> (2019).
Rectangular	Shape used in grooved bearings to increase performance in camshaft bearings (KOPELIOVICH, 2015) used in numerical groove analysis (SHARMA and TOMAR, 2021; XIE <i>et al.</i> , 2022; XIE <i>et al.</i> , 2021; JIN <i>et al.</i> , 2021; SAHU and SHARMA, 2019; AHMADKHAH and KAKAEE, 2021; LIU and CHEN, 2022; KUMAR and SHARMA, 2019), experimental analysis (GONG <i>et al.</i> , 2019) and used in some schematic figures (SAN ANDRES <i>et al.</i> , 2017; BASRI and YANI, 2014; CHATTERTON <i>et al.</i> , 2017; WODTKE and LITWIN, 2021; REN, 2020). Also, the shorter height.
Trapezoidal	Shape compared to the rectangular and also used in grooved bearings to increase performance in camshaft bearings (KOPELIOVICH, 2015), numerical groove analysis (KUMAR and SHARMA, 2019) and used in a schematic figure (BRITO <i>et al.</i> , 2014; DWIVEDI and PATHAK, 2021).
Circular	Greater in height, with shape joining the bearing inner race and groove as smoothly as possible, used in numerical groove analysis (KUMAR <i>et al.</i> , 2019; SHARMA and TOMAR, 2021; JOY and ROY, 2016; XIE <i>et al.</i> , 2022; XIE <i>et al.</i> , 2021; KUMAR and SHARMA, 2019) and in schematic figure (WAGNER <i>et al.</i> , 2010; NOWALD <i>et al.</i> , 2015). Based on half-circle, called also half-moon groove

Groove shape	Reason for groove shape choice
Triangular	The original shape, used in numerical groove analysis (JIN <i>et al.</i> , 2021; KUMAR <i>et al.</i> , 2019; SHARMA and TOMAR, 2021; XIANG <i>et al.</i> , 2020; XIE <i>et al.</i> , 2022; XIE <i>et al.</i> , 2021; SAHU and SHARMA, 2019; KUMAR and SHARMA, 2019) and used in schematic figure (MOBLEY, 2001; SUBBIAH and LITTLETON, 2018)

3.3.3. Axial grooves shapes and dimensions

As presented in Chapter 2, the axial grooves shapes are chosen considering other shapes already studied. However, all these studies analyzed the TD conditions and/or overall vibration levels). The seven new brand shapes considering RD concepts to provide better overall stability levels.

To preserve the influence of axial groove shape in the TD and RD behaviors, the new axial grooves is drawn and measured in Autodesk AutoCAD 2019 and produced in the wire EDM considering for all grooves:

- Same number of original axial grooves for each journal bearing: 5;
- Same axial distance between the grooves: 72°;
- Same perimeter projection of each groove: 1.0897 mm;
- Same area of each groove: 0.1714 mm²

Under these conditions, it is guaranteed that the same amount of oil used in lubrication and the same effective bearing area is maintained in all grooves.

Figure 22 presents the methodology used to obtain the perimeter projection and area of each triangular original groove:

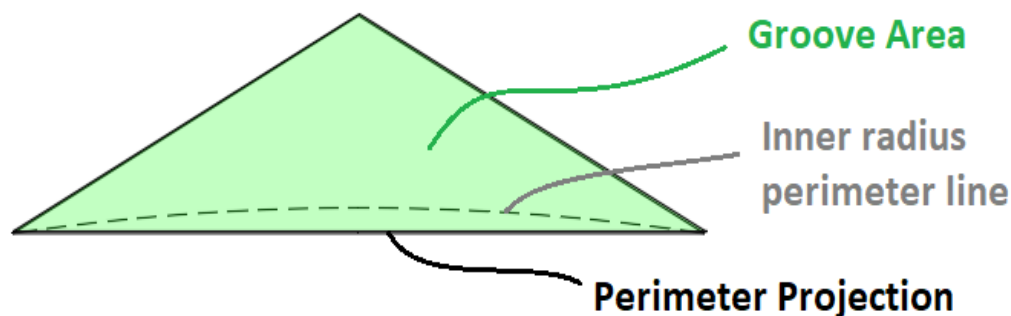





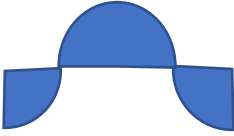



Figure 22 – Groove perimeter projection and area

With these assumptions, the following definitions are made for each groove shape and presented in Table 3.

Table 3 – Groove shape and design descriptions assumptions

Groove shape	Design descriptions
Half-ellipse 	<ul style="list-style-type: none"> • Half of area of a ellipse; • Ellipse major axis equals as perimeter projection; • Ellipse semi-minor axis equals as triangle height.
Quarter-ellipse 	<ul style="list-style-type: none"> • A quarter of area of a ellipse; • Ellipse semi-major axis equals as perimeter projection; • Ellipse semi-minor axis equals as triangle height; • Quarter ellipse curvature for the left side (shaft rotates clockwise).
Inverted quarter-ellipse 	<ul style="list-style-type: none"> • A quarter of area of a ellipse; • Ellipse semi-major axis equals as perimeter projection; • Ellipse semi-minor axis equals as triangle height; • Quarter ellipse curvature for the right side (shaft rotates clockwise).
Rectangular 	<ul style="list-style-type: none"> • A complete area of a rectangle; • Rectangle width equals as perimeter projection; • Height to keep the same area.
Trapezoidal 	<ul style="list-style-type: none"> • A complete area of an isocetes trapezoid; • Greater base trapezoid width equals as perimeter projection; • 45° both base angles; • Height to keep the same area.
Circular 	<ul style="list-style-type: none"> • Radius equals as ellipse semi-minor axis of hal-ellipse groove; • Semi-circle offset upside to create the two ends and maintain same perimeter; • Approx. 50% of area of semi-circle and 25% of area for each quarter circle end.
Triangular 	<ul style="list-style-type: none"> • The same as the original, but produced with EDM machining.

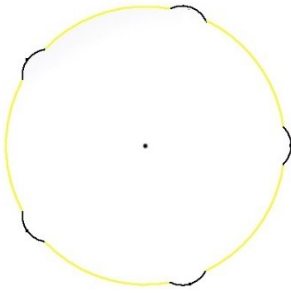
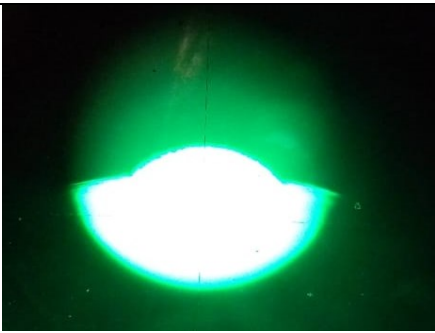
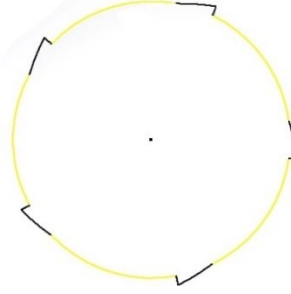

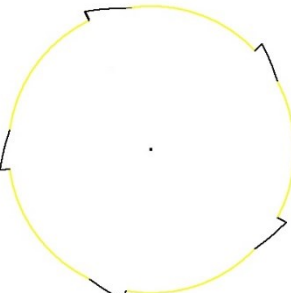
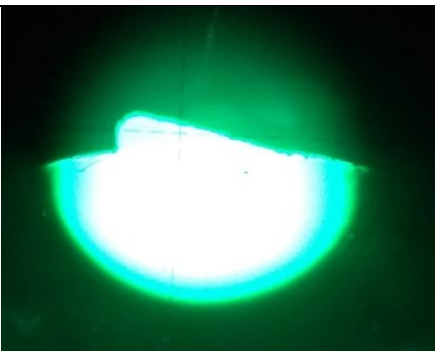
After the machining, all the grooves are analyzed in the microscope in the Metrology Lab of UFMG, as shown in Appendix B. This analysis has two goals: a qualitative and a quantitative verification of each groove. The qualitative analysis is made via observation of compliance with the shapes indicated within the CAD tool.

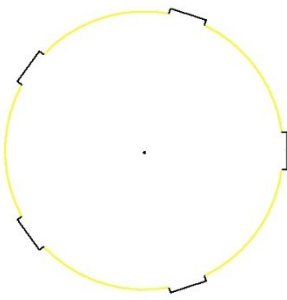
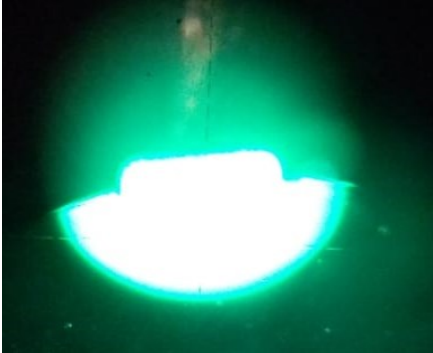
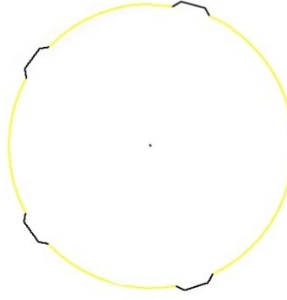

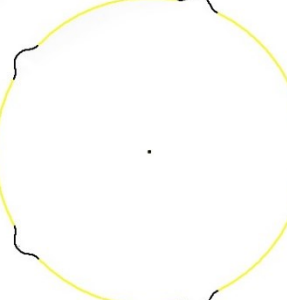
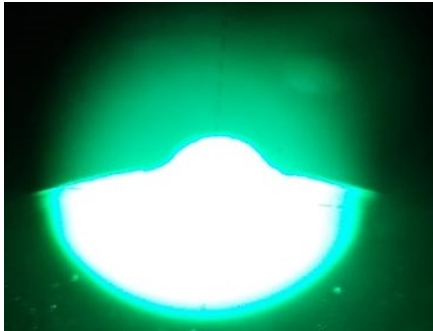
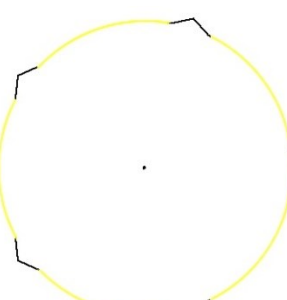

Table 4 shows the proportional drawing of axial grooves shapes into each journal bearing, as a zoom of each groove shape by the photos obtained direct from the eye lens with 150 times magnification for that qualitative analysis.

Due to wire diameter used (0.1 mm) during machining, the corners of each groove are rounded. It is important to reaffirm that the equipment positioning accuracy is 1/40 of the wire diameter, i.e., ± 0.0025 mm.

The quantitative analysis and the final dimensions and areas of each groove before the rotor-bearing assemblies is presented in Appendix B.

Table 4 – Grooves proportional drawing in bearing and enlarged

Groove shape	Proportional drawing	Groove photos (150 X)
Half-ellipse		
Quarter-ellipse		
Inverted quarter-ellipse		

Groove shape	Proportional drawing	Groove photos (150 X)
Rectangular		
Trapezoidal		
Circular		
Triangular		

3.4. TURBOCHARGERS ASSEMBLIES

The turbochargers assemblies are done also at MGFC Ltd. to guarantee all necessary setups during the assembly and balancing processes.

For a better logistics at the workbench tests, each brand new bearing is mounted at new rotor systems.

After the rotor-bearing assembly, this new part goes to a balancing set using a cold balancing machine to keep all turbochargers below the maximum imbalance level. Figure 23 and Table 5 indicate the machine.

The turbocharger core (i.e., compressor, turbine, rotor-bearing assembly and central housing) is connected on the balancing machine. The supply and return lubricant ducts of the machine are connected to the turbocharger core using quick couplings. Then, the protective cover is closed and the assembly is accelerated by the actuation of a pneumatic pump that blows cold air directly to the turbine. The set reaches 180,000 krpm in approximately 3 to 5 seconds. The amplitude and phase of synchronous response are obtained by an accelerometer connected to the balancing machine in a position close and rigid to the turbocharger core assembly. Based on these data, the technician performs the grinding of the base of the compressor wheel in the position indicated by the balancing machine to balance all the assembly. After it, the technician closes the protective cover again, and restarts the process. The process ends when the synchronous vibration amplitude response is below 1.5 G, according to the company internal standard.

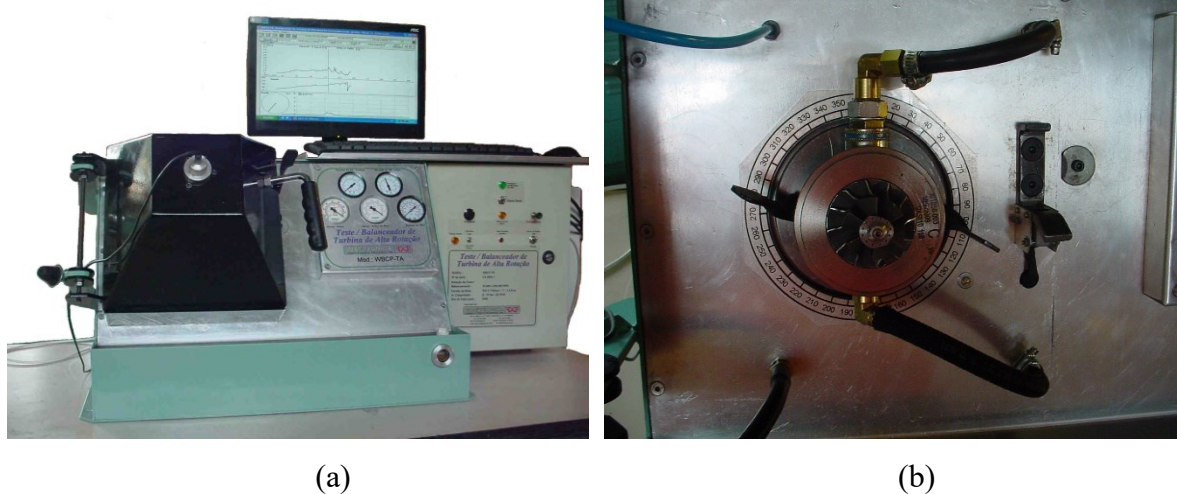


Figure 23 – The cold balancing machine (a) with the protection cover, and (b) detail of rotor-bearing assembly coupled to the machine.

Table 5 – Balancing TC machine characteristics

Data	Balancing machine
Manufacturer	Wattécnica
Model	WBCP-TA
Hardware Processor	Intel® Celeron® 2.40 GHz, 128K Cache, 400 MHz FSB
Maximum ICE power to use the TC	800 HP
Idle start speed	15,000 rpm
Maximum speed	300,000 rpm
Measurement system	Piezoelectronic accelerometer
Measurement data	Synchronous response
Measurement time	3 to 8 seconds

After balancing, all the seven final approved sets are separated, as shown in Figure 24.



Figure 24 – The seven rotor-bearing sets after balancing

After the balancing, the rotor-bearing sets are approved and released with new turbocharger housing and miscellany parts (Figure 25).

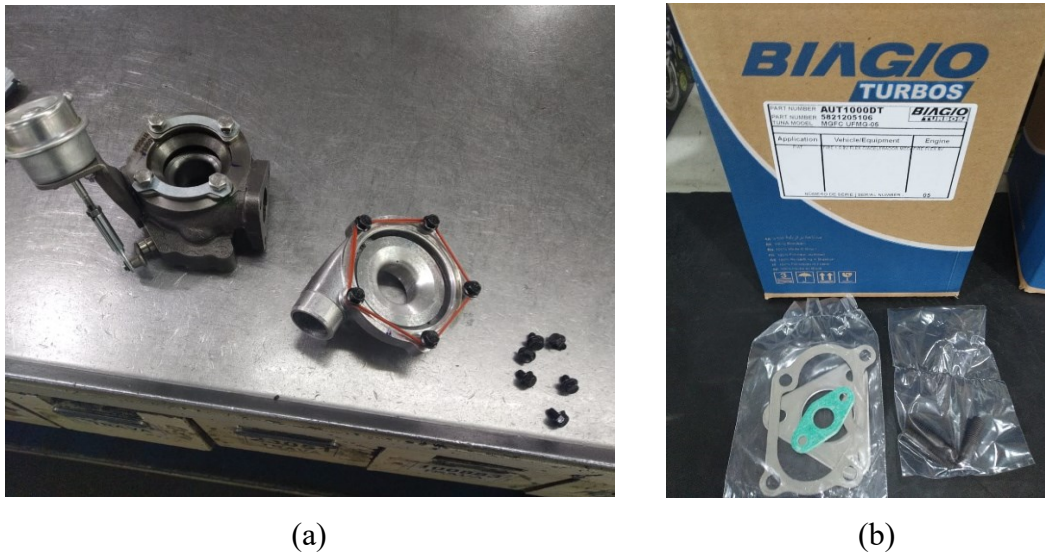


Figure 25 – (a) New turbine and compressor housing and (b) miscellaneous parts and final packaging

Even with new housings for each rotor-bearing assembly, the compressor and turbine housings are the same at all the workbench in this work to facilitate the complete assembly with the workbench pipe connections and to maintain the compressor and turbine input and output with the same setup, as shown in Figure 26.



Figure 26 – Workbench with the AUT1000 compressor and turbine housing and without the rotor-bearing set

3.5. WORKBENCH (SYSTEMS AND INSTRUMENTATION)

The experimental setup parameters of the workbench are presented in this work in two parts: thermodynamic (TD) instruments and rotordynamic (RD) instruments.

The thermodynamic SAE standard methodology to obtain the main parameters, as stabilization of the centrifugal compressor (i.e., the continuous rotor speed during different air flows), criteria for detection of surge threshold points, warm-up criteria and compressor data acquisition points, will be presented in general. Additional information could be obtained in the last projects at LABTURBO-CTM as Sandoval (2019), Hanriot *et al.* (2019) and Teixeira (2020) as the instrumentation system are the same used in these references.

The rotordynamic system shows all the instrumentation and data record setup to obtain the adequate parameters in different conditions with high inertial loads, shaft whirl, vibration and instabilities. Correct instrumentation and measurement techniques in rotordynamics are important to improve the rotordynamic analysis and make an assertive turbomachinery troubleshooting projects (Vance, 1988).

In this chapter, the components of the turbocharger test bench used for the TD maps and graphs and RD plots and graphs obtained are presented, dividing them into systems described in Section 3.1.

3.5.1. Turbine Power System

The turbocharger test bench used works with hot flow, i.e., the turbine supply is composed of gas heated by an auxiliary energy source, in this case, a combustion chamber that burns air and fuel. This type of turbocharger supply represents more reliably the exhaust gases of an internal combustion engine than one with a cold flow (SANDOVAL, 2019).

The air line consists of two air compressors, a compressed air reservoir and a flow control valve as shown in Figure 27. The compressors used to generate pressurized air are two industrial compressors ATLAS COPCO model GA55VSD AFF as illustrated in Figure 28. The compressor are screw type and regulated according to the demand of the experiment carried out and have the capacity to supply a pressure of 400 kPa and a maximum air flow of 1.6 kg/s. The reservoir has a volume of 5 m³ and is essential for operating with a constant air flow. The valve used to control the air flow is a general service valve with a pneumatic actuator.

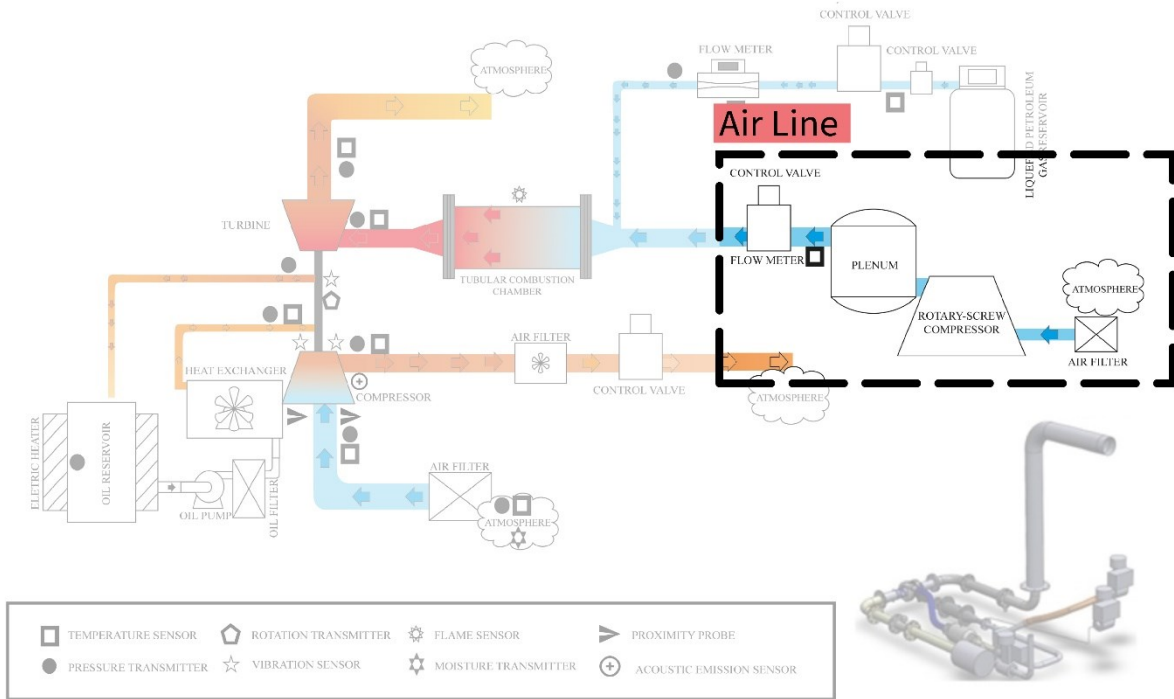


Figure 27 – Schematic drawing of the LABTURBO/CTM UFMG air line

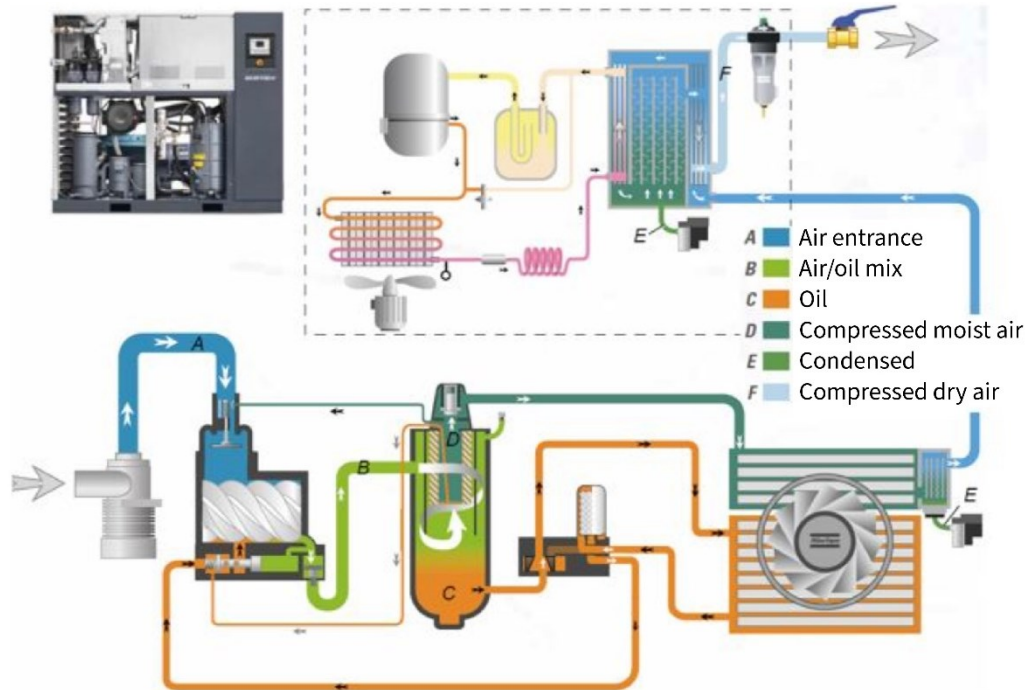


Figure 28 – ATLAS COPCO GA55VSD AFF compressor configuration installed

The fuel line consists of fuel tank, safety valve, flow control valve, pressure regulator, universal controller and flow meter. The fuel used is liquefied petroleum gas (LPG) and it is stored in gallons with a capacity of 45 kg. The safety valve is a solenoid type with an emergency on/off button and the fuel flow control valve is a general service valve

with pneumatic actuator and electro-pneumatic positioner. Figure 29 presents a schematic drawing of fuel line.

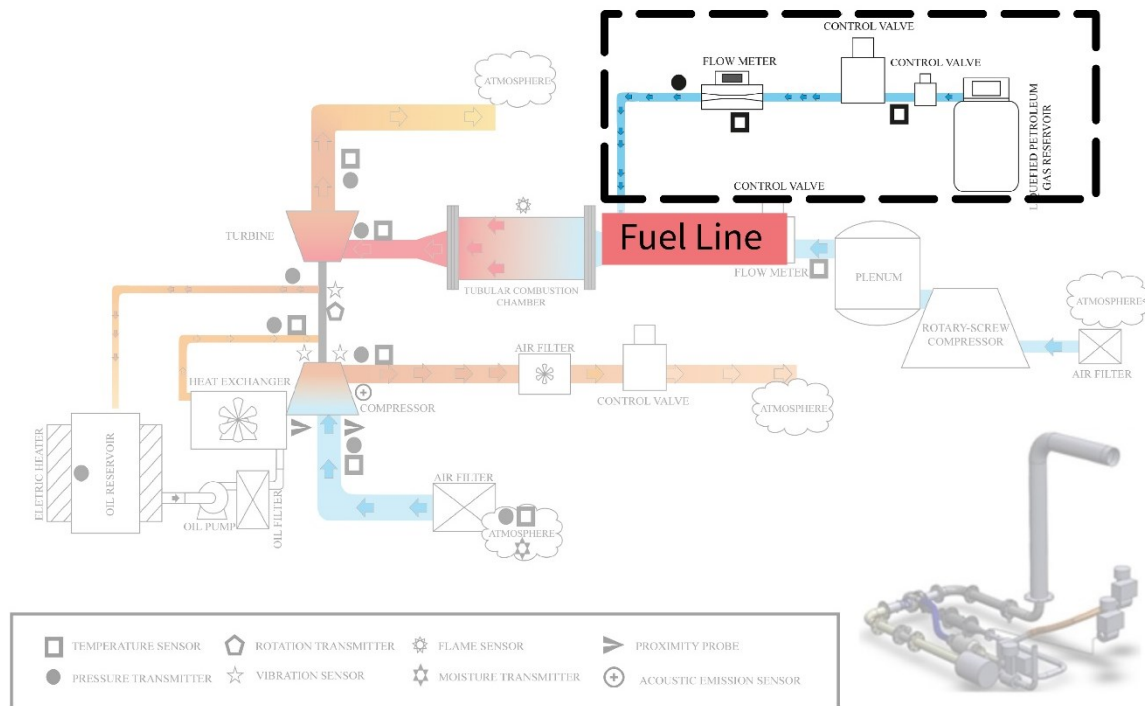


Figure 29 – Schematic drawing of the LABTURBO/CTM UFMG fuel line

3.5.2. Combustion chamber

The combustion chamber was first developed by Barros (2003) and later improved by Venson (2007). All the dimensions of the combustion chamber is drawn in Figure 30.

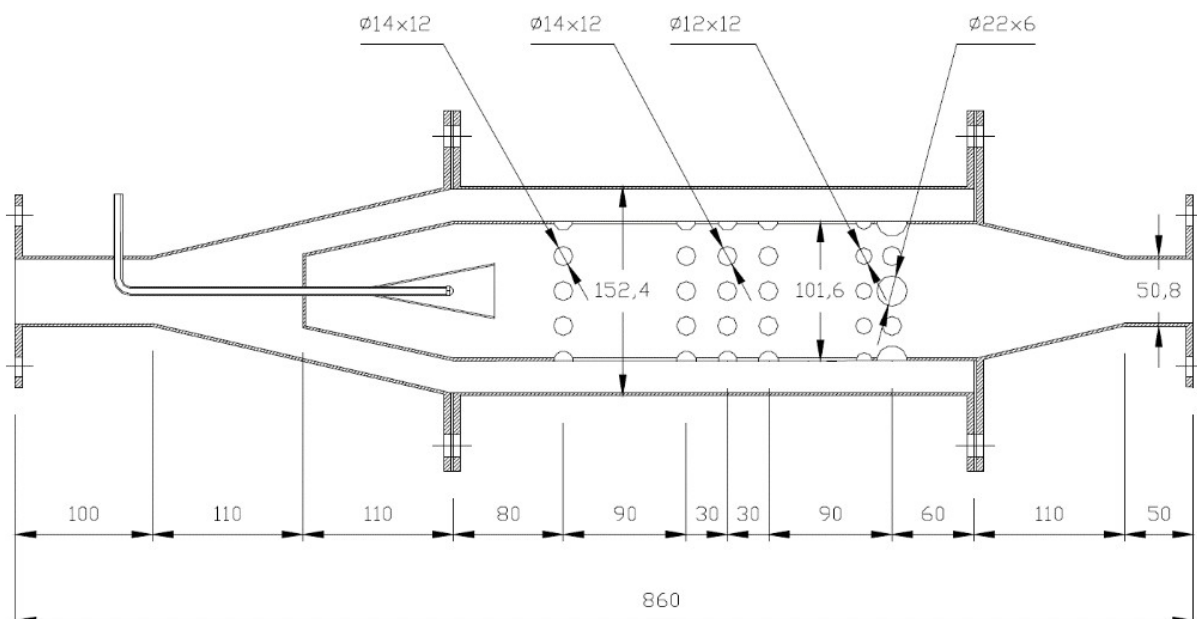


Figure 30 – Tubular combustion chamber (dimensions in millimeters)

The chamber is fed by the air and fuel lines via a conical fuel injector nozzle, concentric to the air piping. It is manufactured in AISI 304 stainless steel, with a concentric tube to the chamber, with radial holes in order to promote a stable combustion through a better mixing and distribution in all burning regions. Two spark plugs that ignite the mixture of air and fuel with an electric arc are installed, as shown in Figure 31.

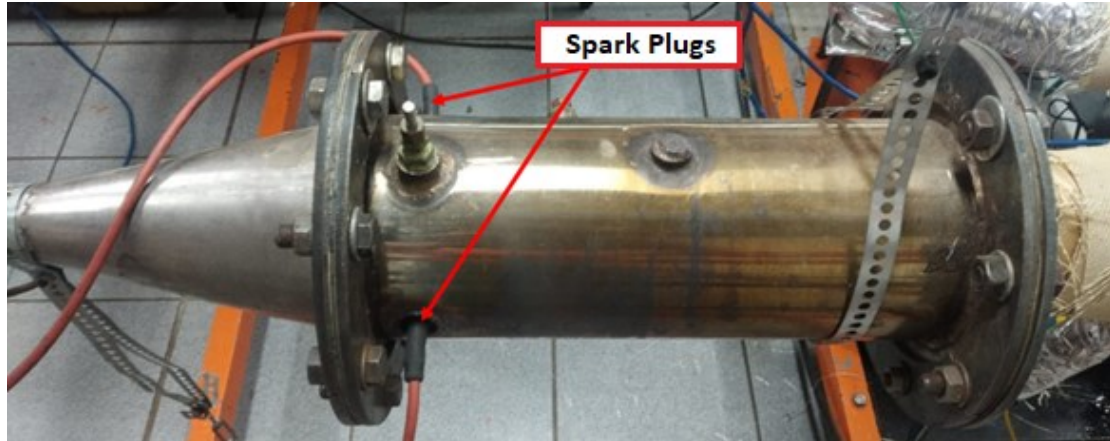


Figure 31 – Combustion chamber

3.5.3. Compression Line

The compression line is composed of an air filter (an autotrucks model), a mass flow transducer and a valve to control the flow. This valve is a general service valve with pneumatic actuator and electro-pneumatic positioner and is controlled by a universal controller. Figure 32 indicates the compressing line.

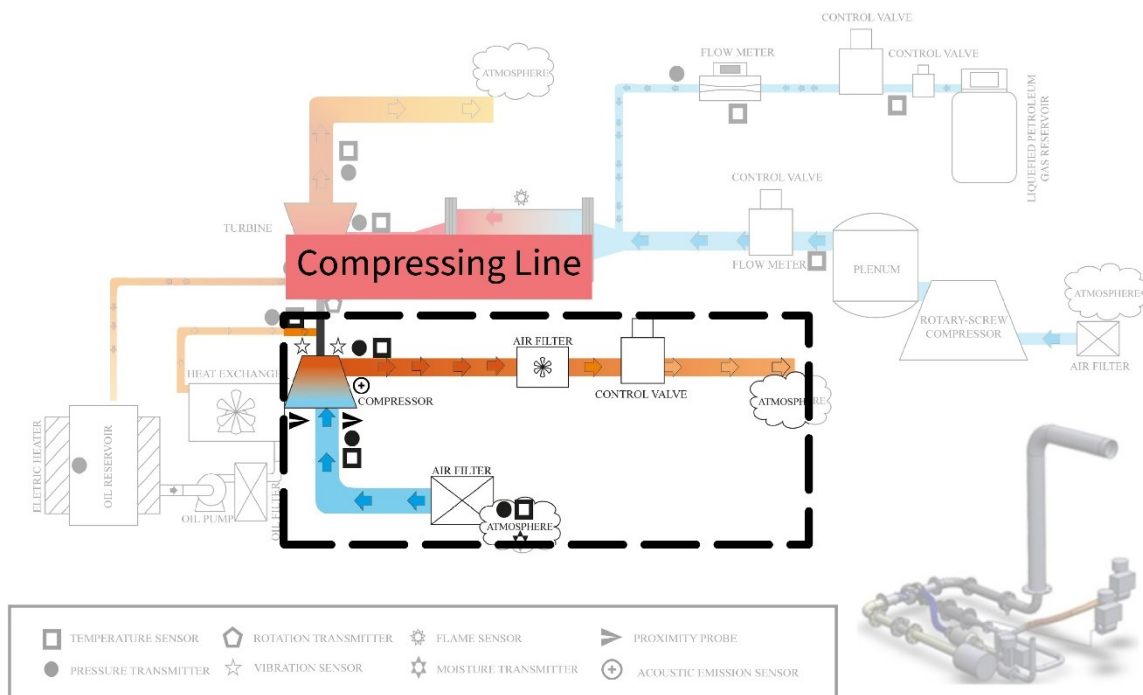


Figure 32 – Schematic drawing of the LABTURBO/CTM UFMG compressing line

3.5.4. Lubrication System

The lubrication system supplies oil to the journal and thrust bearings of the turbochargers and is composed of a motor pump, an oil filter, an oil cooler, a fan, an oil reservoir, a heating resistor and a frequency inverter. The motor-pump pumps oil at a pressure of up to 2,450 kPa and its speed is controlled by the frequency inverter, which is therefore used to regulate the oil injection pressure. The oil filter retains solid particles that can contaminate the lubricant. The radiator contributes to the cooling of the recently used oil by increasing the heat exchange area of the heated oil with the atmosphere, further aided by the forced convection promoted by the fan. In addition, an agitator is installed inside the oil reservoir and homogenizes the temperature of the amount of stored lubricant, which is heated by the resistance ceramic collar with thermostat for temperature regulation. Figure 33 shows the schematic drawing.

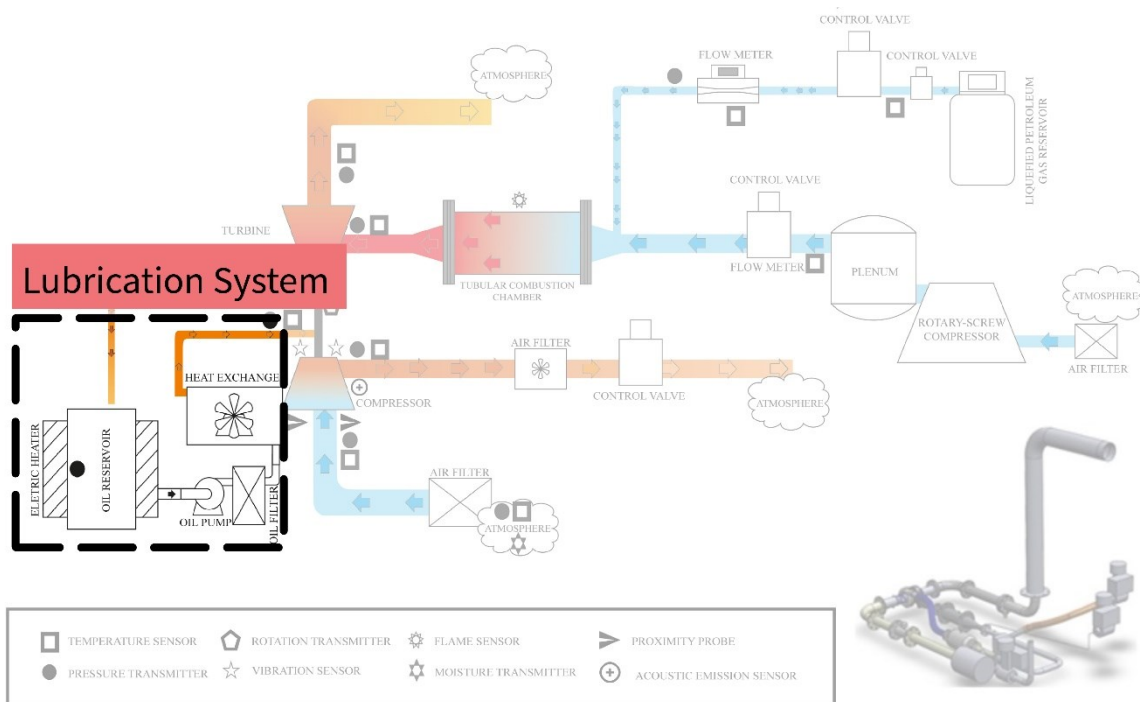


Figure 33 – Schematic drawing of the LABTURBO/CTM UFMG lubrication system

For the tests described in this work, based on the results obtained by previous experiments, an oil injection pressure of 200 kPa and a temperature of 90°C for the oil in the reservoir are regulated. Figure 34 shows the lubrication system used.

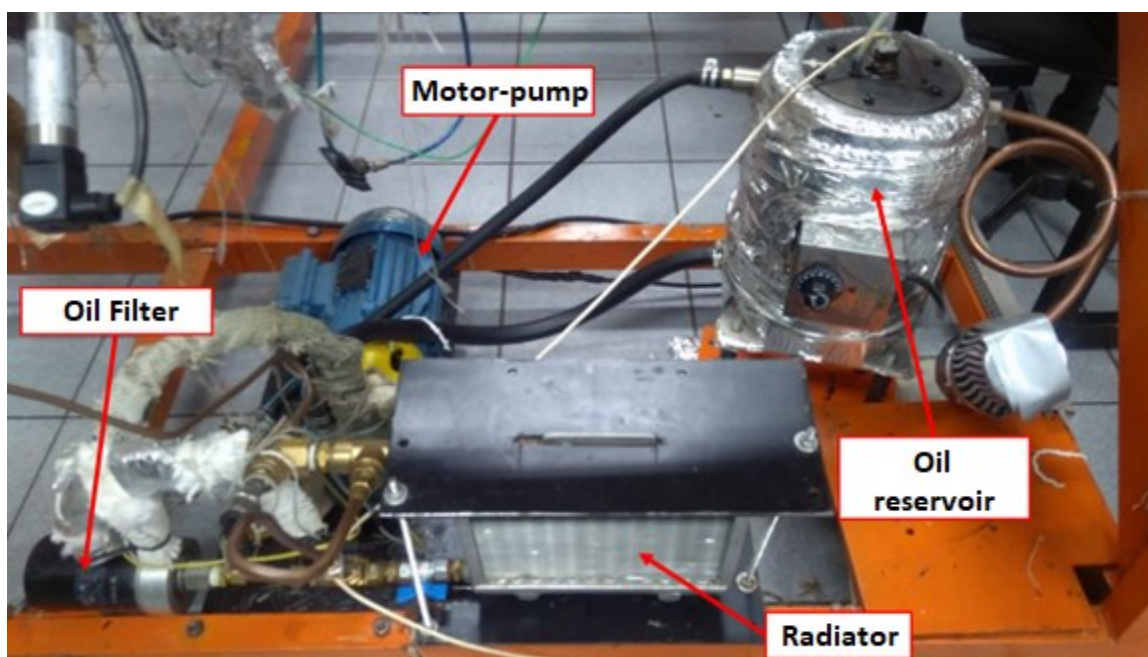


Figure 34 – Lubrication system

3.5.5. The control room

The control room for TCs tests and to obtain the thermodynamic and rotordynamics data is composed by a control room is a space inside the LABTURBO-CTM laboratory with an area of 12 m², being divided in three independent spaces. The first is called (i) TC command center, as it allows develop the centrifugal compressor test remotely. The second space is a (ii) power board and TD data acquisition, where the devices that control the installed valves and the devices that perform the TD experimental data recording. The last is the (iii) RD data acquisition, with a industrial-Lab deck, computational processor and specific data acquisition board for acoustic and vibration (high-speed data acquisition system for acoustic emission).

Section 3.6 presents the TC command center, power board, TD data devices and RD data devices.

3.5.6. Pressure measurements

Piezoresistive electrical pressure transducers are used to generate the signals to be measured by the data acquisition boards, signals which are proportional to the pressure exerted on these transducers. According to Sandoval (2019), piezoresistive pressure transducers reconcile the low cost, compared to piezoelectric sensors, with the ability to

measure rapid changes in pressure and mean pressures. Table 6 shows the characteristics and applications of the pressure gauges used on the workbench for the experiments.

Table 6 – Technical data of the pressure transducers

Data	Pressure Transducers			
Manufacturer	SpiraxSarco	Wika	Warme	Nuova Fima
Model	TP7	R1	WTP-4010	ST 18
Measuring range	0 a 1000 kPa	0 a 600 kPa	-50 a 50 kPa	0 a 1000 kPa
Type of measurement	Gauge	Gauge	Gauge	Gauge
Power supply	8 a 30 VDC	8 a 30 VDC	8 a 30 VDC	8 a 30 VDC
Exit sign	4 a 20 mA	0 a 5 V	0 a 10 V	4 a 20 mA
Precision	$\leq 0,5\%$	$\leq 2\%$	$\leq 0,25\%$	$\leq 0,5\%$
Measuring point	Turbine inlet/outlet	Oil inlet	Compressor inlet	Compressor outlet

3.5.7. Temperature measurements

According to Sandoval (2019), the following characteristics are fundamental for the effective measurement of temperature on a hot flow bench: fast response, thermal stability and capability of measuring high temperatures. Therefore, for temperature measurements on the bench, type K thermocouples are used, whose technical data are listed in Table 7.

Table 7 – Technical data of the temperature transducers

Data	Thermocouples	
Manufacturer	NOVUS	CAMTEC – MIT EXACTA
Model	Cromel – Alumel (K)	Cromel – Alumel (K)
Element	Simple, 1 thermocouple measurement	Simple, 1 thermocouple measurement
Measuring range	0 – 1200 °C	0 – 1080 °C
Sensitivity	0,040 mV/°C	0,039 mV/°C
Precision	0,75% of the final scale	0,75% of the final scale
Measuring point	Compressor inlet; Compressor output; Environment; Oil inlet; Oil reservoir.	Oil outlet; Gas inlet.

Figure 35 shows the compressor inlet and outlet line schematic illustrating location and position of pressure and temperature transducers.

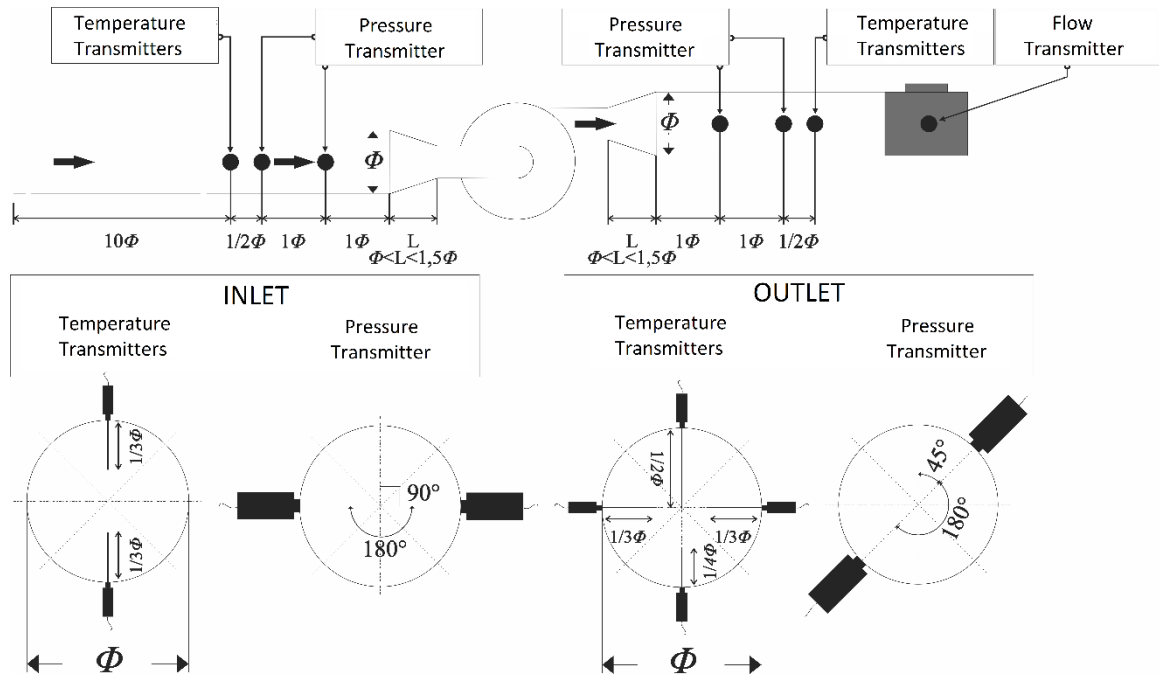


Figure 35 – Compressor inlet and outlet line schematic illustrating location and position of pressure and temperature transducers

3.5.8. Air flow measurements in the centrifugal compressor

The measurement of the air flow that passes through the compressor of the turbocharger is carried out by a turbine-type flow transducer, allocated into the centrifugal compressor discharge. The air that passes through this discharge causes the transducer rotor spin and the rotational speed is converted into air flow by a microprocessor. Table 8 shows the technical data for this transducer.

Table 8 – Turbine-type flowrate Transducer Technical Data. Font: Sandoval (2019).

Data	Transducer
Manufacturer	INCONTROL
Type	Turbine flow
Model	VTG100
Amplifier/Processor	MEV3000
Operating Temperature	-40 to 180 °C
Operating gauge pressure	Up to 3000 kPa
Measuring range	51 to 1869 m ³ /h
Precision	0,2%
Nominal diameter	400 mm
Reading point	Compressor outlet

3.5.9. Turbocharger rotating speed measurement

The measurement of the rotational speed of the turbocharger is performed by an optical sensor pointed at the end of the shaft on the compressor and before the fastening nut. The end shaft and the rotor fastening nut is painted with black paint with low reflectivity (phosphatizing base paint) and a strip of reflective paint, as shown in Figure 36. Thus, as this rotor part spins, the laser of the sensor is reflected at the same frequency as the turbocharger rotation. This frequency of light signal received by the optical sensor is used to detect the developed rotational speed.

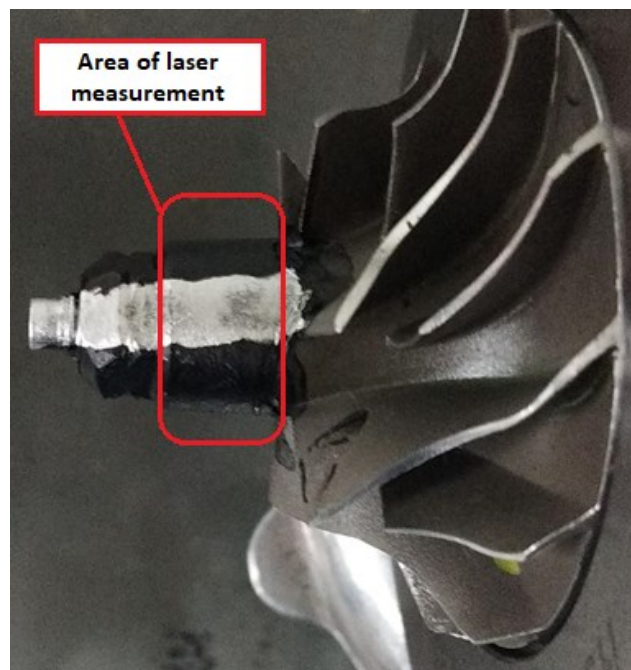


Figure 36 – Area at the shaft end for measuring rotational speed

The optical sensor data acquisition frequency is 10 kHz, which is more than four times the rotation frequency of the highest speed reached in the tests, which is approximately 142,000 rpm. The accuracy of this sensor is $\pm 0.2\%$ (DI BATTISTA *et al.*, 2015). Figure 37 shows the installation of the laser and its reflection for measuring the number of rotations over time.

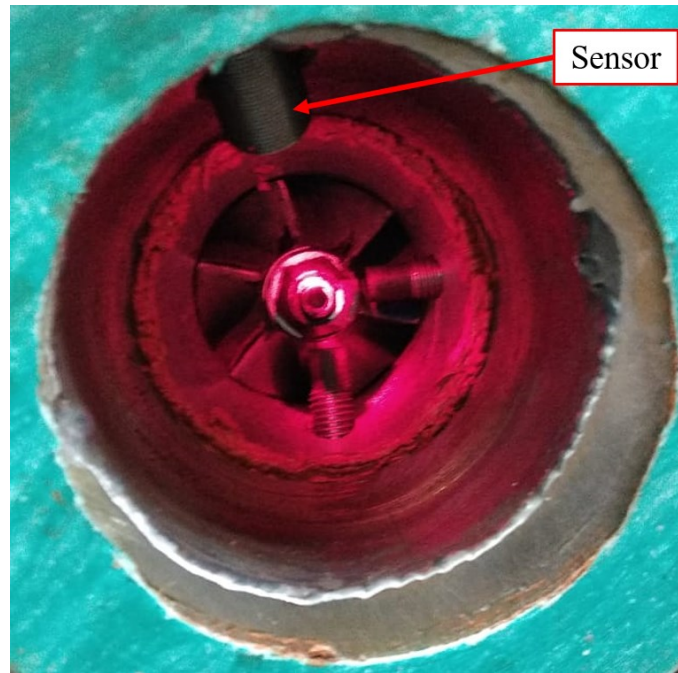


Figure 37 – Rotating speed measurement by optical sensor

Table 9 shows the data from the equipment used in measuring and converting the rotating speed signal of the turbocharger.

Table 9 – Technical data of the rotary speed sensor and signal converter system.

Data	Rotating speed sensor	Signal converter system
Manufacturer	AVL	AVL
Model	TS350	TB350
Measurement characteristic	Laser	-
Operating Temperature	-10 °C to 70 °C	-
Measuring range	6000 to 200000 rpm	-
Accuracy	+/- 0.2%	
Wave-length	645 nm (red, visible)	-
Power signal	5 VDC	-
Exit signal	-	0...10 V 2,5 V ± 10% pulses
Application	Rotating speed of turbocharger rotor	Modulation for the computer

3.5.10. Rotordynamic test apparatus

In order to monitor the rotor dynamic response the acceleration transducers, proximity probes and acoustic emission (AE) transducer are employed. Acceleration

transducers are installed on the vertical and horizontal directions transversally to the shaft of the TC at the compressor housing, as well as in the axial direction near the compressor connection flange. Proximity sensors are positioned radially in a compressor housing prepared with precise threads. Acoustic emission sensors are also positioned directly on the compressor housing, aiming at the lower temperature point due to the thermal limit of the sensor. There is also an intrusive optical type rotation sensor positioned directly to a specific part of the rotor as explained in Section 3.7 to indicate the speed of rotordynamics manual datatrigger.

The control and data acquisition system are used to control the valves, the ignition system, the lubrication system, to measure temperature, pressure and flow data and to monitor the TC (rotation and rotordynamic responses).

Three instrumentation systems are used in the rotordynamic response tests of the rotors supported in the different support systems of the TC: (i) for vibration (accelerometers); (ii) AE system; and (iii) for proximity probes data.

The rotordynamic characteristics of the rotor-bearing system include the global levels of vibration at different speeds and acceleration conditions, as well the shaft whirling orbits. For the acceleration levels measurement, in the tests of vibration, a system are made up of a frequency analyzer, based on the principle of fast Fourier transformation, and piezoelectric accelerometers to obtain data from 100 to 10,000 Hz. For the AE measurements, an AE sensor are used to obtain all data from 20,000 and 1,000,000 Hz to analyze as function of time using wavelet and bandwidth signal processing. For the rotor whirling motion amplitude determination, in the vibration tests, an instrumentation composed by inductive proximity transducers and data acquisition system as function of time are used. A detailed description of the structure and instrumentation sets used are clarified in the next subsections.

3.5.11. Accelerometers and frequency analyzer

The acceleration and deceleration during the start and stop between successive tests should be observed, mainly due to changes in temperature, which directly influence the final result (LIFSON and SIMMONS, 1990). Instabilities modes in TCs can be detected by analyzing the frequency spectrum at constant speed (YING *et al.*, 2009) and waterfall plots (KIRK and ALSAEED, 2011) using accelerometers. Rotordynamic instabilities TCs are strongly influenced by temperature changes and high accelerations and decelerations during their operation with ICES.

Piezoelectric acceleration transducers (accelerometers) and a frequency spectrum analyzer are used in the vibration measurement system. Table 10 describes the type of accelerometer that are used in the tests. The characteristics of the frequency analyzer employed in this work are presented in Table 11.

Table 10 – Technical data of the accelerometer

Data	Accelerometer
Manufacturer	PCB Piezotronics
Model	333B50
Sensitivity	1000 [mV/g]
Resonance Frequency	≥ 20 [kHz]
Measuring range	± 5 [g pk]
Mass	0,007 [kg]
Sampling rate used	20 [kHz]

Table 11 – Technical data of the frequency analyzer

Information	Frequency Analyzer
Manufacturer	National Instruments
Model	PXI-4462
Applications	Accoustic and Vibration
Number of simultaneously sampled input channels	4
Samples-per-second (S/s)	204.8 [kS/s] (maximum)

The rotating system vibration response is evaluated by frequency spectra at different velocities (constant speeds), waterfalls for acceleration and deceleration of the rotors (time-varying speeds) and analysis of the sub-synchronous (rotordynamic instability) due to variation of some fluid dynamic pressure around the circumference of a rotor component (VANACE, 1988) and synchronous (imbalance) vibration response in function of the rotor speed.

The accelerometers are attached on the compressor housing. The sensor bases are glued to plain surfaces with a cyanoacrylate-based adhesive (high-resistance, quick-drying instant glue), as recommended by the sensor manufacturer. Three uniaxial accelerometers are used with its normal directed to each of the three Cartesian axes, as shown in the figure below. Thus, two accelerometers are positioned in radial directions (x- and y-axes) of the rotor (spaced at 90°) and one in the axial direction (z-axis).

Figure 38 shows the accelerometers position in TC. These positions are used in the tests and kept the same for all configurations of bearings and pressure and flow injected to the TC compressor, as no changes are made in compressor housing and flanges for each test.

The complete TC mass is approximately 1,500 times larger than the mass of the accelerometer used, reducing any interference of the accelerometers in the vibration measurements.

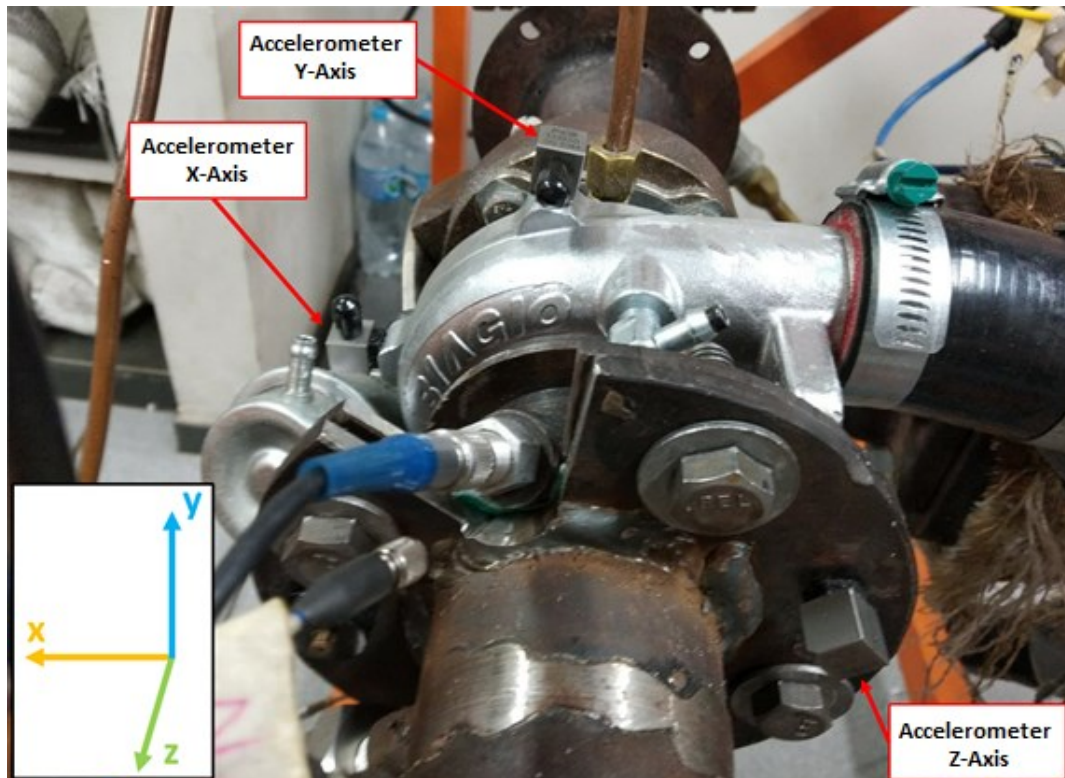


Figure 38 – Turbocharger assembly on the workbench. X-axis, Y-axis and Z-axis positions indicate the mounting location of the accelerometers.

3.5.12. Proximity probes and drivers

Proximity probes (noncontacting displacement probes) are one of the most widely used rotary radial axis displacement measurement systems. Vance (1988) shows that these probes are used on all industrial turbomachinery due to the importance of observing the small vibration responses in flexible bearing and heavy housings, as well as corroborating data from housing-mounted transducers (accelerometers) even in stiff bearings such as in aircraft engines. API Standard 670 (API, 2014) indicates the types of turbomachines where the use of this type of sensor is mandatory.

For turbochargers, the use of proximity probes to analyze the orbit is shown by Kerth (2003) and Conley *et al.* (2019). Proximity probes are considered essential for experimental and analytical investigation of rotordynamics of turbochargers (CONLEY and SADEGHI, 2021). Ying *et al.* (2009) also shows that orbit analysis must occur together with frequency spectra, both at constant speeds.

The radial displacements are measured over the time, evaluating the orbital vibration amplitudes and the shape of the orbits formed by the theoretical center point of the shaft. Operating conditions produce several variations in orbits that are primordial importance for the evaluation of the stability of rotating machines.

For the tests in this work, two displacement transducers are used, mounted on the compressor housing through a threaded hole for each of the sensors, which also have a threaded body and a nut for fixation, positioned in perpendicular directions, ensuring an analysis of the displacement in the two orthogonal axes of the rotor. They are positioned in the radial direction of the turbo rotating assembly, with the end of the sensors positioned approximately 1.25 mm away from the surface near the tip of the compressor impeller.

Table 12 shows the main characteristics of the displacement sensor used. Figure 39 presented the installation of the proximity probes.

Table 12 – Technical Data of the Displacement Sensor.

Information	Displacement Sensor
Manufacturer	PVTVM (former ProvibTech)
Model	Predictech TM0105
Sensitivity	7,87 [V/mm]
Probe diameter	5 [mm]
Linear Range	0.25 to 2.25 [mm]
Driver Model	Preditech TM0182
Temperature for current calibration	-35 a 120 [°C]
Linearity	0.0254 mm (sensor + driver calibration)
Samples-per-second	24 [kHz]

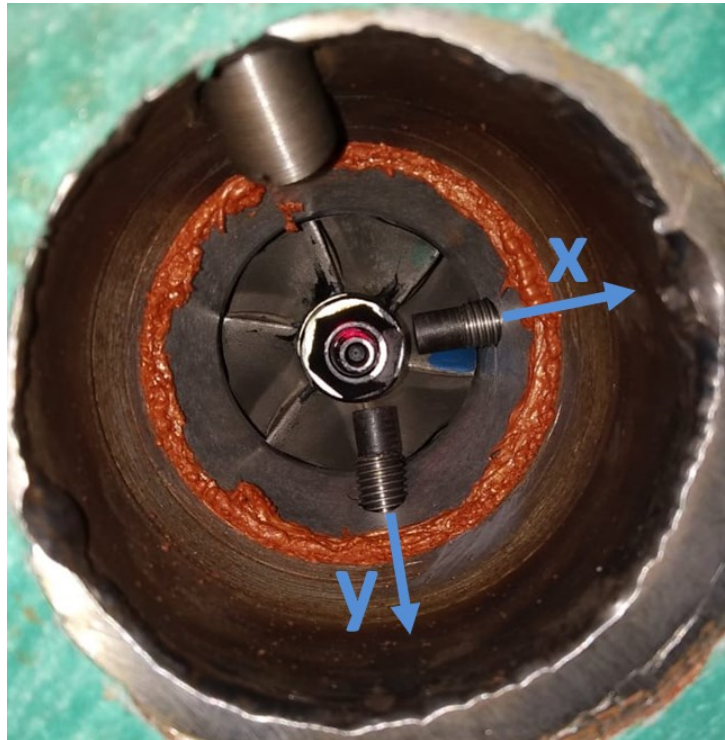


Figure 39 – Turbocharger extended axle with installed proximity probe

For a correct installation of the proximity probes, an original TC compressor housing is modified with new holes and threads to ensure the same axial distance and the sensor face is always at 90° from the shaft. Figure 40 shows the modified compressor housing used to obtain the orbits.

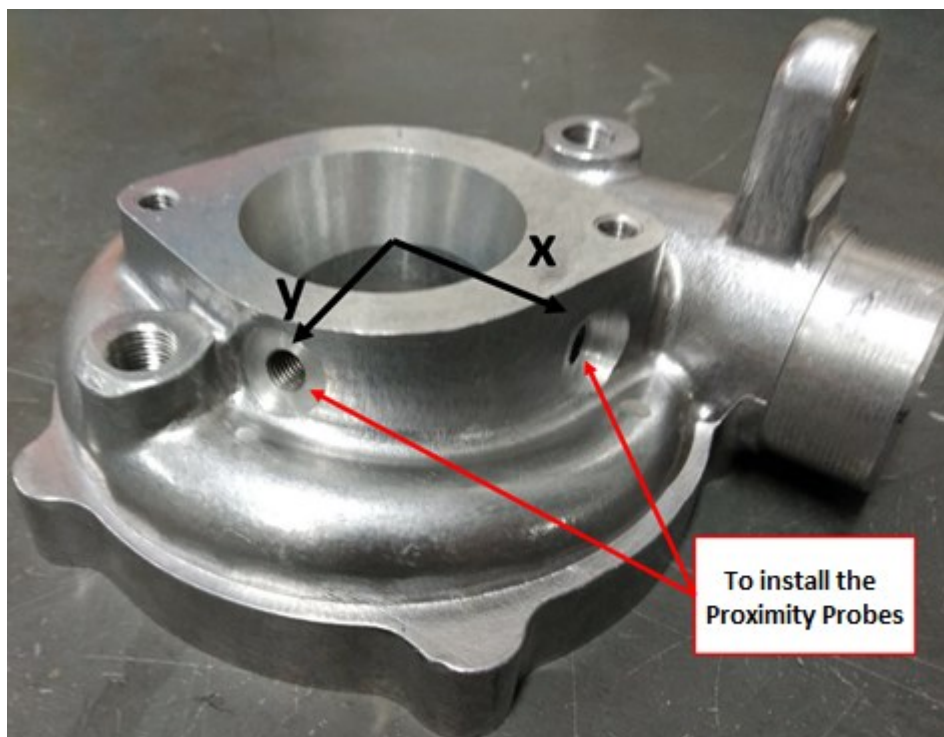


Figure 40 – Turbocharger compressor housing modified to install the proximity probes

The frequency used to obtain rotor orbit data are 10 kHz (standard frequency of the driver mode) for 3 seconds, totaling 30,000 points for each orbit.

In addition, the software *MathWorks Matlab*© version 2021 are used to eliminate points out of the curves and create rotor orbits, but its use must be done with caution in order to avoid undesirable effects in the time domain (VANCE, 1988). Since one of this study aim is to obtain the orbits of the synchronous response of the rotating system, the cutoff frequency is adjusted before and after the synchronous vibration peak, removing all the subsynchronous and supersynchronous vibrations.

3.5.13. Acoustic emission sensor

The Acoustic Emission (AE) data acquisition system (DAQ) consists of an AE transducer PAC S9208. The AE sensor allows obtaining AE signals at frequencies up to 1 MHz.

The signal amplitude is captured in volts. The real numbers in each recorded *Labview*© datafile are converted into floating point double precision numbers by using the *Labview*© function Float64. Then, those files are transferred into *Matlab*© by using the package Wavelet 1-D, at which the analysis of the AE signal files is performed.

The AE sensor is mounted on the horizontal radial direction and next to the bearings, using a bakelite base, a set of money rubber and mineral grease within the contact surfaces to guarantee the adequate capture of the AE signals, as shown in Figure 41. Table 13 describes the type of AE sensor that are used in the tests. The characteristics of the DAQ used are presented in Table 14 and better explained in Section 3.6.3.



Figure 41 – AE set mounted on compressor housing

Table 13 – Technical data of the AE sensor

Information	AE sensor
Manufacturer	Physical Acoustics
Model	S9208
Ressonant Frequency	500 [kHz]
Frequency Range	20-1000 [kHz]
Weight	0,009 [kg]

Table 14 – Technical data of the DAQ for AE sensor

Information	DAQ
Models Manufacturer	National Instruments
Deck Model	PXI-1042
Controller Model	PXI-8106
I/O Module Model	PXI-6115
Terminal Block Model	TB-2708

3.5.14. Control and monitoring systems

Control of valves

The valves with pneumatically trigger are controlled by the command center via devices which regulated the opening percentage of each valve and is perceived according to the received current signal. These devices are the SX-UNI type from the manufacturer SPIRAX SARCO and are connected to the electro-pneumatic positioner board of each valve. The communication protocol is Modbus via RS-485 connection, which is converted to USB (Universal Serial Bus) to connect with the command center computer.

The controlling of valves opening has a fundamental work in carrying out tests on the workbench. Through programming routines implemented in the command center, the signals generated by the SX-UNI devices go through an integral derivative proportional controller (PID) in order to control parameters such as oil injection temperature, gas exhaust temperature and the rotational speed of the turbocharger rotor.

To control the mass flow of air entering the combustion chamber is used the general service valve of the SPIRAX SARCO model LLA31 PTSUSS R3 illustrated in Figure 42. This valve works in conjunction with a pneumatic actuator model PN9123E fitted with a mechanical stroke indicator and a rolling diaphragm that ensures linearity of opening.

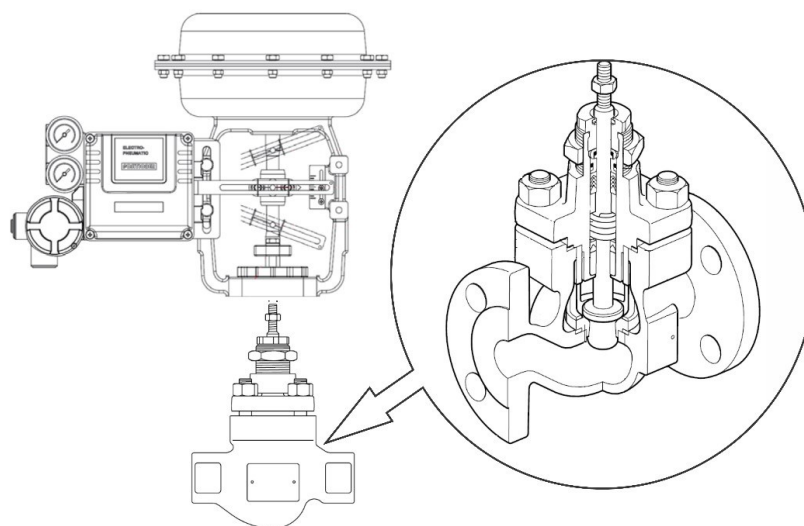


Figure 42 – Compressed air inlet control valve

Control of the combustion system

The main parameters for the analysis, characterization and control of combustion are: mixture of air and fuel ratio, flow rate and temperature of the exhaust gases, which will supply the turbocharger turbine. These parameters are controlled and measured by the valves, flowmeters and thermocouples that make up the workbench.

The control of the combustion system refers to the activation of the ignition in the combustion chamber. This system consists of two spark plugs, an ignition transformer (COFI IGNITIONS brand, model TRS 1020/1), responsible for the polarization of the spark plug electrodes, and a flame programmer connected to a relay on an Arduino MEGA 2560 board, which receives a signal from the command center (Figure 43). The spark plugs are positioned inside the combustion chamber so that the ground and centre electrodes are close enough to overcome the dielectric strength of the air and, thus, form an electrical arc that ignites the mixture of air and fuel gas. Table 15 presents the technical data of the flame programmer used in this work.



Figure 43 – Layout of the combustion ignition system

Table 15 – Technical data of the flame programmer

Data	Flame programmer
Manufacturer	SELCON
Model	PRG-E-U-11-C10-P1
Power supply	20 VCA + 10-15% 60 Hz \pm 3%
Ignition time	6 seconds
Purge time	10 seconds
Application location	Combustion chamber

3.6. THERMODYNAMIC AND ROTORDYNAMIC DATA ACQUISITION DEVICES

3.6.1. Standards and Procedures

The main technical standards followed for carrying out the tests are SAE J1723 (SAE, 1995) and SAE J1826 (SAE, 2022), which also established conditions for the design and manufacture of the turbocharger test bench.

To measure the thermodynamic variables it is necessary to follow all methodology to obtain the compressor performance map, as well as to evaluate the correct point within this map (pressure and flow) and to obtain other important thermodynamic responses from the different rotor-bearing assembly of each TC. Further details of standards and procedure to obtain performance maps and graphs are presented by Sandoval (2019).

Turbocharger operating temperature stabilization

In the absence of recommendations from the turbocharger manufacturer for performing this procedure, the turbocharger operating temperature stabilization procedures are defined by the SAE J1723 (1995) standard and consists of a sequence of variations in the rotational speed and the total compression ratio of the turbocharger by changing the opening of the compressor discharge valve. This procedure is performed at the beginning of each trial, in order to establish equivalent initial conditions for the experiments and, thus, guarantee a better comparative basis.

Table 16 presents all the steps for standard heating of each centrifugal compressor.

Table 16 – Steps for the standard operating temperature stabilization of the centrifugal compressor

STEP	STEP time	Speed	Compressor valve closing
1	10 minutes	~ 40 krpm	0%
2	5 minutes	~ 80 krpm	50%
3	3 minutes	~ 100 krpm	75%
4	5 minutes	~ 80 krpm	50%
5	5 minutes	~ 40 krpm	0%

Thermal stability

The thermal stability criterion defines the standard condition under which experimental data from a test in a centrifugal compressor must be collected. The SAE J1826 (SAE, 2022) standard determines that, to be considered to have reached the condition of thermal stability (Ψ), the maximum variation of the dimensionless parameter (ζ) of temperature change must be less than 0.5%. Equations 3.1 and 3.2 used to calculate this parameter are presented, where T_1 e T_2 are, respectively, the compressor inlet and outlet temperatures.

$$\zeta = \frac{T_2 - T_1}{T_1} \quad (3.1)$$

$$\Psi = \frac{\zeta_{t2} - \zeta_{t1}}{\zeta_{t1}} < 0,5\% \quad (3.2)$$

Romero (2004) points out that the time interval between measurements (ζ_{t1} e ζ_{t2}) for the analysis of the variation of the dimensionless temperature parameter to be carried out is five seconds. Therefore, if the system maintains its thermal conditions within the allowed tolerance of 0.5%, it is concluded that measurements can be carried out. Thus, there is a better comparative basis for evaluating the data measured for different operating conditions.

Table 17 shows the test points for the AUT1000 Biagio centrifugal compressor.

Table 17 – Test Points for the AUT1000 Biagio Centrifugal Compressor

Speed	Compressor valve closing percentage					
	Point 1	Point 2	Point 3	Point 4	Point 5	Point 6
67 krpm	0% (fully open)	36%	63%	81%	90%	Percentage for surge condition
89 krpm	0% (fully open)	31%	55%	70%	78%	Percentage for surge condition
105 krpm	0% (fully open)	31%	54%	69%	77%	Percentage for surge condition
121 krpm	0% (fully open)	30%	53%	68%	75%	Percentage for surge condition
135 krpm	0% (fully open)	28%	49%	63%	75%	Percentage for surge condition

Thermal insulation

The SAE J1723 (SAE, 1995) standard establishes that the TCs output lines must be thermally isolated from the environment, up to a minimum distance equal to the nominal diameter of the piping, counting from the temperature measurement in these output paths. In general, the thermal insulation of the tested components promotes larger control over the test conditions by reducing the heat transfer to the environment. In this way, thermal insulation is important for places where measurements are taken and that reach high temperatures, which would promote larger thermal exchange.

Thus, for the tests in this work, thermal blankets and reflective materials are used to insulate all sensors, piping and other components, especially in regions close to the turbocharger and in the lubrication system. Figure 44 shows the arrangement of insulating materials in the turbocharger region.

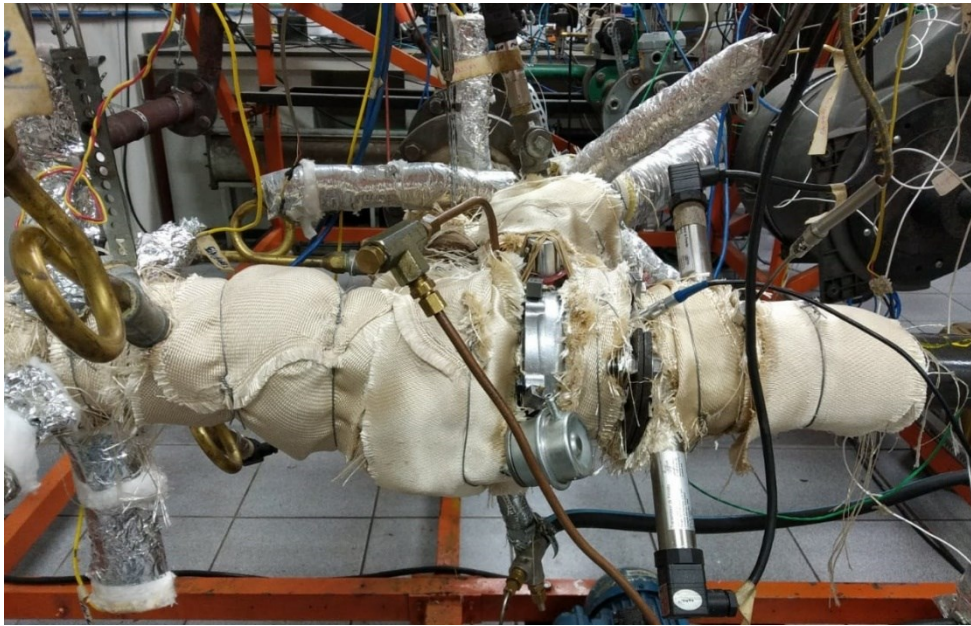


Figure 44 – Thermal insulation of components.

3.6.2. TD data acquisition device

The TD data acquisition system is formed by automated test equipment. An NI USB 6009 board is used to communicate the command center computer and TD data collector modules. It also allowed, with the supervisory program on the LabVIEW platform, the monitoring of data collected in real time during the experiments (as explained in Section 3.6.4).

An SCXI-1000 chassis is used to power and synchronize the SCXI-1102 module with the SCXI-1308 accessory, which collected the signals from the flow sensor in the centrifugal compressor and from the pressure sensors at the compressor and turbine turbine inputs and outputs and from air plenum box.

A NI USB 6009 board is used to acquire the signals from the rotary speed sensor, the PWM (pulse width modulation) of the lubricating oil cooling fan, the analog signal of the WEG C08 variable-frequency drive and atmospheric air relative humidity data provided by the WTUTA-5700 Warme humidity transducer.

A cDAQ-9178 chassis powered and synchronized the NI-9212 and NI-9205 modules. As high frequency phenomena are not expected for the data to be collected by these modules, the configured sampling rate is 2 kHz. In addition, a NOVUS TxRail temperature converter is used to perform the thermocouple connections not served by the NI-9212 module at the NI-9205 module.

The NI-9212 module with NI TB-9214 accessory performed the acquisition of signals from thermocouples installed in the compressor and turbocharger turbine inputs and outputs. The NI-9205 module with accessory 781081-01, on the other hand, collected signals from other thermocouples and pressure gauges. These thermocouples are installed at the centrifugal compressor inlet, at the compressor and turbocharger turbine outlets, at the fuel gas inlet, at the combustion air inlet, at the turbocharger's lubricating oil inlet and outlet. These pressure gauges are installed at the turbocharger compressor and turbine inlets, at the fuel gas inlet, at the air inlet for combustion and at the turbocharger's lubricating oil injection.

Figure 45 shows the TD signal measurement system used in the turbocharger test bench.

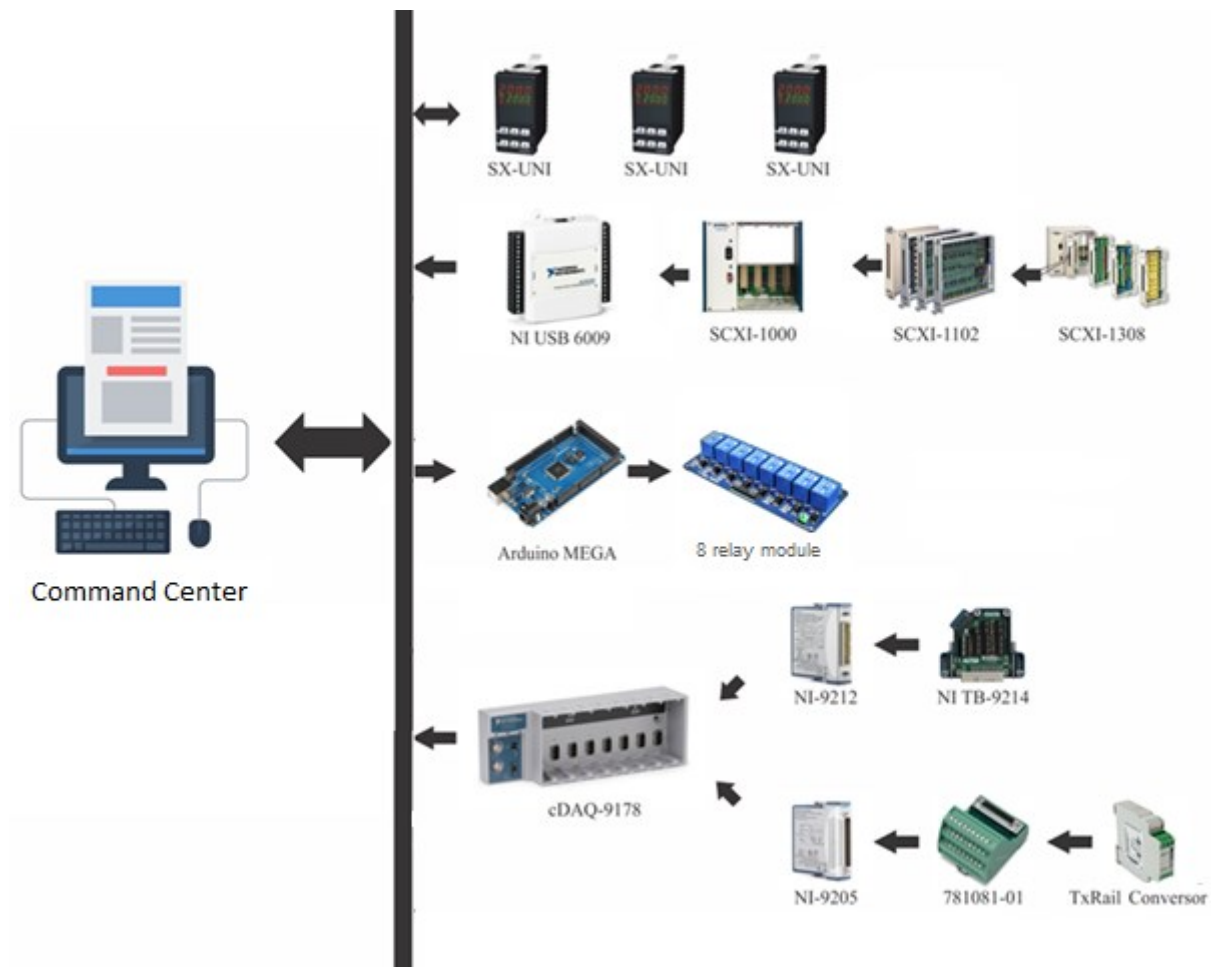


Figure 45 – TD data acquisition system

3.6.3. RD data acquisition device

The RD data acquisition system is composed by transducers of acceleration, displacement and acoustic emission and conditioning acquisition boards.

The accelerometer and AE data acquisition is composed by an NI PXI 1042 console with interface with a LabVIEW program and has the following characteristics: an NI PXI 8106 controller board with Dual-Core Intel Core 2 Duo Dual-channel 667 MHz DDR2 processor RAM with 512 MB.

The NI PXI 4462 Board is used for accelerometer signal acquisition and has four channels with an acquisition frequency of up to 204,800 Hz. The board is configured with an acquisition rate of 20 kHz, with 2,000 points every 0.1 second, since the highest frequencies to be performed, accelerometer measurements are close to 10 kHz. With this system, it is possible to use the tools of the LabVIEW program for real-time signal analysis.

The DAQ NI PXI6115 and the terminal block DAQ NI TB-2708 PXI are used for AE signal acquisition. A preamplifier with selected 40dB gain is used in the instrumentation system. The NI Sound and Vibration kit is used to capture continuously the AE signals at sampling frequency of 2 MHz and acquisition time of 0.1 second, recording 200,000 points. The software Labview© permits to analyze the AE signals in real time.

Another NI USB 6009 board is used to acquire the proximity probe signals (with PREDICTECH TM0182 driver) and uses the same command center from TD system.

Figure 46 indicates the RD signal measurement system used in the turbocharger test bench.

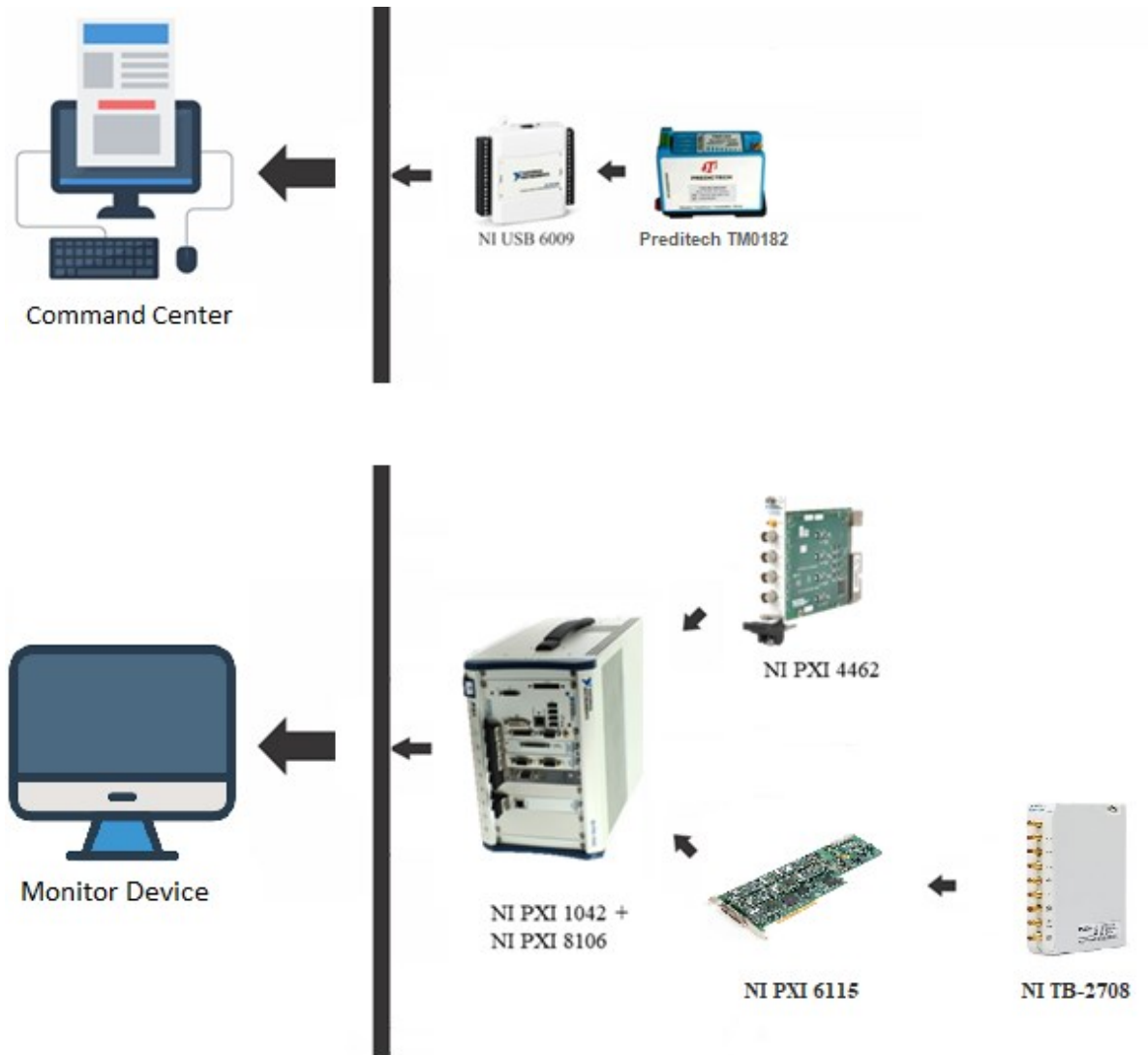


Figure 46 – RD data acquisition systems

3.6.4. TC command center + TD and Proximity probe data recorder

In the command center, illustrated in Figure 47, there is the supervision room of the experimental tests, as well as the computer hardware that contains the variable control software such as pressurized air flow, fuel flow, compressor rotation, temperature and pressure of the lubrication system, ignition system, and others. On this computer, the signals from TD data acquisition boards are also collected.

The computer hardware is an ASUS LGA1150 device, with 16 GB of RAM memory, 2TB HD, LGA1150 Intel Core i7-4790K processor and 4GHz processing, which allowing automatically and reliably monitor of important TD variables in an experimental test, enabling the execution of corrective measures quickly and controlled.



Figure 47 – Command center and TD data monitoring and recording set

The supervisory system of the TC TD data (temperatures, flows and pressures) is composed of an interface related to a program developed on the LabVIEW platform, integrated to the command center computer. This system allows real-time monitoring and control of test bench input parameters during tests.

Figure 48 shows the interface used to monitor the pressure and injection temperature of the lubricating oil in the turbocharger, the oil temperature in the reservoir, the inlet and outlet pressures of the centrifugal compressor and turbine, the flow and pressure in the reservoir of compressed air used for combustion.

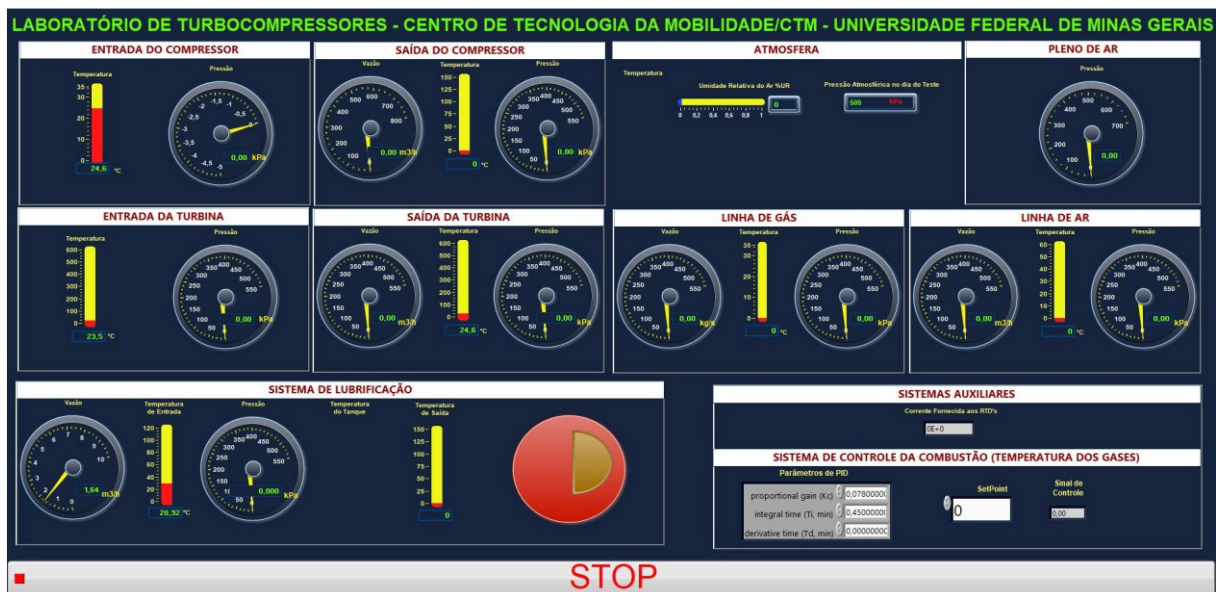


Figure 48 – Fluid pressure and temperature supervision interface

The interface shown in Figure 49 allows manual control of the compressed air valve, the fuel gas valve and the air outlet valve on the centrifugal compressor, by which its working point is modified. In addition, it confirms that the lubrication system and instrumentation controls are turned on and working. In this way, this interface presents options to modify the activation of the ignition in the combustion chamber, as the rotational speed of the turbocharger and the injection temperature of its lubricating oil.



Figure 49 – Fluid pressure and temperature supervision interface.

Finally, the interface shown in Figure 50 allows the monitoring of relative air humidity, compressor flow rates, air inlet, fuel gas inlet and exhaust in the combustion chamber, as well as the temperatures and pressures at the inlets and outlets turbine and compressor of the turbocharger, which are commonly used information to identify the surge threshold during the eorkbench operation in the tests.

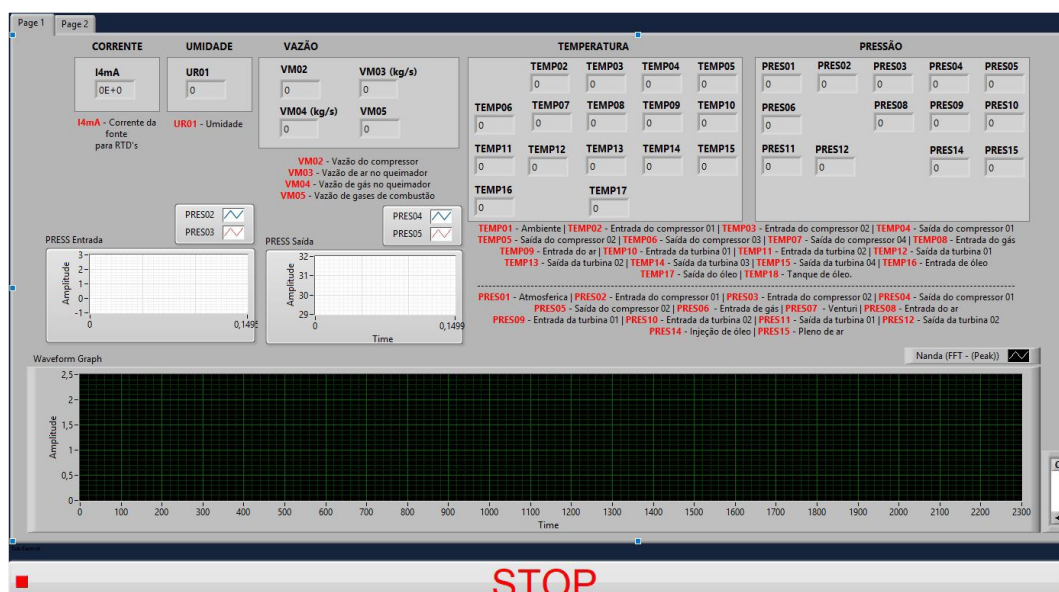


Figure 50 – Fluid pressure and temperature supervision interface

3.6.5. DAQ sets for accelerometer and AE data recording

A National Instruments DAQ set is used with a monitor device as illustrated in Figure 51 to view the x-, y- and z-axis accelerometer and AE signals recorded in real time.



Figure 51 – The National Instruments DAQ set

The accelerometer and AE amplitude signals are captured in volts. The real numbers in each recorded *Labview*® datafile are converted into floating point double precision numbers by using the *Labview*® function Float64. All data are recorded as raw data, i.e., amplitude versus time, with further processing based on data analysis that will be explained in Chapter 4.

Figure 52 shows the accelerometer and acoustic emission real time data monitoring and recording interface in LabView.

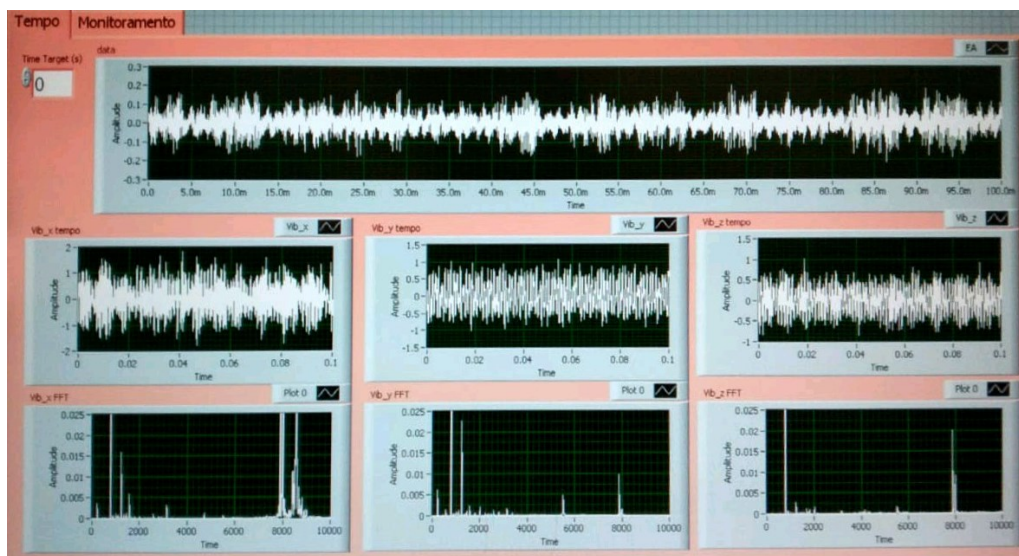


Figure 52 – RD accelerometer and acoustic emission data monitoring and recording interface.

3.7. THERMODYNAMIC AND ROTORDYNAMIC DATA ACQUISITION PROCEDURE

3.7.1. Turbocharger Thermodynamic Maps and Graphs

The instrumentation installed on the workbench and the data acquisition system are responsible for collecting the pertinent information for the thermodynamic maps elaboration of the turbochargers to be presented in this work.

At the beginning of each test (one for each of seven TCs) the heating warm-up determined by SAE J1723 (SAE, 1995) is performed. Then, the TC maintain constant rotational speeds (speed lines) for simultaneous variation and data collection of mass flow rates, pressures and temperatures to be used for the construction of maps.

As recommended by Romero (2004), the tests started at the lowest to the highest speed lines, in order to obtain a shorter temperature stabilization time. Therefore, the setpoint values are stipulated for the controller to maintain each speed line to change the mass flows by opening and closing valves. As the compression and expansion ratios are dependent of these variables, this magnitude is also changed.

All the seven Biagio AUT1000 turbarchargers are tested at six operating points in each speed line in order to decrease the interpolation interval of the compressor map, where 67, 89, 105, 121 and 135 krpm speed lines are controlled by a PID algorithm developed in LabVIEW. Thus, 30 point are obtained for each TC.

The change in each speed line is done by gradually increasing the exhaust gases discharge from the combustion chamber. When the target speed line is reached, the air valve at the outlet of the centrifugal compressor is gradually closed, in order to decrease the air mass flow and increase the compression ratio, obtaining the necessary point for that speed line. Compressor valve closing conditions are defined as a number of points (n) that are tested for each rotation curve, i.e., each speed line, in order to reduce the need for interpolations, where a $(n+1)$ th test point is characterized by instability in the compressor to present the surge condition.

For the tests developed in this work, data is collected at five speed lines and, for each of them, temperature, pressure and mass flow data are measured at five different points (combinations of corrected mass flow and compression or expansion ratio). A sixth point for each speed line (surge point) is induced by the lack of flow at the compressor inlet. Once the surge line point is reached, the valve at the compressor outlet returns to full opening and,

from that point, registers the next speed line to be tested in the controller. This process must be repeated until all the intended speed lines are tested.

During the experiments, the supervisory system is used to establish the operating conditions and provide information for the control of the tested thermodynamic parameters. To identify the surge thresholds, the detection technique by sinusoidal variation of the centrifugal compressor discharge pressure (ZHENG *et al.*, 2017) is applied.

Figure 53 shows examples of (a) performance map and (b) compressor efficiency, and (c) performance map and (d) turbine and rotor-bearing set efficiency for turbochargers.

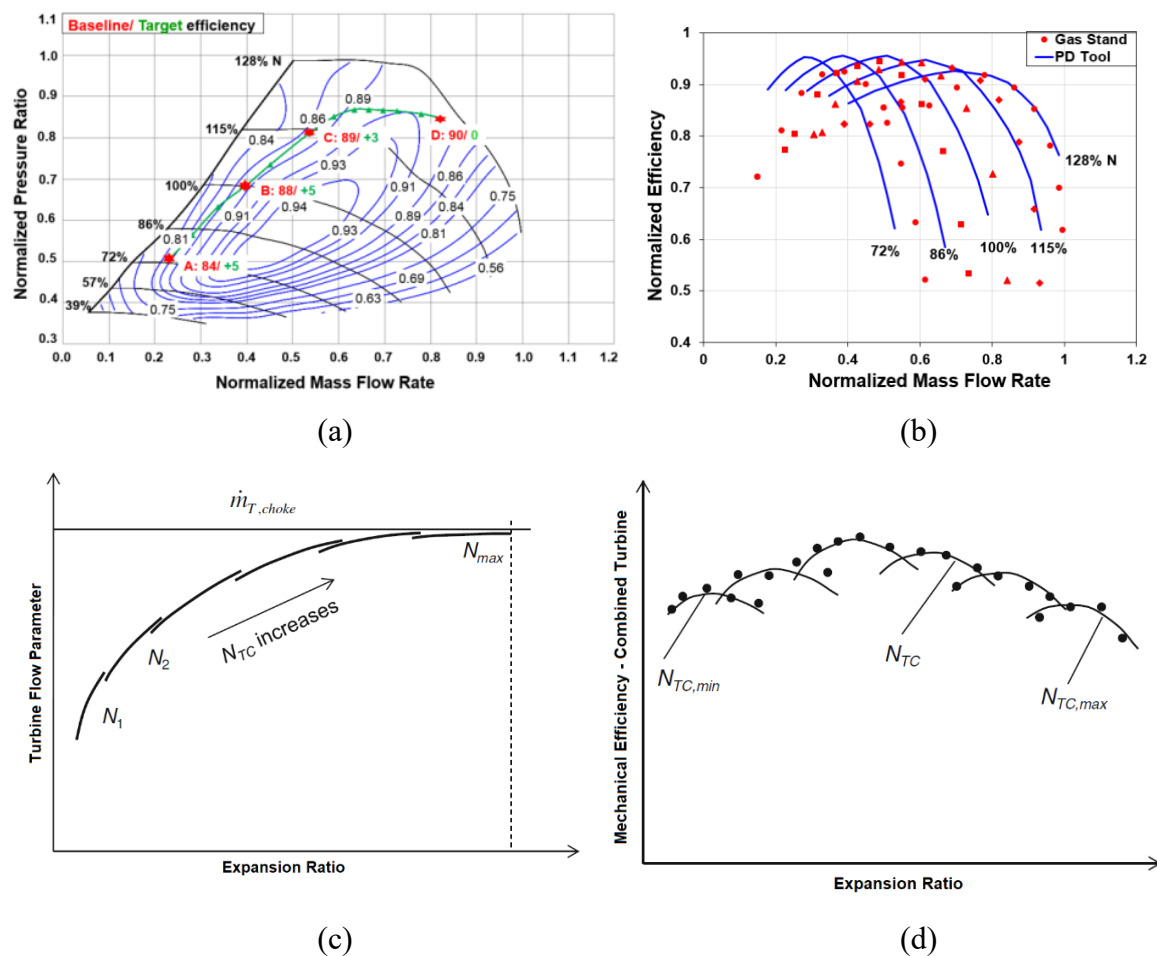


Figure 53 – Examples of turbocharger compressor (a) performance and (b) efficiency maps (Font: DHINAGARAN *et al.*, 2017) and turbine (c) performance and (d) efficiency maps (Font: HUNG-NGUYEN SCHÄFER, 2015).

3.7.2. Turbocharger Rotordynamic Graphs

In addition to the thermodynamic data, the supervisory system also provided information for choosing the instants at which data from accelerometers, proximity probes and AE sensor are measured. For the subsequent processing of the tests of the data measured by these sensors, the MathWorks Matlab© 2021 software is used, in order to obtain the presentation of these data according to the strategies described in the sub-items below.

Accelerometer frequency spectrum (steady-state analysis)

The data collected by accelerometers are graphically represented in frequency spectrum (amplitude versus frequency). Vance (1988) indicates that if the frequency of the expected vibration is greater than 1,000 Hz, you must use an accelerometer and above 250 Hz, the acceleration produces the better output levels. The frequency spectra are obtained using the Fast Fourier Transform (FFT) directly implemented by the Matlab software for the data measured simultaneously with the collection of thermodynamic data used to build the TD maps and graphs. In other words, the acquisition of vibration data for the formation of spectra is carried out in a steady state.

This methodology allows to identify the characteristic frequencies associated with synchronous rotor vibrations and to attenuate the influence of the variation of other parameters that cause displacements and deformations of the housing, such as temperature variation, pressure, and rotor rotational speed.

Vance (1988) reinforces that bearing imperfections produce multiple-frequency excitation even at constant speed, therefore, is an important aspect to be accounted for in the analysis. Figure 54 presents a frequency spectrum obtained for a turbocharger using accelerometer in a constant speed.

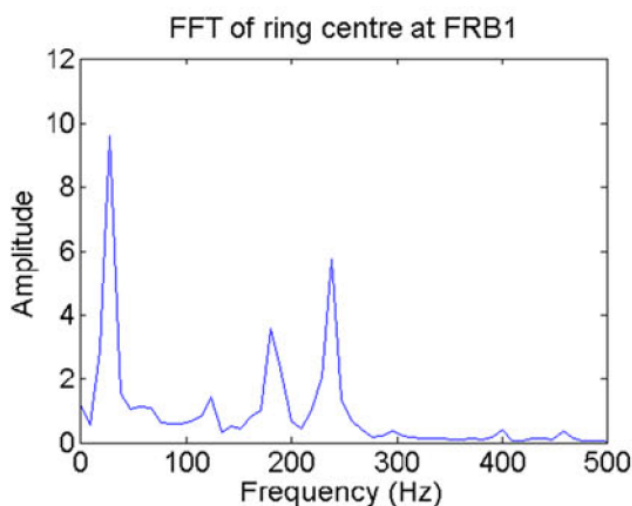


Figure 54 – Turbocharger frequency spectrum (SINGH and GUPTA, 2020)

Accelerometer Waterfalls (transient analysis)

Cascade diagrams, also called waterfalls, are one of the most common RD graphs and provide a better visualization for analyzing the transient effects of the vibrational response of a rotor. The amplitude of whirling motion is analyzed as function of the vibration frequency at the rotating speed range selected for rotor acceleration and deceleration.

The variation of rotating speed of the turbocharger is carried out warm, i.e., with the temperature still high due to the execution of the complete procedure for obtaining the thermodynamic maps, but not completely heated due to the absence of burning in the combustion chamber. Thus, with the turbocharger rotating speed close to idle (about 5 krpm) and without fuel gas injection in the turbine supply line, the compressed air flow in that same line is increased, in order to promote the acceleration of the rotor (run up), and after the stagnation of rotational speed, the air flow is reduced to promote deceleration (coast down).

According to Vance (1988) and Nguyen-Schäfer (2015), waterfalls should be used to identify the critical velocities of non-linear systems, for example, when there is a large amplitude of orbital displacement. In this condition, a simple identification of characteristic frequencies for the identification of critical speeds, which can be done using the Campbell diagram, is inadequate. Furthermore, the effectiveness of attenuating the vibrational response resulting from unbalance can be evaluated by the synchronous vibration amplitude measured during acceleration. As for operation at constant speed, a condition in which the frequency spectra described in the previous section are generated, subsynchronous vibrations are evaluated. Figure 55 shows a waterfall from a turbocharger obtained during acceleration and deceleration of a turbocharger using accelerometer.

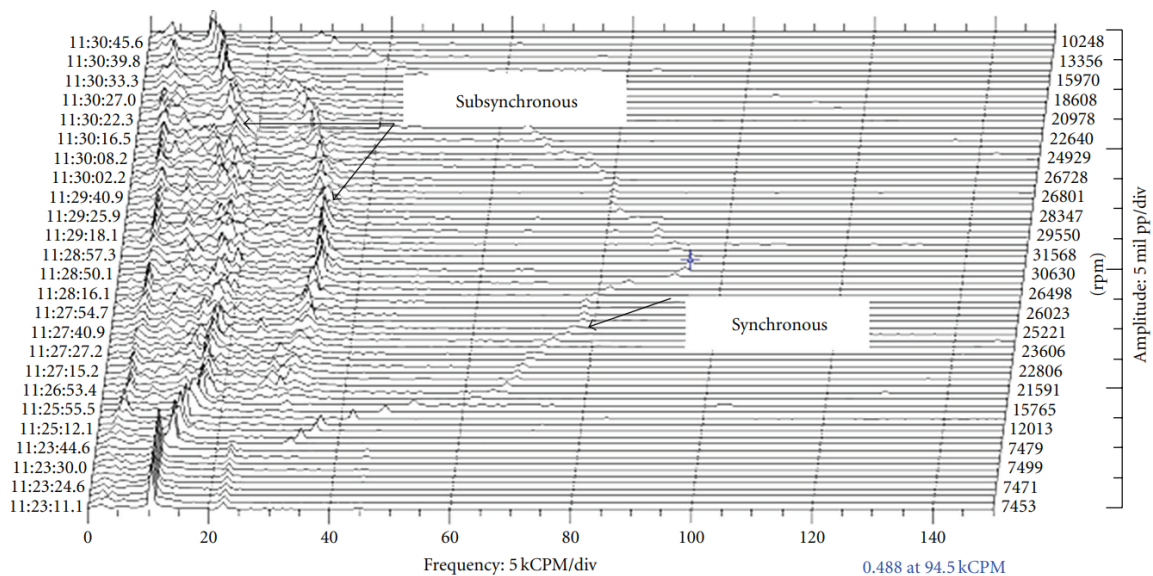


Figure 55 – Turbocharger waterfall during acceleration and deceleration (KIRK and ALSAEED, 2011)

Rotor orbits

Rotor orbit graphs provide a visualization of the trend of the shaft whirling movement for a given operating condition as presented in Figure 56. They show the path taken by the shaft geometric center in a orthogonal plane to the axis of rotation. It is, therefore, a two-dimensional graph with the axes showing the radial displacement of the shaft, in the horizontal and vertical directions. Usually, these orbits must be obtained at steady state conditions, that is, at constant speed and without variation of the other operating parameters (in the case of the turbocharger test bench, the parameters of the air and fuel supply must be maintained).

Therefore, as well as the vibration spectrum, the radial displacement data of the rotor are collected under the same conditions defined in the points of the thermodynamic maps, i.e., at steady state conditions. For this work, the acquisition of shaft displacements is performed through the use of proximity probes attached to the compressor housing and pointed at the tip of the rotary shaft. These data are obtained independently through another separate test, so that there is no change in the compressor inlet airflow that would generate a modified thermodynamic map.

In Nguyen-Schäfer (2013), due to nonlinearity of the oil film bearings, the rotordynamic behavior of the turbocharger becomes more nonlinear at increasing rotor speeds and the rotor orbit provides an important information for high speed TCs. During the analysis of the obtained results, it is possible to observe phase changes in the orbit, that is, changes in the direction of the values of smaller and larger amplitudes. According to Allaire and Flack (1981), this occurs when passing through the critical rotor speed, and sometimes it can be more difficult to detect this effect, since the phase change can be in multiple values of 180° .

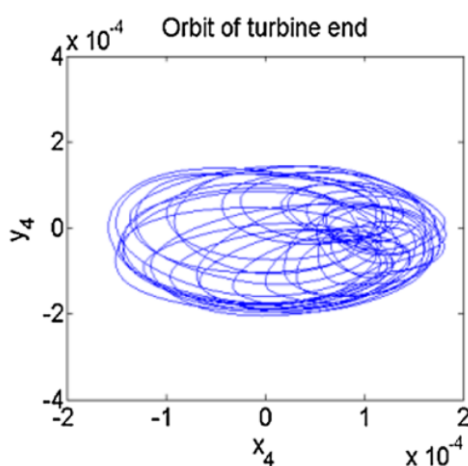


Figure 56 – Turbocharger orbit rotor obtained (SINGH and GUPTA, 2020)

Acoustic emission graphs

Acoustic emission data are most used in the industry to detect cracks in shafts, structures and other types of structural analysis. In rotating equipment, these data can be effective in analyzing cavitation at earlier times than other sensors, such as pressure sensors and accelerometers.

In rotordynamics, some experimental works use AE to detect the level of friction/rubbing in rotor-bearings-seals assemblies and monitoring friction and wear, and can be used to improve numerical models to predict high frequency responses in high speed rotors with journal bearings. One of the main works that uses AE for rotordynamic analysis is presented by Mokhtari *et al.* (2020).

In this work, a AE sensor attached in the housing next to the compressor outlet provides AE data at the same time as the accelerometer data are obtained (at steady state condition). The main models used to filter these signals are performed at MatLab: Wavelet and Bandpass. Data are analyzed using time-based as the peaks or variations in the AE signal are not dependent on frequency and characteristics. Several statistical analysis are done for windowing (one shaft revolution) and full data (all shaft revolutions in 0.1s, producing statistical features such as RMS, skewness, kurtosis, crest factor, clearance factor, Shannon entropy, median frequency etc.

Therefore, the main target in the use of AE is to answer what is possible to observe with AE sensor in high speed TCs and if it is worthwhile in monitoring the condition and/or failure, as surge detection and other TC rotordynamics issues. Figure 57 shows an EA measured data to estimate the cavitation of stainless steel sample using a high speed flow machine test bench and, in the right bottom position, a zoom into one of the peaks. This zoom is called windowing and is intended to perform more detailed analysis of the AE sensor responses.

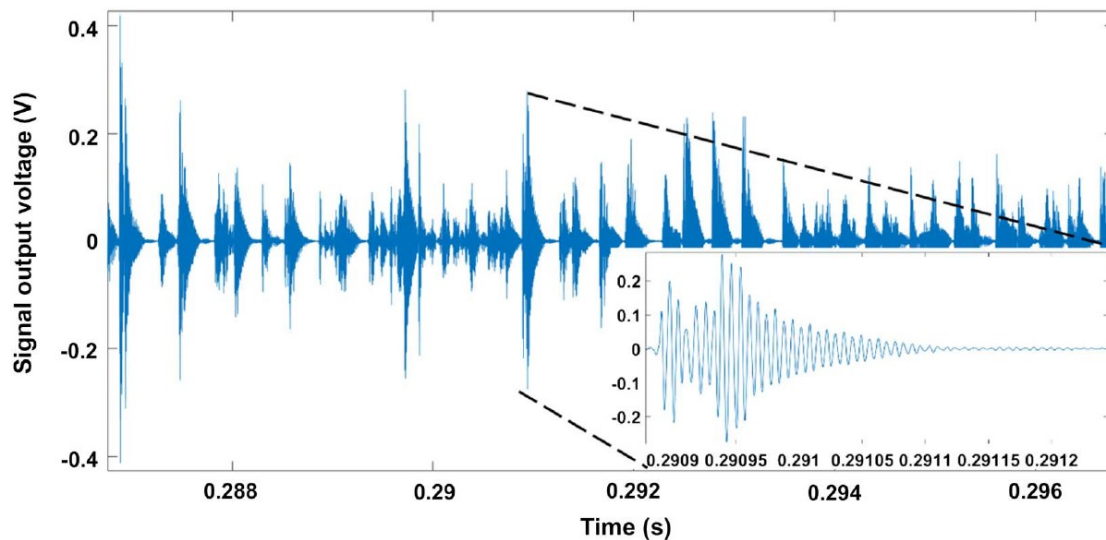


Figure 57 – AE sensor signal in a cavitation test and a zoom (windowing) into one of the peaks (YLÖNEN *et al.*, 2020).

3.8. UNCERTAINTY PROPAGATION ANALYSIS

According to the measurement uncertainties of each instrument used in the tests, the propagation of the uncertainties of the results could be calculated according to what is established by the ASME PTC 19.1 standard (ASME, 2019). In this work, all uncertainties are Type B as in this type the evaluation of standard uncertainty is usually based on scientific judgment using all of the relevant information available, which include measurement data, manufacturer's specifications, data provided in calibration and uncertainties assigned to reference data taken from references.

Sandoval (2019) presents in their study the determination of the propagation of uncertainties for the TD and acceleration results obtained by tests carried out with the turbocharger test bench used for this work.

For displacement sensors, the calculated uncertainty that will be considered is equal to the maximum error reported by the manufacturer of these sensors: ± 0.038 mm.

For the acoustic emission sensor, calibration data based on ASTM E976 (PHYSICAL ACOUSTICS CO., 2009) and conventional pencil lead breaking are used. This methodology presents a good repeatability in the registered AE signals (BABAK, FILONENKO, KALITA, 2006). The entire procedure for the test is based on AFIAP, 2004 with a sampling rate of 2MHz for 2 seconds (totaling 4,000,000 points). The device (pencil lead break) is an aid to simulate an acoustic emission event using the fracture of a brittle graphite lead in a suitable fitting. The calibrating device comes down to making a proper head, automatic pencil and marking points of 2H hardness and the gauge of 0.5 mm. The calibration signal

is generated in the Hsu-Nielsen system at the moment of breaking a sensitive graphite pin cased by a properly adapted tip put on the automatic pencil. The head and the marking point pulled out to 3 mm ensure the same breaking angle at each test, which also means generation of a repeatable acoustic surface wave. This method is classified as one of the pulse calibration methods (BOCZAR and LORENC, 2006). This method also generates an intense acoustic signal, quite similar to a natural AE source, which the sensors detect as a strong burst (LAMY *et al.*, 2013). Figure 58 presents the pencil with the graphite length used and the support device created to perform lead break method in the correct angle. The support device is the adaptation of the Nielsen shoe (ASTM E976, 2015; ATG, 2021) and is made by PA6 polyamide. This type of source is also referred to as the Hsu-Nielsen source, based on the original works of Hsu (HSU and BRECKENRIDGE, 1981).

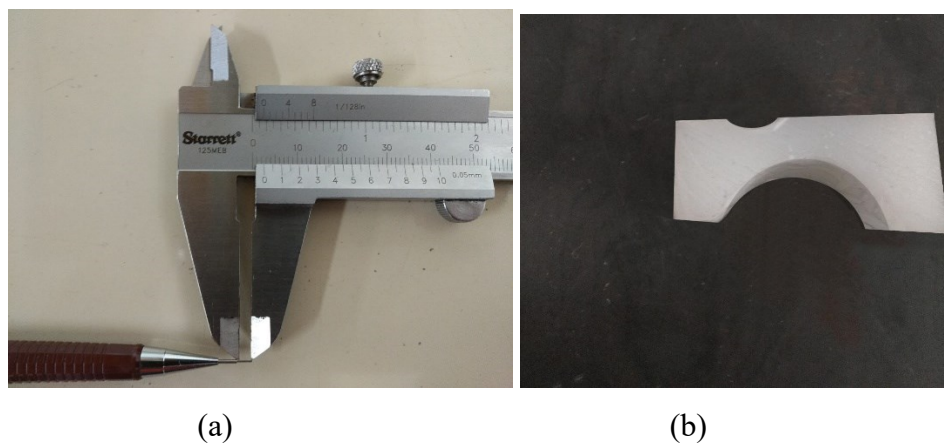


Figure 58 – (a) Measurement of graphite to calibrate and (b) a PA6 adaptive base to use on the compressor housing with the automatic pencil

The results are compared with others already performed with this same sensor (LINHARES, 2011), showing good correlation. Additionally, an interpretation of the AE signal to verify possible distortions (AE signal saturation and temporary vanishing of the amplitude caused by overload of the pre-amplifier) is performed using the methodology proposed by Jemielniak (2001). These calibration results are then, a posteriori, filtered to determine the uncertainties, according to filters also used in the CT results (to be presented in Chapter 4) based on the measurement frequencies and for each filter (the Monte Carlo method (MCM) is used) using the implementation of MatLab 2021 as Solaguren-Beascoa Fernández *et al.* (2009) and Jie *et al.* (2011) for the evaluation of measurement uncertainties. A 95% probability symmetrical inclusion range is determined using Huang *et al.* (2019) methodology. The maximum uncertainties obtained for each frequency filter is shown in Table 18. The presentation of uncertainties for acoustic emission sensors is also presented

as a function of measurement frequencies by Keprt and Benes (2009), being a less generalist form of uncertainties for this sensor.

Table 18 – Uncertainties considered for evaluating the results of this work

Result Type	Uncertainty
Total compression ratio	$\pm 2.3\%$ of the calculated value
Corrected mass flow in the compressor	$\pm 0.8\%$ of the calculated value
Compressor isentropic efficiency	$\pm 8.3\%$ of the calculated value for low rotational speeds and points close to the surge; $\pm 2.5\%$ of the calculated value for the other points.
Total expansion ratio	$\pm 5.0\%$ of the calculated value
Corrected mass flow in the turbine	$\pm 4.3\%$ of the calculated value for low rotary speeds; $\pm 2.6\%$ of the calculated value for the other points.
Combined turbine efficiency	$\pm 12.0\%$ of the calculated value for low rotational speeds and points close to the surge; $\pm 2.6\%$ of the calculated value for the other points.
Accelerometers	$\pm 10.0\%$ of the read value
Proximity probes	± 0.038 mm
AE sensors	$\pm 11.2\%$ of the read value [20-300 kHz] $\pm 8.8\%$ of the read value [300-700 kHz] $\pm 7.1\%$ of the read value [700-1,000 kHz]

4. RESULTS AND DISCUSSION

In this section, the most relevant experimental results obtained by the thermodynamic (TD) and rotordynamic (RD) tests performed on the automotive turbocharger supported on different fluid film bearings are presented accompanied by a discussion about the measured variables selected to describe its behavior. For the TD analysis, the performance and efficiency maps and graphs drawn up with the tests of the evaluated turbochargers will be presented. For the RD analysis, frequency spectra for steady-state condition will be presented, as waterfalls of turbocharger acceleration (run-up) and deceleration (coast-down). Graphs of shaft whirling orbits developed by the rotor also in permanent condition will be shown and, finally, an in-depth study of the acoustic emission signals and their statistical analyses. Thermal maps and vibration response diagrams are obtained for the seven turbochargers. Each bearing gives the turbocharger slightly different characteristics. The TCs are compared and ranked using a decision matrix by the MCDM Pugh method.

4.1. TD MAP AND GRAPHS

The experimental thermodynamic results for the turbochargers analyzed will be presented and compared. For TD analysis of the TC, compressor and turbine performances are presented as indicated by Nguyen-Schäfer (2015). Schwarz and Andrews (2014) complement that is important also to show the overall TC efficiency (η_{TC}), and this data are measured at speed line lines while varying the compressor pressure ratio, getting a combined efficiency based on the compressor (total-to-static) efficiency (η_C) and the combined turbine efficiency (η_T).

4.1.1. Centrifugal compressor performance and efficiency

Compressor efficiency analyses are one of the main procedures for evaluating the thermohydrodynamic performance of turbochargers, as well as mechanical and turbine efficiencies. Ryu and Ashton (2016) describe that the compressor efficiency (η_C) is found as the compressor stage enthalpy changes as a function of pressure and temperature across the stage (Equation 4.1):

$$\eta_C = \frac{(P_2 - P_1)^{\frac{\gamma_a - 1}{\gamma_a}} - 1}{(T_2 - T_1)} \quad (4.1)$$

where P_1 and P_2 are the compressor inlet and discharge pressures, respectively, T_1 and T_2 are the compressor inlet and discharge temperatures, respectively, and γ_a is the specific heat ratio for air.

For the preparation of performance and efficiency maps of the centrifugal compressor, the compression ratio, corrected mass flow and isentropic efficiency data of the compressor are compared in each of the five speed lines (SL) and five compressor outlet air valve closing positions (V.C.). The sixth V.C. position for each SL is observed by the noise and pressure variation and is not used in the compressor maps as it is already in a surge condition, i.e., with a high efficiency decay. Then, the fifth point is the final point before the start of the surge condition. Table 19 summarizes the speed lines and valve positions used in the tests.

Table 19 – Test Points for the Centrifugal Compressor of the Turbocharger

Speed	Compressor valve closing percentage					
	Point 1	Point 2	Point 3	Point 4	Point 5	Point 6
67 krpm	0% (fully open)	36%	63%	81%	90%	93% (surge observed)
89 krpm	0% (fully open)	31%	55%	70%	78%	87% (surge observed)
105 krpm	0% (fully open)	31%	54%	69%	77%	86% (surge observed)
121 krpm	0% (fully open)	30%	53%	68%	75%	85% (surge observed)
135 krpm	0% (fully open)	28%	49%	63%	75%	85% (surge observed)

The selection of the number of points to be measured per map is discussed by Gharaibeh and Costall (2017), which indicates that the time to obtain each point and the need for interpolation between the points should be the two main items to be evaluated during the measurements.

For this work, the selection of five speeds was performed based on the minimum operating speed of the turbocharger, as well as speeds before the critical speeds, close to the first critical speed, between the two critical speeds and the maximum operating speed (i.e., after the second critical speed).

The selection of the valve closing point was based on the consideration of the time needed to stabilize the air flow and speed, where for each point it was five to seven minutes, as well as the presentation in academia and industry of the number of points per speed (Jääskeläinen, 2021; Patterson, 2009; Miller, 2008). There is also evidence that there is no differentiation in the quality of compressor maps for turbochargers of the same size

when measuring five speeds by six valve positions (Sandoval, 2019) with thirty points, compared to measures seven by eight (Teixeira, 2020) with practically twice as many points and twice as long to obtain the data, with fifty-six points.

Figures 59 to 65 show the experimental compressor TCs (a) maps of performance and (b) isentropic efficiency. Each figure depicts maps for each one of the seven turbochargers selected for this work. Each turbocharger is mounted on fluid film bearings with different axial groove shapes, which are: triangular, half-ellipse, quarter-ellipse, inverted quarter-ellipse, rectangular, trapezoidal and circular. The performance map data was provided by interpolation methods to obtain the better efficiency islands. The main point is to evaluate the influence of the bearing axial groove shape on the behavior of TCs.

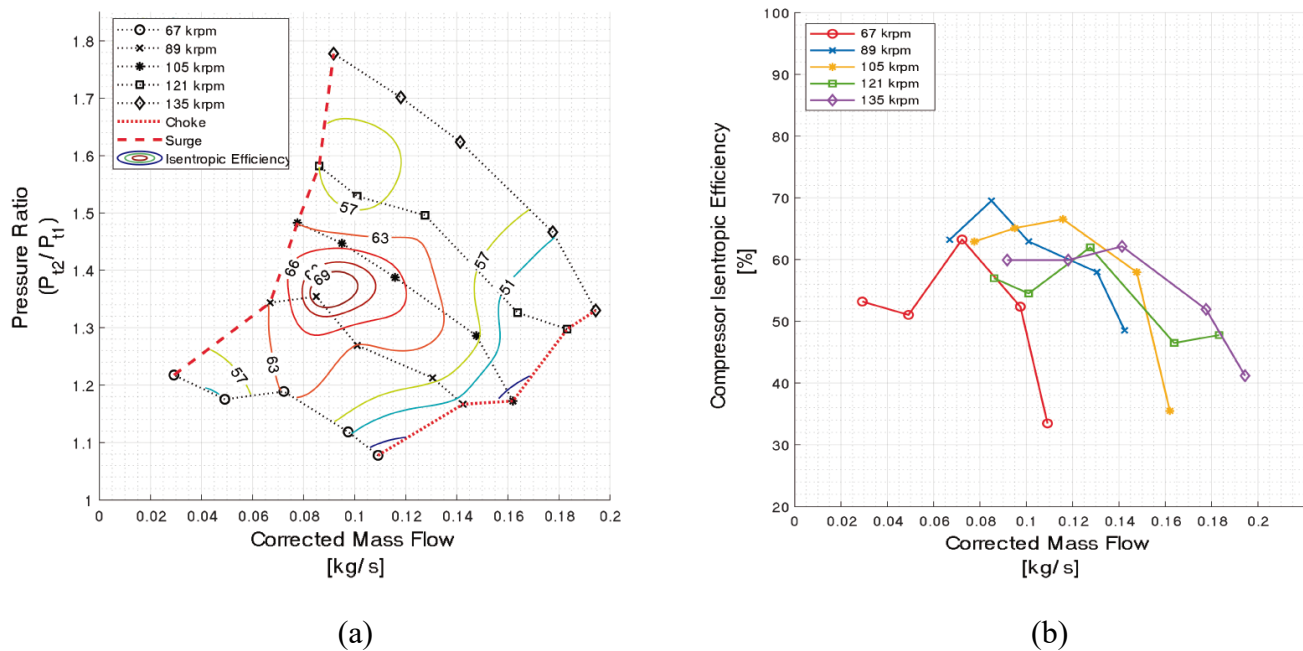
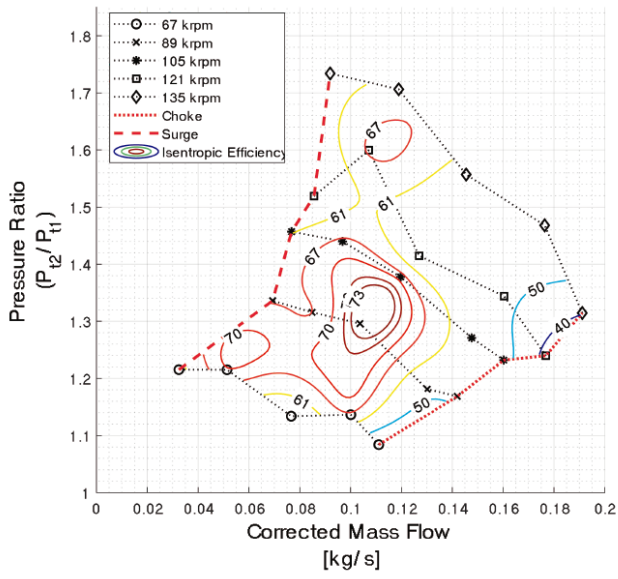
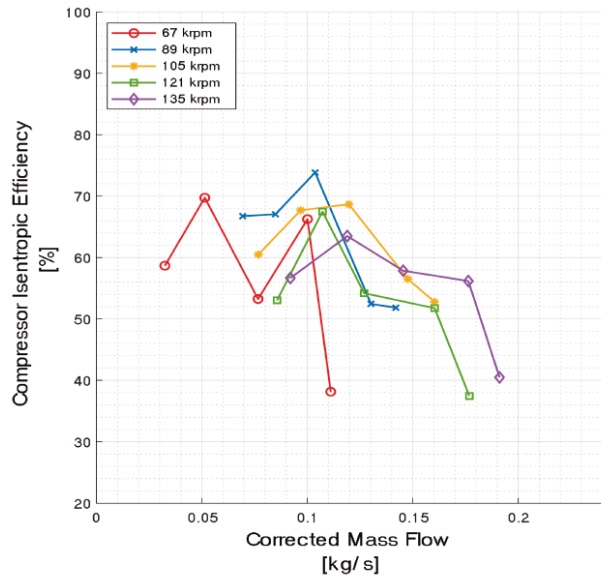


Figure 59 – (a) Performance and (b) Efficiency maps for the turbocharger supported on bearings with triangular shape grooves

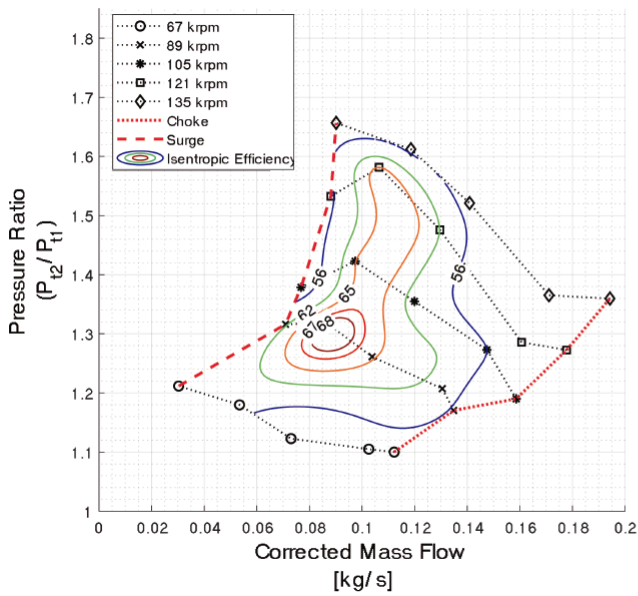


(a)

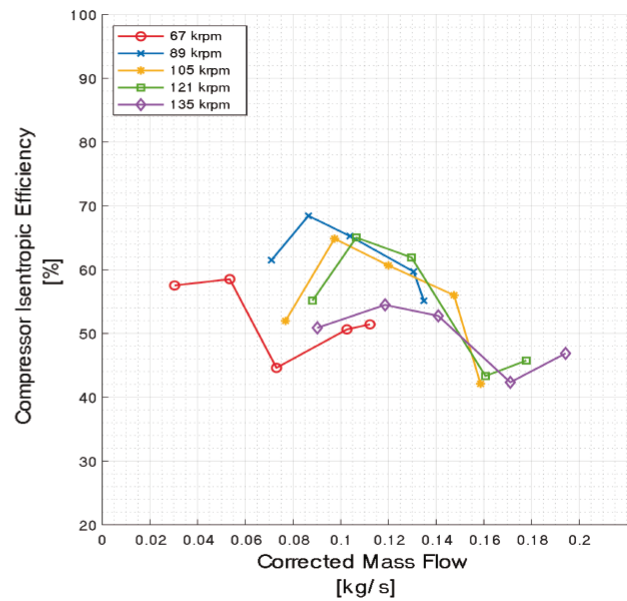


(b)

Figure 60 – (a) Performance and (b) Efficiency maps for the turbocharger supported on bearings with half-ellipse shape grooves

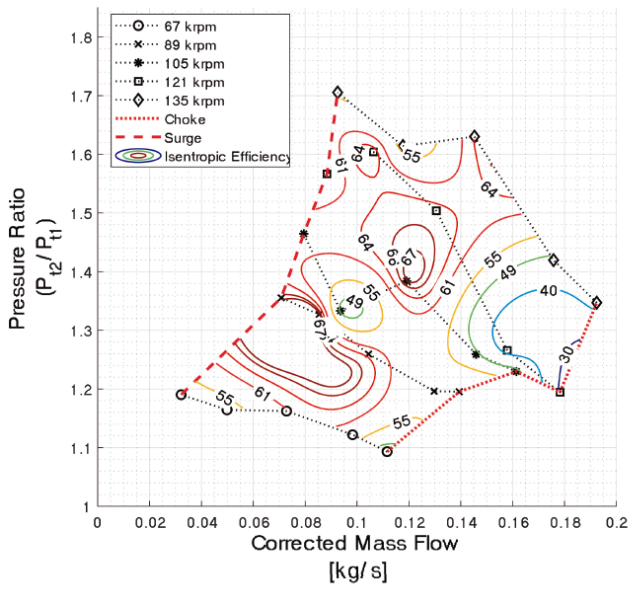


(a)

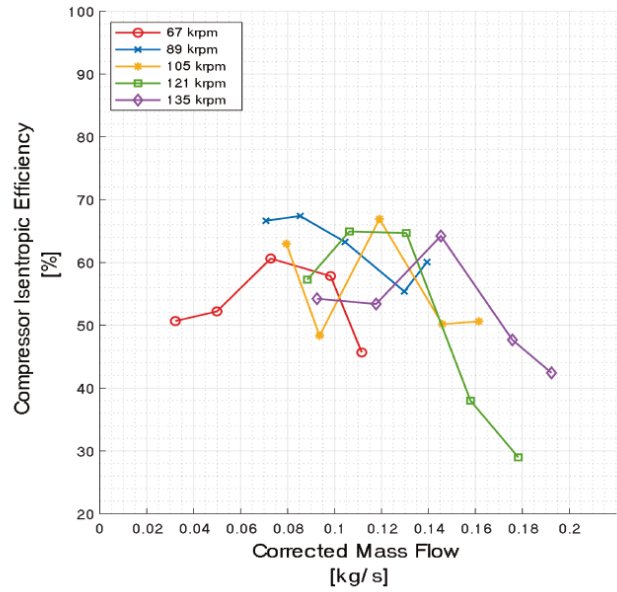


(b)

Figure 61 – (a) Performance and (b) Efficiency maps for the turbocharger supported on bearings with quarter-ellipse shape grooves

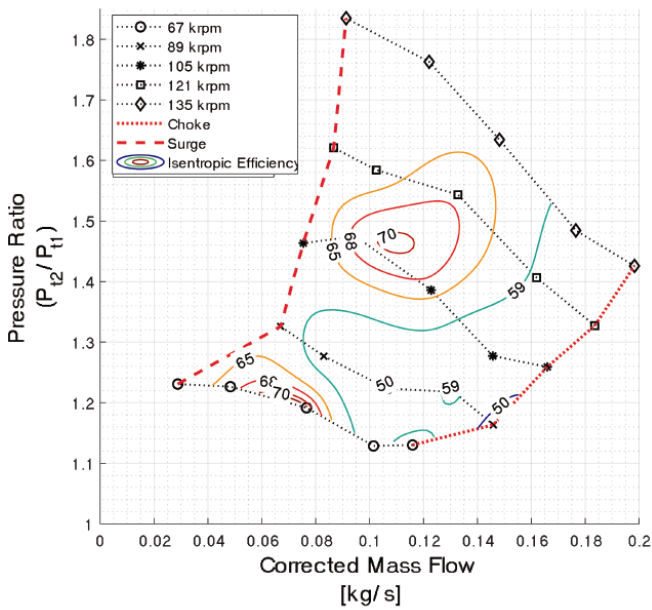


(a)

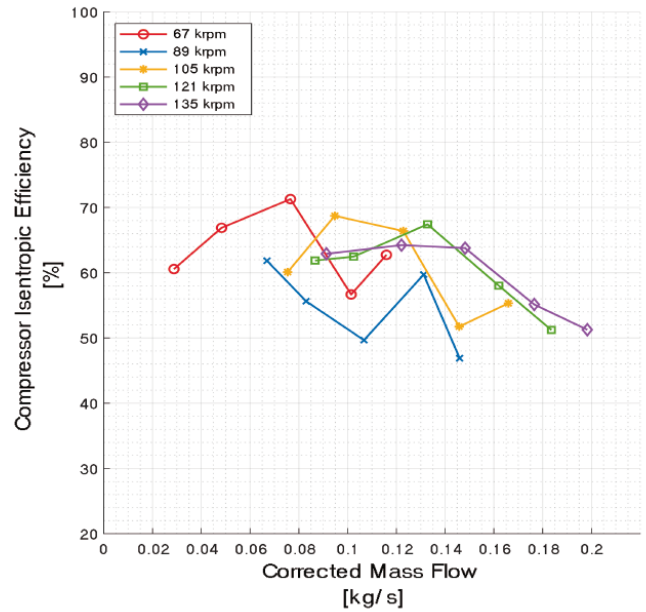


(b)

Figure 62 – (a) Performance and (b) Efficiency maps for the turbocharger supported on bearings with inverted quarter-ellipse shape grooves

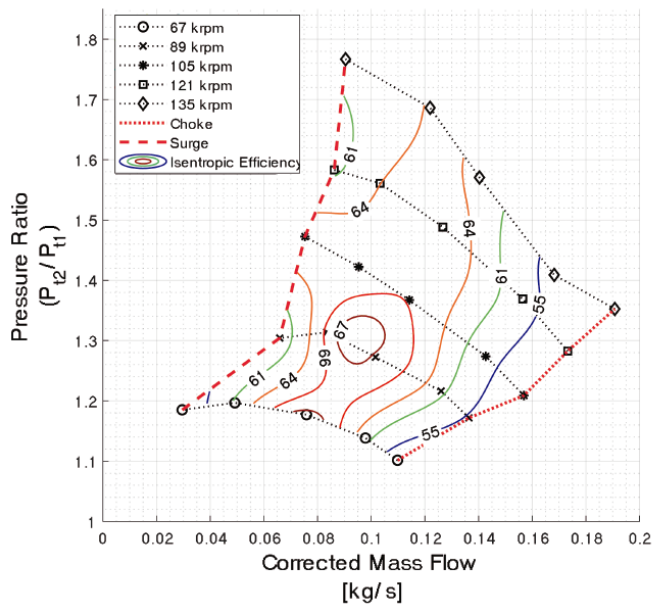


(a)

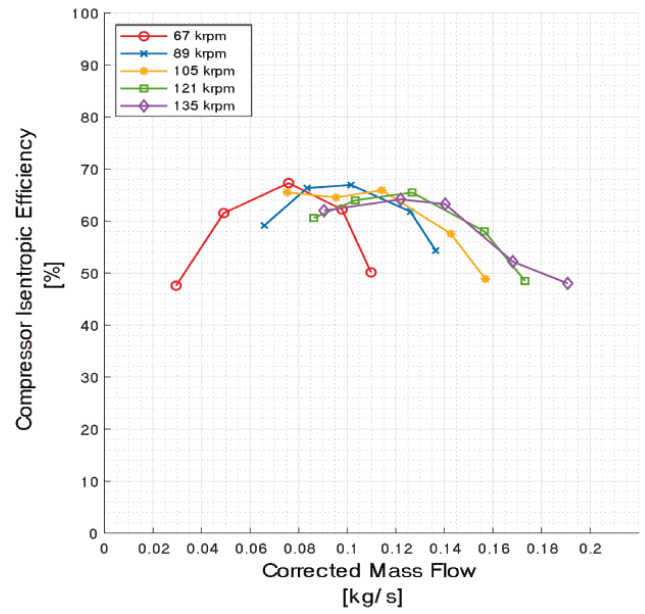


(b)

Figure 63 – (a) Performance and (b) Efficiency maps for the turbocharger supported on bearings with rectangular shape grooves

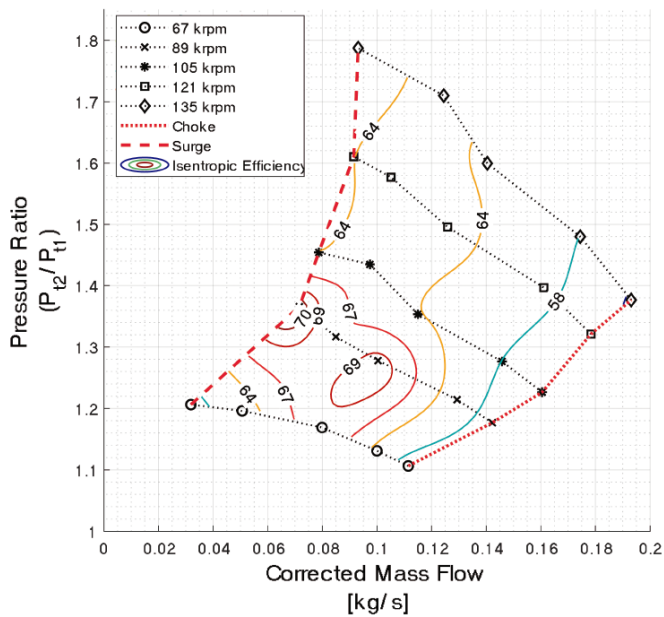


(a)

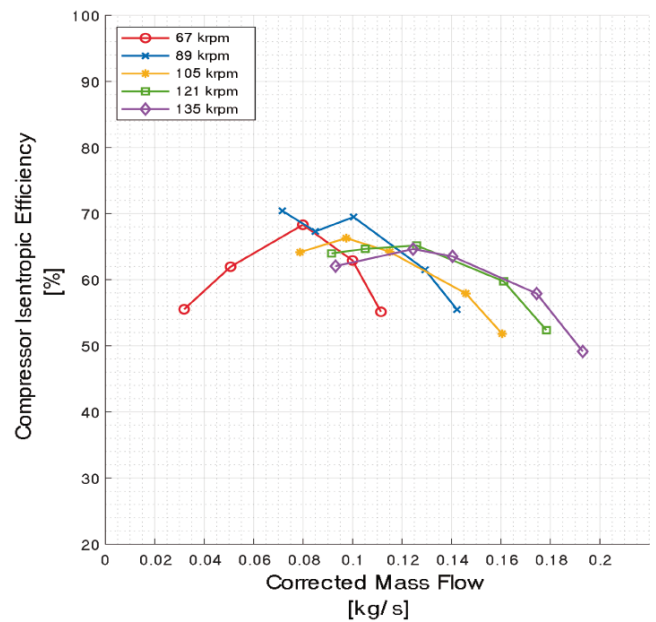


(b)

Figure 64 – (a) Performance and (b) Efficiency maps for the turbocharger supported on bearings with trapezoidal shape grooves



(a)



(b)

Figure 65 – (a) Performance and (b) Efficiency maps for the turbocharger supported on bearings with half-moon shape grooves

Performance Maps

For the first TC (Figure 59(a) – triangular shape), the maximum compression ratio achieved in its characterization test is 1.78, at a corrected mass flow rate of 0.092 kg/s. Second TC ((Figure 60(a) – half-ellipse shape) presented the maximum compression ratio of 1.73, at a mass flow rate of 0.092 kg/s. The third TC (Figure 61(a) – quarter-ellipse) 1.68 at 0.090 kg/s. Fourth TC (Figure 62(a) – inverted quarter-ellipse) 1.71 at 0.093 kg/s. The fifth TC (Figure 63(a) – rectangular) 1.84 at 0.091 kg/s. Sixth TC (Figure 64(a) – trapezoidal) 1.78 at 0.090 kg/s. And the last TC (Figure 65(a) – half-circle) 1.79 at 0.093 kg/s. All these seven maximum compression ratios happened at speed line 5 (135 krpm).

The compressor performance map is used to indicate the general isentropic efficiency as well as efficiency islands, and this is one of the reasons why it is highly used in the industry. In this context, is possible to analyze that the maximum reached by the TC 1 is a 69% efficiency island in the area between speed line 2 and speed line 3 (speed line 2-3 area), next to the valve closing points number 4 (V.C.s #4). The TC 2 got a maximum 73% efficiency island in the speed line 2-3 area, next to the V.C.s #3. TC 3 presented a maximum 68% efficiency island in the speed line 1-3 area, next to the V.C.s #3 and #4. TC 4 showed two maximums 67% efficiency island: a larger one in the speed line 1-2 area, next to the V.C.s #3 and #5, and a small one in the speed line 3-4 area, next to the V.C. #3. The TC 5 presented also two maximums 70% efficiency island: one in the speed line 1-2 area, next to the V.C.s #3 and #4, and another in the speed line 3-4 area, next to the V.C. #3 and #4 as well. TC 6 reached another also two maximums 67% efficiency island: one in the speed line 1-3 area, next to the V.C.s #3 and #4, and a small one in the speed line 1-2 area, next to the V.C. #3. For the last, the TC 7 got a maximum 70% efficiency island in the speed line 1-2 area, next to the V.C.s #5.

The relative difference among the maximum compression ratios for the turbochargers analyzed is 9.6%, which is greater than the 2.3% uncertainty for calculating this magnitude. The relative difference of the corrected mass flow results for these points is 3.3%, also higher than the uncertainty of 0.8% for calculating this magnitude. However, the difference between each of the data presented among the subsequent turbochargers (from largest to smallest) is always within the uncertainty range. Therefore, the results are presented with their uncertainty limits, and this is considered in the classification of grooves, presented later in this work.

Based on the aforementioned considerations, it is concluded that the maximum compression ratios are higher for TC 5 (rectangular). Considering the maximum isentropic

compressor efficiency, the TC 2 (half-ellipse) presented the greatest value. The results summarized above are summarized in Table 20.

Table 20 – Comparative thermodynamic performance characteristics of the turbochargers supported on bearings with different axial grooves

Turbocharger (bearing axial groove shape)	Parameters		
	Maximum compression ratio	Corrected mass flow for maximum compression ratio (kg/s)	Maximum isentropic compressor efficiency (%)
TC 1 (triangular)	1.78 ± 0.01	0.092 ± 0.001	69 ± 1
TC 2 (half-ellipse)	1.73 ± 0.01	0.092 ± 0.001	73 ± 1
TC 3 (quarter-ellipse)	1.68 ± 0.01	0.090 ± 0.001	68 ± 1
TC 4 (inverted quarter-ellipse)	1.71 ± 0.01	0.093 ± 0.001	67 ± 1
TC 5 (rectangular)	1.84 ± 0.01	0.091 ± 0.001	70 ± 1
TC 6 (trapezoidal)	1.78 ± 0.01	0.091 ± 0.001	67 ± 1
TC 7 (half-circle)	1.79 ± 0.01	0.093 ± 0.001	70 ± 1
<i>Mean</i>	<i>1.76</i>	<i>0.092</i>	-

Isentropic efficiency graphs

The complete analysis of centrifugal compressor isentropic efficiency is based in the maximum values reached for each of 5 speed lines. Moreover, the difference between the maximums and minimums indicates how constant the efficiency is at a certain compressor rotation speed with the change of mass flow.

The TC1 (Figure 59(b)) presents the respective maximums and minimums (max; min) for each speed line (SL 1 to 5): at 67 krpm (SL 1), 63% and 33%; at 89 krpm (SL 2), 69% and 49%; at 105 krpm (SL 3), 67% and 35%; at 121 krpm (SL 4), 62% and 49%; and at 135 krpm (SL 5), 62% and 41%.

For TC 2 (Figure 60(b)), the maximums and minimums are: at SL 1, 70% and 38%; at SL 2, 73% and 52%; at SL 3, 69% and 53%; at SL 4, 67% and 37%; at SL 5, 64% and 40%.

TC 3 (Figure 61(b)) shows the following numbers (maximums and minimums): at SL 1, 58% and 45%; at SL 2, 68% and 43%; at SL 3, 65% and 42%; at SL 4, 65% and 43%; at SL 5, 54% and 42%.

The maximums and minimums for TC4 (Figure 62(b)) are: at SL 1, 61% and 46%; at SL 2, 67% and 55%; at SL 3, 67% and 48%; at SL 4, 67% and 51%; at SL 5, 64% and 42%.

TC 5 (Figure 63(b)) presents the following maximums and minimums: at SL 1, 71% and 57%; at SL 2, 61% and 47%; at SL 3, 69% and 52%; at SL 4, 65% and 29%; at SL 5, 64% and 51%.

For TC 6 (Figure 64(b)), the maximums and minimums are: at SL 1, 67% and 47%; at SL 2, 67% and 54%; at SL 3, 66% and 49%; at SL 4, 65% and 49%; at SL 5, 64% and 48%.

And Finally, TC 7 (Figure 65(b)) presents the maximums and minimums: at SL 1, 68% and 55%; at SL 2, 70% and 55%; at SL 3, 66% and 52%; at SL 4, 65% and 52%; at SL 5, 65% and 49%.

Table 21 summarizes the values of compressor efficiencies for each TC at different 5 speed lines, including the maximums, minimums and the differences:

Table 21 – Comparison between compressor isentropic efficiency data

Turbocharger (bearing axial groove shape)	Efficiency (%)	Speed line 1 @ 67 krpm	Speed line 2 @ 89 krpm	Speed line 3 @ 105 krpm	Speed line 4 @ 121 krpm	Speed line 5 @ 135 krpm
TC 1 (triangular)	<i>Maximum</i>	63 ± 1	69 ± 1	67 ± 1	62 ± 1	62 ± 1
	<i>Minimum</i>	33 ± 1	49 ± 1	35 ± 1	49 ± 1	41 ± 1
TC 2 (half- ellipse)	<i>Maximum</i>	70 ± 1	73 ± 1	69 ± 1	67 ± 1	64 ± 1
	<i>Minimum</i>	38 ± 1	52 ± 1	53 ± 1	37 ± 1	40 ± 1
TC 3 (quarter- ellipse)	<i>Maximum</i>	58 ± 1	68 ± 1	65 ± 1	65 ± 1	54 ± 1
	<i>Minimum</i>	45 ± 1	43 ± 1	42 ± 1	43 ± 1	42 ± 1
TC 4 (inverted quarter-ellipse)	<i>Maximum</i>	61 ± 1	67 ± 1	67 ± 1	67 ± 1	64 ± 1
	<i>Minimum</i>	46 ± 1	55 ± 1	48 ± 1	51 ± 1	42 ± 1
TC 5 (rectangular)	<i>Maximum</i>	71 ± 1	61 ± 1	69 ± 1	65 ± 1	64 ± 1
	<i>Minimum</i>	57 ± 1	47 ± 1	52 ± 1	29 ± 1	51 ± 1
TC 6 (trapezoidal)	<i>Maximum</i>	67 ± 1	67 ± 1	66 ± 1	65 ± 1	64 ± 1
	<i>Minimum</i>	47 ± 1	54 ± 1	49 ± 1	49 ± 1	48 ± 1
TC 7 (half- circle)	<i>Maximum</i>	68 ± 1	70 ± 1	66 ± 1	65 ± 1	65 ± 1
	<i>Minimum</i>	55 ± 1	55 ± 1	52 ± 1	52 ± 1	49 ± 1
<i>Mean</i>	<i>Maximum</i>	65.4	67.9	67.0	65.1	62.4
	<i>Minimum</i>	45.9	50.7	47.3	44.3	44.7

It is important to note that, considering that some differences in results outweigh their uncertainties, some TCs present different values of compressor efficiency considering the uncertainty range in the isentropic efficiency, compression ratio and corrected mass flow. It can be observed that the bearing axial groove geometry has large influence on the thermodynamic behavior of the turbocharger compressors.

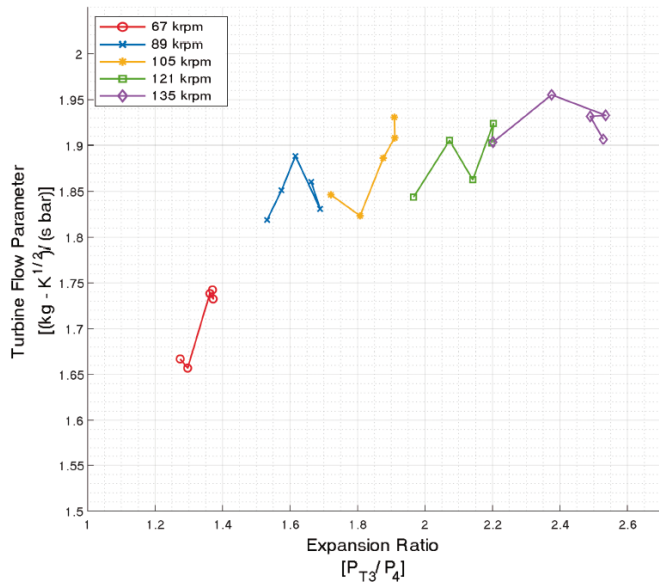
4.1.2. Combined Turbine performance and efficiency

The thermodynamic performance of turbochargers is based as well in mechanical and turbine efficiencies combined. The turbine combined efficiency (η_T) accounts for both the turbine aerodynamic efficiency and the bearing system frictional losses by solving based on the power delivered to the compressor (Equation 2) (RYU and ASHTON, 2016):

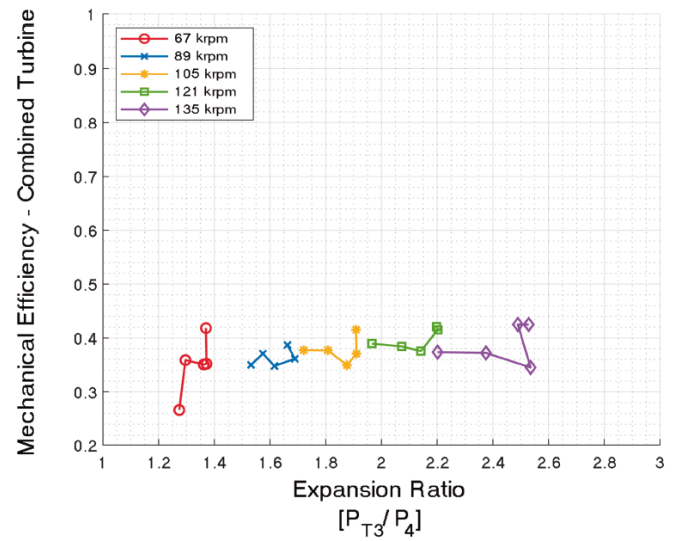
$$\eta_T = \frac{\dot{W}_C}{\dot{m}_T C_{p,ex} T_3 \left[1 - (P_4 - P_3)^{\frac{\gamma_{ex}-1}{\gamma_{ex}}} \right]} \quad (4.2)$$

where \dot{W}_C is the compressor power, \dot{m}_T is the turbine mass flow rate, $C_{p,ex}$ is the specific heat of exhaust gas, T_3 is the turbine inlet temperature, P_3 is the turbine inlet pressure, P_4 is the turbine discharge pressure, and γ_{ex} is the specific heat ratio of exhaust gas.

For the turbine performance and efficiency graphs, parameters indicated by Pesiridis *et al.* (2012) are used. Figures 66 to 72 show the experimental mass flow performance versus outlet/inlet pressure ratio, and the combined efficiency (turbine + rotor-bearing assembly) versus expansion ratio for the turbochargers mounted on bearings with different axial groove geometry.

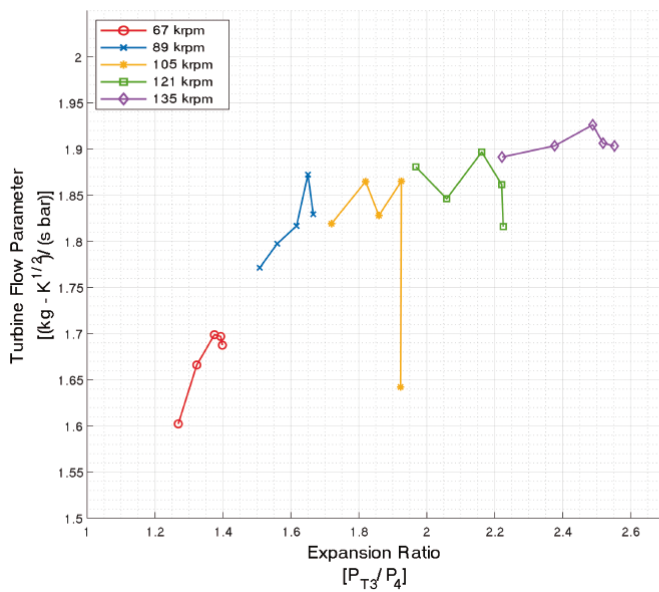


(a)

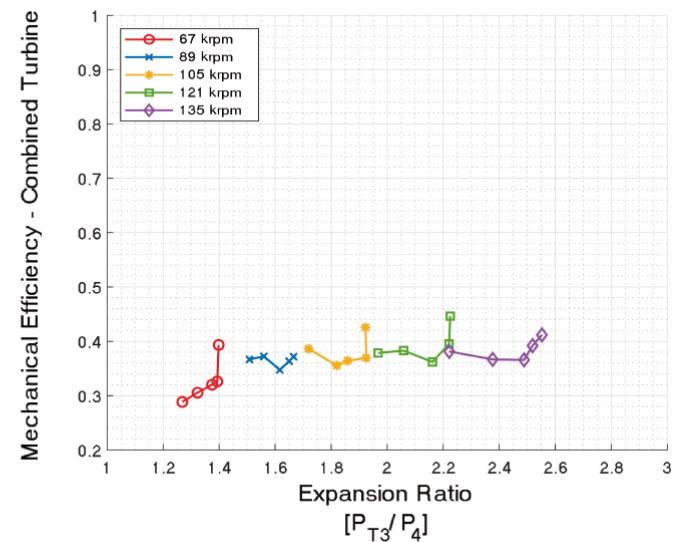


(b)

Figure 66 – Turbine (a) performance and (b) efficiency maps for the turbocharger supported on bearings with triangular shape grooves

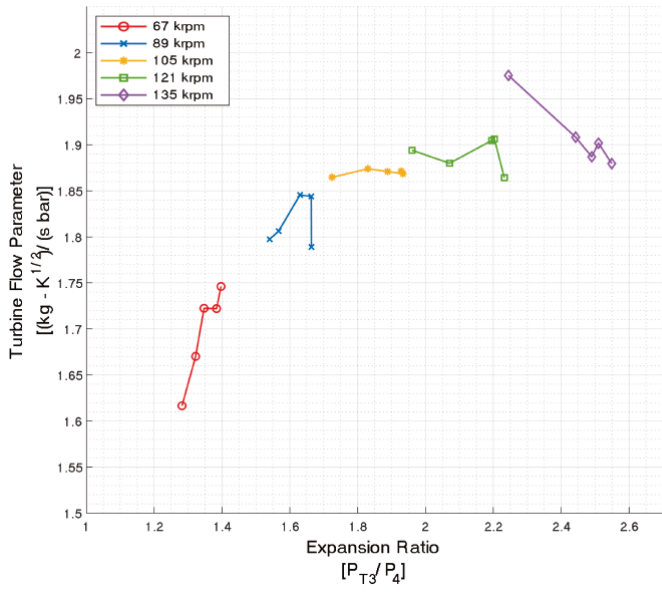


(a)

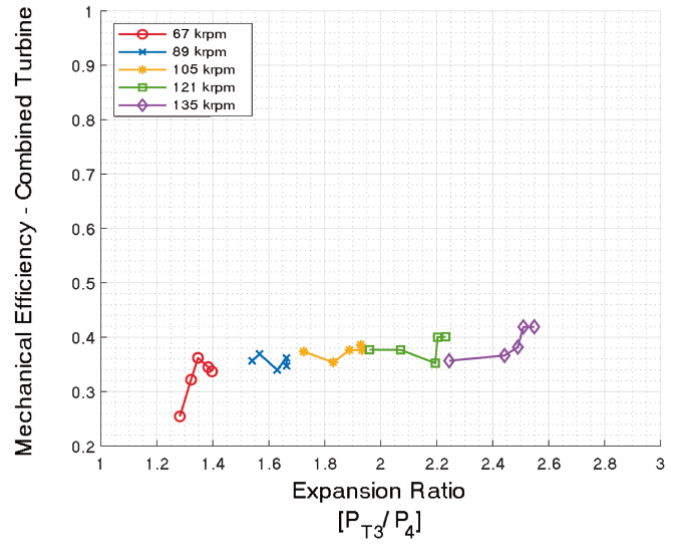


(b)

Figure 67 – Turbine (a) performance and (b) efficiency maps for the turbocharger supported on bearings with half-ellipse shape grooves

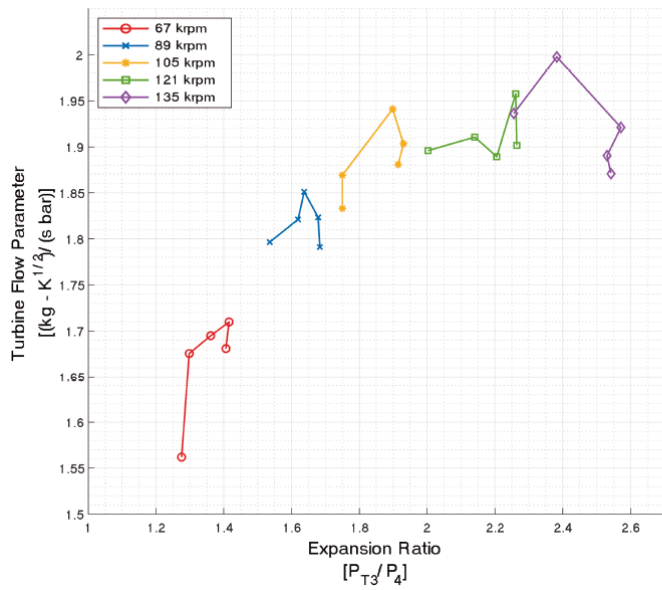


(a)

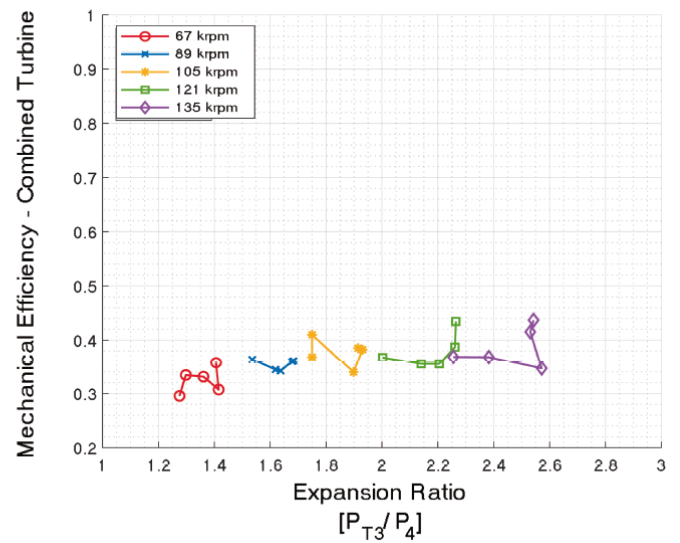


(b)

Figure 68 – Turbine (a) performance and (b) efficiency maps for the turbocharger supported on bearings with quarter-ellipse shape grooves

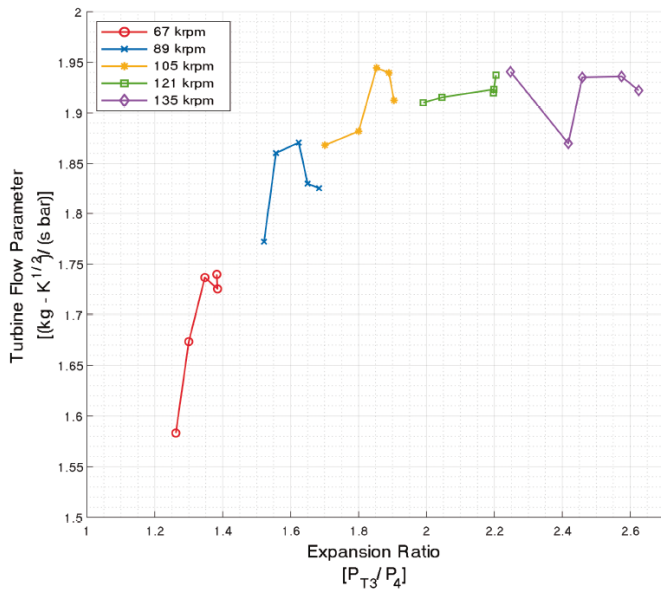


(a)

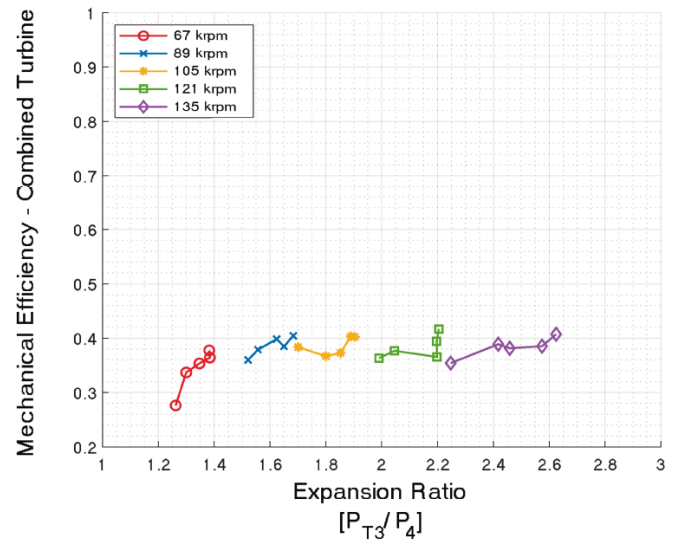


(b)

Figure 69 – Turbine (a) performance and (b) efficiency maps for the turbocharger supported on bearings with inverted quarter-ellipse shape grooves

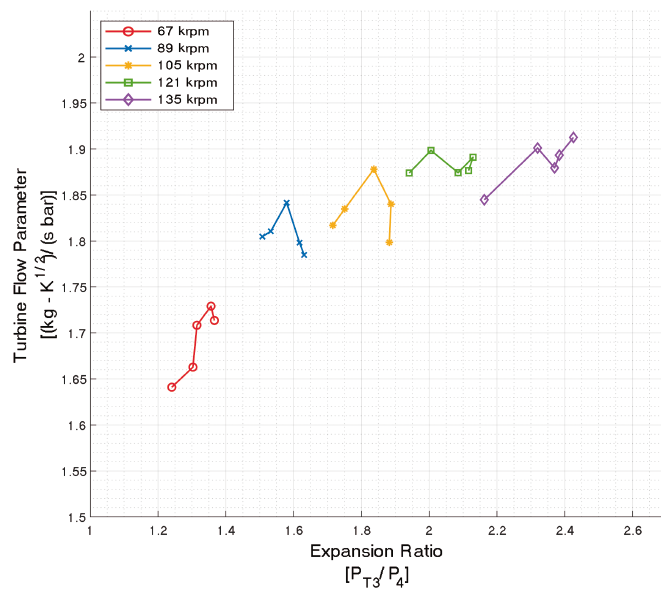


(a)

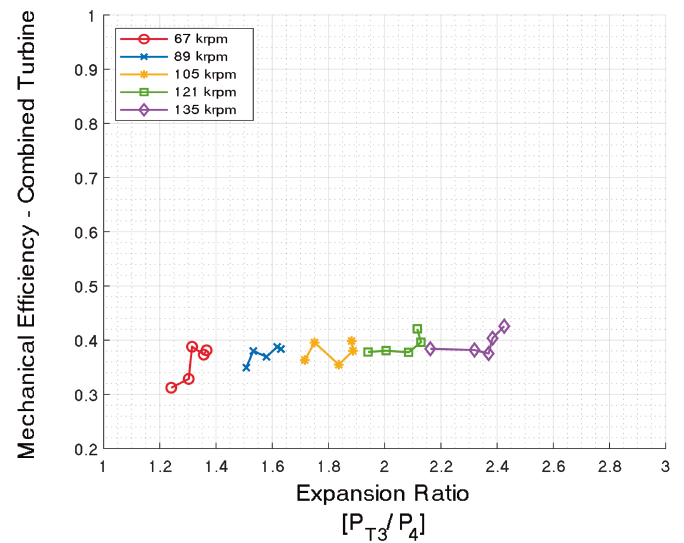


(b)

Figure 70 – Turbine (a) performance and (b) efficiency maps for the turbocharger supported on bearings with rectangular shape grooves

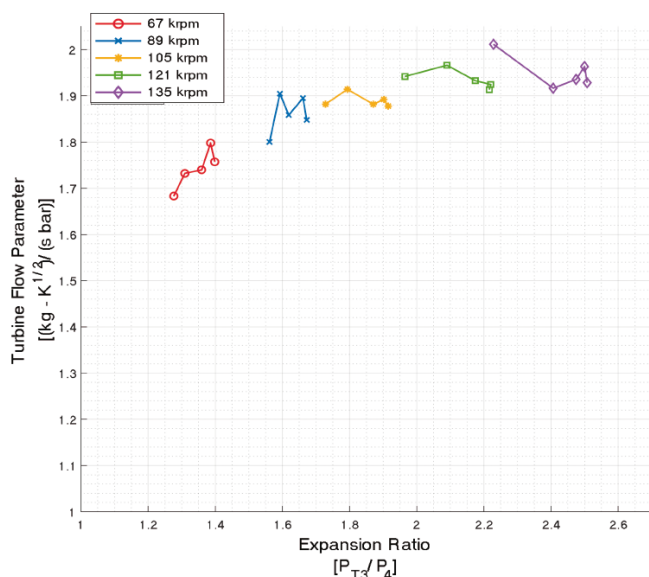


(a)

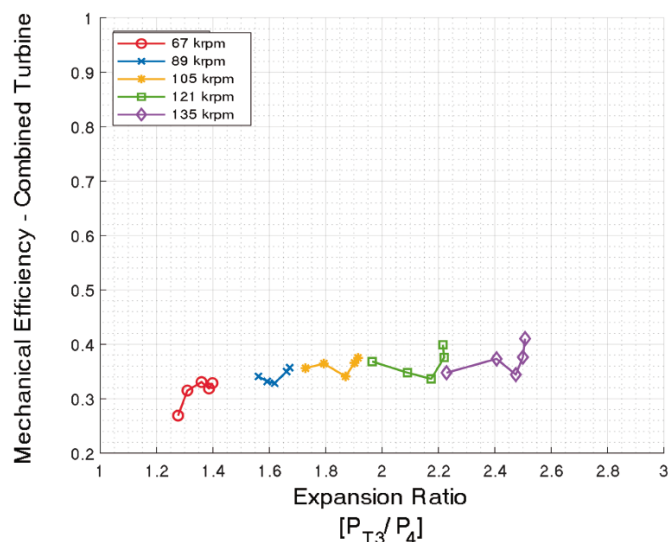


(b)

Figure 71 – Turbine (a) performance and (b) efficiency maps for the turbocharger supported on bearings with trapezoidal shape grooves



(a)



(b)

Figure 72 – Turbine (a) performance and (b) efficiency maps for the turbocharger supported on bearings with half-moon shape grooves

Mass flow performance

The volume flow capability of any turbine, known as the swallowing capacity, sets the air cycle operating pressure for a given air mass flow rate. In the TC, if the exhaust gas mass flow rate increases, the gas cycle pressure must increase to allow the turbine to swallow more gas (ROWELL and JASWAL, 2017).

Katrašnik *et al.* (2003) explain that the mass flow of the combustion air through the engine is proportional to the engine speed and to the boost air pressure. Swallowing characteristic of the turbocharger turbine is progressive: when mass flow through the turbine is increased, there is a steep increase of the pressure ratio across the turbine and of the developed torque.

For the TC 1 (Figure 66(a)), the maximum expansion ratio achieved in his test is 2.54, at a corrected mass flow rate of 1.93 [(kg.K^{1/2})/(s.bar)]. TC 2 (Figure 67(a)) presented the maximum expansion ratio achieved in his test is 2.55, at a corrected mass flow rate of 1.90 [(kg.K^{1/2})/(s.bar)]. TC 3 (Figure 68(a)) showed the maximum expansion ratio achieved in his test is 2.55, at a corrected mass flow rate of 1.88 [(kg.K^{1/2})/(s.bar)]. TC 4 (Figure 69(a)) indicated the maximum expansion ratio achieved in his test is 2.57, at a corrected mass flow rate of 1.92 [(kg.K^{1/2})/(s.bar)]. The TC 5 (Figure 70(a)) showed the maximum expansion ratio achieved in his test is 2.63, at a corrected mass flow rate of 1.92

$[(\text{kg.K}^{1/2})/(\text{s.bar})]$. TC 6 (Figure 71(a)) showed the maximum expansion ratio achieved in his test is 2.43, at a corrected mass flow rate of 1.91 $[(\text{kg.K}^{1/2})/(\text{s.bar})]$. And the TC 7 (Figure 72(a)) presented the maximum expansion ratio achieved in his test is 2.51, at a corrected mass flow rate of 1.93 $[(\text{kg.K}^{1/2})/(\text{s.bar})]$. All these seven maximum turbine expansion ratios happened at speed line 5 (135 krpm).

The relative difference among the maximum expansion ratio results for the turbochargers analyzed is 8.2%, which is greater than the 5% uncertainty for calculating this magnitude. The relative difference of the corrected mass flow results for these points is 2.6%, same value of the uncertainty for this measurement. For the maximum efficiency, however, as happened with the compressor, the difference among the data presented for the subsequent turbines of the turbochargers (from largest to smallest) is always within the uncertainty range. Then, the results are indicated with their uncertainty limit, considered in the classification of grooves and presented later in this work.

Using the results for the mass flow performance, it is possible to conclude that the maximum turbine expansion ratio occurs in TC 5 (rectangular). The results presented are summarized in Table 22.

Table 22 – Comparative values of turbine mass flow for the turbochargers supported on bearings with different axial grooves.

Turbocharger (bearing axial groove shape)	Parameters	
	Maximum expansion ratio	Corrected mass flow for maximum expansion ratio $[(\text{kg.K}^{1/2})/(\text{s.bar})]$
TC 1 (triangular)	2.54 ± 0.13	1.93 ± 0.05
TC 2 (half-ellipse)	2.55 ± 0.13	1.90 ± 0.05
TC 3 (quarter-ellipse)	2.55 ± 0.13	1.88 ± 0.05
TC 4 (inverted quarter-ellipse)	2.57 ± 0.13	1.92 ± 0.05
TC 5 (rectangular)	2.63 ± 0.13	1.92 ± 0.05
TC 6 (trapezoidal)	2.43 ± 0.12	1.91 ± 0.05
TC 7 (half-circle)	2.51 ± 0.13	1.93 ± 0.05
<i>Mean</i>	<i>2.54</i>	<i>1.91</i>

Combined efficiency

Similar as done in 4.1.1.2, the analysis of turbine efficiency is based in the maximum values reached for each of 5 speed lines. The difference among the maximums

and minimums indicates how constant the efficiency is at a certain turbine rotation speed, now versus the turbine expansion ratio.

The TC1 (Figure 66(b)) presents the respective maximums and minimums (max; min) for each speed line (SL 1 to 5): at 67 krpm (SL 1), 42% and 26%; at 89 krpm (SL 2), 39% and 35%; at 105 krpm (SL 3), 42% and 38%; at 121 krpm (SL 4), 42% and 38%; and at 135 krpm (SL 5), 42% and 35%.

For TC 2 (Figure 67(b)), the maximums and minimums are: at SL 1, 39% and 29%; at SL 2, 37% and 35%; at SL 3, 43% and 36%; at SL 4, 45% and 36%; at SL 5, 41% and 37%.

TC 3 (Figure 68(b)) shows the following numbers (maximums and minimums): at SL 1, 36% and 25%; at SL 2, 37% and 34%; at SL 3, 39% and 35%; at SL 4, 40% and 38%; at SL 5, 42% and 36%.

The maximums and minimums for TC4 (Figure 69(b)) are: at SL 1, 36% and 30%; at SL 2, 36% and 34%; at SL 3, 41% and 34%; at SL 4, 43% and 35%; at SL 5, 44% and 35%.

TC 5 (Figure 70(b)) presents the following maximums and minimums: at SL 1, 38% and 28%; at SL 2, 40% and 36%; at SL 3, 40% and 37%; at SL 4, 42% and 36%; at SL 5, 41% and 35%.

For TC 6 (Figure 71(b)), the maximums and minimums are: at SL 1, 39% and 31%; at SL 2, 38% and 35%; at SL 3, 40% and 36%; at SL 4, 42% and 38%; at SL 5, 43% and 38%.

And the TC 7 (Figure 72(b)) presents the maximums and minimums: at SL 1, 33% and 27%; at SL 2, 36% and 33%; at SL 3, 38% and 34%; at SL 4, 40% and 34%; at SL 5, 41% and 34%.

Table 23 depicts the combined turbine efficiencies at different 5 speed lines, including the maximums, minimums and the differences for the turbochargers supported on bearings with different axial grooves.

Table 23 – Comparative values of turbine efficiency for the turbochargers supported on bearings with different axial grooves.

Turbocharger (bearing axial groove shape)	Efficiency (%)	Speed line 1 @ 67 krpm	Speed line 2 @ 89 krpm	Speed line 3 @ 105 krpm	Speed line 4 @ 121 krpm	Speed line 5 @ 135 krpm
TC 1 (triangular)	<i>Maximum</i>	42 ± 1	39 ± 1	42 ± 1	42 ± 1	42 ± 1
	<i>Minimum</i>	26 ± 1	35 ± 1	38 ± 1	38 ± 1	35 ± 1
TC 2 (half-ellipse)	<i>Maximum</i>	39 ± 1	37 ± 1	43 ± 1	45 ± 1	41 ± 1
	<i>Minimum</i>	29 ± 1	35 ± 1	36 ± 1	36 ± 1	37 ± 1
TC 3 (quarter-ellipse)	<i>Maximum</i>	36 ± 1	37 ± 1	39 ± 1	40 ± 1	42 ± 1
	<i>Minimum</i>	25 ± 1	34 ± 1	35 ± 1	38 ± 1	36 ± 1
TC 4 (inverted quarter-ellipse)	<i>Maximum</i>	36 ± 1	36 ± 1	41 ± 1	43 ± 1	44 ± 1
	<i>Minimum</i>	30 ± 1	34 ± 1	34 ± 1	35 ± 1	35 ± 1
TC 5 (rectangular)	<i>Maximum</i>	38 ± 1	40 ± 1	40 ± 1	42 ± 1	41 ± 1
	<i>Minimum</i>	28 ± 1	36 ± 1	37 ± 1	36 ± 1	35 ± 1
TC 6 (trapezoidal)	<i>Maximum</i>	39 ± 1	38 ± 1	40 ± 1	42 ± 1	43 ± 1
	<i>Minimum</i>	31 ± 1	35 ± 1	36 ± 1	38 ± 1	38 ± 1
TC 7 (half-circle)	<i>Maximum</i>	33 ± 1	36 ± 1	38 ± 1	40 ± 1	41 ± 1
	<i>Minimum</i>	27 ± 1	33 ± 1	34 ± 1	34 ± 1	34 ± 1
<i>Mean</i>	<i>Maximum</i>	37.6	37.6	40.4	42.0	42.0
	<i>Minimum</i>	28.0	34.6	35.7	36.4	35.7

Considering the uncertainty range in the estimates of isentropic efficiency, expansion ratio, and corrected mass flow, some turbochargers present slight distinct thermodynamic behavior. The results rendered for the turbine thermodynamic performance indicate that the axial groove geometry affects less the thermal response of the turbocharger turbine compared to the compressor.

4.1.3. Overall TC performance and efficiency – TD classification

The TC performance is the measure of quality of the work done by the TC. Efficiency is the ratio of output to the required input for the TC.

By combining the two terms (η_C and η_T) into an overall TC efficiency (η_{TC}), the effect of the bearing system on the efficiency can be isolated. Ryu and Ashton (2016), Zeng *et al.* (2016) and Ryu and Ashton (2017) present some conditions to consider the effect of the bearing system in this way.

For this work, all the TC parts are produced under the several manufacturing and metrological classification, as well as the assemblies processes, all these from MGFC Ltd.. Then, it could be considered that every main part in this TD analysis, i.e., compressor, turbine, shaft, thrust bearing, is the same. The journal bearing is also considered the same, except for the difference in the axial groove shapes. Therefore, for the overall TC efficiency (η_{TC}), the difference is expected to be associated with the axial groove shape.

The performance compressor and turbine maps are an important stage in the TD analysis. There are some scientific discussions about the best and/or the most correct way to present both performances (MORALL and KOLMANOVSKY, 1999; SIRAKOV and CASEY, 2013; CHECCUCCI *et al.*, 2018, ANANTHAKRISHNAN *et al.*, 2020; ALEXANDER and PORPATHAM, 2021). This occurs due to the need for the best match between TC and ICE. However, Miller (2008) reinforces that both compressor and turbine are important to get the best match with the ICE. Thus, in this work, the TD performance analysis considered only the turbocharger itself, with the target on the influence of SFRB internal grooves shapes. Therefore, the performances of the compressor and turbine have the same analysis weight.

TC performance rank

For the compressor performance rank, the most important characteristic of overall TC is the maximum compression (ratio of the compressor outlet to the inlet pressure). At the maximum compression, the secondary characteristic to be analyzed is the mass flow. The smaller the air mass flow, the less kinetic energy required to achieve the highest expansion ratio.

For turbine performance rank, the most important data is also the maximum expansion ratio (ratio of the turbine outlet to the inlet pressure). And the turbine flow parameter (or turbine mass flow parameter or reduced turbine mass flow) must also be considered. The mass flow parameter is the mass flow rate reduced by the ratio of the square root of inlet total temperature to the inlet total pressure. Chung *et al.* (2019) explain that the reduced turbine mass flow rate expresses the corrected flow rate that can be converted to a Mach number. This definition derived from the ratio of local flow velocity and sound velocity and is based on the aerodynamic characteristics of the turbine. Thus, the smaller at the same expansion ratio, the larger the ability of the turbine to expand the gas, even with a turbine has lower inlet mass flow.

Same procedures are employed to evaluate the compressor and turbine performance. A 9-point scale modified Pugh weighted matrix is chosen.

The criteria scores for the performance are presented in Figure 73 for the compressor maximum compression and Figure 74 for the compressor corrected flow at maximum compression, and Figure 75 for the turbine maximum expansion and Figure 76 for the turbine corrected flow at maximum expansion.

For the compressor, the mean of the maximum compression ratio is 1.76 and 0.092 kg/s for the corrected mass flow. For the turbine, the maximum expansion ratio is 2.54 and 1.91 kg.K^(1/2)/s.bar for the corrected mass flow.

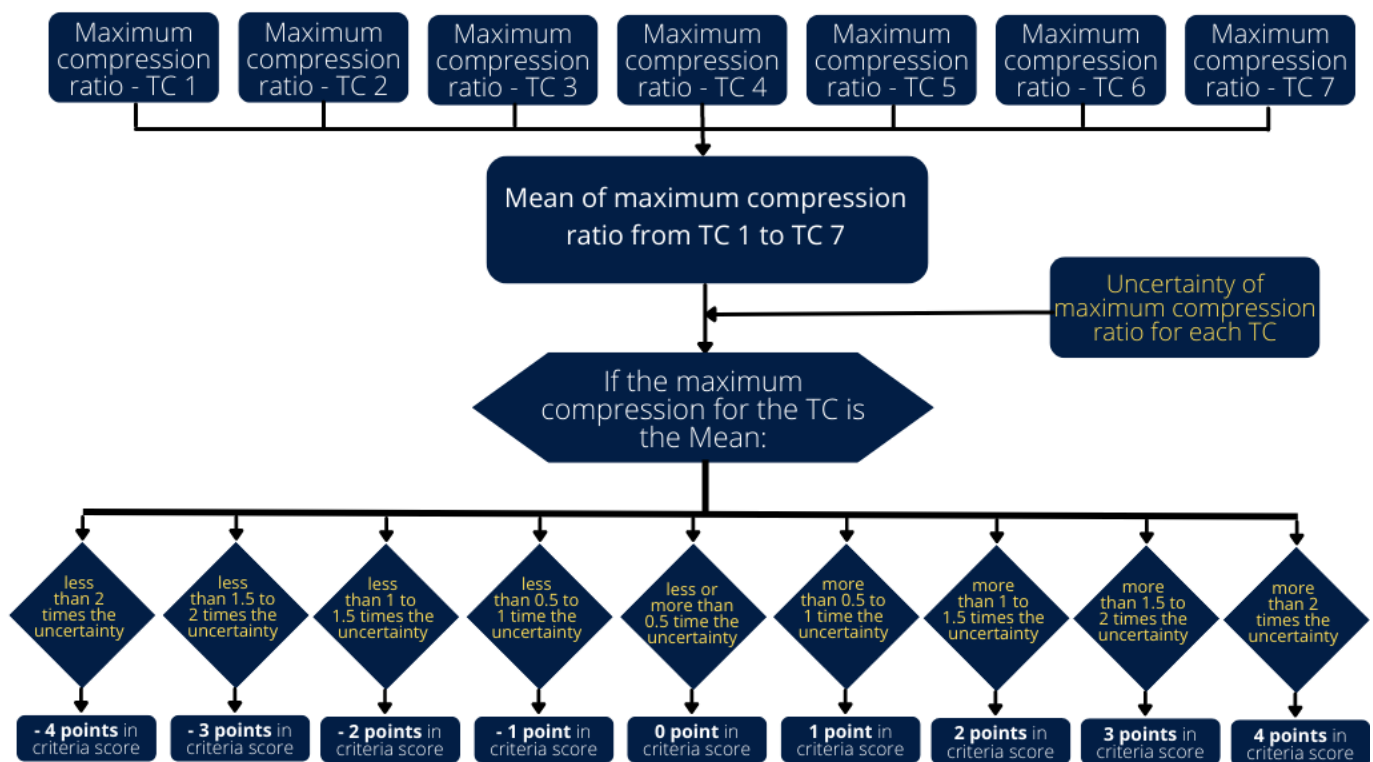


Figure 73 – Criteria score for the compressor maximum compression

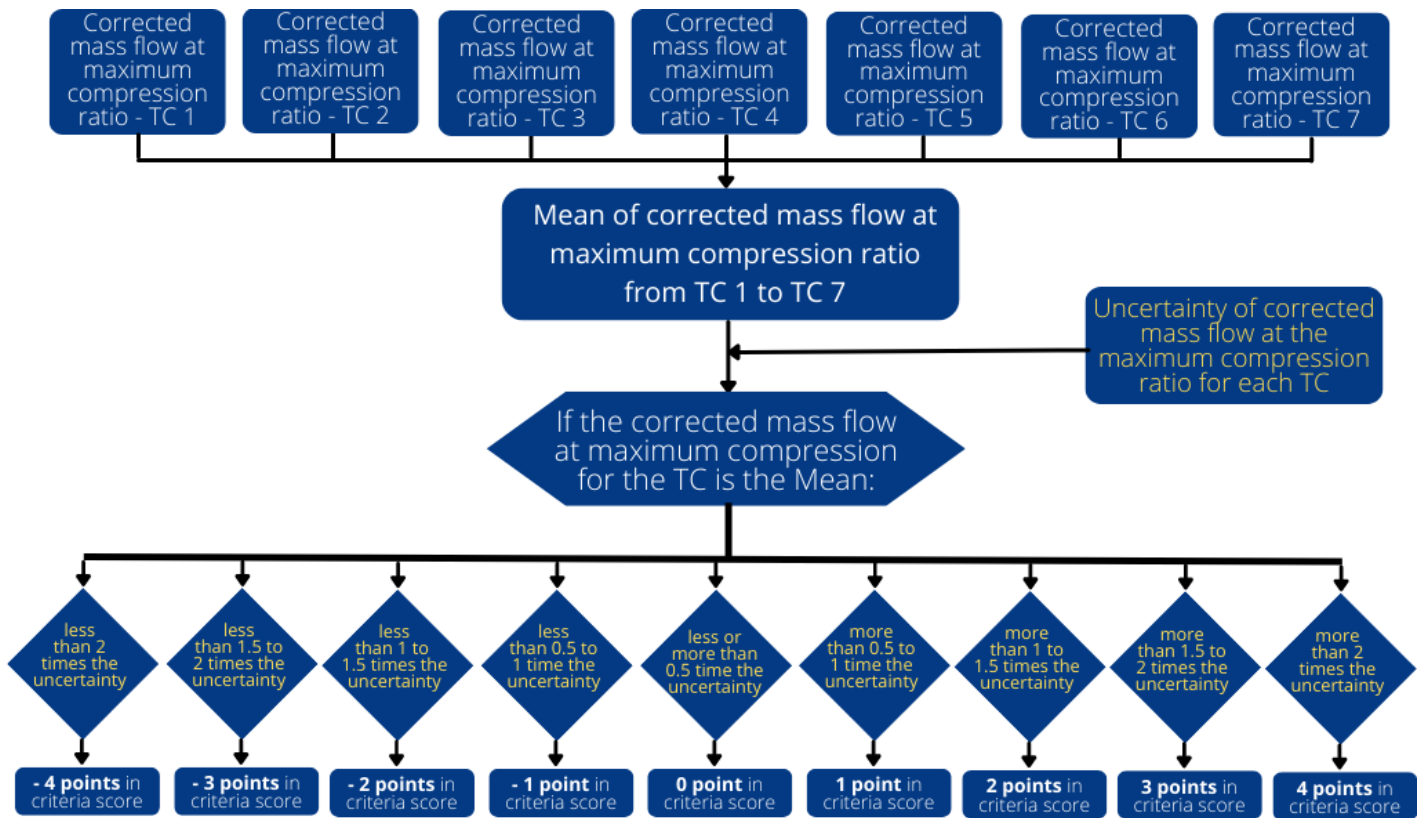


Figure 74 – Criteria score for the compressor corrected mass flow at maximum compression

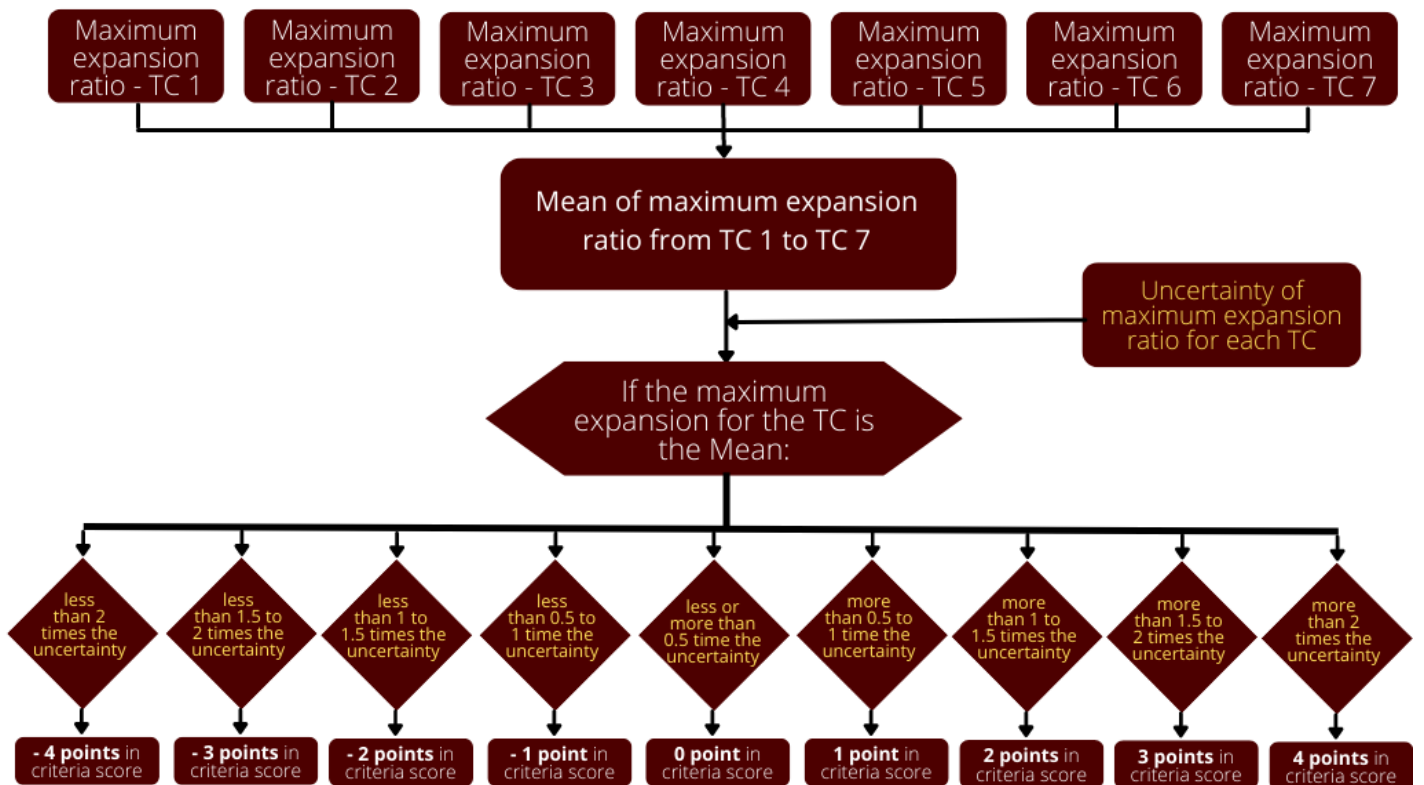


Figure 75 – Criteria score for the turbine maximum expansion

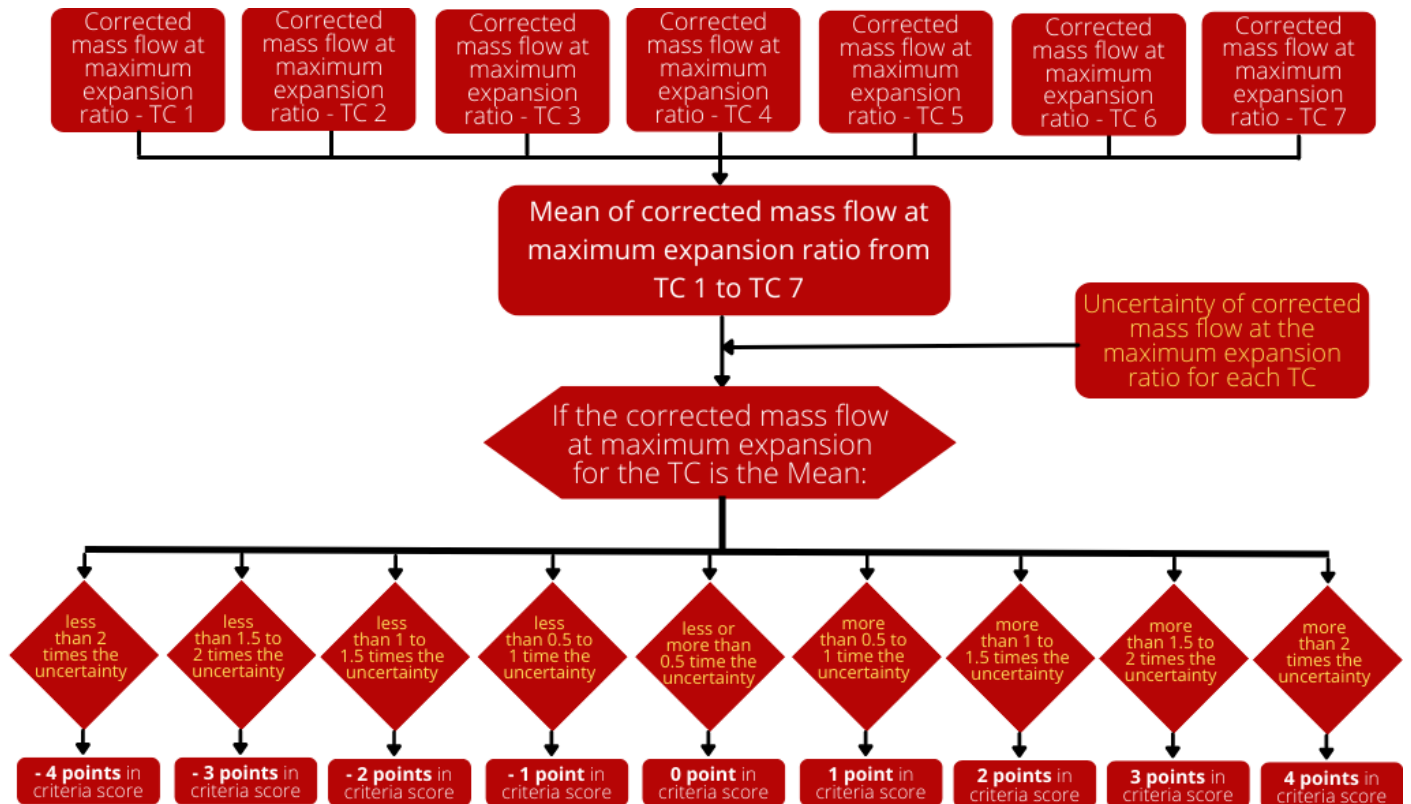


Figure 76 – Criteria score for the turbine corrected mass flow at maximum expansion

Table 24 presents the TC compressor and turbine performance criteria and their importance based on the preliminary thermodynamic analysis.

The maximum compression (compressor) or expansion (turbine) are the most important values in the analysis, with a weight of 1 (one) in the score criteria. However, it is also important to verify the higher mass flow as a secondary analysis. Due this it is considered in this work with a weight of 0.25.

Table 24 – MCDM matrix for Compressor and Turbine Performance

Turbocharger (bearing axial groove shape)	Compressor Performance				Turbine Performance				Final TC Performance Points
	<u>Maximum compression</u>		<u>Corrected mass flow</u>		<u>Maximum expansion</u>		<u>Corrected mass flow</u>		
	Points	Weight	Points	Weight	Points	Weight	Points	Weight	
TC 1 (triangular)	1	1	0	0.25	0	1	0	0.25	1
TC 2 (half- ellipse)	-1		1		0		0		
TC 3 (quarter- ellipse)	-3		-3		0		-1		
TC 4 (inverted quarter- ellipse)	-2		2		0		0		
TC 5 (rectangular)	3		0		1		0		
TC 6 (trapezoidal)	1		-2		-1		0		
TC 7 (half- circle)	1		4		0		0		

TC efficiency rank

The TC efficiency rank is obtained using the compressor efficiency (Table 21) and combined turbine efficiency (Table 23). The maximum efficiency for each speed line is important item for compressor and turbine efficiency. The minimum efficiency normally is a not used parameter but provides the worst case efficiency of the same speed by varying the mass flow. The higher the minimum efficiency, the better is the compressor or turbine in cases where mass flow is the worst tested conditions.

A new 9-point scale modified Pugh weighted matrix is used again. For this analysis, the preliminary considerations for compressor and turbine efficiency are:

The new criteria scores for the efficiency are presented for compressor at maximum, Figure 77, and at minimum efficiencies, Figure 78. For the turbine, Figure 79 shows the maximum and Figure 80 the minimum efficiencies.

For the compressor, the means of the maximum and minimum efficiencies are:

1. 65.4% and 45.9% at Speed Line 1;
2. 67.9% and 50.7% at Speed Line 2;
3. 67.0% and 47.3% at Speed Line 3;
4. 65.1% and 44.3% at Speed Line 4;
5. 62.4% and 44.7% at Speed Line 5;

For the turbine, the means of the maximum and minimum efficiencies are:

1. 37.6% and 28.0% at Speed Line 1;
2. 37.6% and 34.6% at Speed Line 2;
3. 40.4% and 35.7% at Speed Line 3;
4. 42.0% and 36.4% at Speed Line 4;
5. 42.0% and 35.7% at Speed Line 5;

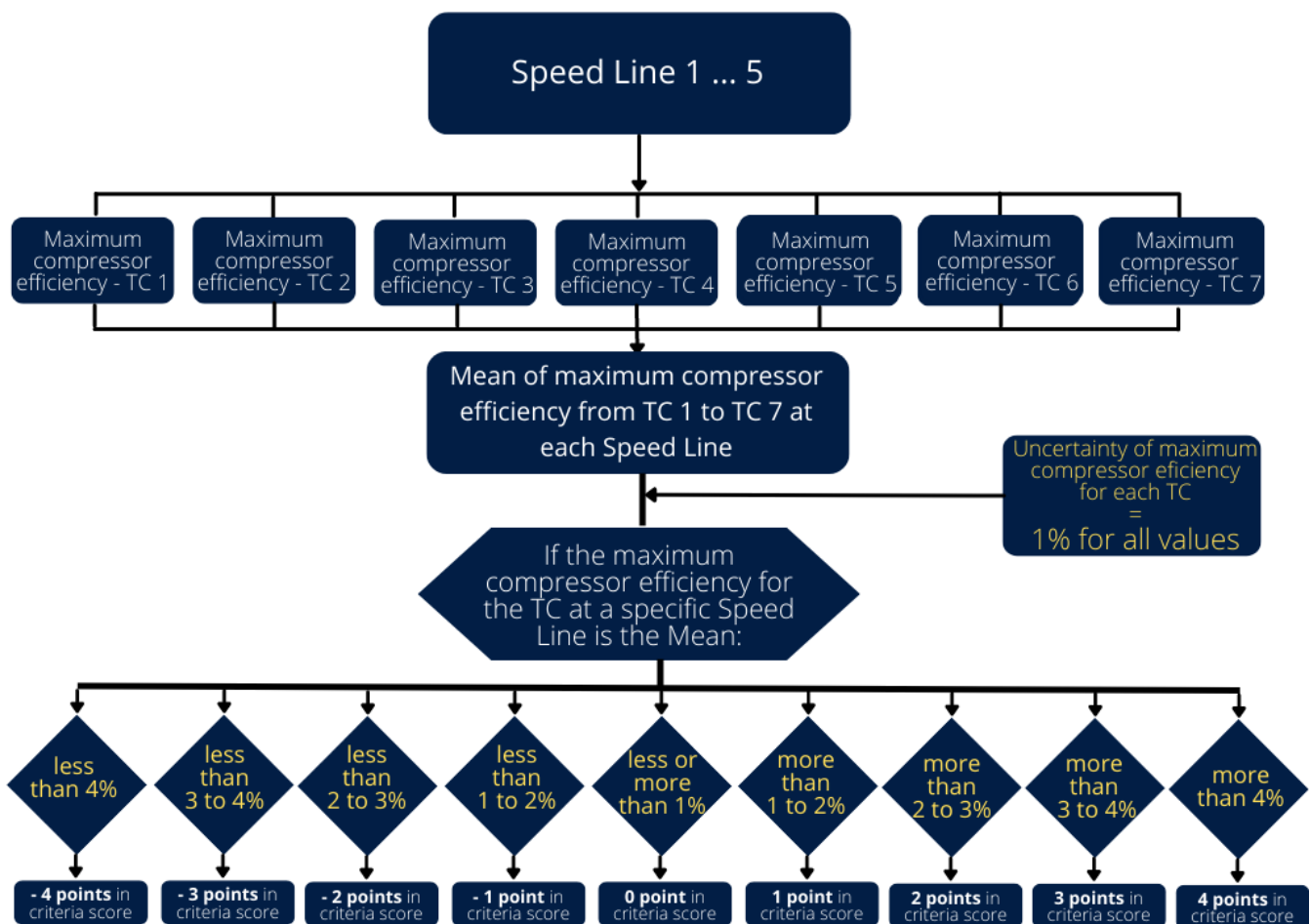


Figure 77 – Criteria score for the maximum compressor efficiency

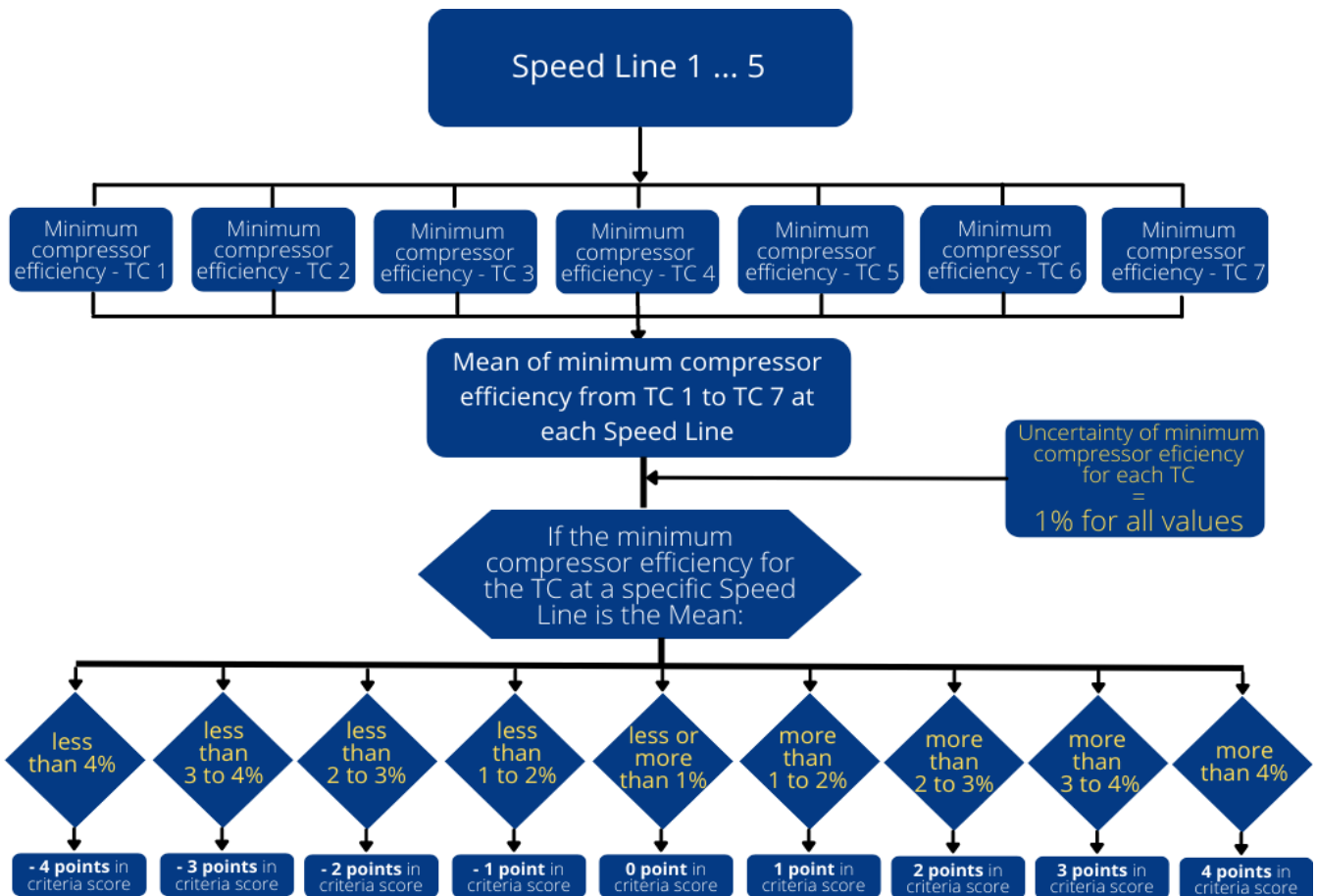


Figure 78 – Criteria score for the minimum compressor efficiency

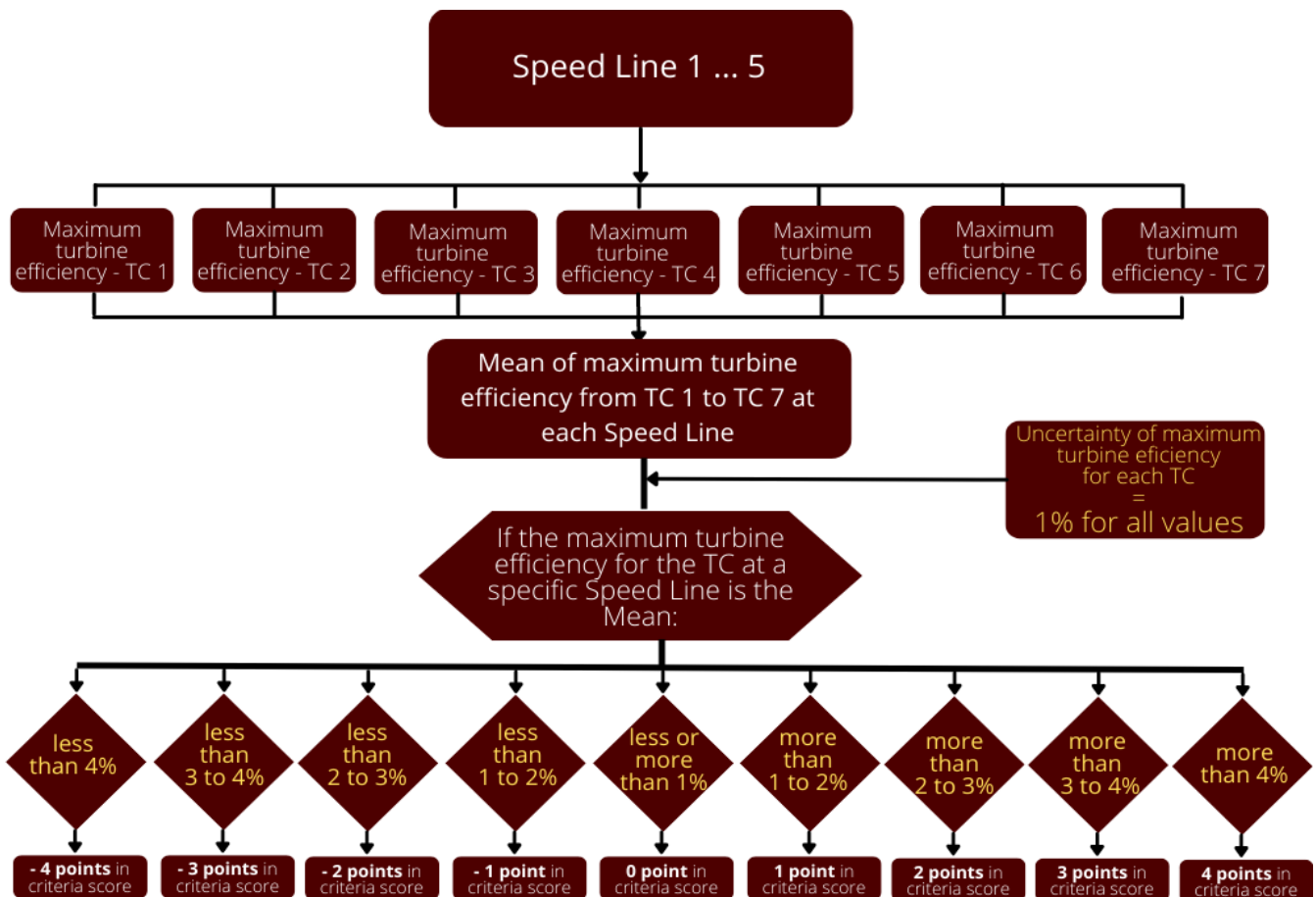


Figure 79 – Criteria score for the maximum turbine efficiency

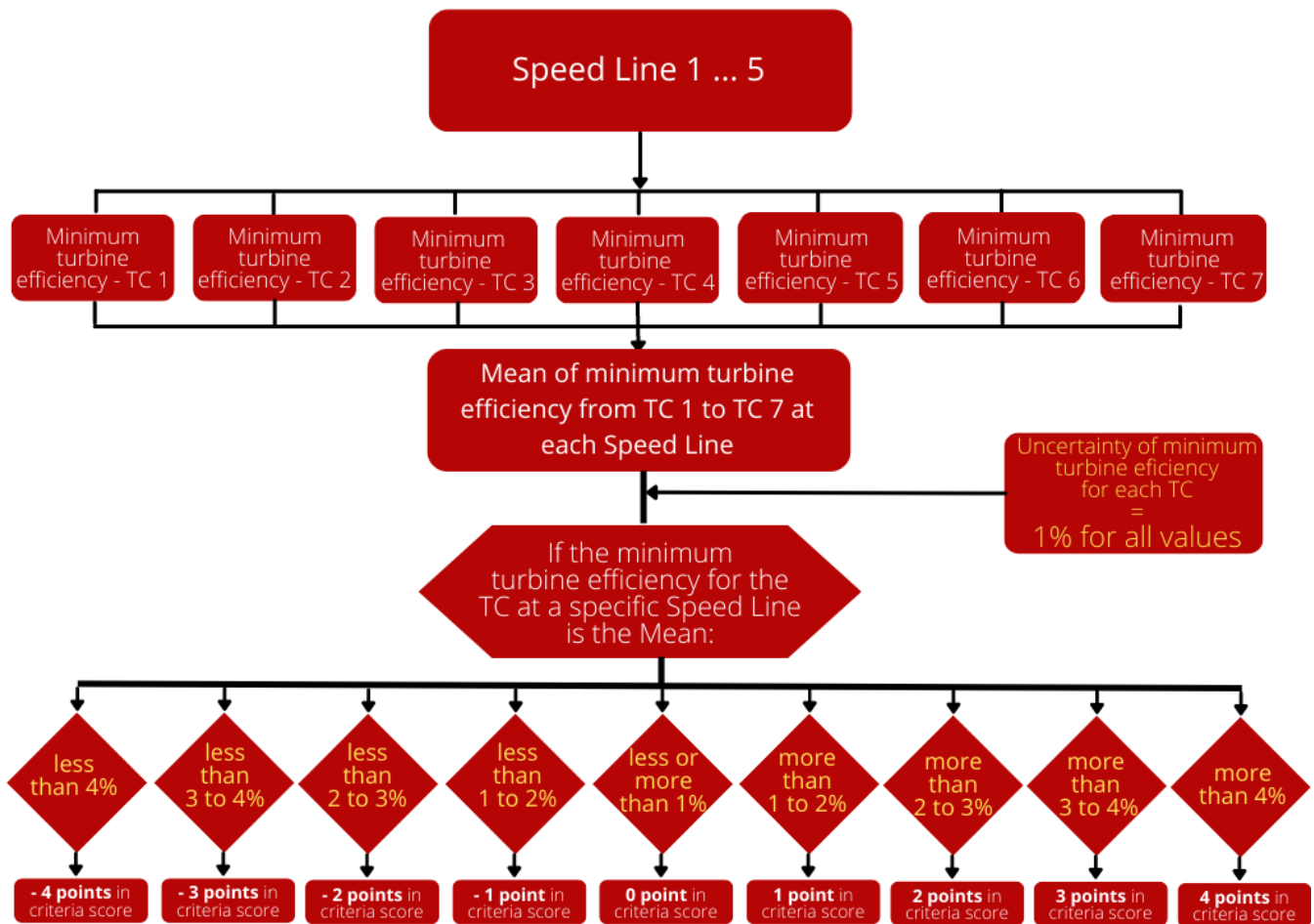


Figure 80 – Criteria score for the minimum turbine efficiency

Table 25 presents the TC compressor maximum and minimum efficiency criteria and their importance based on the preliminary thermodynamic analysis.

The maximum and minimum efficiencies at each speed line are important in the TD analysis. While the maximum efficiency is the one that most important evaluation criteria, the minimum efficiency also is important, but on a smaller scale. Thus, it is determined that the weights would be 1 for maximum efficiency and 0.5 for minimum efficiency in this work.

Table 26 presents the TC turbine maximum and minimum efficiency criteria and their importance based on the preliminary thermodynamic analysis.

Table 25 – MCDM matrix for Compressor Maximum and Minimum Efficiency

Turbocharger (bearing axial groove shape)	Compressor Efficiency											Compressor Efficiency Pre-Points	
	Maximum efficiency						Minimum efficiency						
	Pts SL1	Pts SL2	Pts SL3	Pts SL4	Pts SL5	weight	Pts SL1	Pts SL2	Pts SL3	Pts SL4	Pts SL5		weight
TC 1 (triangular)	-2	1	0	-3	0	1	-4	-1	-4	4	-3	0.5	-8
TC 2 (half- ellipse)	4	4	2	1	1		-4	1	4	-4	-4		8.5
TC 3 (quarter- ellipse)	-4	0	-2	0	-4		0	-4	-4	-1	-2		-15.5
TC 4 (inverted quarter-ellipse)	-3	0	0	1	1		0	4	4	4	-2		4
TC 5 (rectangular)	4	-4	2	0	1		4	-3	-4	-4	4		1.5
TC 6 (trapezoidal)	1	0	-1	0	1		1	3	4	4	3		8.5
TC 7 (half- circle)	3	2	-1	0	2		4	4	4	4	4		16

Table 26 – MCDM matrix for Turbine Maximum and Minimum Efficiency

Turbocharger (bearing axial groove shape)	Turbine Efficiency											Turbine Efficiency Pre-Points	
	Maximum efficiency						Minimum efficiency						
	Pts SL1	Pts SL2	Pts SL3	Pts SL4	Pts SL5	weight	Pts SL1	Pts SL2	Pts SL3	Pts SL4	Pts SL5		weight
TC 1 (triangular)	4	1	1	0	0	1	-2	0	2	1	0	0.5	6.5
TC 2 (half- ellipse)	1	0	2	3	-1		1	0	0	0	1		6
TC 3 (quarter- ellipse)	-1	0	-1	-2	0		-3	0	0	1	0		-5
TC 4 (inverted quarter-ellipse)	-1	-1	0	1	2		2	0	-1	-1	0		1
TC 5 (rectangular)	0	2	0	0	-1		0	1	1	0	0		2
TC 6 (trapezoidal)	1	0	0	0	1		3	0	0	1	2		5
TC 7 (half- circle)	-4	-1	-2	-2	-1		-1	-1	-1	-2	-1		-13

Table 27 shows the TC compressor and turbine efficiency scores described on Table 25 and Table 26:

Table 27 – MCDM matrix for Compressor and Turbine Efficiency

Turbocharger (bearing axial groove shape)	Compressor Efficiency Scores	Turbine Efficiency Scores	Final TC Efficiency Scores
TC 1 (triangular)	-8	6.5	-1.5
TC 2 (half-ellipse)	8.5	6	14.5
TC 3 (quarter-ellipse)	-15.5	-5	-20.5
TC 4 (inverted quarter-ellipse)	4	1	5
TC 5 (rectangular)	1.5	2	3.5
TC 6 (trapezoidal)	8.5	5	13.5
TC 7 (half-circle)	16	-13	3

4.1.4. Turbocharger Thermodynamic rank

Based on Tables 24 and 27, Table 28 presents the final TD classification, where a 7-point Pugh score is used, with a 3 to -3 points from 1st to 7th, respectively:

Table 28 – Ranking of turbochargers based on the thermodynamic analysis

Turbocharger (bearing axial groove shape)	Final TD Performance Rank	Final TD Efficiency Rank	Final TD rank
TC 1 (triangular)	3rd	6th	5th
TC 2 (half-ellipse)	5th	1st	2nd
TC 3 (quarter-ellipse)	7th	7th	7th
TC 4 (inverted quarter-ellipse)	6th	3rd	5th
TC 5 (rectangular)	1st	4th	1st
TC 6 (trapezoidal)	4th	2nd	2nd
TC 7 (half-circle)	2nd	5th	4th

4.2. RD GRAPHS AND RESULTS

In this section, the experimental results rendered from the rotordynamic analysis of TCs are presented and analyzed.

Constant speed and varying speed measurements of the vibration response of the turbochargers are performed using accelerometers, obtaining the main synchronous (mainly due to unbalance response) and subsynchronous (mainly due to shaft/bearing rub, oil whirl and oil whip) data.

For the subsynchronous analysis, orbit graphs are obtained for the different TCs supported on bearing with different axial grooves.

At last, an acoustic emission analysis is performed on the different turbochargers in a wide frequency range, from 20kHz until 1MHz, to observe more detailed characteristics associated with the dynamic response of the machines.

4.2.1. Preliminary rotor-bearing balancing and synchronous responses

Initially, it is presented balancing procedure employed by the manufacturer of on each TC rotor-bearing assembly, which is necessary to ensure the lowest possible synchronous response for the TCs. The rotor is accelerated from 0 to approximately 175 krpm in 4~5 seconds with constant air mass flow, generating a synchronous response curve.

This section presents the first and last synchronous response curves for each of the seven TCs. The last curves are the final balance conditions and show that the system is balanced for transient conditions without reaching an operating regime, which requires an initial stabilizing temperature procedure. The TC is not balanced at working conditions, but it is a way to quickly check the experimental balancing condition in an industrial production.

The synchronous response curve allows determining the critical speeds of each rotor-bearing assembly. At the beginning of the process, high peaks are observed in most cases, reaching acceptable values after the mass balancing.

Figures 81 to 87 show the synchronous response curves in (a) initial condition and (b) last condition obtained for each TC supported on bearings with different axial grooves. The initial condition curve indicates the first and second critical speeds (1st C.S. and 2nd C.S.), and the last condition indicates the critical speeds values.

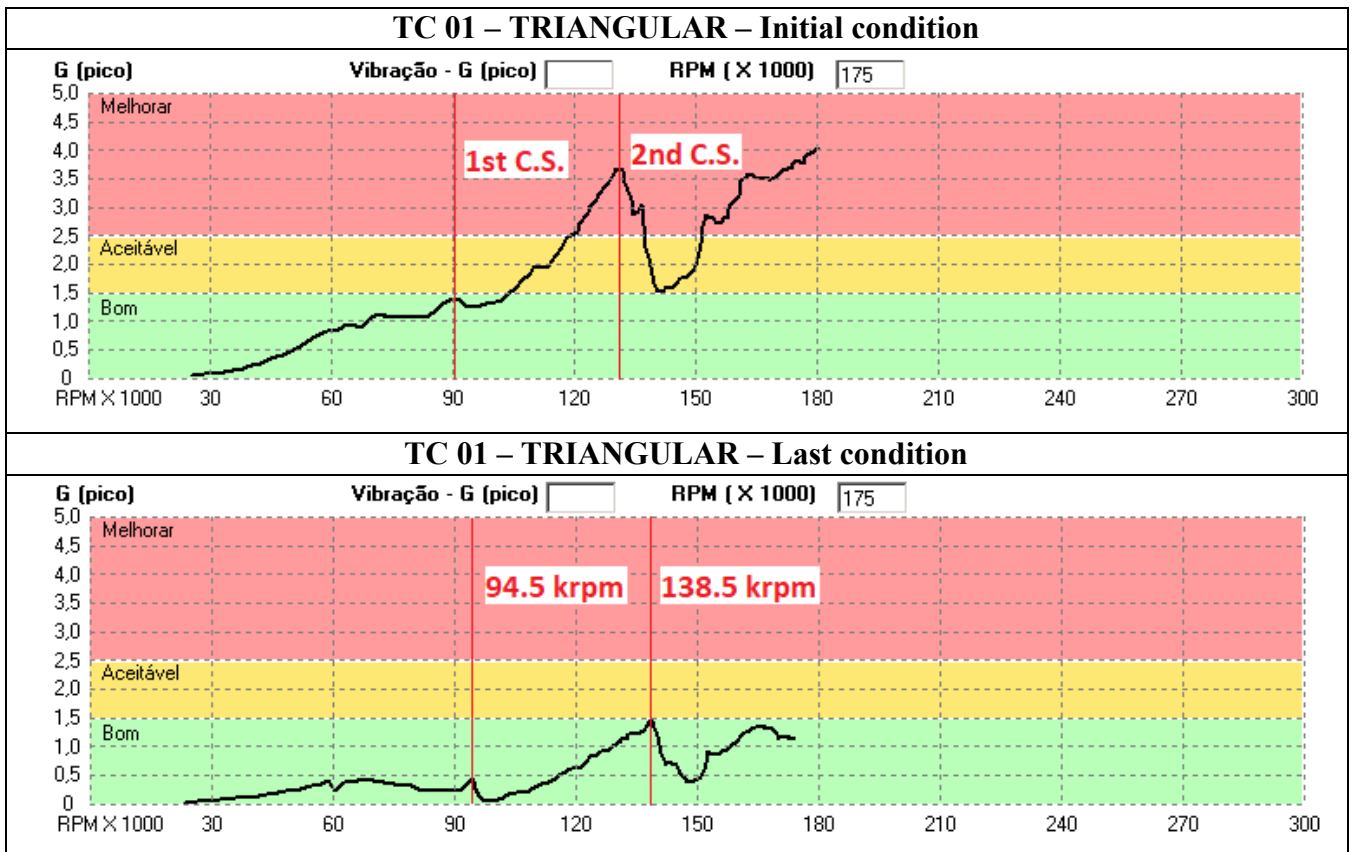


Figure 81 – Synchronous curves for the turbocharger TC 1 with bearings with triangular axial grooves at the initial and last balancing conditions

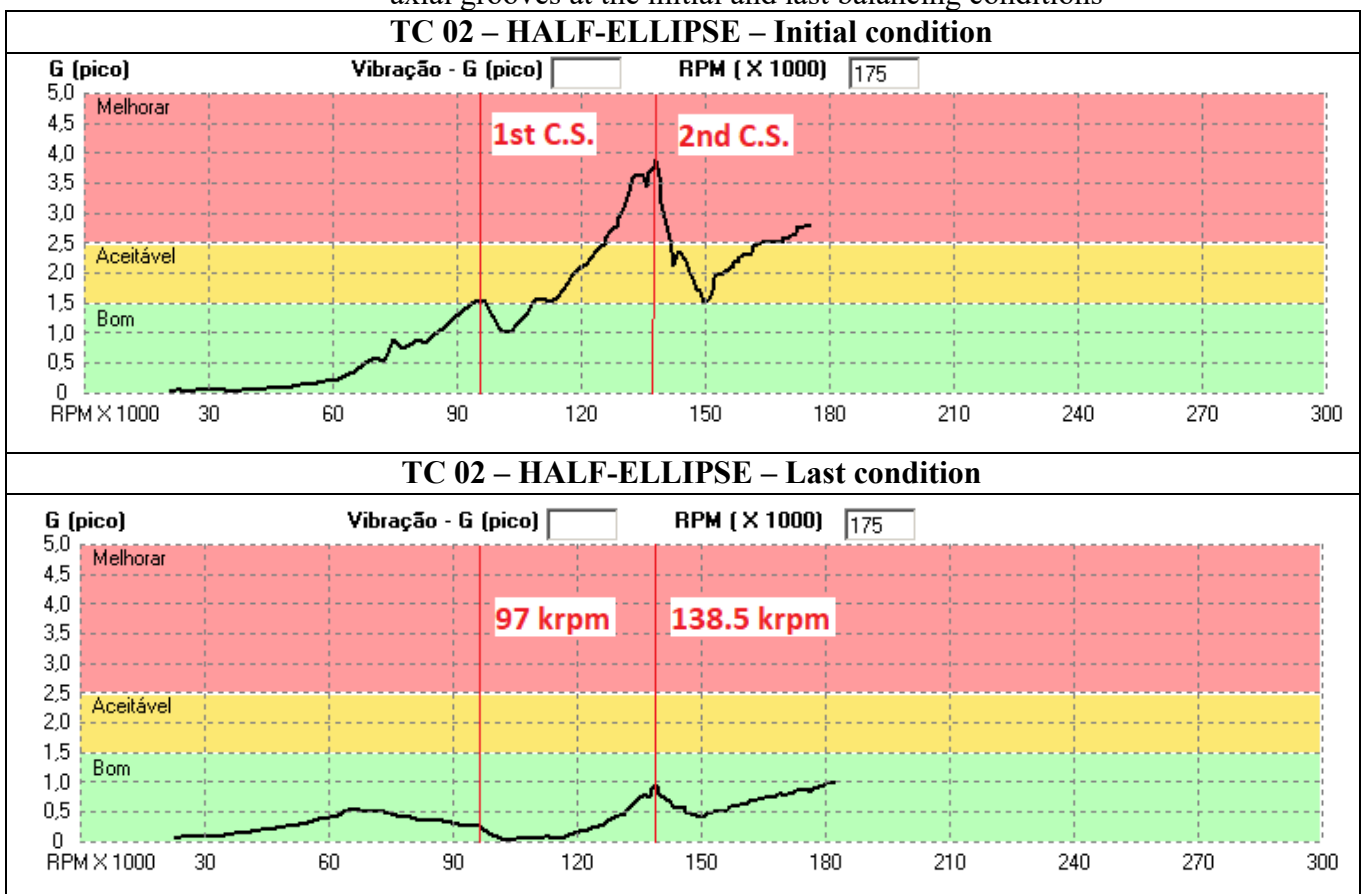


Figure 82 – Synchronous curves for the turbocharger TC 2 with bearings with half-ellipse axial grooves at the initial and last balancing conditions

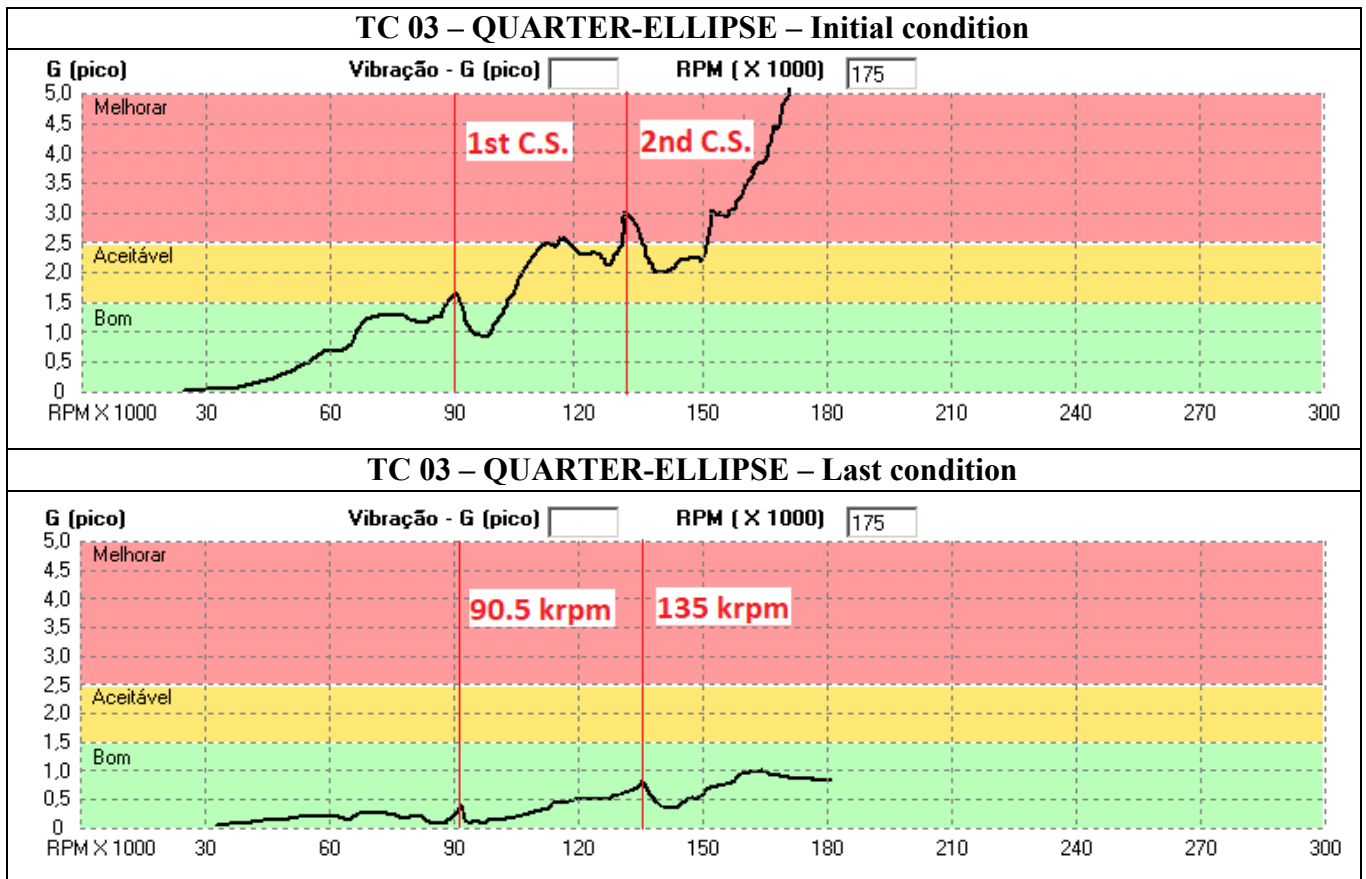


Figure 83 – Synchronous curves for the turbocharger TC 3 with bearings with quarter-ellipse axial grooves at the initial and last balancing conditions

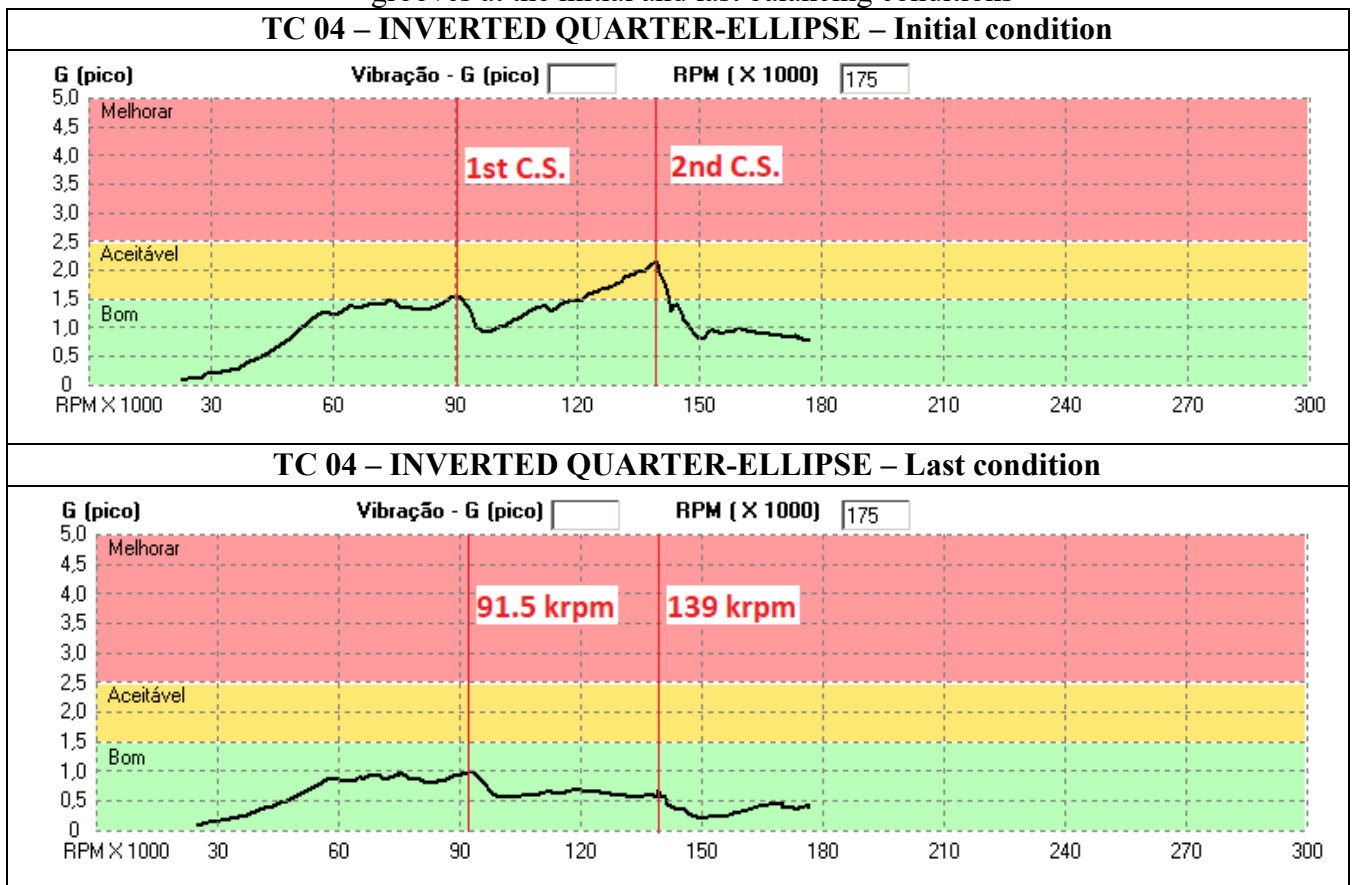


Figure 84 – Synchronous curves for the turbocharger TC 4 with bearings with inverted quarter-ellipse axial grooves at the initial and last balancing conditions

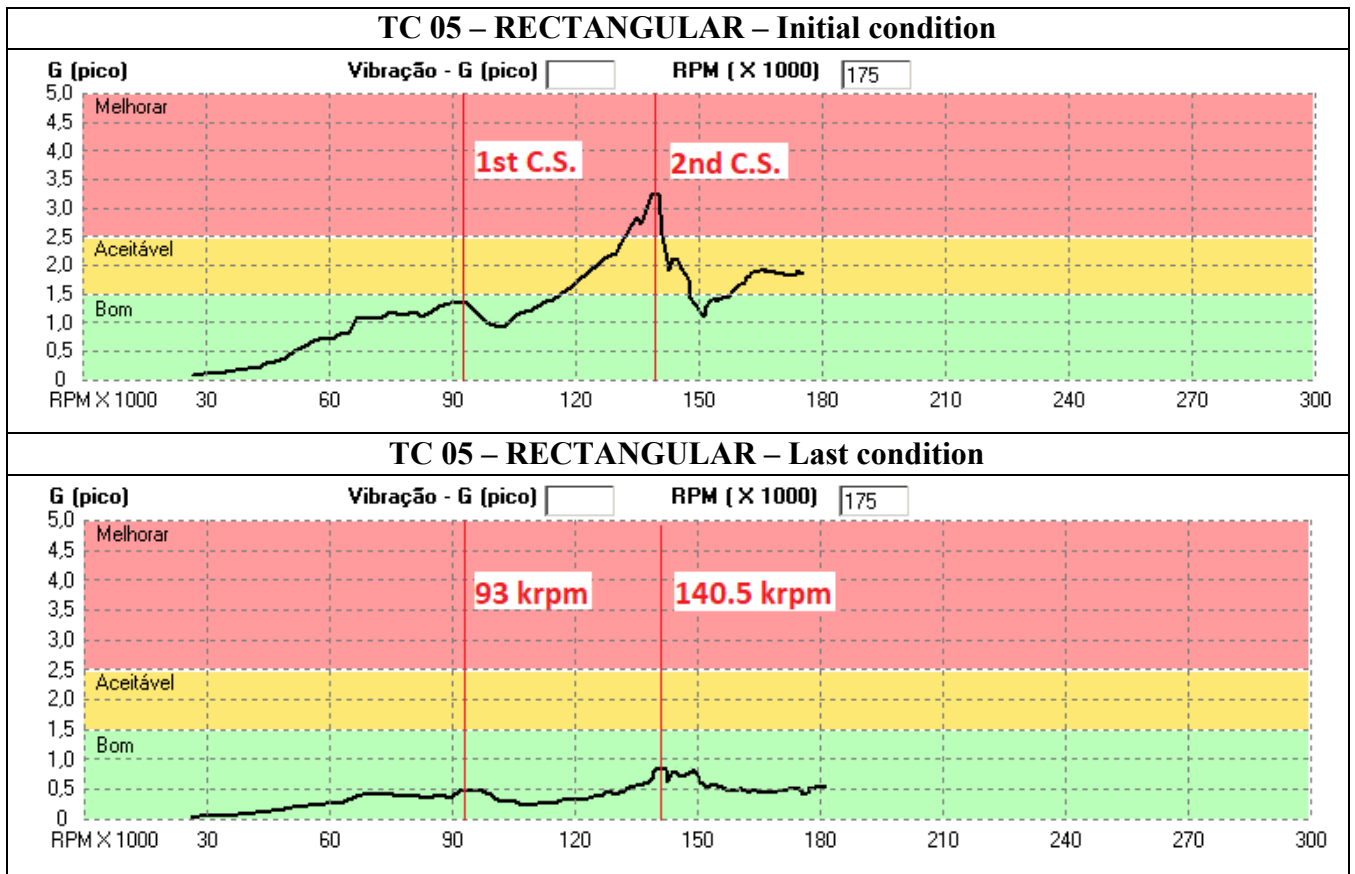


Figure 85 – Synchronous curves for the turbocharger TC 5 with bearings with rectangular axial grooves at the initial and last balancing conditions

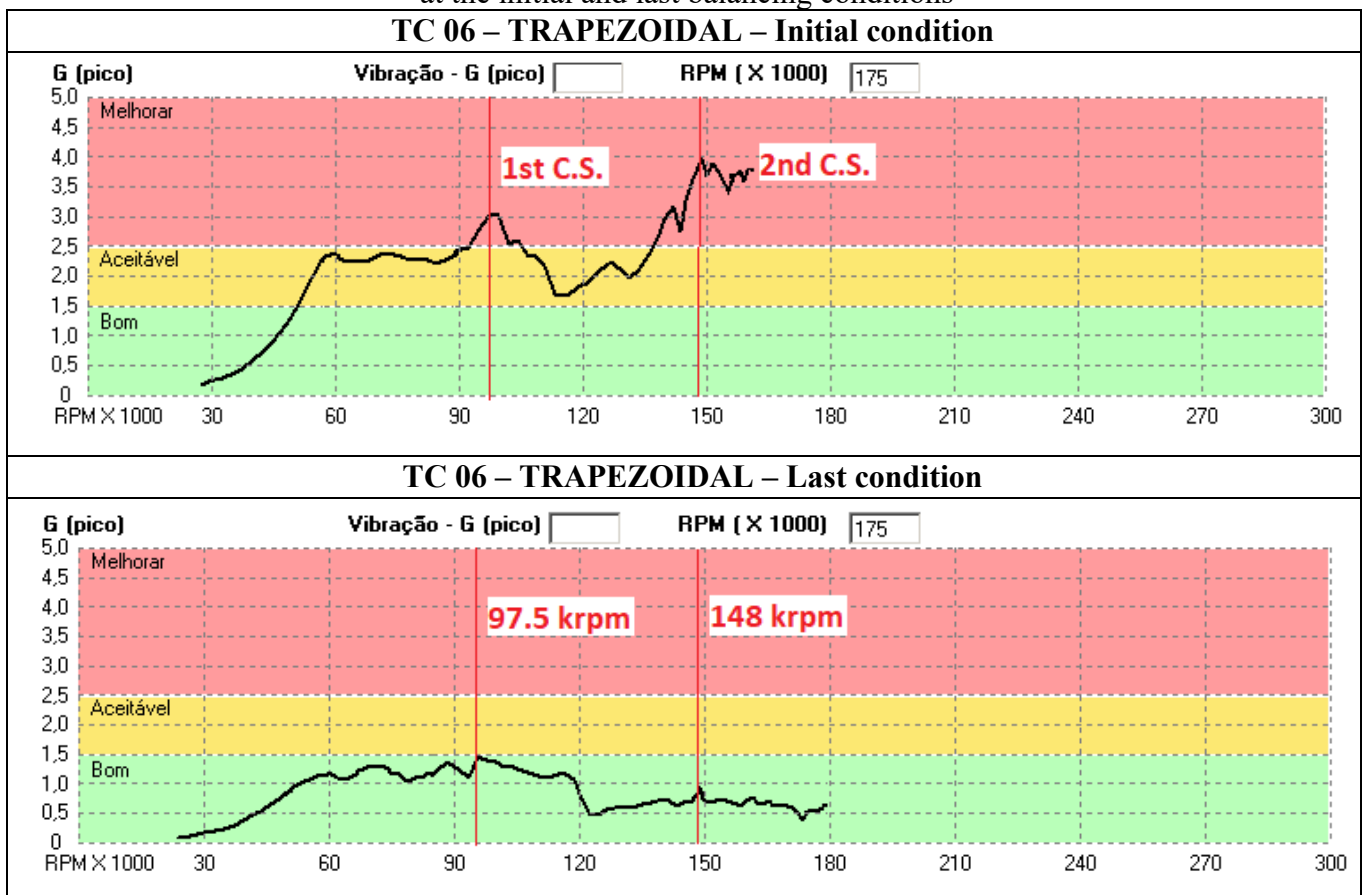


Figure 86 – Synchronous curves for the turbocharger TC 6 with bearings with trapezoidal axial grooves at the initial and last balancing conditions

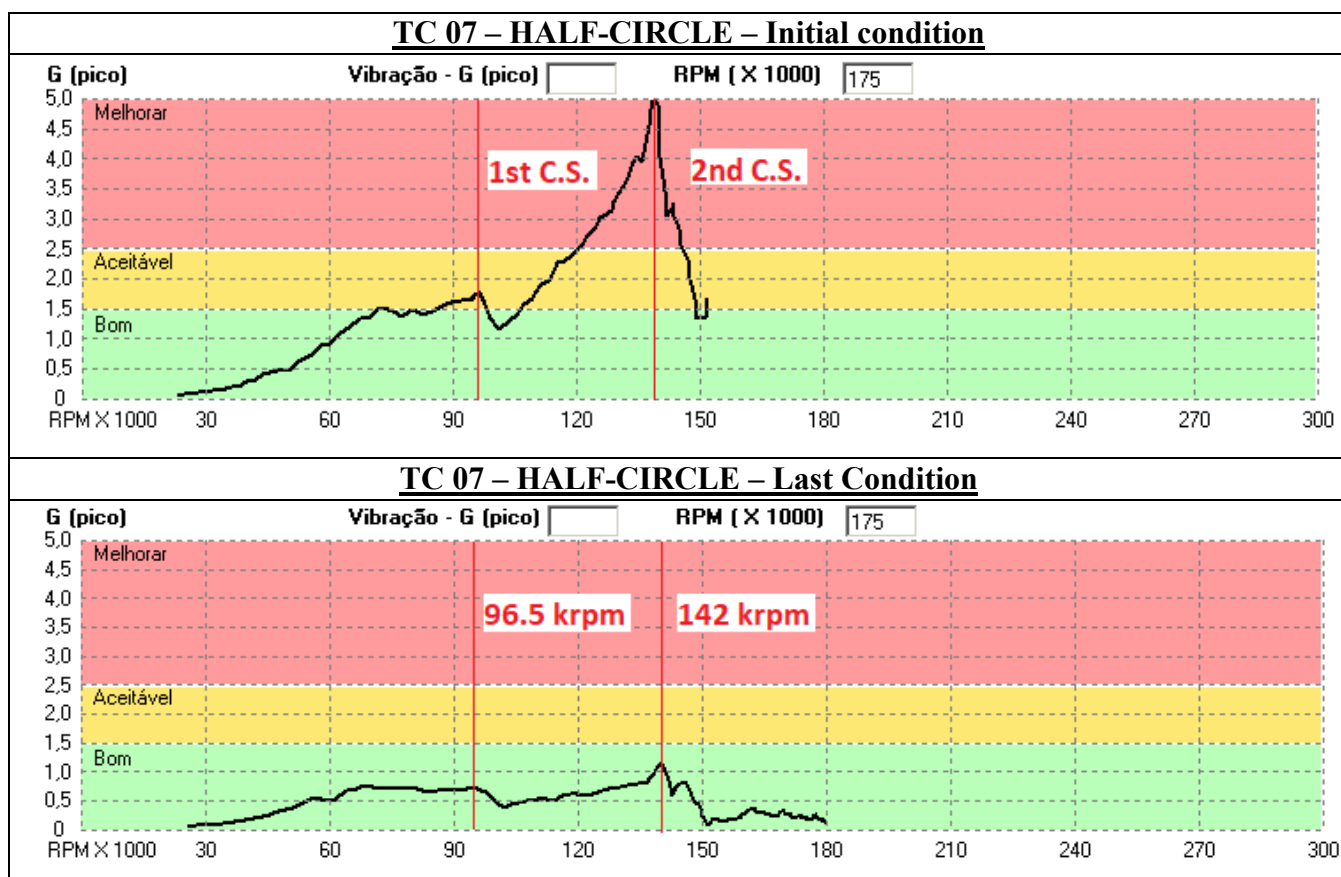


Figure 87 – Synchronous curves for the turbocharger TC 7 with bearings with half-moon axial grooves at the initial and last balancing conditions

The first curves (TCs Initial Conditions) are presented because they generate high synchronous vibrational responses that are unquestionable indicators of the passage through the critical rotor speeds, since after final balancing it is possible to observe, especially in the first critical speed (1st C.S.), low vibration variation gradients as a function of the rotor speed.

The curves clearly indicate that the turbochargers pass through two critical speeds. This information is important for the other results presented ahead in this work for the proper analysis of the results obtained at transient and steady-state conditions.

Table 29 presents the critical speed values obtained during the balancing of the TCs.

With these results, Table 30 presents the relation of each speed line of this work in relation to the critical speeds.

The results confirm what is presented by Nguyen-Schäfer (2015) that the geometric and operating properties of small turbochargers with maximum speeds between 130 and 150 krpm generate maximum TC operating conditions after the 1st critical speed and below the 2nd critical speed. However, it is possible to observe that for the TCs used, the

maximum speed line (135 krpm) is very close to the second critical speed, a speed that Nguyen-Schäfer also indicates as, in many cases, the generation of complete instability.

Table 29 – 1st and 2nd critical speeds for each TC

Turbocharger (bearing axial groove shape)	1st Critical Speed	2nd Critical Speed
TC 1 (triangular)	94.5 krpm	138.5 krpm
TC 2 (half-ellipse)	97 krpm	138.5 krpm
TC 3 (quarter-ellipse)	90.5 krpm	135 krpm
TC 4 (inverted quarter-ellipse)	91.5 krpm	139 krpm
TC 5 (rectangular)	93 krpm	140.5 krpm
TC 6 (trapezoidal)	97.5 krpm	148 krpm
TC 7 (half-circle)	96.5 krpm	142 krpm

Table 30 – Relationship between Speed lines and Critical Speeds

Speed lines	1st Critical Speed	2nd Critical Speed
SL 1 (67 krpm)	Far	Very far
SL 2 (89 krpm)	Very close	Very Far
SL 3 (105 krpm)	Close	Far
SL 4 (121 krpm)	Far	Close
SL 5 (135 krpm)	Very far	Very close

4.2.2. Frequency spectrum

The constant speed measurements are performed using accelerometers attached to the centrifugal compressor housing (two accelerometers on the transverse orthogonal directions) and on the piping flange close to the inlet compressor (an accelerometer on the axial direction), at each speed indicated by the point of operating conditions on the thermodynamic maps, i.e., at approximately constant speed. Thus, for each of the three coordinate axes, six frequency are obtained (at six valve closing positions) for five speed lines plus the surge condition, totaling 30 spectra per axis, 90 for each turbocharger, giving a total of 630 steady-state vibration spectra.

In view of the purpose of this study and the large number of frequency spectra generated, the presentation of all these spectra is in Appendix C. To permit a comparative analysis of the results rendered by each TC, the amplitude and frequency scales for each

curve are the same in the Appendix. The results obtained for axial vibration among the turbochargers with different axial grooves shapes do not show significant variations. Therefore, only the results for the lateral vibration will be shown. For the two transverse orthogonal directions analyzed, the highest RMS value of the acceleration at synchronous response is always considered, as well as the highest value of the response to rotordynamic instabilities – oil whirl/oil whip from both the inner and outer oil films, Alford's force, centrifugal dynamics, and others (subsynchronous vibration). All subsynchronous vibrations are considered in the analysis, except the originated from shaft rub.

Hereafter, two tables with the values of synchronous and subsynchronous responses that present larger amplitudes of vibration for each speed line and surge will be presented. Additionally, curves are prepared for each turbocharger and tested speed line, identifying the maximum synchronous and subsynchronous vibration amplitudes. An efficiency map format is used for a better visualization of the steady-state vibration responses for each turbocharger.

Synchronous response measured at constant speed

Tables 31 and 32 present the results of synchronous vibrations for each TC at each measurement point. The XY measurement point (M.P.) presents the X speed line at the Y position of valve opening. Based on the data of synchronous response of all turbochargers, a classification based on five qualitative grades – excellent, good, satisfactory, poor, and very poor – is presented for the RMS values of synchronous response (where G is the acceleration of gravity). This evaluation criterion is based on the manufacturer's standard used for synchronous responses during the set balancing added to the Mean Time Between Failure (MTBF) recorded history. Using these two factors, the following values are defined):

- Excellent: < 0.5 G;
- Good: ≥ 0.5 G and < 1.0 G;
- Satisfactory: ≥ 1.0 G and < 1.5 G;
- Poor: ≥ 1.5 G and < 2.0 G;
- Very Poor: ≥ 2.0 G

It is important to state that all tests are performed under operating conditions, after the system has reached a stabilized temperature condition. Thus, the dynamic response of the turbochargers is different from that observed during the balancing because of the temperature conditions.

Table 31 – Amplitude of synchronous response for TCs 1 to 4

TC 01 - TRIANGULAR				TC 02 – HALF-ELLIPSE				TC 03 - 1/4 ELIPSE				TC 04 - INVERTED 1/4 ELIPSE			
<u>M.P.</u>	<u>V.C.</u>	<u>Value (G)</u>	<u>Response</u>	<u>M.P.</u>	<u>V.C.</u>	<u>Value (G)</u>	<u>Response</u>	<u>M.P.</u>	<u>V.C.</u>	<u>Value (G)</u>	<u>Response</u>	<u>M.P.</u>	<u>V.C.</u>	<u>Value (G)</u>	<u>Response</u>
11	0%	0.4	Excellent	11	0%	0.25	Excellent	11	0%	0.1	Excellent	11	0%	0.65	Good
12	36%	0.4	Excellent	12	36%	0.3	Excellent	12	36%	0.15	Excellent	12	36%	0.65	Good
13	63%	0.45	Excellent	13	63%	0.2	Excellent	13	63%	0.1	Excellent	13	63%	0.65	Good
14	81%	0.45	Excellent	14	81%	0.3	Excellent	14	81%	0.1	Excellent	14	81%	0.6	Good
15	90%	0.5	Good	15	90%	0.15	Excellent	15	90%	0.1	Excellent	15	90%	0.6	Good
16	<i>Surge</i>	0.45	Excellent	16	<i>Surge</i>	0.25	Excellent	16	<i>Surge</i>	0.2	Excellent	16	<i>Surge</i>	0.55	Good
21	0%	0.4	Excellent	21	0%	0.2	Excellent	21	0%	0.25	Excellent	21	0%	1.4	Satisfactory
22	31%	0.6	Good	22	31%	0.15	Excellent	22	31%	0.25	Excellent	22	31%	1.35	Satisfactory
23	55%	0.65	Good	23	55%	0.2	Excellent	23	55%	0.4	Excellent	23	55%	1.6	Poor
24	70%	0.9	Good	24	70%	0.1	Excellent	24	70%	0.4	Excellent	24	70%	1.45	Satisfactory
25	78%	0.55	Good	25	78%	0.1	Excellent	25	78%	0.15	Excellent	25	78%	1.4	Satisfactory
26	<i>Surge</i>	0.45	Excellent	26	<i>Surge</i>	0.05	Excellent	26	<i>Surge</i>	0.5	Good	26	<i>Surge</i>	1.95	Poor
31	0%	0.35	Excellent	31	0%	0.2	Excellent	31	0%	0.4	Excellent	31	0%	0.95	Good
32	31%	0.4	Excellent	32	31%	0.2	Excellent	32	31%	0.45	Excellent	32	31%	1.25	Satisfactory
33	54%	0.4	Excellent	33	54%	0.2	Excellent	33	54%	0.55	Good	33	54%	1.3	Satisfactory
34	69%	0.35	Excellent	34	69%	0.2	Excellent	34	69%	0.45	Excellent	34	69%	0.95	Good
35	77%	0.35	Excellent	35	77%	0.3	Excellent	35	77%	0.4	Excellent	35	77%	1.4	Satisfactory
36	<i>Surge</i>	0.25	Excellent	36	<i>Surge</i>	0.05	Excellent	36	<i>Surge</i>	0.4	Excellent	36	<i>Surge</i>	1	Satisfactory
41	0%	1.3	Satisfactory	41	0%	1.75	Poor	41	0%	1.7	Poor	41	0%	2.3	Very Poor
42	30%	1.2	Satisfactory	42	30%	1.65	Poor	42	30%	1.55	Poor	42	30%	2.75	Very Poor
43	53%	1.05	Satisfactory	43	53%	2	Very Poor	43	53%	2.4	Very Poor	43	53%	2	Very Poor
44	68%	0.9	Good	44	68%	1.5	Poor	44	68%	1.7	Poor	44	68%	1.95	Poor
45	75%	0.7	Good	45	75%	1.75	Poor	45	75%	1.95	Poor	45	75%	2.15	Very Poor
46	<i>Surge</i>	0.8	Good	46	<i>Surge</i>	0.95	Good	46	<i>Surge</i>	1.15	Satisfactory	46	<i>Surge</i>	1.6	Poor
51	0%	1.6	Poor	51	0%	1.75	Poor	51	0%	1.15	Satisfactory	51	0%	1.1	Satisfactory
52	28%	1.75	Poor	52	28%	1.6	Poor	52	28%	1.25	Satisfactory	52	28%	1	Satisfactory
53	49%	1.9	Poor	53	49%	2.05	Very Poor	53	49%	1.45	Satisfactory	53	49%	1.3	Satisfactory
54	63%	0.85	Good	54	63%	1.65	Poor	54	63%	2.05	Very Poor	54	63%	1.05	Satisfactory
55	75%	0.75	Good	55	75%	1.5	Poor	55	75%	1.85	Poor	55	75%	1.25	Satisfactory
56	<i>Surge</i>	0.5	Good	56	<i>Surge</i>	0.85	Good	56	<i>Surge</i>	1.3	Satisfactory	56	<i>Surge</i>	0.4	Excellent

Table 32 – Amplitude of synchronous response for TCs 5 to 7

TURBO 05 - RECTANGULAR				TURBO 06 - TRAPEZOIDAL				TURBO 07 – HALF-CIRCLE			
<u>M.P.</u>	<u>V.C.</u>	<u>Value (G)</u>	<u>Response</u>	<u>M.P.</u>	<u>V.C.</u>	<u>Value (G)</u>	<u>Response</u>	<u>M.P.</u>	<u>V.C.</u>	<u>Value (G)</u>	<u>Response</u>
11	0%	0.45	Excellent	11	0%	0.85	Good	11	0%	1.05	Satisfactory
12	36%	0.5	Good	12	36%	1	Satisfactory	12	36%	0.8	Good
13	63%	0.45	Excellent	13	63%	1.15	Satisfactory	13	63%	0.85	Good
14	81%	0.55	Good	14	81%	0.75	Good	14	81%	0.95	Good
15	90%	0.5	Good	15	90%	0.9	Good	15	90%	0.7	Good
16	<i>Surge</i>	0.55	Good	16	<i>Surge</i>	1.15	Satisfactory	16	<i>Surge</i>	1	Satisfactory
21	0%	0.9	Good	21	0%	1.35	Satisfactory	21	0%	1.5	Poor
22	31%	0.95	Good	22	31%	1.65	Poor	22	31%	1.55	Poor
23	55%	1	Satisfactory	23	55%	2	Very Poor	23	55%	1.45	Satisfactory
24	70%	0.9	Good	24	70%	1.5	Poor	24	70%	2.1	Very Poor
25	78%	0.75	Good	25	78%	1.6	Poor	25	78%	2.2	Very Poor
26	<i>Surge</i>	0.9	Good	26	<i>Surge</i>	2.1	Very Poor	26	<i>Surge</i>	2.5	Very Poor
31	0%	0.55	Good	31	0%	0.9	Good	31	0%	0.95	Good
32	31%	0.65	Good	32	31%	1.45	Satisfactory	32	31%	1.45	Satisfactory
33	54%	0.6	Good	33	54%	1.55	Poor	33	54%	1.45	Satisfactory
34	69%	0.5	Good	34	69%	1.4	Satisfactory	34	69%	1.6	Poor
35	77%	0.45	Excellent	35	77%	1.5	Poor	35	77%	1.25	Satisfactory
36	<i>Surge</i>	0.5	Good	36	<i>Surge</i>	2	Very Poor	36	<i>Surge</i>	1.8	Poor
41	0%	2.05	Very Poor	41	0%	1.15	Satisfactory	41	0%	2.6	Very Poor
42	30%	1.85	Poor	42	30%	1	Satisfactory	42	30%	2.4	Very Poor
43	53%	1.45	Satisfactory	43	53%	1.45	Satisfactory	43	53%	2.55	Very Poor
44	68%	1.45	Satisfactory	44	68%	1	Satisfactory	44	68%	1.7	Poor
45	75%	0.9	Good	45	75%	0.7	Good	45	75%	2.45	Very Poor
46	<i>Surge</i>	0.55	Good	46	<i>Surge</i>	0.95	Good	46	<i>Surge</i>	2	Very Poor
51	0%	1.05	Satisfactory	51	0%	1.05	Satisfactory	51	0%	2.2	Very Poor
52	28%	1	Satisfactory	52	28%	1.05	Satisfactory	52	28%	1.9	Poor
53	49%	0.75	Good	53	49%	0.9	Good	53	49%	2.4	Very Poor
54	63%	1.05	Satisfactory	54	63%	0.75	Good	54	63%	1.7	Poor
55	75%	0.65	Good	55	75%	1	Satisfactory	55	75%	1.95	Poor
56	<i>Surge</i>	0.8	Good	56	<i>Surge</i>	0.5	Good	56	<i>Surge</i>	1.7	Poor

Figures 88 and 89 present the condition of maximum synchronous response described by Tables 31 and 32, respectively, using the compressor map. Lines of the first (1st C.S.) and second (2nd C.S.) critical speeds are also displayed on each figure to show where they occur:

Figure 88 – Maximum amplitude of synchronous response for TCs 1 to 4 using efficiency map.

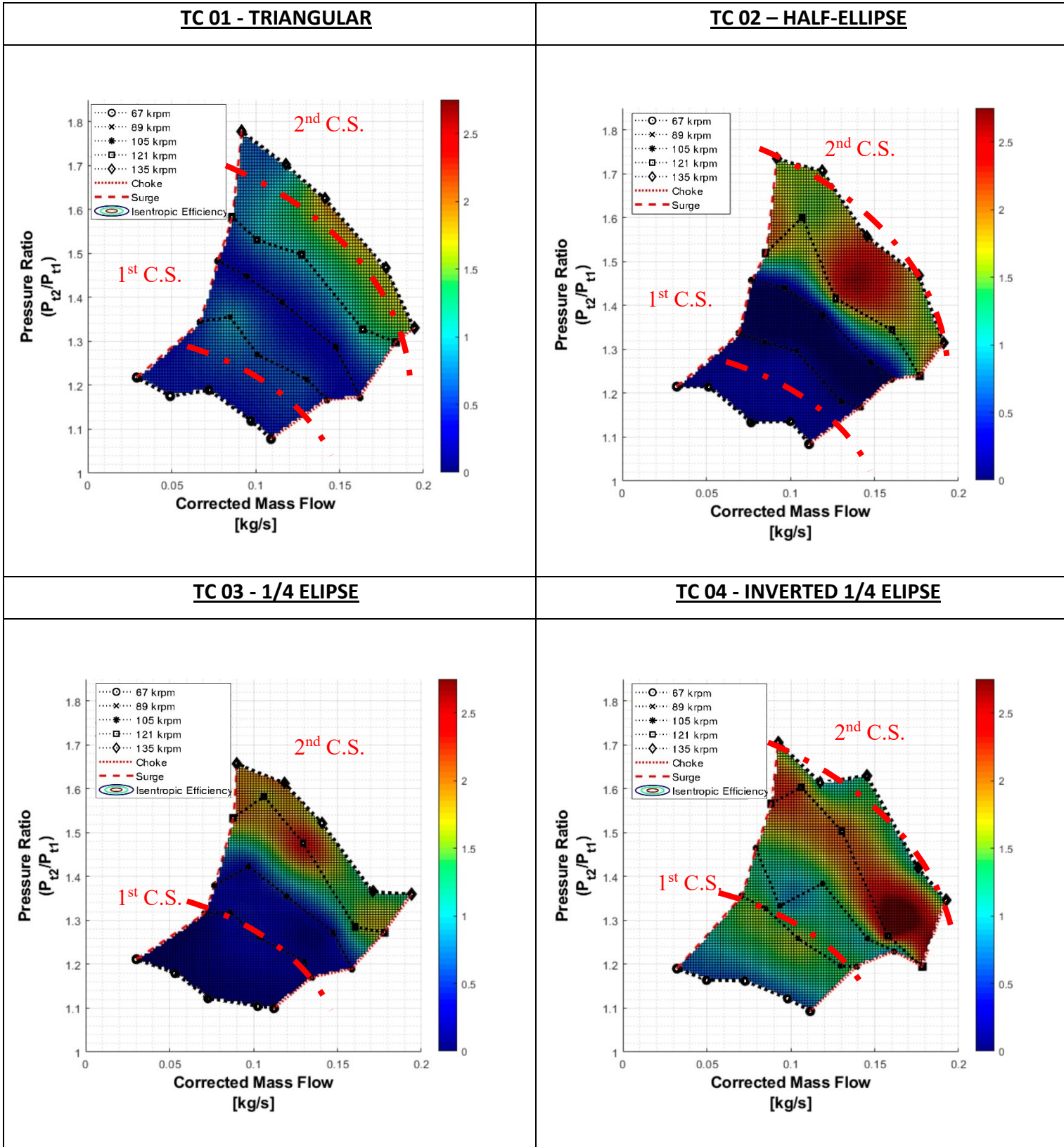
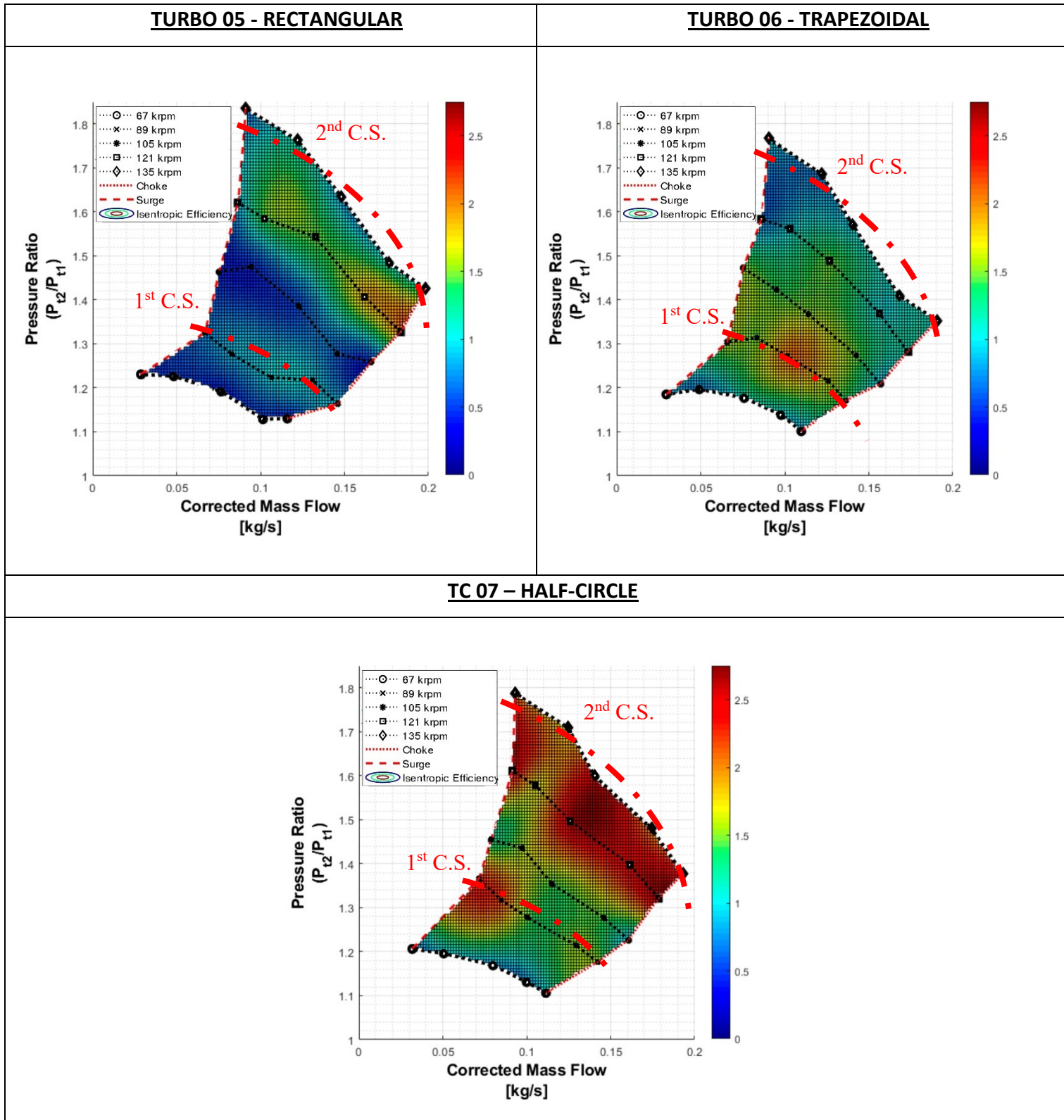


Figure 89 – Maximum amplitude of synchronous response for TCs 5 to 7 using the efficiency map.



Subsynchronous response measured at constant speed

The Table 33 and Table 34 present the subsynchronous vibrations for each TC at each measurement point. The same classification based on five qualitative grades – excellent, good, satisfactory, poor, and very poor – is used for the RMS values of subsynchronous response (where G is the acceleration of gravity). In the case of subsynchronous vibrations, the best condition considers a value very close to zero, i.e., it does not have a direct influence on the dynamic behavior of the rotor. The other conditions were considered from the behavior analysis of the turbocharger when it presents measurable values of subsynchronous vibration added with the empirical experience of the manufacturer.

- Excellent: $< 0.1 \text{ G}$;
- Good: $\geq 0.1 \text{ G}$ and $< 0.5 \text{ G}$;
- Satisfactory: $\geq 0.5 \text{ G}$ and $< 1.0 \text{ G}$;
- Poor: $\geq 1.0 \text{ G}$ and $< 1.5 \text{ G}$ s;
- Very Poor: $\geq 1.5 \text{ G}$ s

Table 33 – Amplitude of subsynchronous response for TCs 1 to 4

TURBO 01 - TRIANGULAR				TURBO 02 – HALF-ELLIPSE				TURBO 03 - 1/4 ELLIPSE				TURBO 04 - INVERTED 1/4 ELLIPSE			
<u>M.P.</u>	<u>V.C.</u>	<u>Value (G)</u>	<u>Response</u>	<u>M.P.</u>	<u>V.C.</u>	<u>Value (G)</u>	<u>Response</u>	<u>M.P.</u>	<u>V.C.</u>	<u>Value (G)</u>	<u>Response</u>	<u>M.P.</u>	<u>V.C.</u>	<u>Value (G)</u>	<u>Response</u>
11	0%	0	Excellent	11	0%	0	Excellent	11	0%	0	Excellent	11	0%	0.1	Excellent
12	36%	0	Excellent	12	36%	0	Excellent	12	36%	0	Excellent	12	36%	0.1	Excellent
13	63%	0	Excellent	13	63%	0	Excellent	13	63%	0	Excellent	13	63%	0.1	Excellent
14	81%	0	Excellent	14	81%	0	Excellent	14	81%	0	Excellent	14	81%	0.1	Excellent
15	90%	0	Excellent	15	90%	0	Excellent	15	90%	0	Excellent	15	90%	0.1	Excellent
16	<i>Surge</i>	<i>0</i>	<i>Excellent</i>	16	<i>Surge</i>	<i>0.05</i>	<i>Excellent</i>	16	<i>Surge</i>	<i>0</i>	<i>Excellent</i>	16	<i>Surge</i>	<i>0.1</i>	<i>Excellent</i>
21	0%	0.4	Good	21	0%	0.05	Excellent	21	0%	0.3	Good	21	0%	0.2	Good
22	31%	0.55	Satisfactory	22	31%	0.05	Excellent	22	31%	0.45	Good	22	31%	0.2	Good
23	55%	0.5	Satisfactory	23	55%	0.05	Excellent	23	55%	0.2	Good	23	55%	0.4	Good
24	70%	0.6	Satisfactory	24	70%	0.1	Excellent	24	70%	0.1	Excellent	24	70%	0.4	Good
25	78%	0.6	Satisfactory	25	78%	0.1	Excellent	25	78%	0.4	Good	25	78%	0.4	Good
26	<i>Surge</i>	<i>0</i>	<i>Excellent</i>	26	<i>Surge</i>	<i>0.1</i>	<i>Excellent</i>	26	<i>Surge</i>	<i>0.4</i>	<i>Good</i>	26	<i>Surge</i>	<i>0.4</i>	<i>Good</i>
31	0%	0.3	Good	31	0%	0.65	Satisfactory	31	0%	0.45	Good	31	0%	0.2	Good
32	31%	0.4	Good	32	31%	0.75	Satisfactory	32	31%	0.4	Good	32	31%	0.15	Good
33	54%	0.4	Good	33	54%	0.8	Satisfactory	33	54%	0.4	Good	33	54%	0.25	Good
34	69%	0.3	Good	34	69%	0.1	Excellent	34	69%	0.6	Satisfactory	34	69%	0.25	Good
35	77%	0.25	Good	35	77%	0.15	Good	35	77%	0.6	Satisfactory	35	77%	0.25	Good
36	<i>Surge</i>	<i>0.4</i>	<i>Good</i>	36	<i>Surge</i>	<i>0.1</i>	<i>Excellent</i>	36	<i>Surge</i>	<i>0.4</i>	<i>Good</i>	36	<i>Surge</i>	<i>0.2</i>	<i>Good</i>
41	0%	0.4	Good	41	0%	0.8	Satisfactory	41	0%	0.4	Good	41	0%	0.3	Good
42	30%	0.4	Good	42	30%	0.55	Satisfactory	42	30%	0.3	Good	42	30%	0.3	Good
43	53%	0.4	Good	43	53%	0.8	Satisfactory	43	53%	0.55	Satisfactory	43	53%	0.4	Good
44	68%	0.25	Good	44	68%	0.6	Satisfactory	44	68%	0.5	Satisfactory	44	68%	0.4	Good
45	75%	0.25	Good	45	75%	0.15	Good	45	75%	0.4	Good	45	75%	0.45	Good
46	<i>Surge</i>	<i>0.4</i>	<i>Good</i>	46	<i>Surge</i>	<i>0.35</i>	<i>Good</i>	46	<i>Surge</i>	<i>0.45</i>	<i>Good</i>	46	<i>Surge</i>	<i>0.2</i>	<i>Good</i>
51	0%	0.25	Good	51	0%	0.8	Satisfactory	51	0%	0	Excellent	51	0%	0.4	Good
52	28%	0.25	Good	52	28%	1	Poor	52	28%	0	Excellent	52	28%	0.4	Good
53	49%	0.2	Good	53	49%	1	Poor	53	49%	0.3	Good	53	49%	0.15	Good
54	63%	0.2	Good	54	63%	1.05	Poor	54	63%	0.55	Satisfactory	54	63%	0.4	Good
55	75%	0.25	Good	55	75%	0.05	Excellent	55	75%	0.5	Satisfactory	55	75%	0.45	Good
56	<i>Surge</i>	<i>0.6</i>	<i>Satisfactory</i>	56	<i>Surge</i>	<i>0.05</i>	<i>Excellent</i>	56	<i>Surge</i>	<i>0.25</i>	<i>Good</i>	56	<i>Surge</i>	<i>0.15</i>	<i>Good</i>

Table 34 – Amplitude of subsynchronous response for TCs 5 to 7

TURBO 05 - RECTANGULAR				TURBO 06 - TRAPEZOIDAL				TURBO 07 - HALF-CIRCLE			
<u>M.P.</u>	<u>V.C.</u>	<u>Value (G)</u>	<u>Response</u>	<u>M.P.</u>	<u>V.C.</u>	<u>Value (G)</u>	<u>Response</u>	<u>M.P.</u>	<u>V.C.</u>	<u>Value (G)</u>	<u>Response</u>
11	0%	0	Excellent	11	0%	0.1	Excellent	11	0%	0.1	Excellent
12	36%	0	Excellent	12	36%	0.1	Excellent	12	36%	0.05	Excellent
13	63%	0	Excellent	13	63%	0.1	Excellent	13	63%	0.15	Good
14	81%	0	Excellent	14	81%	0.05	Excellent	14	81%	0.1	Excellent
15	90%	0	Excellent	15	90%	0	Excellent	15	90%	0.15	Good
16	<i>Surge</i>	<i>0</i>	<i>Excellent</i>	16	<i>Surge</i>	<i>0.05</i>	<i>Excellent</i>	16	<i>Surge</i>	<i>0.1</i>	<i>Excellent</i>
21	0%	0.4	Good	21	0%	0.5	Satisfactory	21	0%	0.2	Good
22	31%	0.4	Good	22	31%	0.45	Good	22	31%	0.2	Good
23	55%	0.1	Excellent	23	55%	0.55	Satisfactory	23	55%	0.25	Good
24	70%	0.05	Excellent	24	70%	0.45	Good	24	70%	0.35	Good
25	78%	0.05	Excellent	25	78%	0.4	Good	25	78%	0.35	Good
26	<i>Surge</i>	<i>0.05</i>	<i>Excellent</i>	26	<i>Surge</i>	<i>0.4</i>	<i>Good</i>	26	<i>Surge</i>	<i>0.25</i>	<i>Good</i>
31	0%	0.75	Satisfactory	31	0%	0.5	Satisfactory	31	0%	0.4	Good
32	31%	0.85	Satisfactory	32	31%	0.65	Satisfactory	32	31%	0.5	Satisfactory
33	54%	0.6	Satisfactory	33	54%	0.75	Satisfactory	33	54%	0.55	Satisfactory
34	69%	0.5	Satisfactory	34	69%	0.55	Satisfactory	34	69%	0.45	Good
35	77%	0.75	Satisfactory	35	77%	0.6	Satisfactory	35	77%	0.6	Satisfactory
36	<i>Surge</i>	<i>0.8</i>	<i>Satisfactory</i>	36	<i>Surge</i>	<i>0.85</i>	<i>Satisfactory</i>	36	<i>Surge</i>	<i>0.5</i>	<i>Satisfactory</i>
41	0%	0.8	Satisfactory	41	0%	1.3	Poor	41	0%	0.5	Satisfactory
42	30%	0.65	Satisfactory	42	30%	0.75	Satisfactory	42	30%	0.6	Satisfactory
43	53%	0.65	Satisfactory	43	53%	1.2	Poor	43	53%	0.7	Satisfactory
44	68%	0.6	Satisfactory	44	68%	1.3	Poor	44	68%	0.4	Good
45	75%	0.8	Satisfactory	45	75%	0.8	Satisfactory	45	75%	0.5	Satisfactory
46	<i>Surge</i>	<i>0.4</i>	<i>Good</i>	46	<i>Surge</i>	<i>1.3</i>	<i>Poor</i>	46	<i>Surge</i>	<i>0.45</i>	<i>Good</i>
51	0%	0.6	Satisfactory	51	0%	0.8	Satisfactory	51	0%	0.7	Satisfactory
52	28%	0.6	Satisfactory	52	28%	0.75	Satisfactory	52	28%	0.75	Satisfactory
53	49%	0.65	Satisfactory	53	49%	0.6	Satisfactory	53	49%	0.55	Satisfactory
54	63%	0.6	Satisfactory	54	63%	1.5	Very Poor	54	63%	0.7	Satisfactory
55	75%	0.8	Satisfactory	55	75%	1.6	Very Poor	55	75%	0.7	Satisfactory
56	<i>Surge</i>	<i>0.4</i>	<i>Good</i>	56	<i>Surge</i>	<i>1.1</i>	<i>Poor</i>	56	<i>Surge</i>	<i>0.6</i>	<i>Satisfactory</i>

Figures 90 and 91 show the condition of maximum amplitude of subsynchronous vibration given by Tables 33 and 34 using also the compressor map:

Figure 90 – Maximum amplitude of subsynchronous response for TCs 1 to 4 using the efficiency map

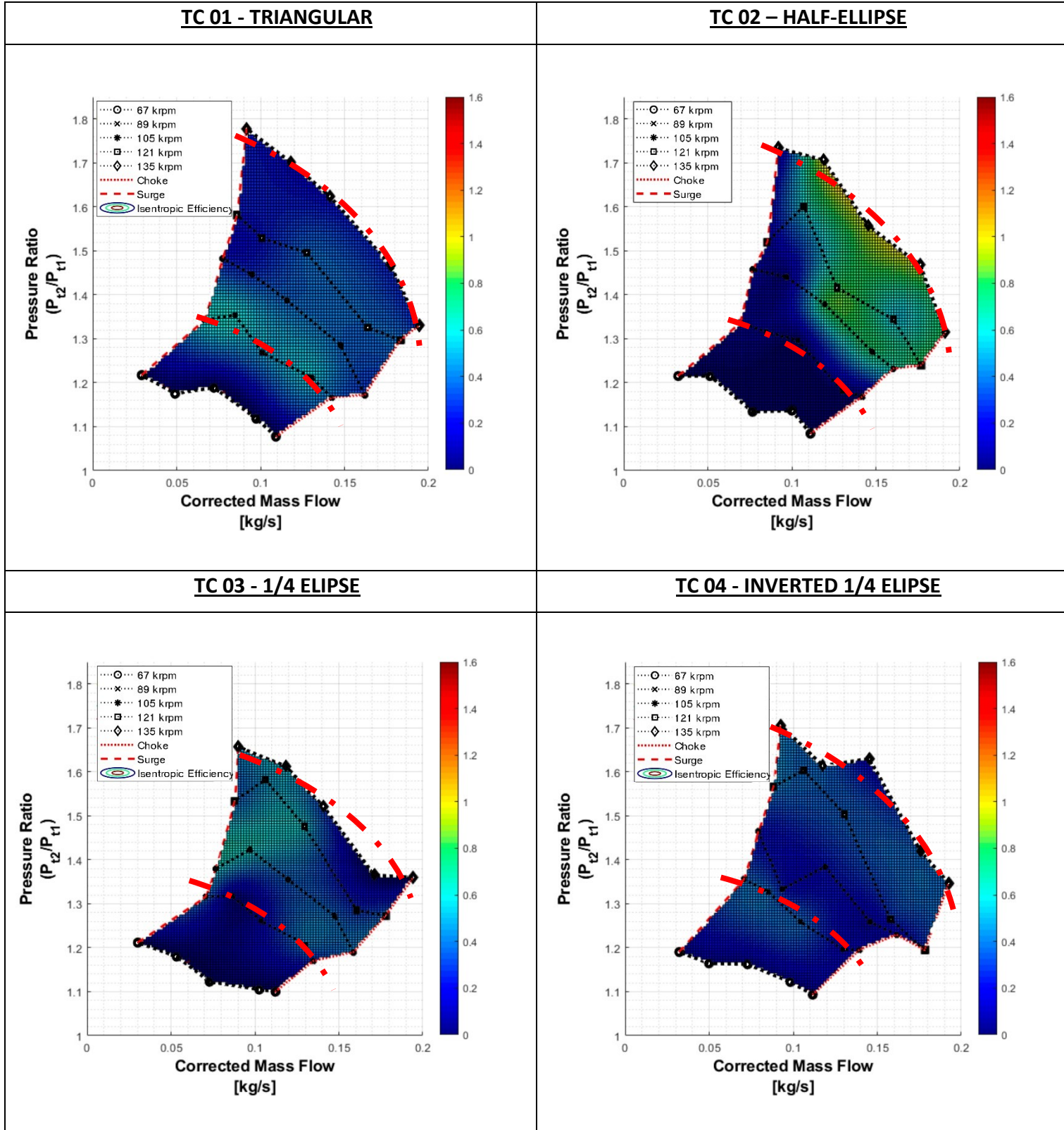
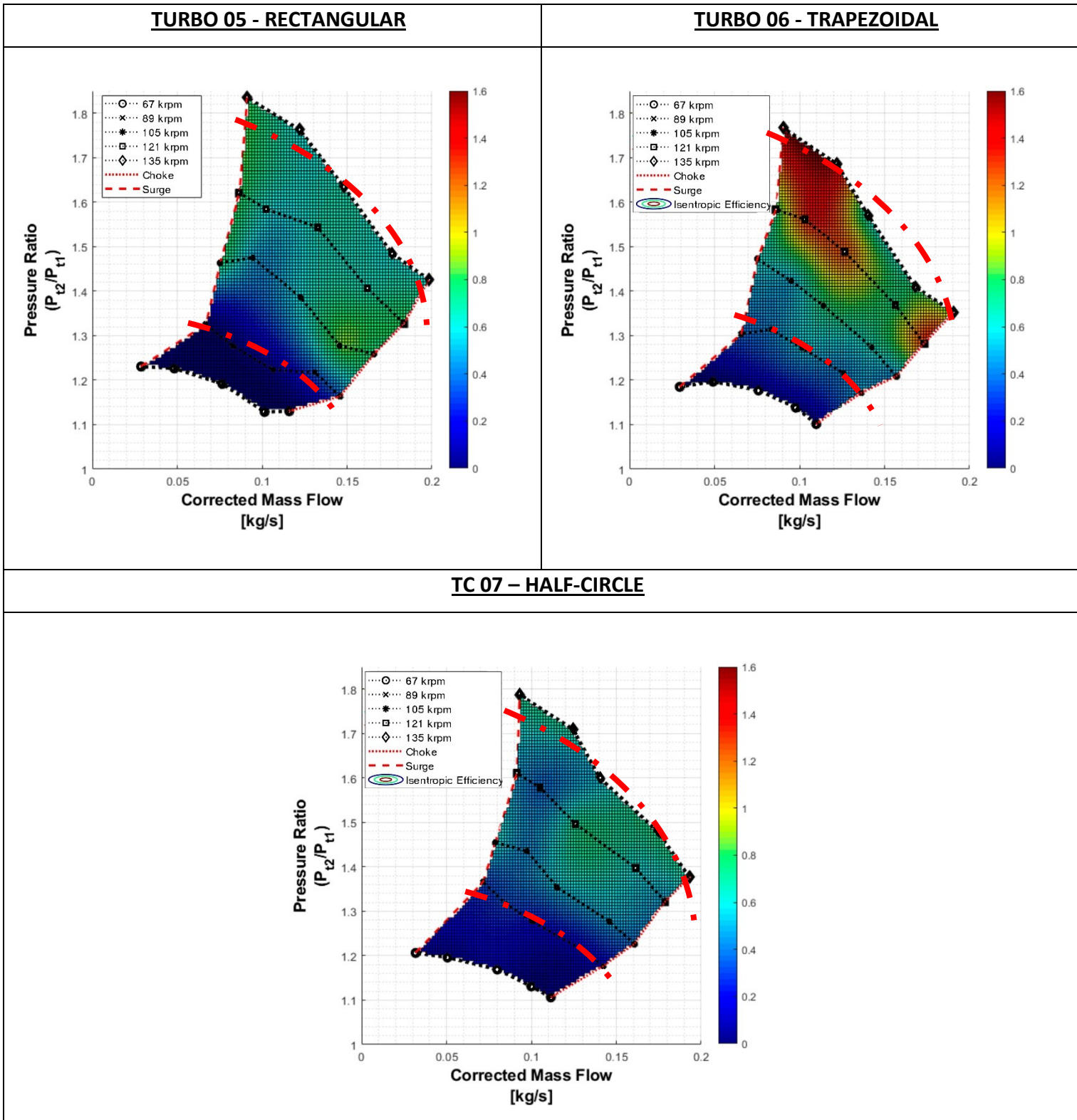


Figure 91 – Maximum amplitude of subsynchronous response for TCs 5 to 7 using the efficiency map



Ranking of turbochargers based on the vibration response measured at constant speed

In order to rank the seven TCs based on the amplitude of synchronous and subsynchronous vibrations, a 5-point Pugh scale matrix is employed. The importance of the synchronous and subsynchronous responses is based on the following classification presented in Tables 31 to 34:

- a. -2 points for Very poor;
- b. -1 point for Poor;
- c. 0 point for Satisfactory;
- d. 1 point for Good;
- e. 2 points for Excellent.

Table 35 presents the results obtained by the Pugh matrix accounting for the maximum amplitudes of synchronous and subsynchronous vibrations measured on the turbochargers supported on bearings with different axial groove shapes.

Table 35 – Pugh scores for imbalance and fluid film instability response (Synchronous and subsynchronous vibrations)

Turbocharger (bearing axial groove shape)	Constant speed frequency spectrum scores												Final TC steady-state vibration score & rank	
	Synchronous response						Subsynchronous							
	Pts SL1	Pts SL2	Pts SL3	Pts SL4	Pts SL5	weight	Pts SL1	Pts SL2	Pts SL3	Pts SL4	Pts SL5	weight		
TC 1 (triangular)	11	8	12	3	0	1	12	3	6	6	5	1	66	1st
TC 2 (half- ellipse)	12	12	12	-5	-5		12	12	5	2	1		58	2nd
TC 3 (quarter- ellipse)	12	11	11	-6	-3		12	7	4	4	6		58	2nd
TC 4 (inverted quarter-ellipse)	6	-2	2	-10	2		12	6	6	6	6		34	5th
TC 5 (rectangular)	8	5	7	-1	3		12	10	0	1	1		46	4th
TC 6 (trapezoidal)	3	-7	-3	2	3		12	4	0	-4	-5		5	6th
TC 7 (half- circle)	4	-8	-1	-11	-8		10	6	2	2	0		-4	7th

It is possible to observe that for the first speed line (67 krpm, below and far from the first critical speed), the triangular, half-ellipse and quarter-ellipse shapes lead to bearing designs that provide superior behavior for the synchronous response, but all shapes present good subsynchronous stability.

In the second speed line (89 krpm, below the two critical speeds, but very close to the first), again the triangular, half-ellipse and quarter-ellipse shapes offer bearing designs that provide superior behavior for the synchronous response, and the others lead to bearing designs with worse performance (except the rectangular one that is maintained), compared to speed line 1. In terms of subsynchronous vibrations, the half-ellipse and rectangular shapes seem to be the more adequate groove shapes.

When entering the third speed line (105 krpm, slightly above the first critical velocity, and far below the second critical velocity), there is no change in relation to the synchronous response of the speed line 2 for each shape. However, greater subsynchronous vibration amplitudes are observed in all shapes, highlighting a significant worsening bearings with rectangular and trapezoidal shapes.

At the fourth speed line (121 krpm, well above the first critical speed, near to the second critical speed), the synchronous responses have high vibration peaks, except for the TC on bearings with trapezoidal shape, which presents satisfactory values for all ranges of air flow inside the compressor. However, for subsynchronous vibrations, there are satisfactory values for all shapes, again except for the trapezoidal one, but in this case with worse performance than the others.

Finally, at the fifth and last speed line (135 krpm, above the first critical speed, but very close to the second critical speed) it can be noticed that the smaller amplitudes of synchronous vibration are observed on TCs on bearings with inverted quarter-ellipse, rectangular, and trapezoidal groove shapes, while for subsynchronous vibrations the triangular, quarter-ellipse, and inverted quarter-ellipse grooves provide bearings with better capability of attenuating the response.

Other important results are:

1. In all TCs, except that on bearings with trapezoidal groove shape, the synchronous response presents increasing amplitude when the shaft crosses the first critical speed towards the second critical speed.
2. The difficulties observed in obtaining TD efficiency maps at speed line 4 (121 krpm) in TCs supported on bearings with ellipse-shaped groove shapes (half-ellipse, quarter-ellipse and inverted quarter-ellipse) are justified by the large synchronous vibrational amplitude of these three shapes observed.

3. At speeds below and close to the first critical speed (speed lines 1, 2 and 3, at 67, 89 and 105 krpm respectively), the TCs with SRFRBs with half-ellipse and quarter-ellipse groove shapes presented the best synchronous responses, while after the 1st critical speed and before the 2nd critical speed (speed lines 4 and 5, 121 and 135 krpm) the trapezoidal, triangular and rectangular shapes showed the best results of synchronous vibration. Considering all speed lines, the triangular shape is the only one to maintain a more constant synchronous vibratory response (and the only one to have no synchronous RMS vibration above 2G).
4. In relation to rotordynamics subsynchronous responses, speed line 1 (much below the first critical speed) does not represent any considerable value in any shape. In speed line 2, only the rotor supported on SFRB with triangular groove shape presents higher vibrational amplitude, but within satisfactory responses. When passing the first critical speed (speed lines 3, 4 and 5), relevant subsynchronous vibrations are already observed in all shapes, except for the triangular and inverted quarter-ellipse, which maintains good subsynchronous attenuation responses throughout the operation.
5. The vibration tests performed on constant speed indicate that the amplitudes of the synchronous or nonsynchronous vibrations are not affected by the valve openings. That means that it is not possible to observe a relationship between the reduction of the compressor inlet air flow and an increase or decrease in the whirling vibration amplitudes.

4.2.3. Rotor whirling orbit

The third part of the rotordynamic study presents the results obtained for the shaft whirling motion carried out using proximity sensors. The diagram of orbit shows the motion of the center of the rotor in relation to the bearing, allowing evaluating the whirling orbit radius for several operating conditions. The shaft whirling orbits are usually obtained at constant speed, i.e., at steady-state operation with various air flow rates.

The shaft whirling orbits in different TC operating conditions (valve closing and speed line) are obtained by proximity sensors for the seven TCs bearing configurations studied in this work.

The orbits are not obtained for surge conditions for three reasons: (i) to obtain orbits, the acquisition time of the proximity probes is larger than those used for the other sensors; (ii) keeping the surge for a long period could lead to a catastrophic failure,

jeopardizing the entire work; and (iii) at surge conditions, the rotor center presents large orbit radius, forcing the shaft surface to approach the probe, which could cause a solid contact capable of damaging the probe.

Again, for ease of observation, the orbit diagrams for each case of rotating system are presented using the compressor efficiency map in order to show the variation of the orbit under different operating conditions. The form of presentation is chosen for convenience.

Each orbit graph is composed of a total scale of 0.1 mm in length, in the horizontal and vertical axes, as shown in Figure 92.

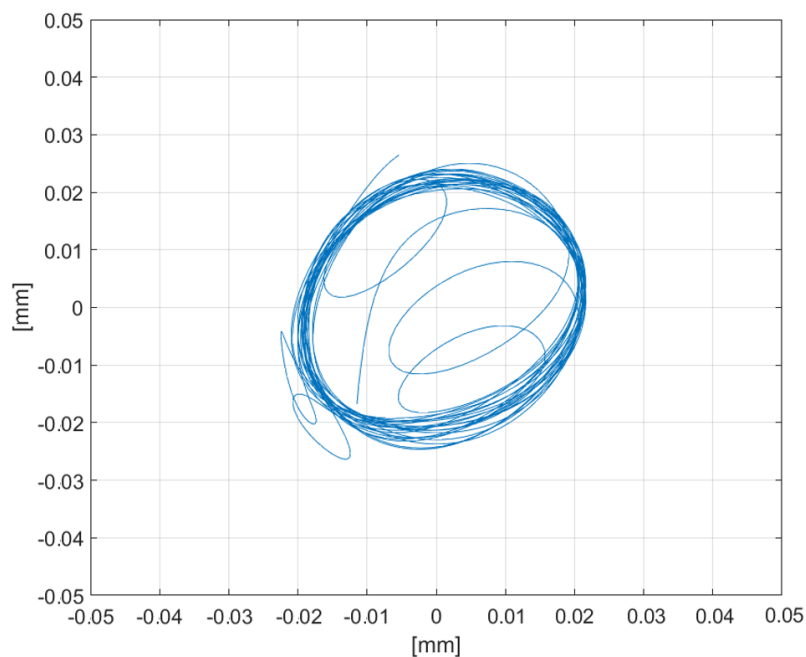


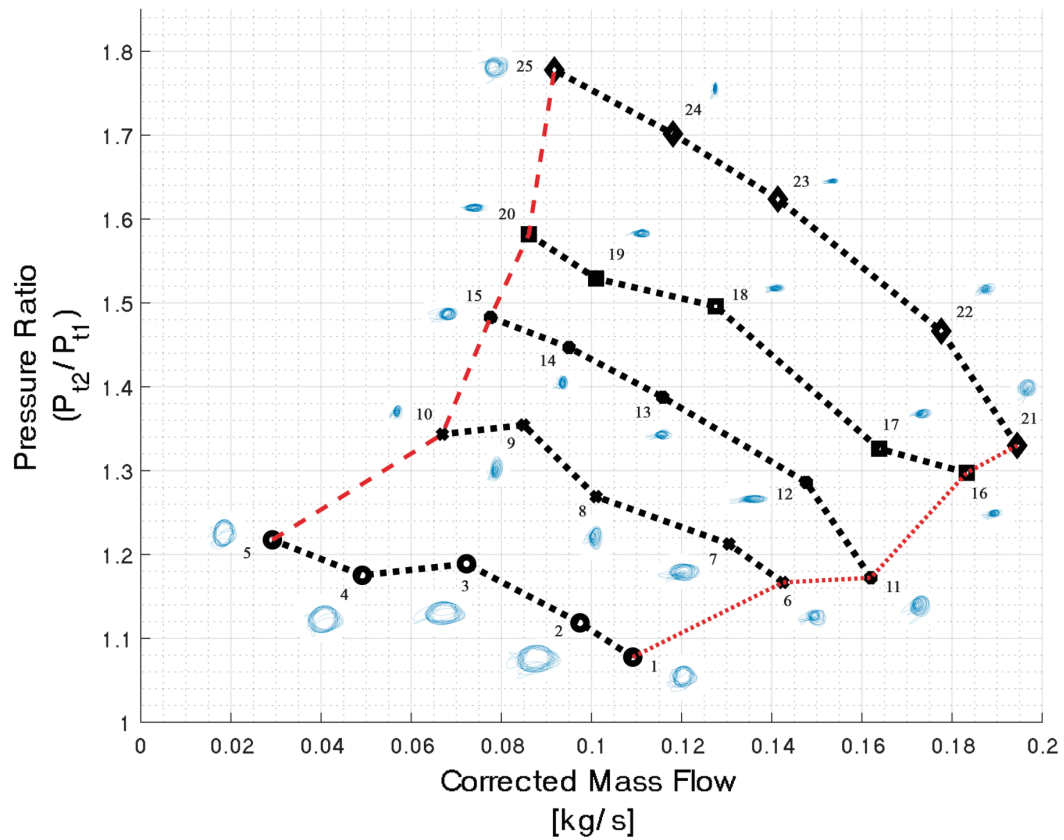
Figure 92 – Example of orbit graph with 0.1 mm x 0.1 mm area

Orbits results

The orbits are obtained by two proximity probes installed in the radial direction of the shaft with a 90° delay (vertical and horizontal), close to the shaft tip at the compressor outlet, with a gap of approximately 1 mm.

The standard frequency for obtaining data from proximity probes is 10 kHz, which is more than enough for an axis that rotates at most 2.25 kHz (135 krpm). Each orbit acquisition was set to three seconds, obtaining a total of 30,000 points for each orbit.

Figure 93 shows the orbits for the five valve opening conditions at each TC1 (triangular) speed line. The measurement of the orbits is carried out in a steady-state condition.



Speed Lines

Outlet Compressor Valve Closing - V.C.

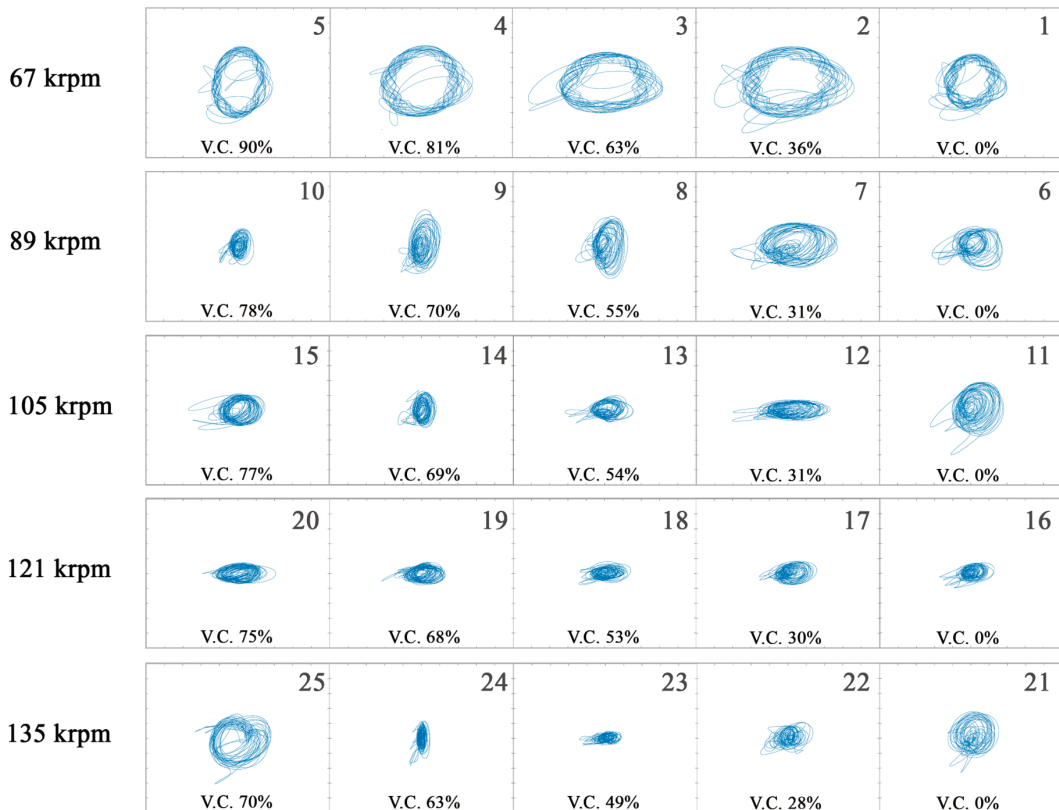


Figure 93 – Rotor orbits of the TC1 supported on bearings with triangular axial grooves and indication of the measurement points on the efficiency map.

Firstly, Figure 93 allows to state that the largest orbits are observed at speed line 1 and there is no significant record of subsynchronous vibrations. The modification of the valve opening seems to cause a phase shift on the orbit, at which the maximum orbit radius changes from the vertical direction to the horizontal direction as the opening increases. The orbit radius reaches the smallest value for the valve fully open.

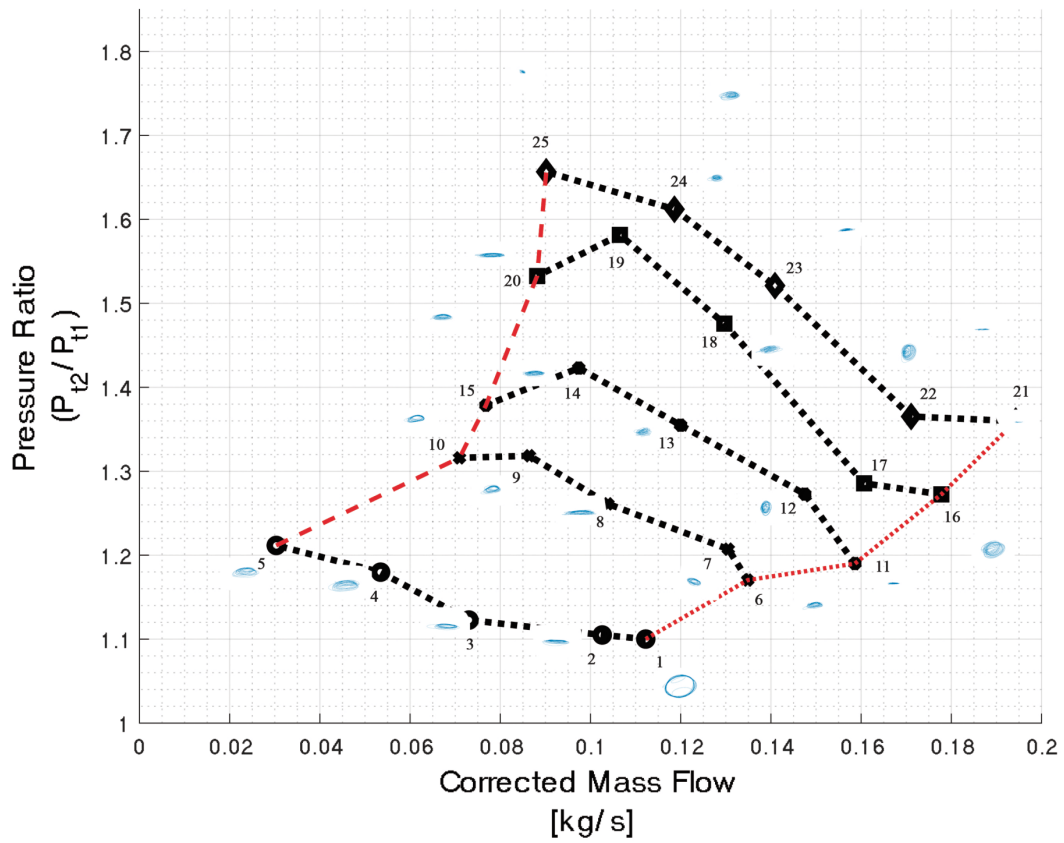
For speed line 2, it is also observed a phase shift on the orbit as the valve opening varies. This phase shift caused by the variation of the mass flow in compressors has been reported in several works, since Alford (1965). Previous experimental works have indicated that when a phase shift takes place, the machine operation can be near to the nominal working conditions and there is great susceptibility for unstable behavior (EHRICH, 1972; WACHEL, 1975; FOWLIE and MILES, 1975). It can be observed that there is no stationary trajectory, indicating that some subsynchronous vibrations take place, trend similar to the orbit shape presented by Nguyen-Schäfer (2015) for inner and outer oil whirls.

On speed line 3, in the region of the first critical speed, non-stationary quasi-circular orbits are observed for the-valve fully open (#11) and orbit phase shift occurs as the valve opening varies. The orbits at speed line 3, in general, present smaller radii than those observed at the previous speed lines.

For speed line 4, it can be noticed that the orbit radii present the smaller values when compared to those at the other speed lines. Furthermore, phase shift is observed when the rotor is running between the first and second critical speeds. At this speed line, the valve opening seems not affect the orbit amplitude.

At speed line 5, the orbit presents a non-stationary trend when the valve is fully open. An orbit phase shift is also observed as the valve opening varies.

Figure 94 shows the orbits for the five valve opening conditions at each speed line for the TC2 rotor mounted on bearings with half-ellipse groove shape.



Speed Lines

Outlet Compressor Valve Closing - V.C.

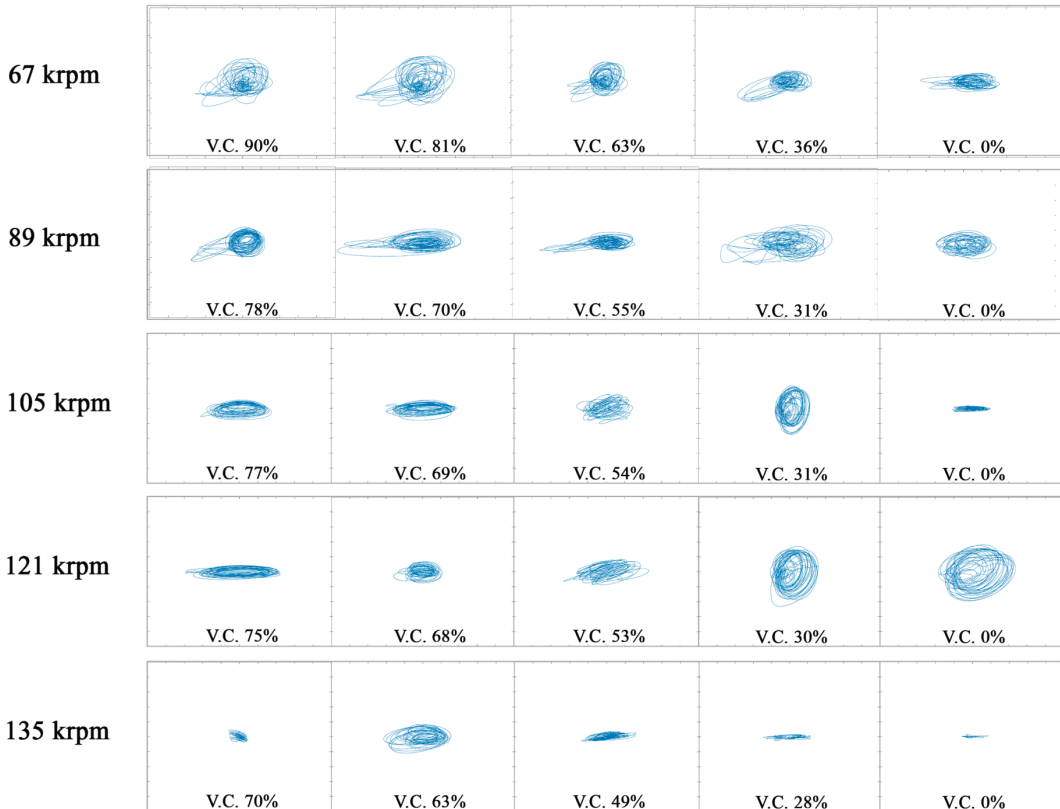


Figure 94 – Rotor orbits of the TC2 supported on bearings with half-ellipse axial grooves and indication of the measurement points on the efficiency map.

In TC2 is possible to observe that the orbit motion does not reach a clear limit-cycle, but the orbit radii do not grow enough to force the solid contact between the shaft and the bearing. It is expected to observe a phase shift whenever the shaft crosses a critical speed, what is evident for speed lines 4 and 5. The air flow impacts the rotor whirling motion, but the increasing or decreasing trend of this motion depends on the speed range analyzed. Above the second critical speed, the orbit radius reaches a minimum value for the valve fully open.

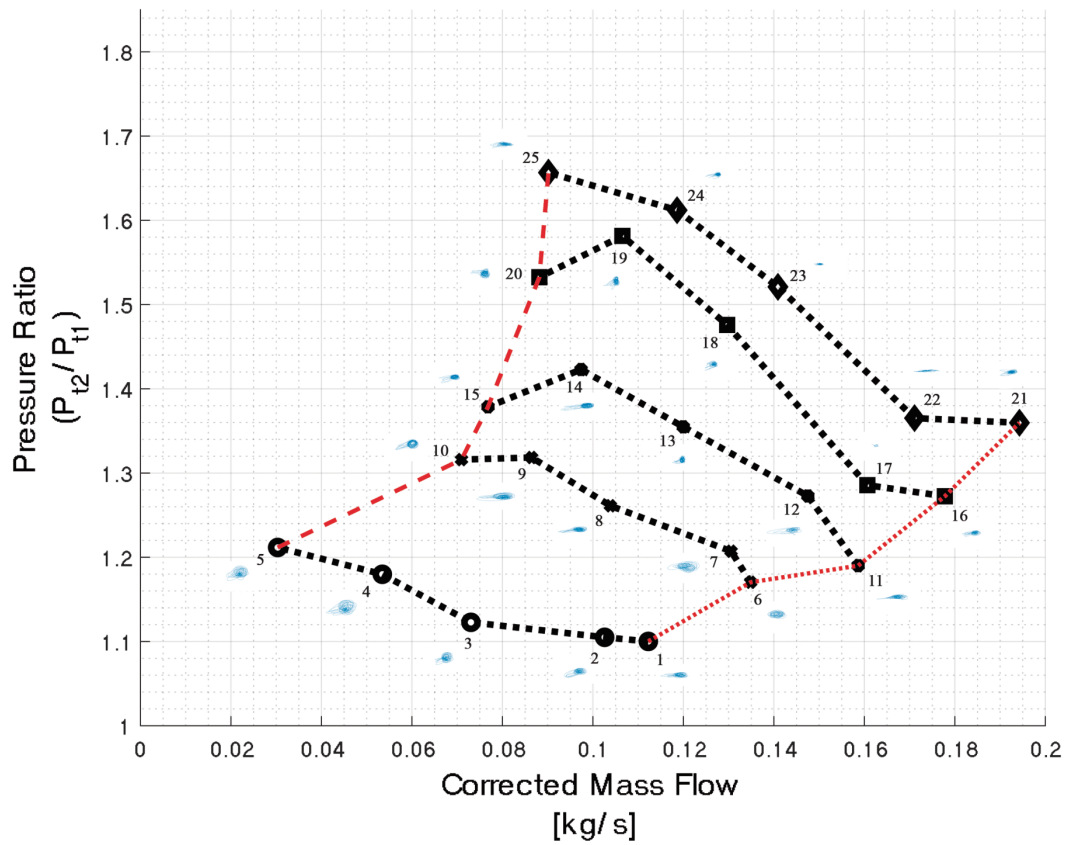
Figure 95 presents the TC3 rotor orbits supported on bearings with quarter-ellipse axial grooves.

TC3 presents low orbit motion in all operation conditions and because of this, it is not possible to see phase change characteristics due to passing through critical speeds or aerodynamic effects. It is possible to observe orbits of smaller amplitudes with the increase of the TC rotor speed.

Figure 96 shows the TC4 rotor orbits supported on bearings with inverted quarter-ellipse axial grooves tested at five speed lines and five valve openings.

For speed line 1, the susceptibility of unstable rotor motions can cause the solid contact between the shaft and the probe. The quarter ellipse groove can be thought as a local pressure dam that helps to retain the thin fluid film on bearing lands. The inverted quarter ellipse groove seems to be an inverted pressure dam, that would make difficult for the fluid to stay in the groove. Thus, it would be expected to observe a smaller capability of attenuating the rotor whirling motion in bearings with inverted quarter ellipse grooves.

Practically in all orbits depicted in Figure 96 it has been observed some rotor motion in direction to the bearing surface. For speed lines 2, 3, 4, and 5, it can be observed some lines departing from the elliptical orbital, which can be called orbit “escapes”, indicating an increasing amplitude of the whirling motion. This behavior indicates the occurrence of light shaft rub on the TC 4 rotor (Figure 97).



Speed Lines

Outlet Compressor Valve Closing - V.C.

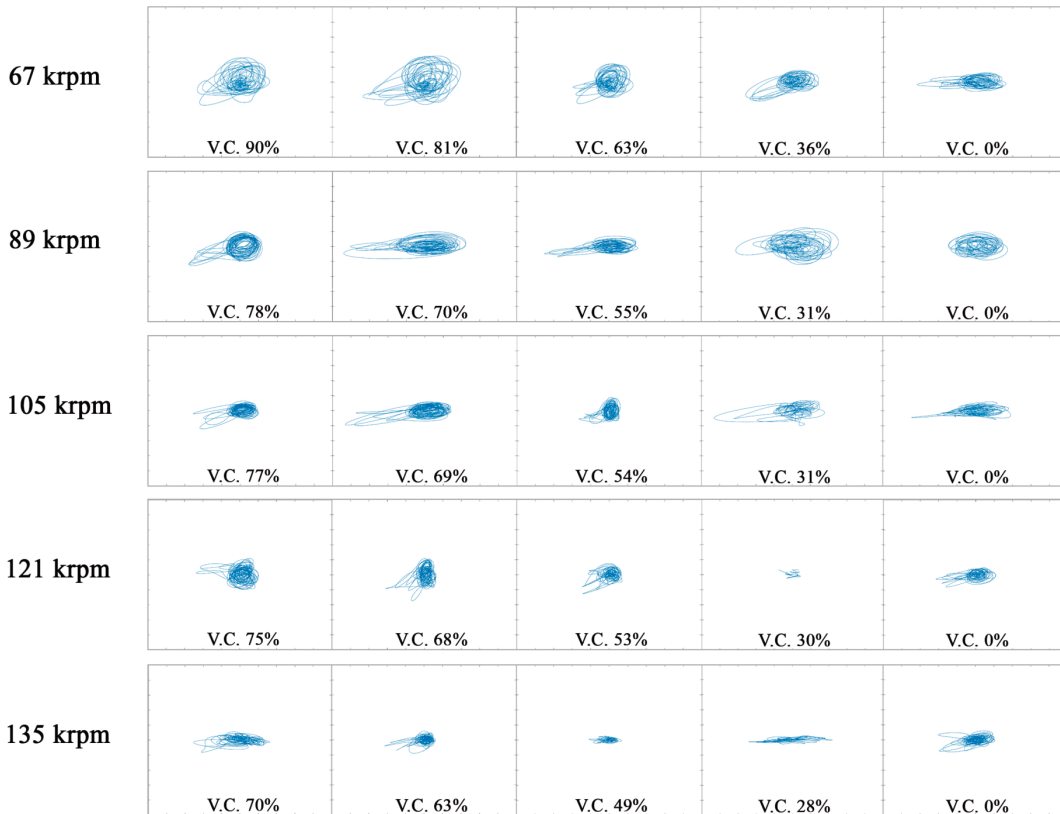
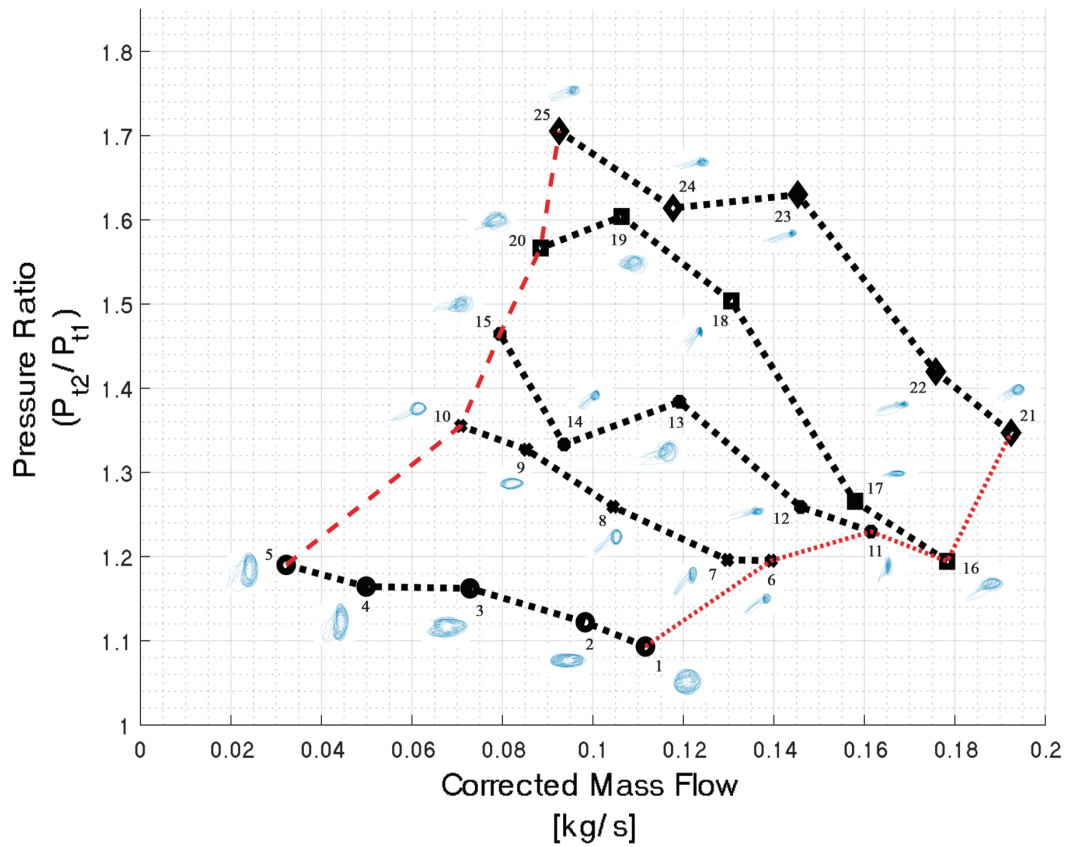


Figure 95 – Rotor orbits of the TC3 supported on bearings with quarter-ellipse axial grooves and indication of the measurement points on the efficiency map.



Speed Lines

Outlet Compressor Valve Closing - V.C.

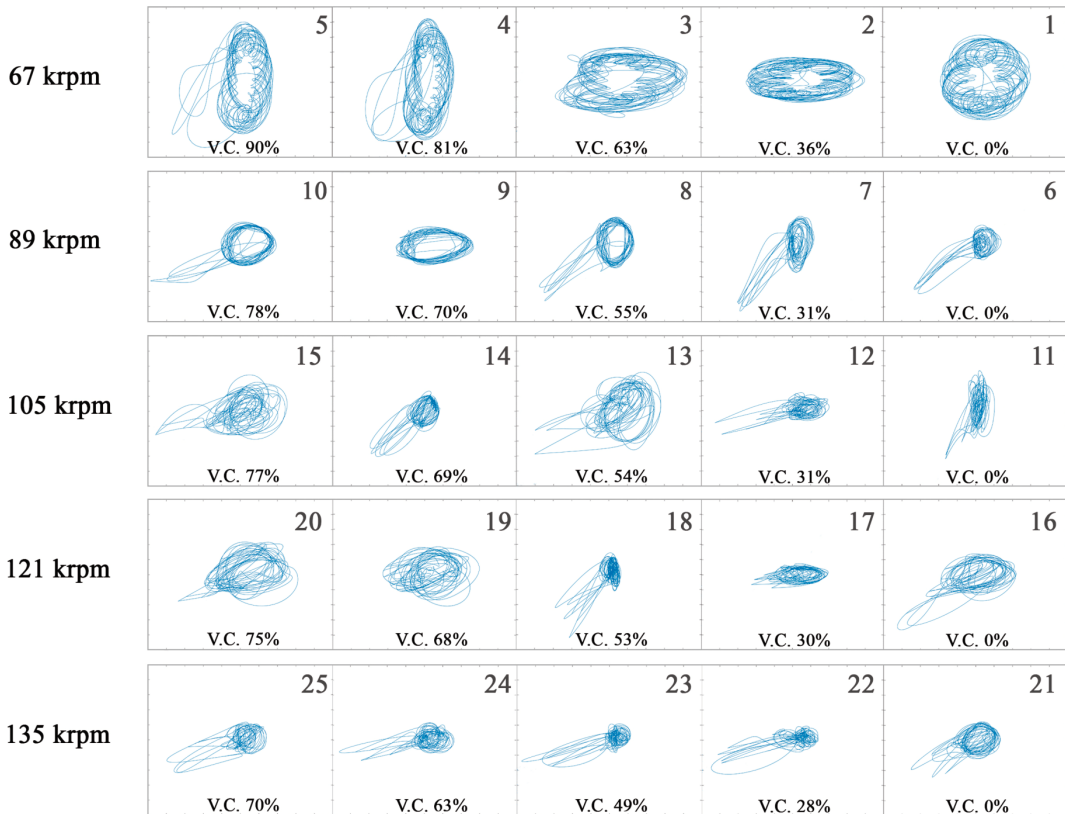


Figure 96 – Rotor orbits of the TC4 supported on bearings with inverted-quarter-ellipse axial grooves and indication of the measurement points on the efficiency map.

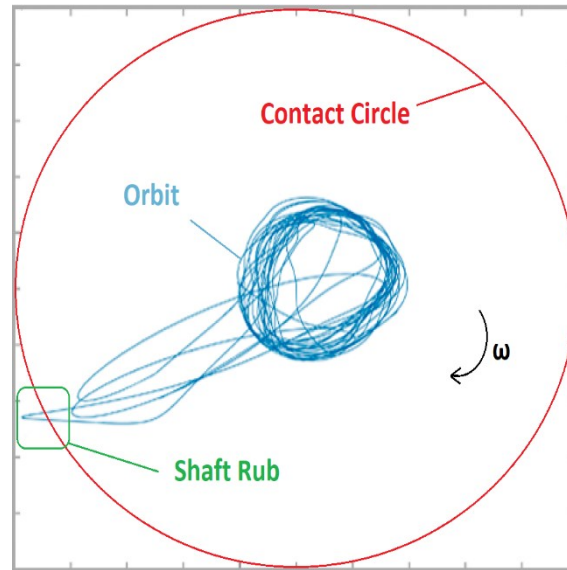


Figure 97 – Orbit of the TC 4 rotor for speed line 2 with 78% of valve closing indicating the occurrence of light shaft rub condition

In the analysis of each speed line, at speed line 1 it occurs the largest orbit among all speed lines of this TC. It is important to note two interesting points: (i) the orbit starts with the valve wide open and it is predominantly circular. As the air flow decreases (valve closing), the orbit becomes elliptical with maximum horizontal deflection, until between phase 2 and 3 of valve closing (in speed line 1, 53% and 81% respectively) that a 90° offset orbit phase shift is observed. In this phase change, there are even more orbit "escapes" than before; in addition (ii) the effect of the inner and outer oil whirls presented by Nguyen-Schäfer (2015) is observed in the five orbits. In the first three orbits, what Nguyen-Schäfer calls limit cycle, which is a stabilized orbit of the rotor within that rotational range, without any escape from the orbit. This condition is confirmed by observing Table 33 which presents the TC4 as the first to have subsynchronous vibrations at speed line 1, as well in Figures 130 and 131 of the Appendix C that show the frequencies of these vibrations is 0.25x, also as described by Nguyen-Schäfer inner oil whirl feature. Figure 98 presents a zoom of 0.25x subsynchronous vibration observed.

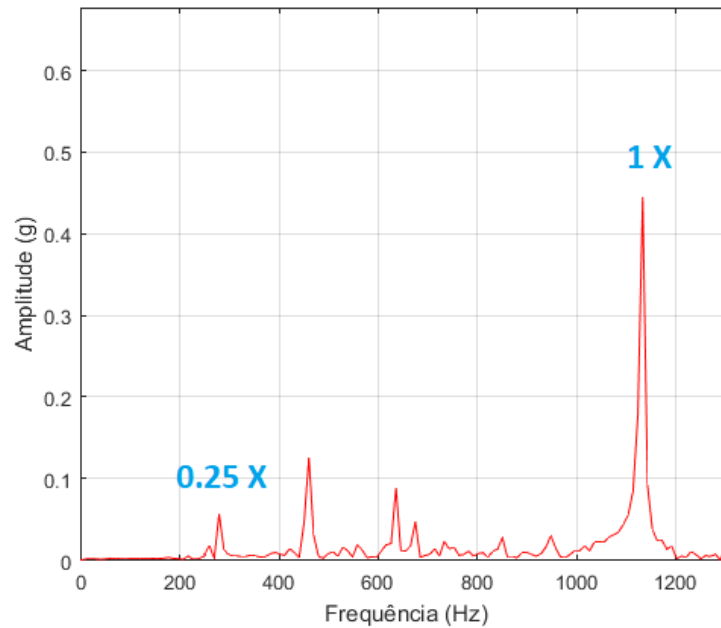


Figure 98 – The inner oil whirl at 0.25 x subsynchronous vibration at TC4 in speed line 1

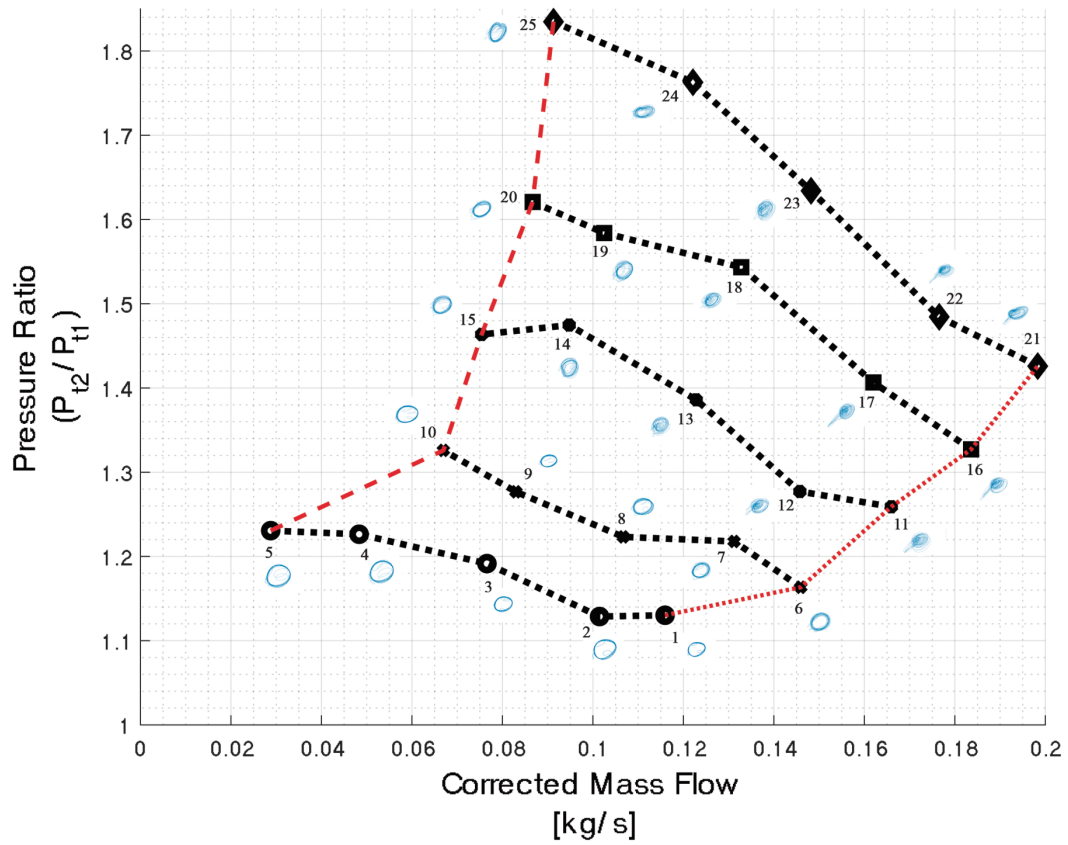
At speed line 2 (near the 1st critical speed) smaller amplitudes are observed in the five orbits and stable orbits in #8, #9 and #10. With the valve fully open, the orbit has a circular shape that, like the speed line 1, becomes elliptical when the valve closes and also between phase 2 and 3 of valve closing (in this speed line, between 55% and 70%) occurs the 90° orbit phase change. The difference is that, while on speed line 1 the ellipse starts with larger deflection horizontally and changes at the end to vertical, on speed line 2 it is the opposite.

After the first critical speed, at the speed line 3 it is observed that all orbits do not reach a stationary trajectory. Highlight for between the 1st and 2nd closure phase (VC @ 31% and 54%) and after the 3rd to the 4th (VC @ 69% and 77%) that have low amplitude orbits and, in the change, present orbits of large amplitude and more unstable than the previous ones.

At speed line 4, there are results similar to those at speed line 3, showing a strong influence between the 1st and 2nd critical speeds with orbits without a stationary trajectory. Only phase 2 (V.C @ 53%) has a small amplitude, but it is not stationary either.

Finally, at the speed line 5, it is observed the best response among all other speeds, with smaller amplitude in all valve closure phases.

As shown in Figure 99, the TC 5 rotor supported on bearings with rectangular grooves presents practically circular orbits with large and constant amplitudes at all speed lines and valve opening conditions, varying between stationary and non-stationary trajectories.



Speed Lines

Outlet Compressor Valve Closing - V.C.

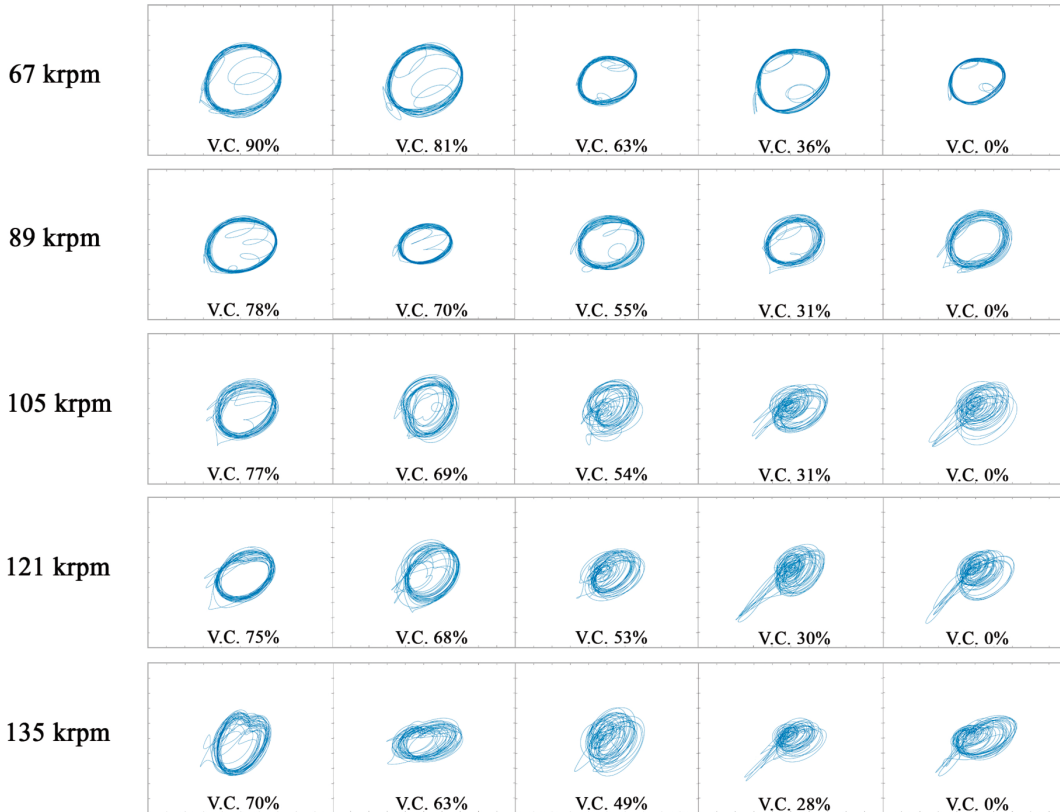


Figure 99 – Rotor orbits of the TC5 supported on bearings with rectangular axial grooves and indication of the measurement points on the efficiency map.

At speed line 1, the TC 5 rotor seems to present more stationary orbits.

On the speed line 2, however, a trend towards larger stability can be seen with a decrease in the air flow (increased valve closure).

After the first critical speed (speed line 3), it is possible to observe the same trend towards larger stability with increasing valve closure, but the orbits are shown to be non-stationary, except well before the surge, in phase 4, ie, VC @ 77 %. This condition holds for speed lines 4 and 5 (with V.C. @ 75% and 70%).

It is important to emphasize that all these non-stationary orbits have small inner loop orbits, which indicates the presence of low-medium amplitude subsynchronous vibrations, results presented on Table 34

The large amplitude of the rotor whirling motion is associated with the rotor synchronous response, but this motion does not put in risk the system integrity in most cases, also confirmed in Table 32.

Figure 100 presents the TC6 with bearings with trapezoidal axial grooves orbits.

The turbocharger mounted on bearings with trapezoidal groove shape presents orbits that indicate the presence of unstable rotor motions, as shown in Figure 100.

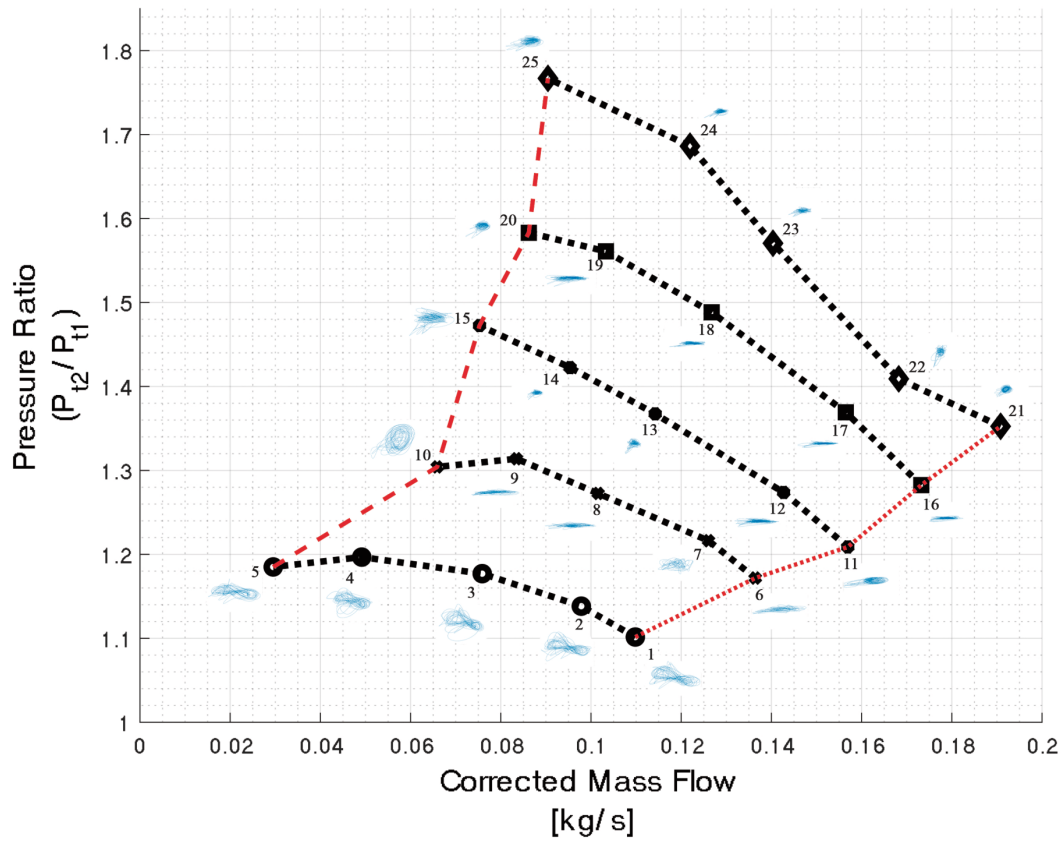
At speed line 1, it can be noticed the unstable subsynchronous motions for all air flow conditions. The orbit shape in form of eight is usual in rotating shafts subjected to half-frequency instability associated with the hydrodynamic action of the fluid film. At supercritical conditions, the half-frequency instability is caused by the incapability of the fluid film to provide enough damping to attenuate the whirling motion. For the TC 6, the orbit with the “lying eight shape” indicates that there is a large difference in the fluid film reaction force components in the horizontal and vertical directions. At unstable conditions, the rotor whirling motion experiences forward and backward loops.

In speed line 2 two distinct features are presented. In phases 1 and 4 (V.C. @ 31% and 78%), the orbits are totally unstable, including shaft rub in phase 4 (orbit #10). In the other phases (0, 2 and 3), the orbits are non-stationary, but inside the contact circle, without shaft rub, with an elliptical shape with the largest deflection ratio between horizontal/vertical axes of all TCs.

The speed line 3 shows elliptical orbits with maximum horizontal deflection in phases 0 and 1, and more circular and smaller amplitude orbit in phases 2 and 3. Finally, again totally unstable orbit in the last phase of valve closure (#15).

In speed line 4 elliptical orbits with high horizontal deflection and very low vertical deflection are again observed in all orbits, except for the last (#20), which has a small circular orbit.

Close to the second critical speed, the orbits in speed line 5 have smaller diameters compared to those observed at the other speed lines, but the subsynchronous orbital motions are still present.



Speed Lines

Outlet Compressor Valve Closing - V.C.

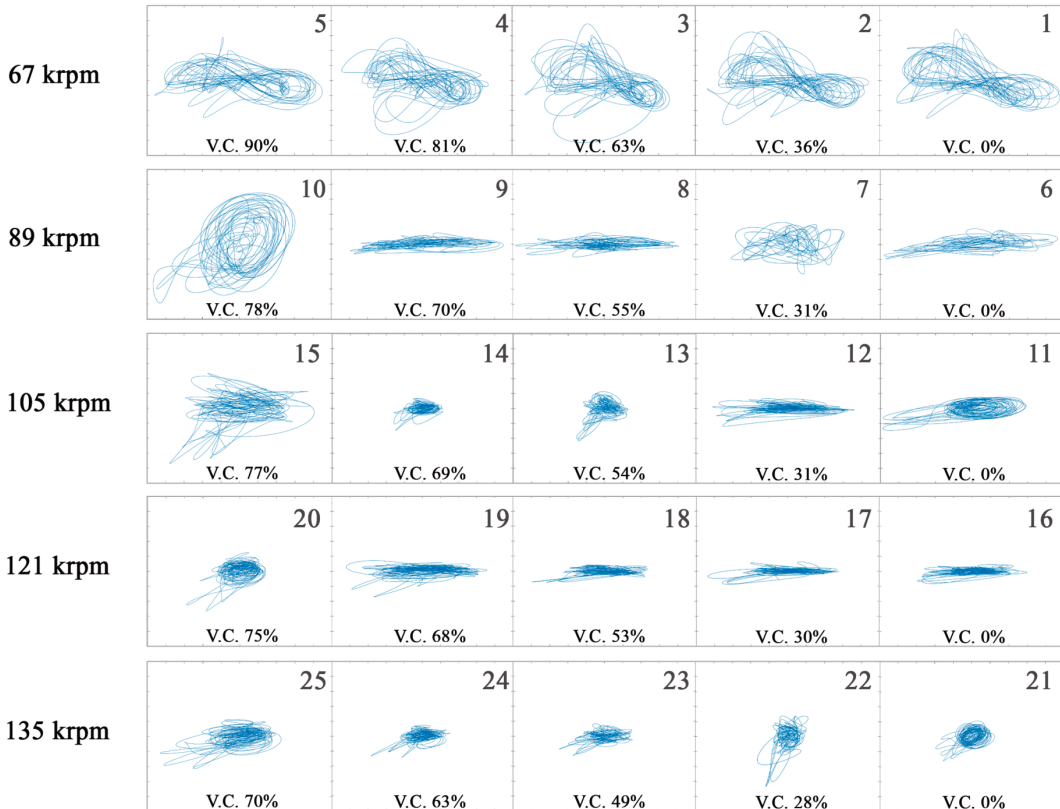
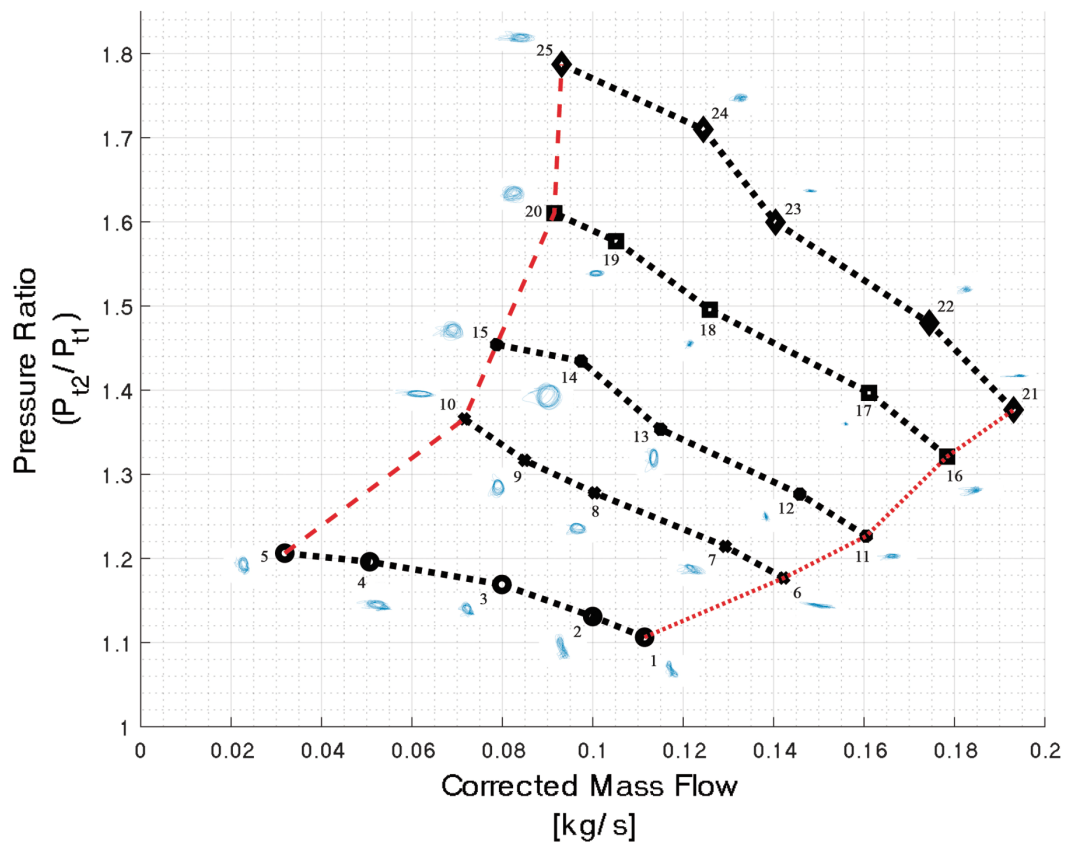


Figure 100 – Rotor orbits of the TC6 supported on bearings with trapezoidal axial grooves and indication of the measurement points on the efficiency map.



Speed Lines

Outlet Compressor Valve Closing - V.C.

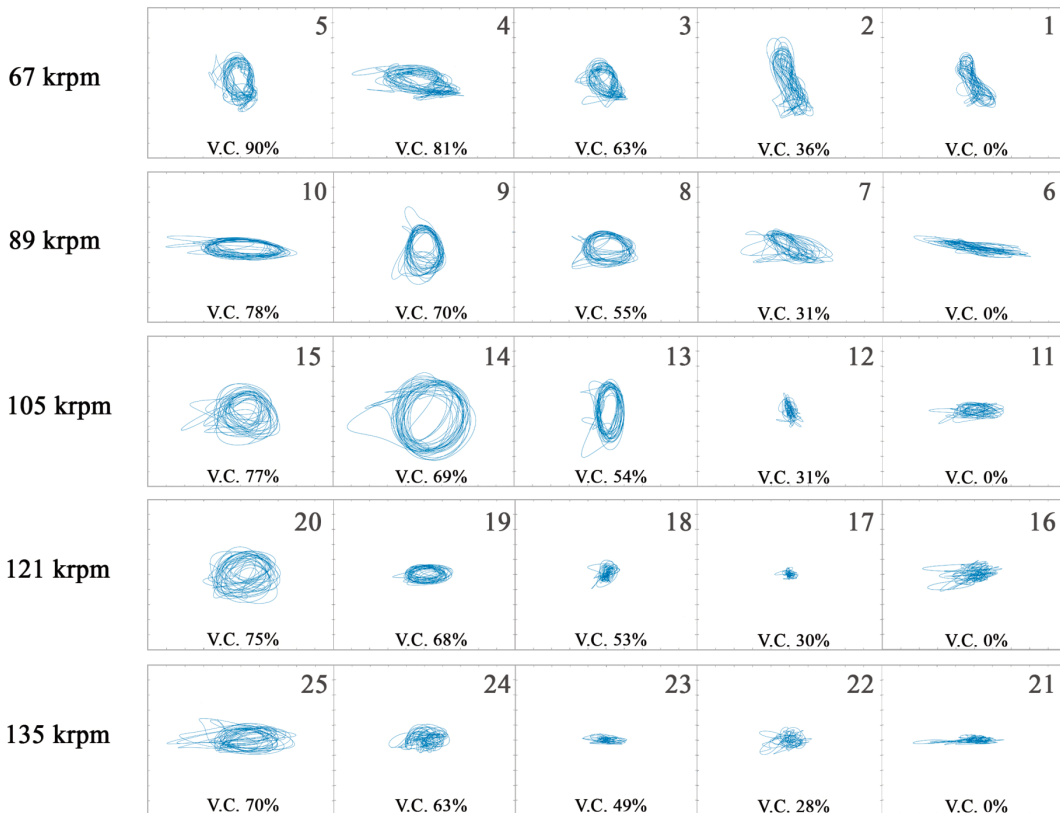


Figure 101 – Rotor orbits of the TC7 supported on bearings with half-moon axial grooves and indication of the measurement points on the efficiency map.

Finally, the whirling motions of the TC 7 rotor, which is supported on bearings with half-circle groove shapes, are presented.

The first two orbits with high air flow (#1 and #2) have the same lying eight shape described in the speed line 1 of the TC 6. The difference is that in these orbits the greatest deflection is in the vertical axis. Orbit #3 has a more circular shape, while #4 is more elliptical, and orbit #5 is similar to the previous one, but with 90° out of phase. Orbits #3, #4, and #5 have outer loops, indicating the strong presence of a backward whirl (confirmed in Table 34).

Orbit shapes and directions have significant variations on speed line 2, but all remain unstable. Starting at orbit #6 with an ellipse with high horizontal deflection, moving to an ellipse more inclined at 45° and smaller in size at orbit #7, until reaching a circle in orbit #8. When further valve closure occurs, there is a 90° phase shift (orbit #9) and again a second 90° shift in the final orbit #10.

At speed line 3, it is observed small amplitudes in orbits #11 and #12, which increase in elliptical shape (orbit #13) and then a circular shape (orbit #14), then reducing the amplitude in orbit #15.

Similar to the previous one, at speed line 4 it is also observed small amplitudes at conditions of large valve openings, (orbits #16, #17 and #18), with an increase in #19 (elliptical shape) and #20 (circular shape).

Finally, at speed line 5 the orbits basically present the same behavior observed in speed line 4: first three orbits with small amplitudes, orbit #24 with magnification and a little higher in the last orbit, the orbit #25.

Orbit response rank

Specifically for the orbits analysis, the number of events for each TC can be evaluated as listed below:

- Contact circle: orbit with successive contacts in the limiting circle to consider as shaft rub;
- Orbit escapes: orbit with successive escapes from the original orbit (limit cycle), showing high instability. Considered successive 0.0225 mm escape or more;
- Large orbital vibration amplitude: any orbital vibration amplitude exceeding 0.0225 mm, regardless of the orbit shape (consequence of synchronous response);

- Frequent occurrence of inner and/or outer loops in the orbit: indicative of subsynchronous vibration formed by backward and/or forward whirls;
- Lying eight shape: half-frequency whirl, characterized by large discrepancy in the radial components of the fluid film reaction force and with forward and backward loops.

These events are considered as weight 1, in each of the 25 orbits for each TC. The greater the number of these events observed, the worse the final rank. The results are shown in Table 36, while the scores based on a 5-point Pugh scale matrix are in Table 37 are the rating are based on 25 orbits rendered for the seven TCs. The scores used are shows as follows:

- 2 points for 8 or more events;
- 1 point for 6 or 7 events;
- 0 point for 4 or 5 events;
- 1 point for 2 or 3 events;
- 2 points for 0 or 1 events.

Table 36 – Number of orbit events for each TC

Turbocharger (bearing axial groove shape)	Contact Circle	Orbit escapes	Large orbital vibration amplitude	Inner and/or outer loops	Lying eight shape
TC 1 (triangular)	0	2	3	25	0
TC 2 (half-ellipse)	0	0	1	7	0
TC 3 (quarter-ellipse)	0	5	0	10	0
TC 4 (inverted quarter-ellipse)	9	18	6	25	0
TC 5 (rectangular)	0	5	6	15	0
TC 6 (trapezoidal)	4	13	16	17	5
TC 7 (half-circle)	0	3	4	10	2

Table 37 – Pugh scores based on for orbit response rank for the TCs

Turbocharger (bearing axial groove shape)	Contact Circle	Orbit escapes	Large orbital vibration amplitude	Inner and/or outer loops	Lying eight shape	Final TC orbit score & rank	
TC 1 (triangular)	2	1	1	-2	2	4	2 nd
TC 2 (half-ellipse)	2	2	2	-1	2	7	1 st
TC 3 (quarter- ellipse)	2	0	2	-2	2	4	2 nd
TC 4 (inverted quarter-ellipse)	-2	-2	-1	-2	2	-5	7 th
TC 5 (rectangular)	2	0	-1	-2	2	1	5 th
TC 6 (trapezoidal)	0	2	-2	-2	0	-2	6 th
TC 7 (half-circle)	2	1	0	-2	1	2	4 th

4.2.4. Waterfall Diagrams

The fourth stage of the experimental study of the dynamic behavior of the seven bearings with different groove shapes designed for this work consists of the variable speed vibration tests. Vibration measurements considering the same positions obtained for the steady-state vibration analysis and performed during acceleration and deceleration of the turbocharger rotor.

To obtain the acceleration and deceleration transient condition, the data are obtained after measurements at constant speeds (i.e., with the correct temperature) using only the direct air flow from the plenum, without combustion, due to the limitation of burning due to the high flux variation and the flame-out event, common in tubular combustion chambers and verified.

The cascade diagrams (or waterfalls) show the changes in the vibration frequency spectrum as a function of the machine rotation speed and time, always at normal TC operating temperature. Waterfall graphics are used in the general analysis of the behavior of vibration frequencies as a function of rotational speed. This type of graph, which is obtained during the acceleration or deceleration of the rotating machine, incorporates transient effects of the speed variation in the vibratory response of the rotating assembly and allows for more efficient evaluation of the trends in variation of the vibration amplitude peaks as a function of the rotation speed.

The verification of possible dynamic potential instabilities of the rotating system can be done through cascade diagrams.

In the TC operating speed range, 0 to 135~140 krpm, different frequency spectra are obtained during the rotor acceleration time. Due to the response time between the electronic input of the full opening of the plenum airflow valve and its response (at acceleration), the response curves have an "S" shape and, therefore, the vertical data in waterfalls, i.e., the spectra with stagnant speed during the beginning and the end of the "S" curve, are ignored in the analysis.

In the comparison between the acceleration and deceleration graphs, noise levels in the response are higher in the acceleration in all CTs, most likely due to the influences of the shock wave of the airflow on acceleration (the bench has a maximum mass flow limitation of air in the inlet). In the deceleration graphs, it is possible to observe several rotordynamic behaviors that we seek to present in this work. In this way, the graphics used are all of the deceleration of the turbochargers.

In order to capture the response in 10,000 Hz, the sampling rate of 20,000 Hz of the constant speed measurements is used for the varying speed measurements

The vibration measurements from the accelerometers mounted orthogonally on the turbocharger basically present the same trend for the cascade plots. Therefore, only the results obtained from the accelerometer mounted horizontally are used to render the rotor orbits.

Waterfall color marks

Different colors are employed on the waterfalls presented in this section to improve the clarity of the graphs:

- the blue line represents synchronous response line (1 X RPM);
- the red dashed line marks the beginning of the oil whip (total instability);
- the olive-green arrow depicts the "jump" in the diagram;
- the gray transparent area is the stagnation velocity area. This is where the synchronous vibration becomes constant, ending/breaking the "S" curve, and is not analyzed.
- the curves in light green show the presence of subsynchronous vibration referring to any instability, whether oil whirl or shaft rub;

the orange straight lines serve to indicate the presence of the beginning of the oil whip and its harmonics, showing total oil fluid instability. The orange value marked on each

waterfall is based on the start of the straight line (start of instability), that is, on the intersection with the dashed red line of the oil whip.

The results do not indicate 0.1 X RPM vibration as indicated by Nguyen-Schäfer (2015) and Chandrasekaran *et al.* (2021). It can be explained due the bearings used in this work are SFRBs, i.e., it cannot rotate. Then, the outer oil film of SFRB just acts as a squeeze film damper, not generating outer fluid film for support (and, therefore, no oil whirl).

The “jump” in the subsynchronous response is well explained by Schweizer (2009): a first bifurcation emerged from and an instability induced by the inner oil films (at ~ 0.25 X RPM, where the inner oil films excite the gyroscopic conical forward mode of the rotor) called 1st Subsynchronous (Sub1) to a new bifurcation so-called 2nd Subsynchronous (Sub2): the inner oil films remain unstable, but the rotor jumps from the gyroscopic conical forward mode into the gyroscopic translational forward mode. The presence of this "jump" from Sub1 to Sub2 is also demonstrated by Chandrasekaran *et al.* (2021).

Waterfall results

Figures 102 to 108 present the waterfall obtained during the deceleration (transient response) of the 7 TCs.

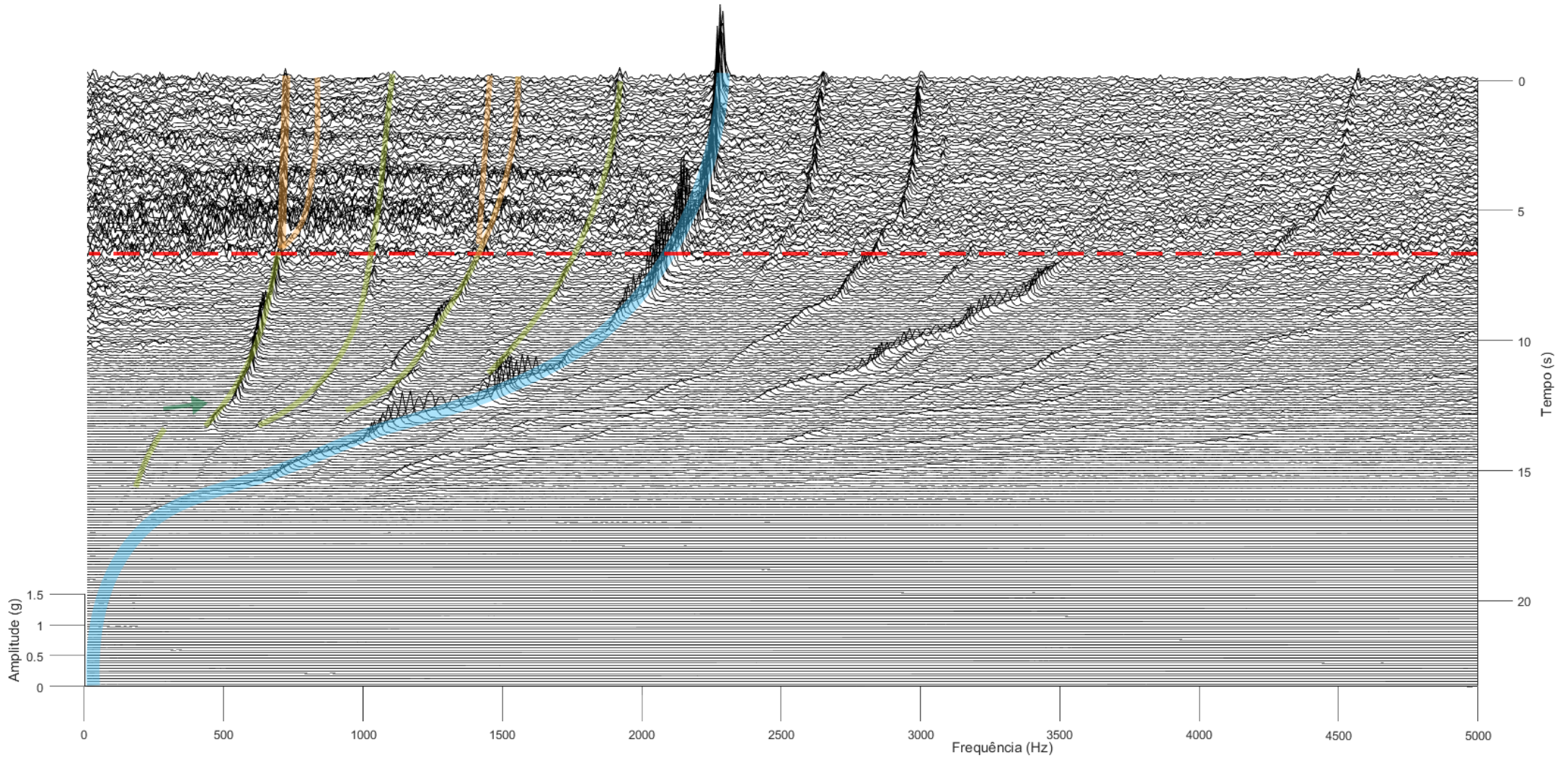


Figure 102 – Cascade diagram of TC 1 mounted with SFRB using triangular axial groove

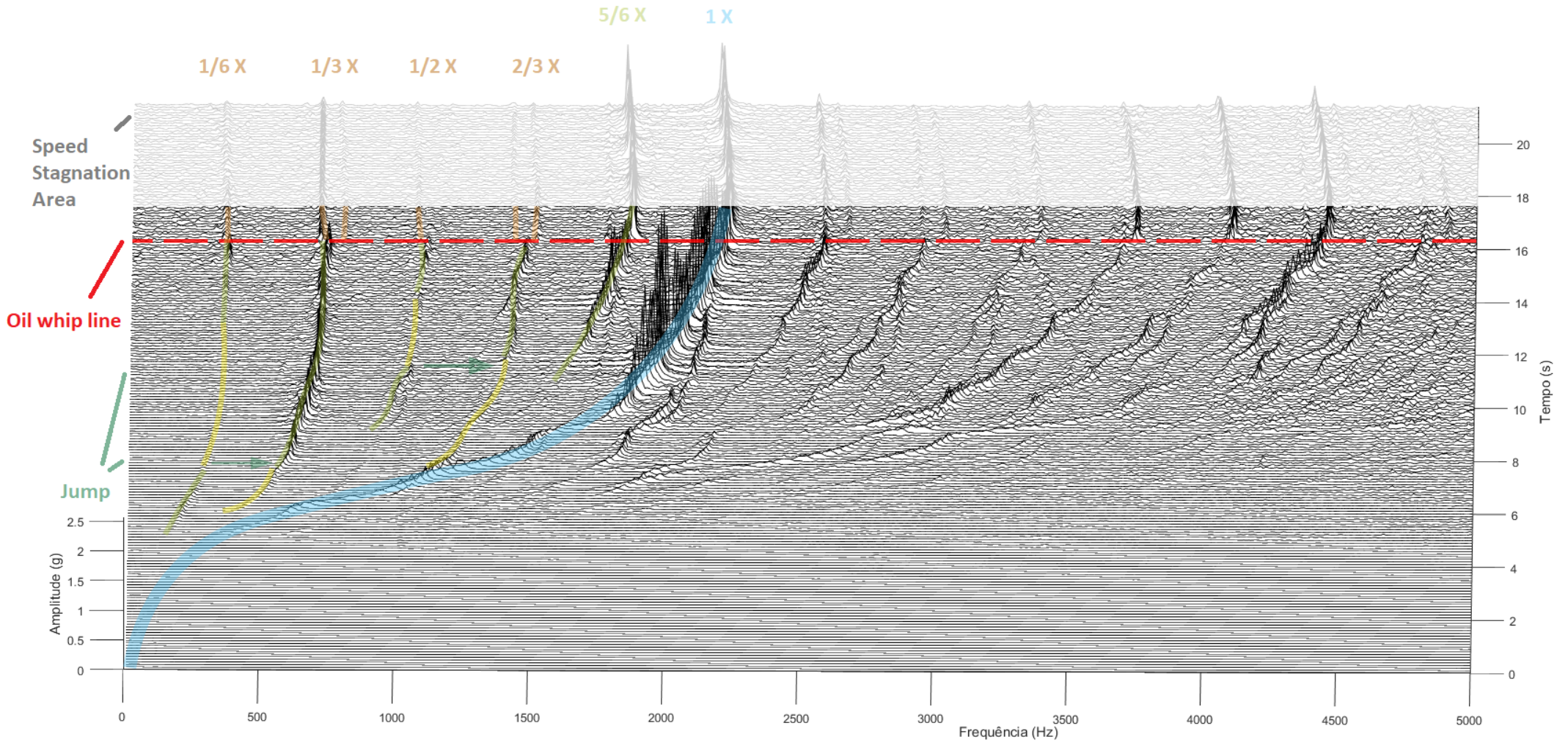


Figure 103 – Cascade diagram of TC 2 mounted with SFRB using half-ellipse axial groove

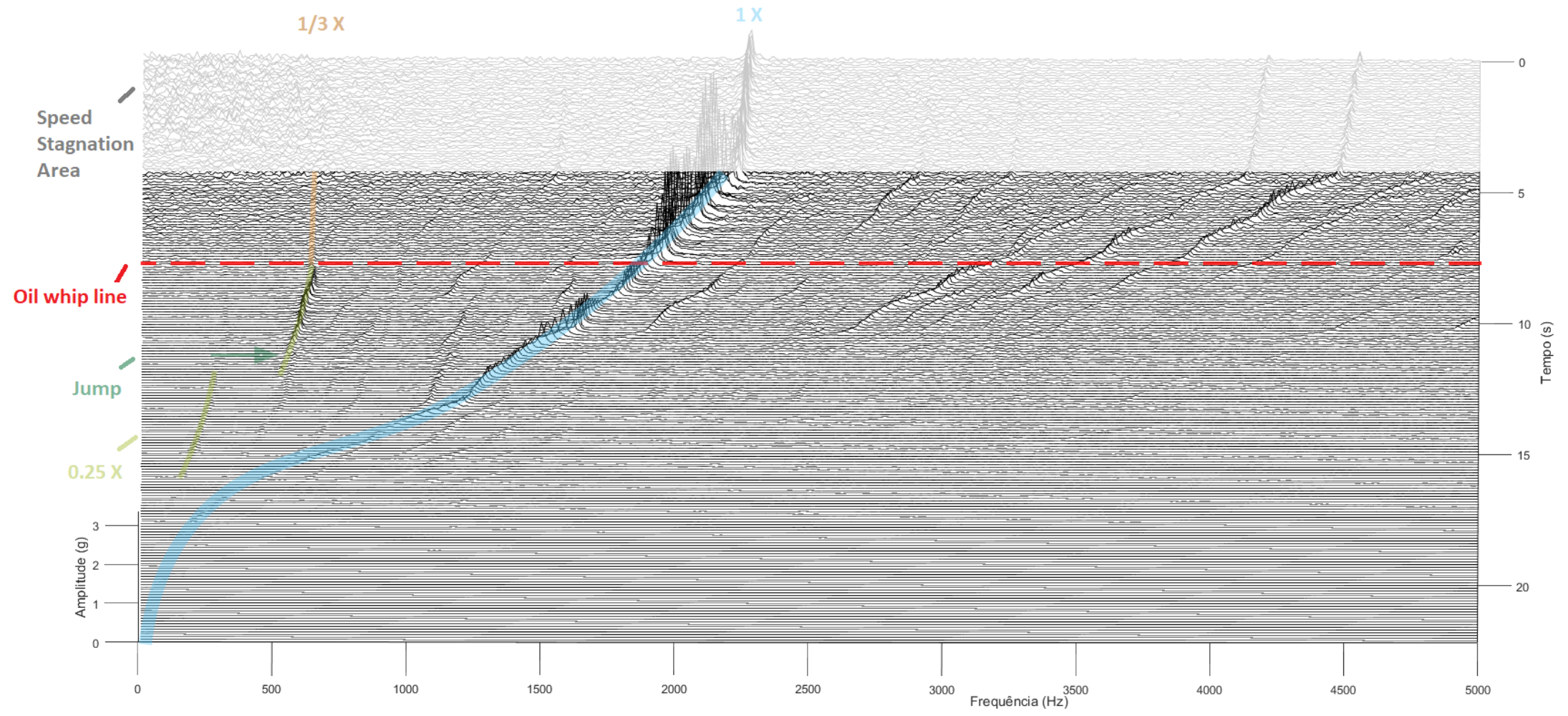


Figure 104 – Cascade diagram of TC 3 mounted with SFRB using quarter-ellipse axial groove

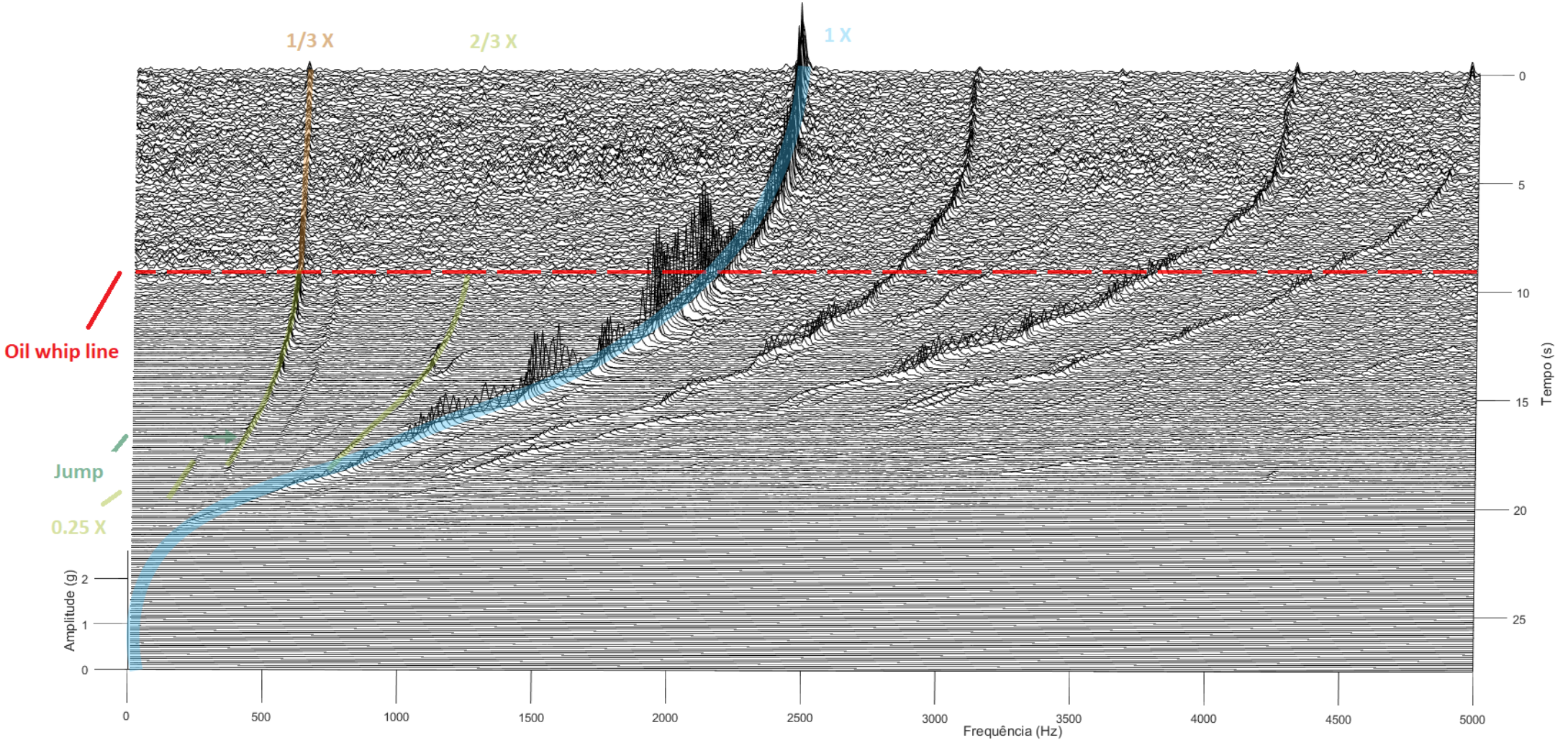


Figure 105 – Cascade diagram of TC 4 mounted with SFRB using inverted quarter-ellipse axial groove

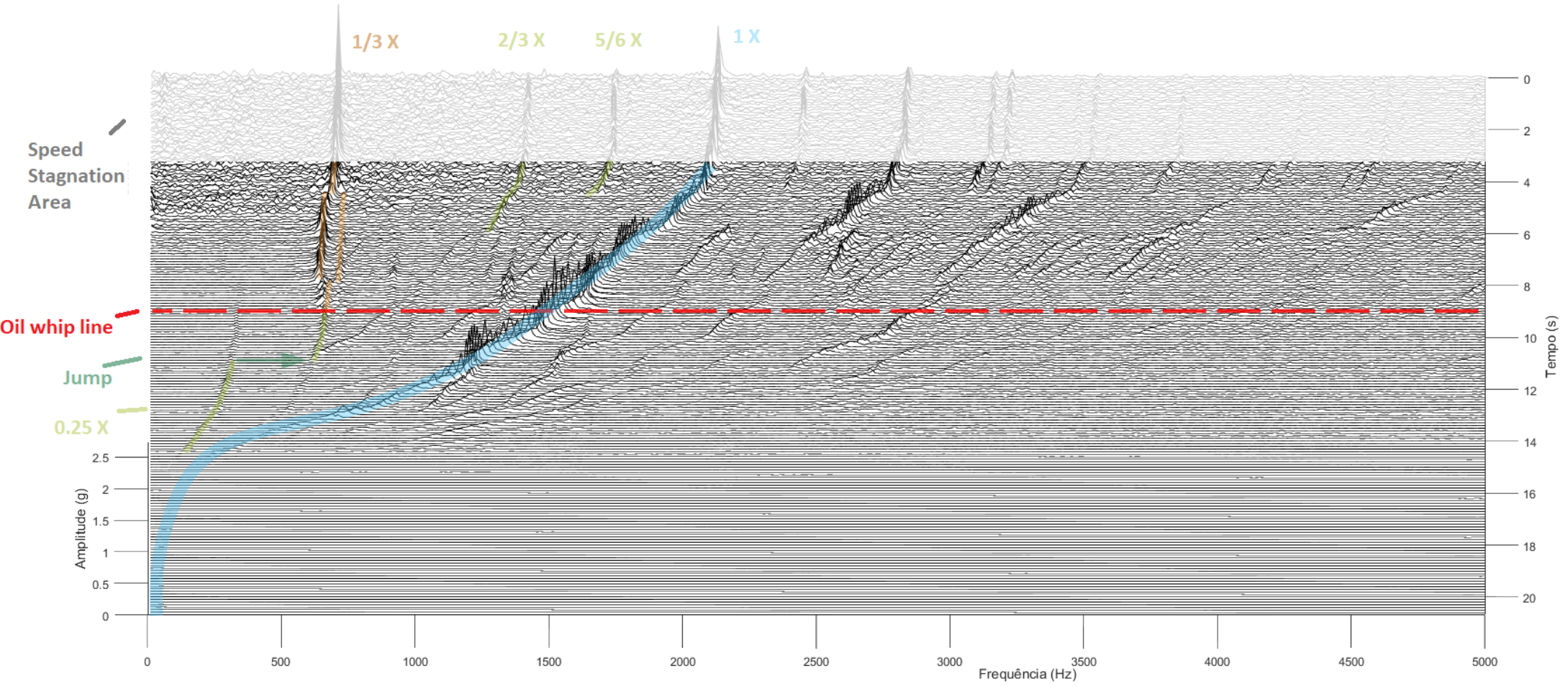


Figure 106 – Cascade diagram of TC 5 mounted with SFRB using rectangular axial groove

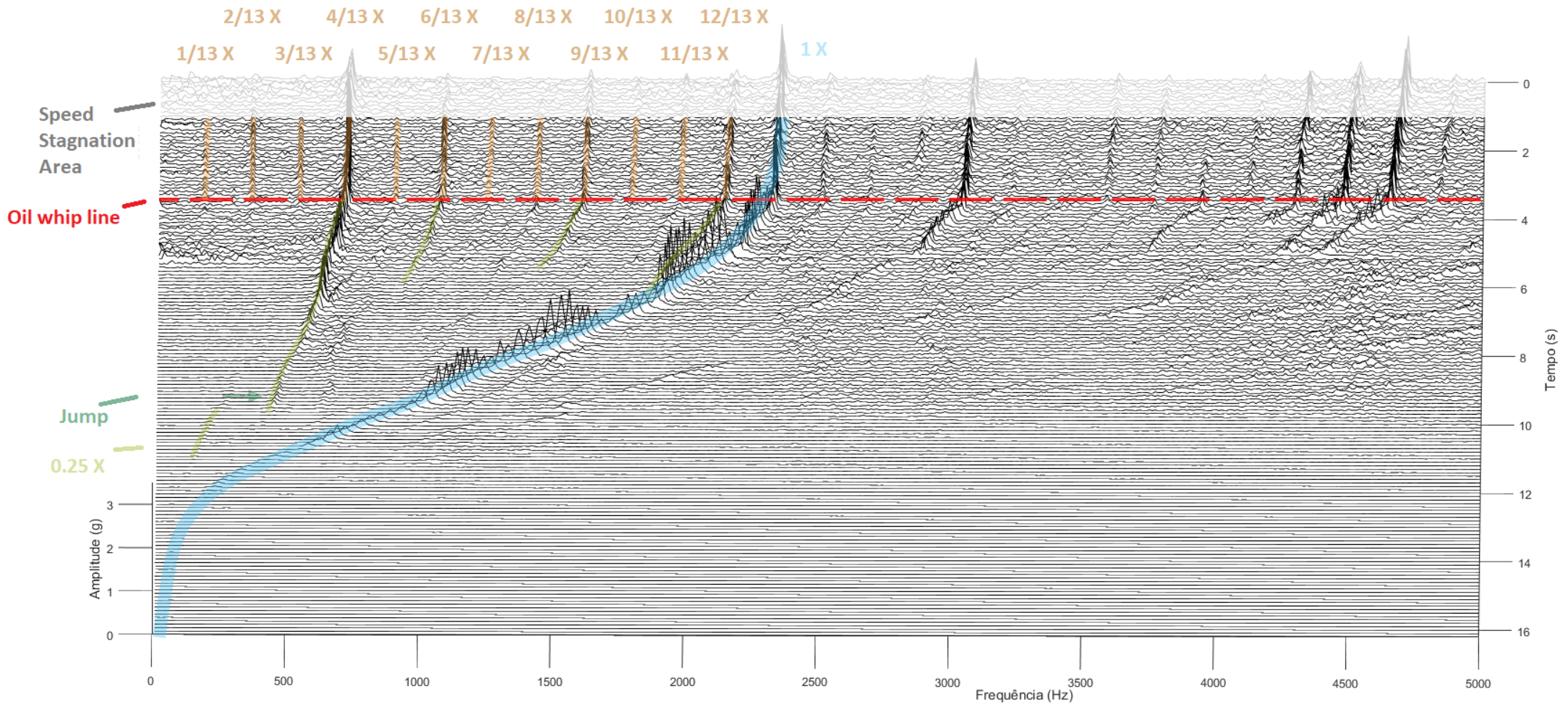


Figure 107 – Cascade diagram of TC 6 mounted with SFRB using trapezoidal axial groove

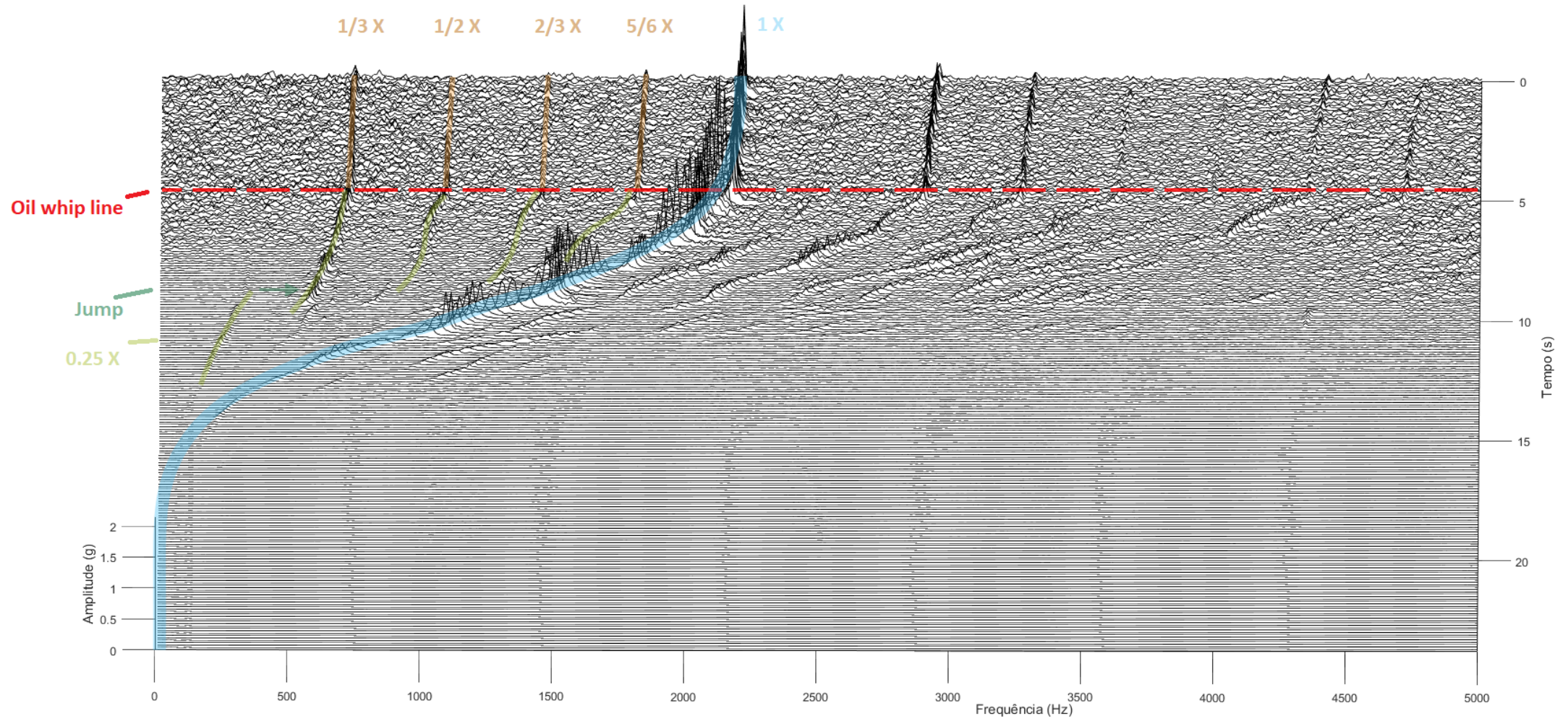


Figure 108 – Cascade diagram of TC 7 mounted with SFRB using circular axial groove

Figure 102 presents the transient response for the TC 1. It is possible to observe that Sub1 starts around 0.25 X RPM and, with the approach to the 1st critical speed, there is a "jump" for Sub2, as well as the appearance of other subsynchronous vibrations. These subsynchronous present six well-defined partitions in this TC, which means that there are six revolutions of the rotor in one orbit cycle (Nguyen-Schäfer, 2015). Only the 1st subsynchronous (1/6 X) has a very low value and is not shown in the graph.

At the beginning of the 2nd critical speed, the beginning of total instability in the system is verified (red dashed line) at approximately 2,100 Hz with oil whip presented at 1/3 X and 2/3 X RPM. Perge *et al.* (2018) present numerical and experimental results of a turbocharger and bearings with geometric properties close to the one used in this work, indicating that the 1/3 X subsynchronous vibration in these bearings is also observed.

The two subsynchronous after the oil whip line at 1/3X and 2/3X is explained by Gooding *et al.* (2020) due the reduced damping that allows Alford-type aerodynamic cross-coupling instabilities. The Figure 93 confirms by the orbit analysis the influence of Alford's force on TC 1.

TC 2 is shown in Figure 103 with similar characteristics to TC 1, such as the "jump" from Sub1 to Sub2 at the 1st critical speed, as well as six well-defined subsynchronous partitions. Again, there is an oil whip start range, but now from approximately 2,250 Hz (oil whip line).

In TC2 there is an upper area of velocity stagnation which is not analyzed.

TC2 has also a new "jump" Sub1 to Sub 2 at the beginning of the 2nd critical speed. In this case, the values of these new-Sub1 and new-Sub2 are twice those of the previous ones, which means that there is a transition of the instability of the inner oil film in the 2nd conical mode to the 2nd translational mode.

The yellow lines in Figure 103 represent the initial onset or trend of subsynchronous vibrations.

Finally, all subsynchronous in the six parts have oil whip responses after the 2nd critical speed, except for the 5th (5/6).

Another feature is the presence again of a split of the whip in the 1/3 X and 2/3 X bands explained by Gooding *et al.* (2020) due the Alford's force. The Figure 94 confirms also by the orbit analysis the influence on TC 2. Another explanation is given by Fan *et al.* (2011) that indicate that oil whip can cause self-excited reverse shaft whirl rub in mechanical seals, known as "dry whip", which is a secondary phenomenon resulting from a primary cause, that is, coexistence of oil whip and dry whip". Nguyen-Schäfer (2015) describes that

shaft rub (dry whip) could be recognized by the sideband frequencies in the measured waterfall diagram.

Figure 104 shows the TC 3 and presents only an evident condition of subsynchronous vibration with low amplitudes in $1/3 X$. As with the previous ones, there is a jump from $0.25 X$ to $0.33 X$ ($1/3 X$) in the 1st critical speed and a very low oil whip frequency observed at the beginning of the 2nd critical speed. However, the oil whip line starts earlier, around 1,900 Hz.

TC 4 in Figure 105 presents a similar condition to TC 3, except for the additional presence, even if low amplitude, of a $2/3 X$ band (corresponding to what Perge *et al.* (2018) states about these small TCs), as well as the beginning of the oil whip line at approximately 2,150 Hz.

The oil whip line on the TC 5 is the one that starts earlier, at approximately 1,500 Hz as presented in Figure 106. It is possible to observe that there is no considerable reduction in vibrations between the 1st and the 2nd critical speed, which indicates the high level of instability. The Alford's force is also observed in the work of Gooding *et al.* (2020), in which is possible to observe only one subsynchronous at the beginning (between 1,500 and 1,600 Hz) and at the end (2,000 and 2,100 Hz), and two subsynchronous between 1,600 and 2,000 Hz due the reduced damping that allows Alford's force to acting at $1/3 X$. In addition, small subsynchronous vibrations at $2/3X$ and $5/6X$ are observed.

Figure 107 shows a completely different condition for the TC 6, not having six revolutions of the rotor in one orbit cycle (as with all other TCs), but thirteen revolutions. This means that the oil whirl occurs at a frequency of $1/13$ of rotor frequency, i.e., more than twice the occurrence of oil whirl in the same time interval compared to the other six TCs.

This high instability of the fluid film generates in all subharmonics the presence of an oil whip from approximately 2,300 Hz. The same "jump" from Sub1 to Sub2 is observed, however, now from $0.25X$ to approximately $0.31X$ ($4/13X$) at the start of the 1st critical speed, and larger oil whirl amplitudes at $4/13X$, $6/13X$, $9/13X$ and $12/13X$ after the start of the 2nd critical speed.

Finally, Figure 108 indicates the TC 7 waterfall, with many similarities to TC 1, even at the beginning of the oil whip line (at 2,100 Hz), except after this line, where all identified subsynchronous ($1/3 X$, $1/2 X$, $2/3X$ and $5/6X$) feature oil whip.

Orbit response rank

In the analysis of the waterfall the following events are observed:

- Number of revolutions of the rotor in one orbit cycle: Number of subsynchronous frequencies presented;
- Start of the oil whip line: Speed at which the oil whip starts;
- Significant Oil Whirl Amplitudes: Regardless of the number of revolutions, subsynchronous "tracks" that have visible amplitudes (in this case, 10 continuous measurements above 0.1 g);
- Number of oil whips presented: Times the oil whirl turned into an oil whip and presence of its harmonics;
- Presence of side bands: Oil whip and dry whip together

All of these are considered as weight 1 of each TC. The greater the number of these events detected, the worse the final rank.

Table 38 – Number of orbit events for each TC

Turbocharger (bearing axial groove shape)	# of revolutions / cycle	Start of oil whip line	Significant oil whirl amplitude	# of oil whips	Presence of whip side band
TC 1 (triangular)	6	2,100 Hz	4	2	0
TC 2 (half-ellipse)	6	2,250 Hz	6	4	2
TC 3 (quarter-ellipse)	6	1,900 Hz	1	1	0
TC 4 (inverted quarter-ellipse)	6	2,150 Hz	2	1	0
TC 5 (rectangular)	6	1,500 Hz	3	1	1
TC 6 (trapezoidal)	13	2,300 Hz	4	12	0
TC 7 (half-circle)	6	2,100 Hz	4	4	0

The results are shown in Table 38, while the scores based on a 7-point Pugh scale matrix are in Table 39 are the rating are based on each TC waterfall:

- f. -3 points for the worst result
- g. -2 points for the 2nd worst result;
- h. -1 point for the 3rd worst result;
- i. 0 point for average result;
- j. 1 point for 3rd best result;
- k. 2 points for 2nd best result.
- l. 3 points for best result

Table 39 – Pugh scores for waterfall response rank for TCs

Turbocharger (bearing axial groove shape)	# of revolutions	Start of oil whip line	Significant oil whirl amplitude	# of oil whip + harmonics	Presence of oil whip side band	Final TC waterfall score & rank	
TC 1 (triangular)	3	0	0	0	3	6	3 rd
TC 2 (half-ellipse)	3	2	-3	-1	-3	-2	7 th
TC 3 (quarter- ellipse)	3	-2	3	3	3	10	2 nd
TC 4 (inverted quarter-ellipse)	3	1	2	3	3	12	1 st
TC 5 (rectangular)	3	-3	1	3	-2	2	5 th
TC 6 (trapezoidal)	-3	3	0	-3	3	0	6 th
TC 7 (half-circle)	3	0	0	-1	3	5	4 th

4.2.5. Turbocharger rotordynamic rank

A final TD rank is presented in Table 40, considering the constant-speed frequency spectrum, rotor orbit at steady-state condition and the waterfall diagram. A 7-point Pugh score is used, with a 3 to -3 points from 1st to 7th, respectively.

Table 40 – Final RD score & rank

Turbocharger (shape)	Steady-state vibration	Steady-state orbit	Transient vibration	<u>Final RD score & rank</u>	
TC 1 (triangular)	1 st	2 nd	3 rd	6	1 st
TC 2 (half-ellipse)	2 nd	1 st	7 th	2	3 rd
TC 3 (quarter-ellipse)	2 nd	2 nd	2 nd	6	1 st
TC 4 (inverted quarter-ellipse)	5 th	7 th	1 st	-1	4 th
TC 5 (rectangular)	4 th	5 th	5 th	-2	5 th
TC 6 (trapezoidal)	6 th	6 th	6 th	-6	7 th
TC 7 (circle)	7 th	4 th	4 th	-3	6 th

4.3. ACOUSTIC EMISSIONS TESTS

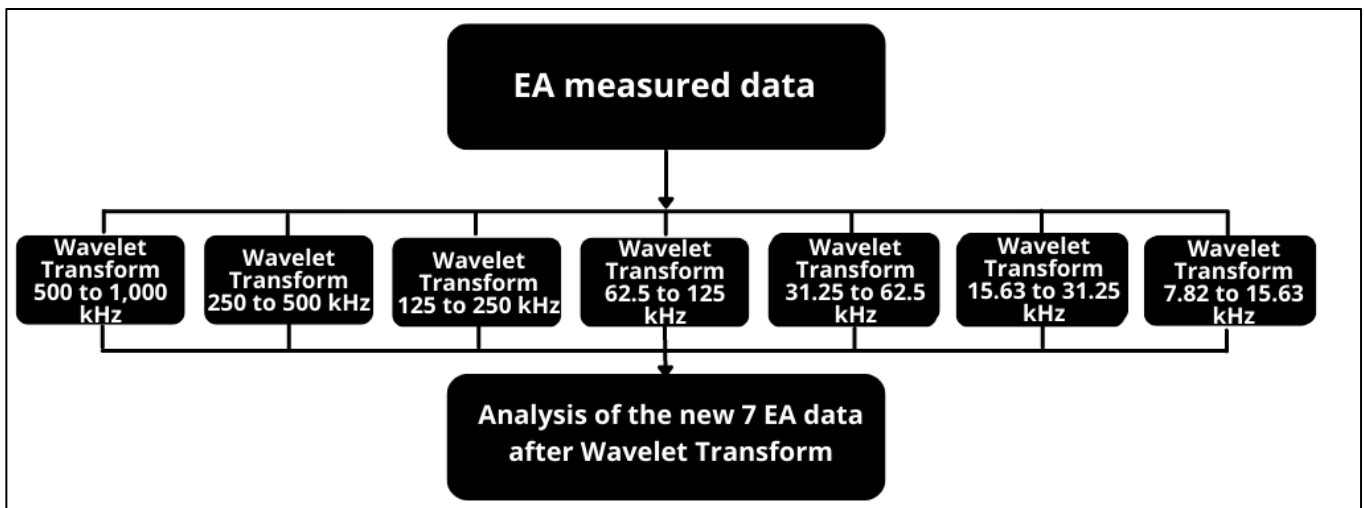
The last part of this work is the acoustic emissions (AE) results during steady-state conditions.

The idea of the AE tests is to evaluate the wave propagation in TCs in order to capture some phenomena related to the fluid-solid interactions. It is expected that the high-frequency AE measurements could be capable of detecting some incipient flow instabilities in the compressor, such as the surge.

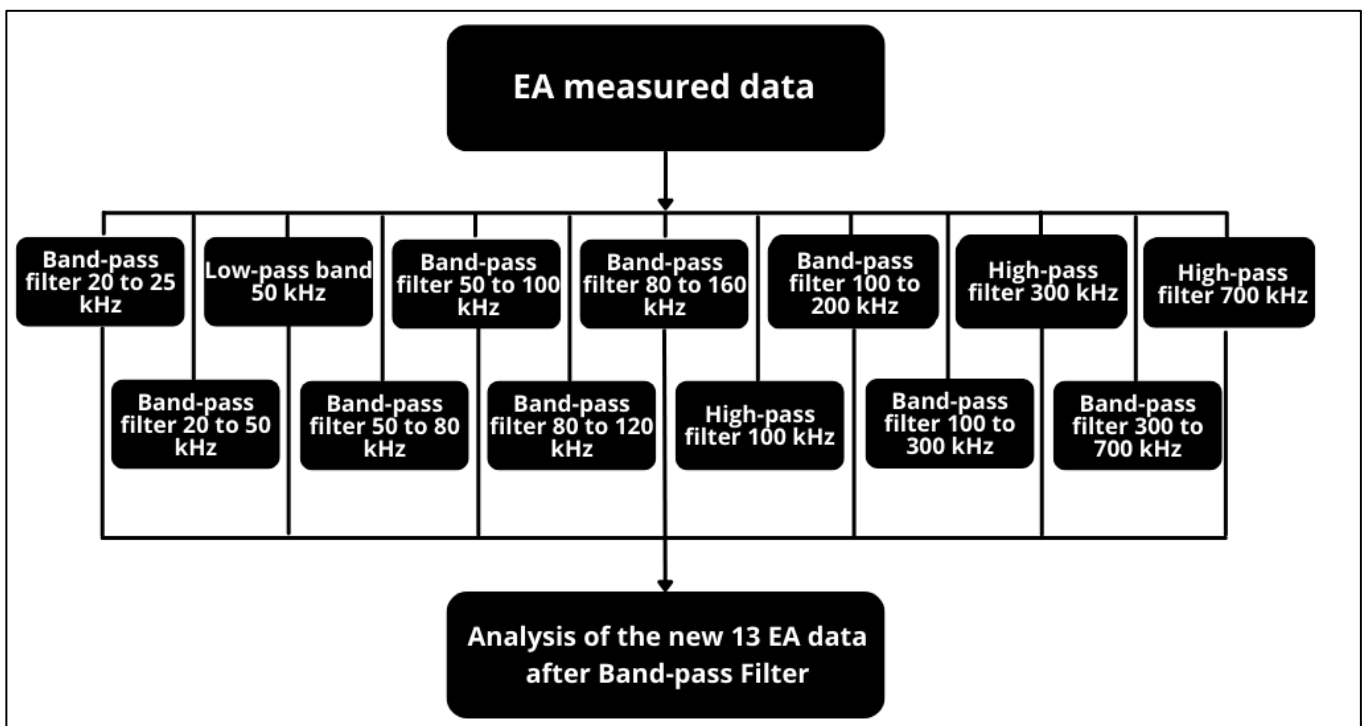
The surge is detected experimentally using variables such as pressure, temperature and acoustic pressure variation. However, these signals have significant variation only at surge start, being late for any action to prevent entrance into this operating regime.

In order to perform the AE tests, the seven turbochargers are monitored at the same speed lines from the previous experiments. The capture of the AE signals is performed at constant speed and the AE data are treated by the procedures presented in Figure 109(a) for Wavelet Transforms and 109(b) for Band-pass Filters.

The Wavelet Transform is based on Faria and Pimentel-Junior (2019). The Band-pass filters are performed based on the works of Mokhtari *et al.* (2020), Hodnett *et al.* (2004), Lee *et al.* (2006), Michlmayr *et al.* (2013), Fritz *et al.* (2001), Sadegh *et al.* (2015), Morgner (1997) and Filippov *et al.* (2017).



(a)



(b)

Figure 109 – EA measured data treated by (a) Wavelet Transform and (b) Band-pass Filter

The new EA data are treated using 20 procedures: (i) Wavelet Transform with 7 levels of the decomposition using Daubechies Wavelet; and (ii) Band-pass Filter with 13 different low-pass, band-pass and high-pass range of frequencies.

For each of the 7 turbochargers, 30 data are obtained (5 closing stages + 1 surge stage for each 5 speed lines analyzed). A total of 4,200 curves are obtained as presented in Figure 110.

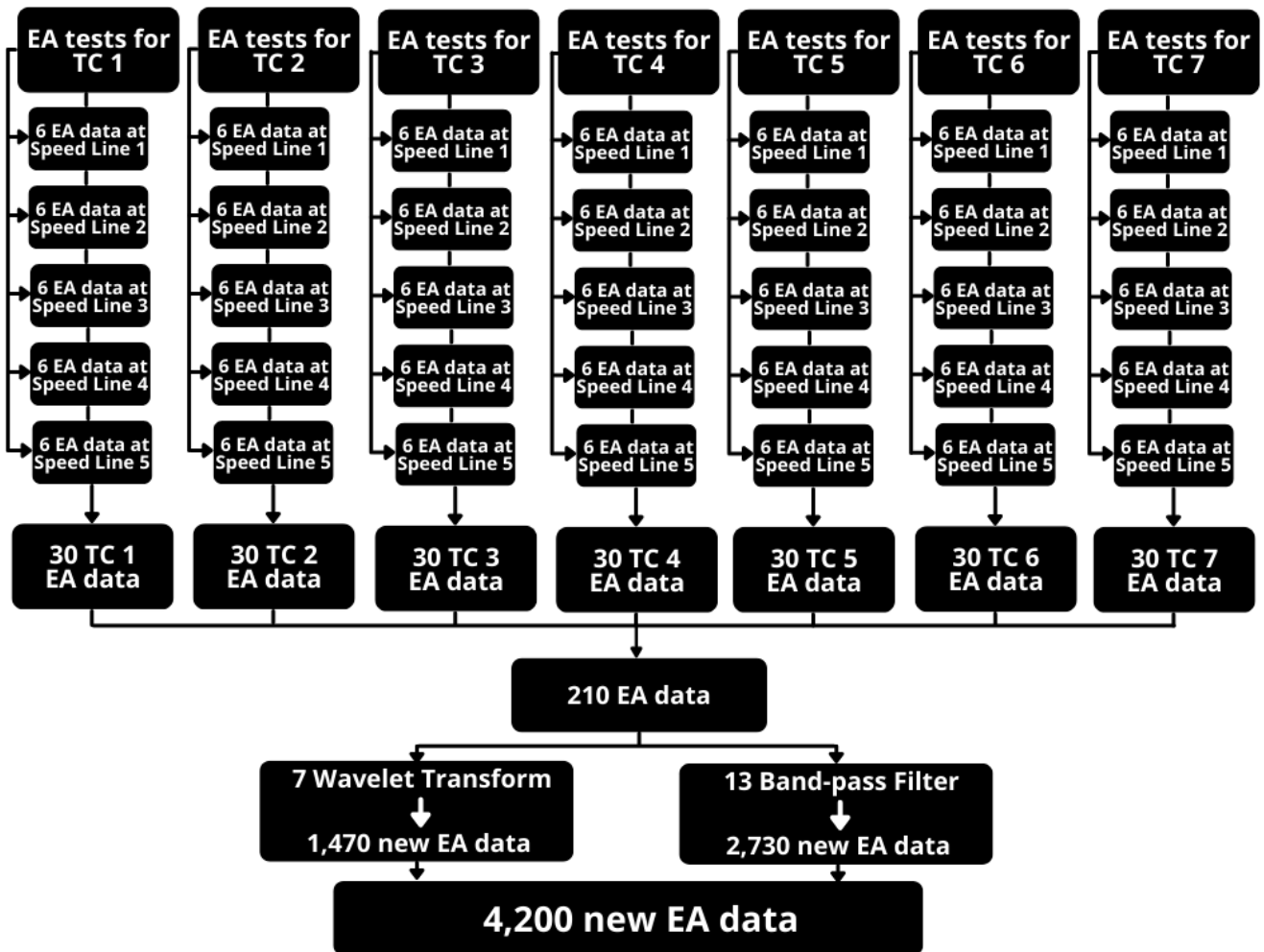


Figure 110 – The 4,200 new EA data obtained from the Wavelet Transforms and Band-pass Filters of 30 measured data from each TC.

Each 4,200 new EA data display 200,000 points captured over a 0.1 second interval, i.e. at a sampling rate of 2 MHz.

For each speed line there are different amounts of points obtained per rotation cycle and different amounts of cycles obtained. Table 41 shows the setups of the AE tests at the five speed lines.

For each speed line, the rotation is divided by 60 to obtain the cycle per second in Hz. The number of points per shaft revolution are obtained by dividing the sampling rate of 2,000,000 Hz by the shaft rotation. For example, for 67 krpm (1,116.7 Hz), there are 1,791 EA values per shaft turn. As the EA measurement is acquired for 0.1 seconds, then 200,000 points are obtained. As indicated in the previous example, for each revolution of 1,791 points, there are 111 complete revolutions to analyze at 67 krpm. It should be noted that only

the complete revolutions of the shaft are analyzed, so the total number of points will be equal to or less than 200,000.

Table 41 – Number of shaft revolutions and points per revolution

Speed line	krpm	Hz	Sample rate (Hz)	Data per revolution	Considered data/rev	Points obtained	Considered rev/file	Total number of points
1	67	1116.7	2,000,000	1,791	1,791	200,000	111	198,801
2	89	1483.3	2,000,000	1,348	1,348	200,000	148	199,504
3	105	1750.0	2,000,000	1,143	1,143	200,000	174	198,882
4	121	2016.7	2,000,000	992	992	200,000	201	199,392
5	135	2250.0	2,000,000	889	889	200,000	224	199,136

Figure 111 shows the windowing example performed for speed line 3, the 105 krpm. At this speed, 174 revolutions are obtained and, for each revolution, 1,143 samples.

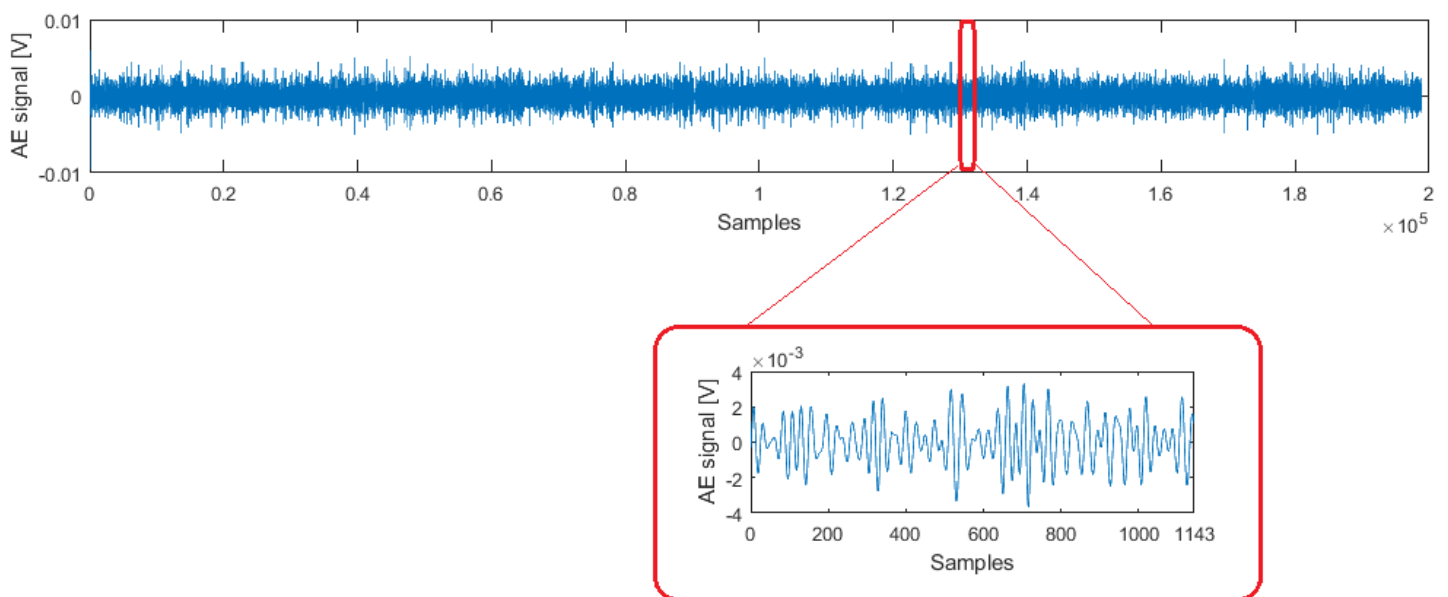


Figure 111 – Windowing of speed line 105 krpm of TC 1 @ 0% V.C.

The threshold (U_t) value used in the analysis is obtained before the turbocharger tests. All equipment on the bench is turned on, as electronic devices, sensors, computer, oil pump, air pump and fuel pump. No start of the combustion chamber are done to start the turbocharger.

For each window, characteristics obtained such as: RMS, Maximum Amplitude (U_{max}), Burst Energy (E) and Counts of Threshold Crossings (C). Figure 112 also presents the data for 1 revolution of the same example as in Figure 110.

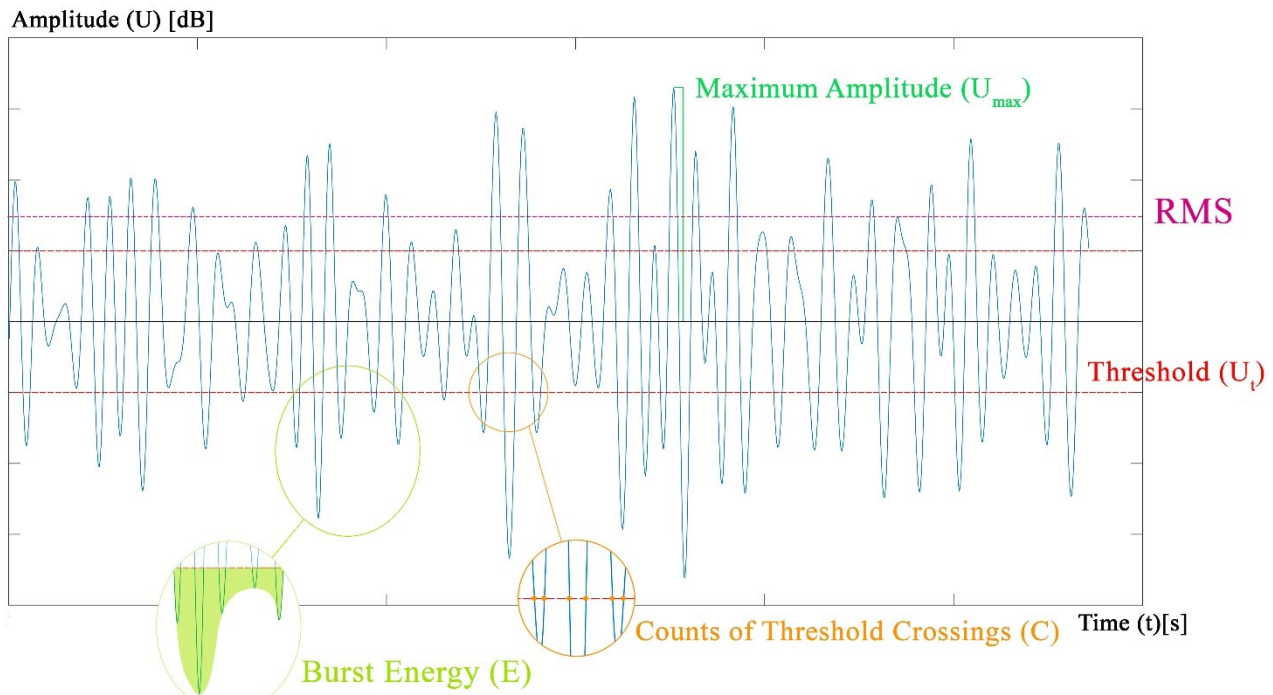


Figure 112 – Information from windowing of speed line 105 krpm of TC 1 @ 0% V.C.

For each of the 4,200 graphs, the following procedures are performed:

1. Windowing for each revolution;
2. For each revolution, 4 characteristics are calculated:
 - 2.1. RMS;
 - 2.2. Maximum Amplitude;
 - 2.3. Count of Threshold Crossings;
 - 2.4. Bust Energy.
3. With the four characteristic obtained for each revolution, 7 statistic functions are obtained for each characteristic, which are:
 - 3.1. RMS;
 - 3.2. Mean;
 - 3.3. Standard deviation
 - 3.4. MAD (median absolute deviation)
 - 3.5. Kurtosis
 - 3.6. Skewness
 - 3.7. Shannon Entropy.
4. For each of the 4,200 EA data treated by Wavelet Transforms and Band-pass Filters, 28 values of each characteristic are obtained, presenting a population of 117,600 points.

Figure 113 presents all the steps to obtain the statistic functions from each characteristic of each treated EA data.

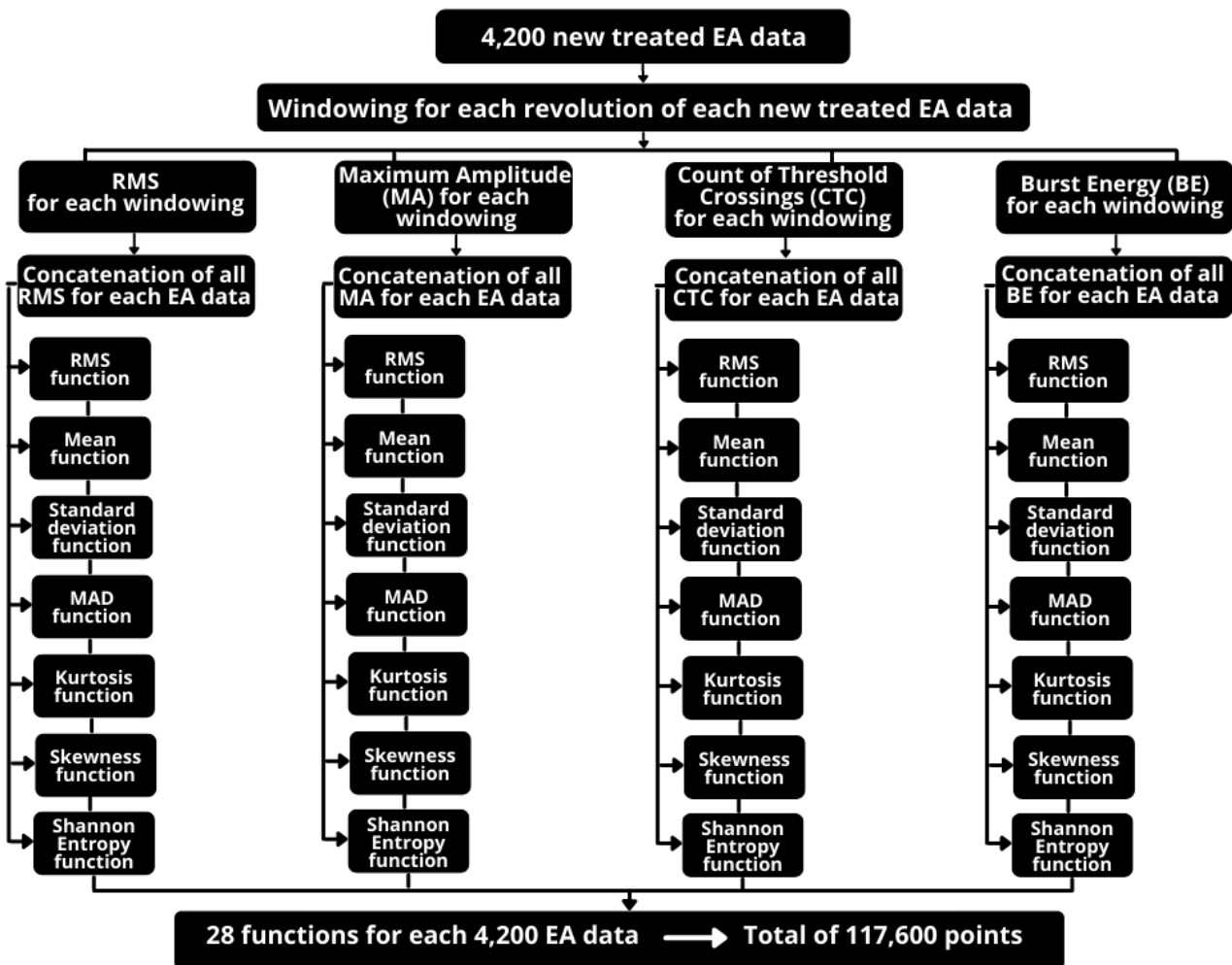


Figure 113 – The 7 statistic function for each 4 characteristic of the 4,200 new treated EA data

These 117,600 characteristics are analyzed considering different groups. The groups chosen are prepared to analyze the following conditions (considering speed lines with XY measurement points, where X is the speed line and Y is the valve position):

1. Same speed line and valve position, different TC:
No new info.
2. Same speed line and TC, different valve position:
No new info.
3. Same valve position and TC, different speed line:
No new info.
4. Trends in pre-surge states:

The analysis of kurtosis function of the RMS characteristic of each valve position of each Turbocharger using a band-pass filter between 50 and 100 kHz showed a potential for surge and pre-surge analysis in turbochargers.

Similarity analysis used cross-correlation between the signals obtained in the data previously presented in this Chapter indicates recognition of patterns already presented before.

The main item observed as presented is related to previous surge detection, where the Kurtosis function obtained by the RMS characteristic of each valve position of each Turbocharger using a band-pass filter between 50 and 100 kHz showed a clear trend in the gradient increase in most 7 TCs in each of the 5 speed lines used.

The position 1 of the valve closing position is the fully open position (0% V.C.). Position 2, 3 and 4 are intermediate turbocharger working positions. The position 5 is the last working position before the start of the surge, while position 6 is the surge point.

The data described in logarithmic scale and with highlight for the curves between positions 4 to 5 (normal to pre-surge) and 5 to 6 (pre-surge to surge) are presented in figures 114 to 118.

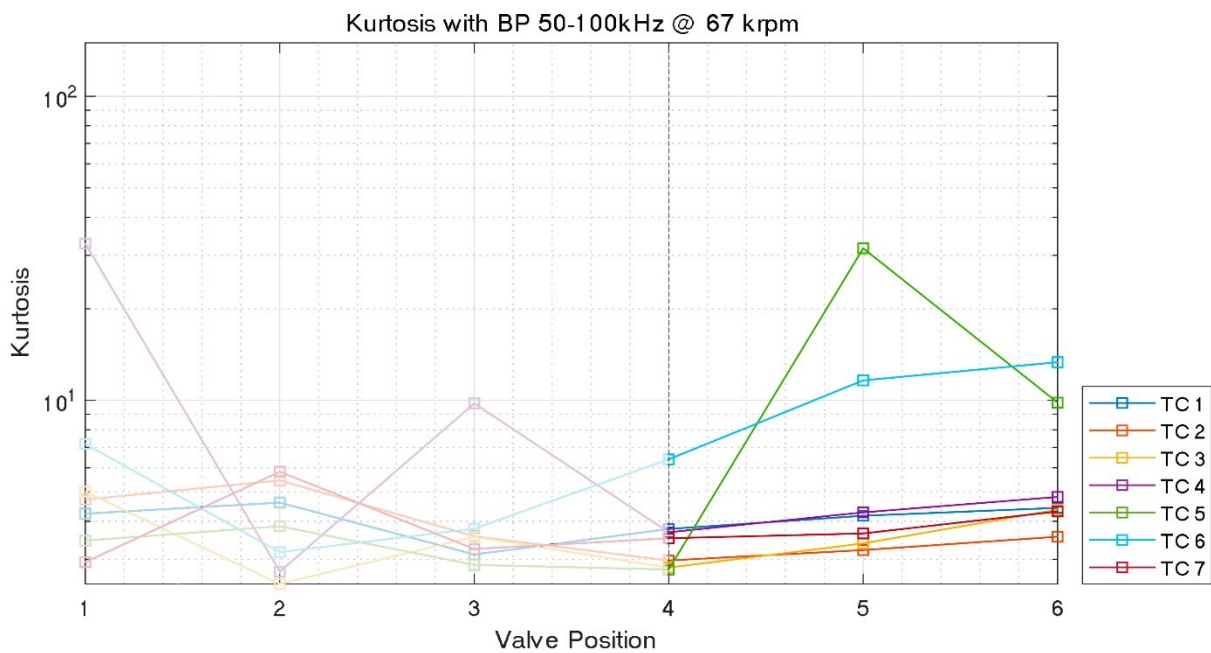


Figure 114 – Kurtosis of RMS from each rotation in different valve closing position with a band-pass filter of 50 to 100 kHz for each TC at 67 krpm (speed line 1)

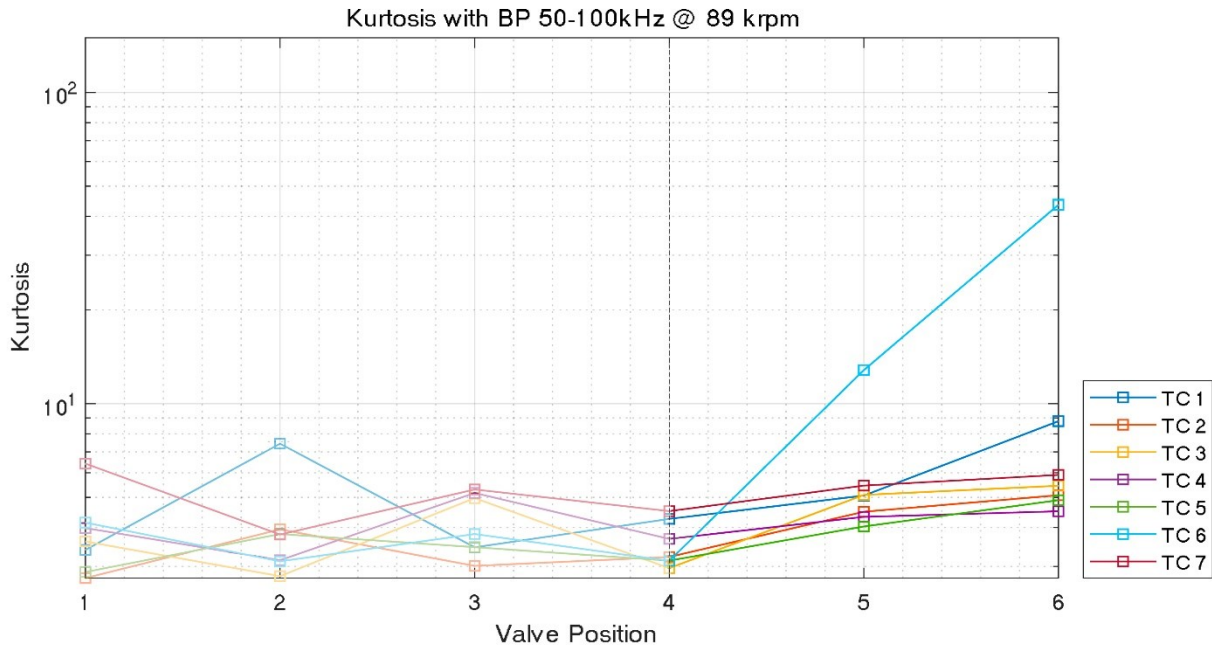


Figure 115 – Kurtosis of RMS from each rotation in different valve closing position with a band-pass filter of 50 to 100 kHz for each TC at 89 krpm (speed line 2)

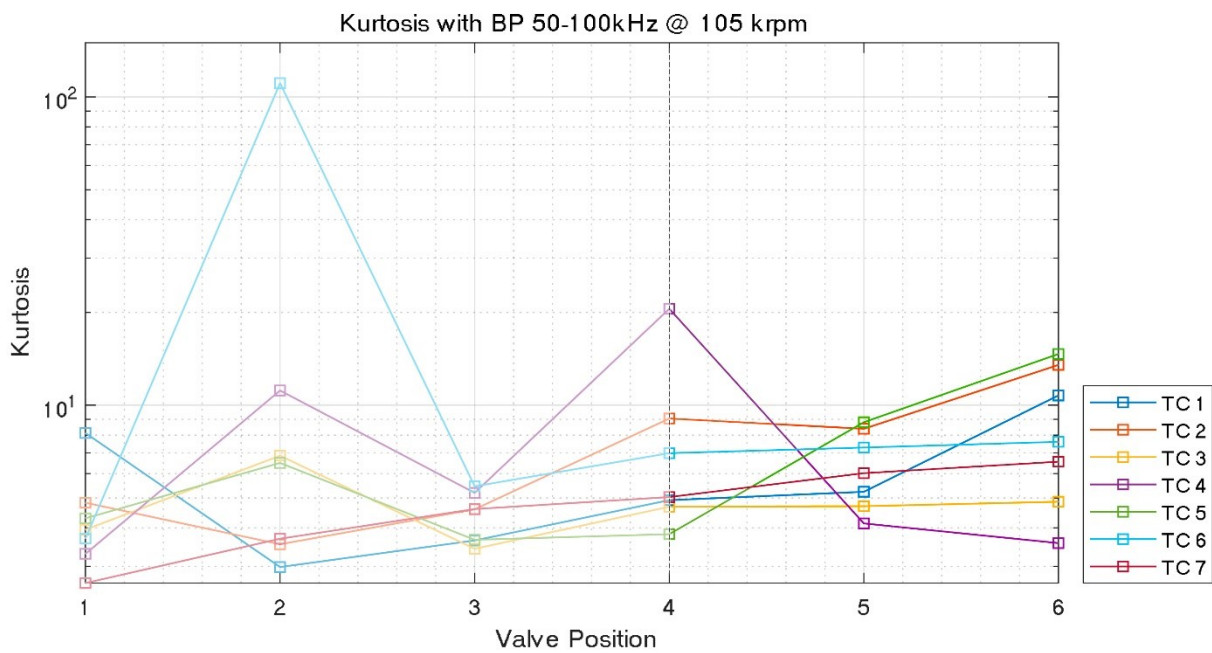


Figure 116 – Kurtosis of RMS from each rotation in different valve closing position with a band-pass filter of 50 to 100 kHz for each TC at 105 krpm (speed line 3)

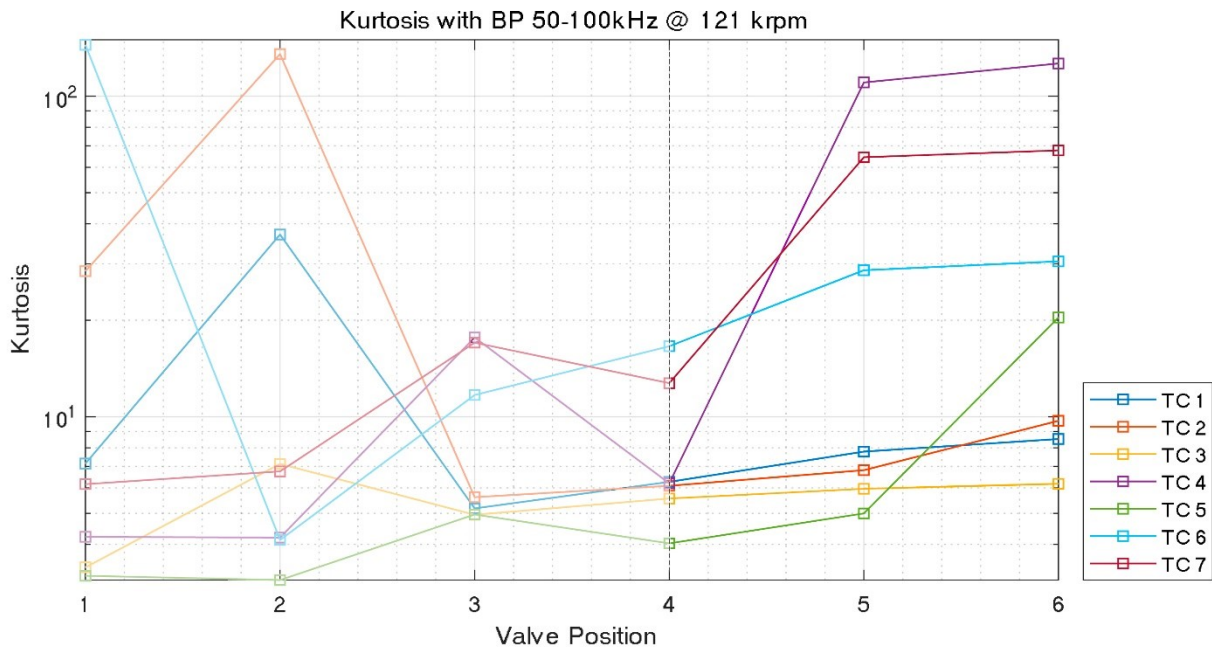


Figure 117 – Kurtosis of RMS from each rotation in different valve closing position with a band-pass filter of 50 to 100 kHz for each TC at 121 krpm (speed line 4)

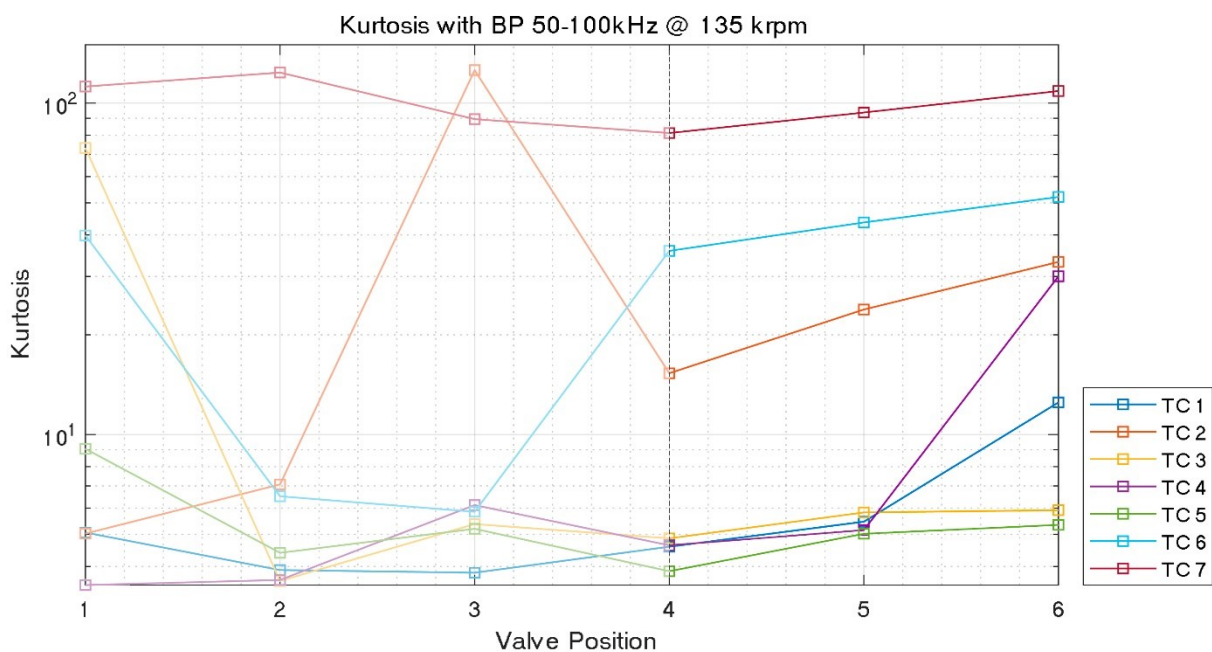


Figure 118 – Kurtosis of RMS from each rotation in different valve closing position with a band-pass filter of 50 to 100 kHz for each TC at 135 krpm (speed line 5)

It is possible to observe an evident increase of Kurtosis between the valve closing position 4 (normal) and 5 (pre-surge) and it is maintained also in the position 5 (pre-surge) to 6 (surge).

The results of Figures 114 to 118 are summarized on Tables 42 to 46, respectively.

Table 42 – Kurtosis of RMS from each rotation in valve closing positions 4, 5 and 6 with a band-pass filter of 50 to 100 kHz for each TC at 67 krpm (speed line 1)

Turbocharger (bearing axial groove shape)	Kurtosis @ Position 4	V.C. @ Position 4	Kurtosis @ Position 5	V.C. @ Position 5	Difference 4 to 5	Kurtosis @ Position 6	V.C. @ Position 6	Difference 5 to 6
TC 1 (triangular)	3.7756	81%	4.1724	90%	10.5%	4.4299	92.5%	6.2%
TC 2 (half-ellipse)	2.9732	81%	3.2181	90%	8.2%	3.5605	93%	10.6%
TC 3 (quarter-ellipse)	2.8178	81%	3.3849	90%	20.1%	4.3713	93%	29.1%
TC 4 (inverted quarter-ellipse)	3.6822	81%	4.2809	90%	16.3%	4.8125	92%	12.4%
TC 5 (rectangular)	2.7782	81%	31.631	90%	1038.5%	9.8275	92%	-68.9%
TC 6 (trapezoidal)	6.3969	81%	11.633	90%	81.9%	13.3524	93%	14.8%
TC 7 (half-circle)	3.5196	81%	3.6494	90%	3.7%	4.311	92.5%	18.1%

Table 43 – Kurtosis of RMS from each rotation in valve closing positions 4, 5 and 6 with a band-pass filter of 50 to 100 kHz for each TC at 89 krpm (speed line 2)

Turbocharger (bearing axial groove shape)	Kurtosis @ Position 4	V.C. @ Position 4	Kurtosis @ Position 5	V.C. @ Position 5	Difference 4 to 5	Kurtosis @ Position 6	V.C. @ Position 6	Difference 5 to 6
TC 1 (triangular)	4.2633	70%	5.066	78%	18.8%	8.7853	91%	73.4%
TC 2 (half-ellipse)	3.2169	70%	4.495	78%	39.7%	5.0799	91%	13.0%
TC 3 (quarter-ellipse)	2.961	70%	5.0917	78%	72.0%	5.4489	91%	7.0%
TC 4 (inverted quarter-ellipse)	3.6766	70%	4.3276	78%	17.7%	4.5105	91.5%	4.2%
TC 5 (rectangular)	3.1303	70%	4.0308	78%	28.8%	4.897	91%	21.5%
TC 6 (trapezoidal)	3.1254	70%	12.825	78%	310.3%	43.571	92%	239.7%
TC 7 (half-circle)	4.5158	70%	5.4555	78%	20.8%	5.9039	91.5%	8.2%

Table 44 – Kurtosis of RMS from each rotation in valve closing positions 4, 5 and 6 with a band-pass filter of 50 to 100 kHz for each TC at 105 krpm (speed line 3)

Turbocharger (bearing axial groove shape)	Kurtosis @ Position 4	V.C. @ Position 4	Kurtosis @ Position 5	V.C. @ Position 5	Difference 4 to 5	Kurtosis @ Position 6	V.C. @ Position 6	Difference 5 to 6
TC 1 (triangular)	4.919	69%	5.2368	77%	6.5%	10.759	87%	105.4%
TC 2 (half-ellipse)	9.052	69%	8.3836	77%	-7.4%	13.5112	89%	61.2%
TC 3 (quarter-ellipse)	4.6829	69%	4.7018	77%	0.4%	4.8621	90%	3.4%
TC 4 (inverted quarter-ellipse)	20.552	69%	4.1337	77%	-79.9%	3.5691	90.5%	-13.7%
TC 5 (rectangular)	3.8162	69%	8.806	77%	130.8%	14.664	90%	66.5%
TC 6 (trapezoidal)	6.988	69%	7.2873	77%	4.3%	7.6066	91%	4.4%
TC 7 (half-circle)	5.034	69%	6.0185	77%	19.6%	6.5565	91%	8.9%

Table 45 – Kurtosis of RMS from each rotation in valve closing positions 4, 5 and 6 with a band-pass filter of 50 to 100 kHz for each TC at 121 krpm (speed line 4)

Turbocharger (bearing axial groove shape)	Kurtosis @ Position 4	V.C. @ Position 4	Kurtosis @ Position 5	V.C. @ Position 5	Difference 4 to 5	Kurtosis @ Position 6	V.C. @ Position 6	Difference 5 to 6
TC 1 (triangular)	6.2662	68%	7.7883	75%	24.3%	8.5259	85%	9.5%
TC 2 (half-ellipse)	6.092	68%	6.8156	75%	11.9%	9.7173	87%	42.6%
TC 3 (quarter-ellipse)	5.561	68%	5.963	75%	7.2%	6.181	90%	3.7%
TC 4 (inverted quarter-ellipse)	6.1996	68%	110.37	75%	1680.3%	126.47	89.5%	14.6%
TC 5 (rectangular)	4.0291	68%	4.9964	75%	24.0%	20.412	88%	308.5%
TC 6 (trapezoidal)	16.597	68%	28.649	75%	72.6%	30.54	90%	6.6%
TC 7 (half-circle)	12.733	68%	64.498	75%	406.5%	67.752	90%	5.0%

Table 46 – Kurtosis of RMS from each rotation in valve closing positions 4, 5 and 6 with a band-pass filter of 50 to 100 kHz for each TC at 135 krpm (speed line 5)

Turbocharger (bearing axial groove shape)	Kurtosis @ Position 4	V.C. @ Position 4	Kurtosis @ Position 5	V.C. @ Position 5	Difference 4 to 5	Kurtosis @ Position 6	V.C. @ Position 6	Difference 5 to 6
TC 1 (triangular)	4.5887	63%	5.4596	75%	19.0%	12.502	86%	129.0%
TC 2 (half-ellipse)	15.31	63%	23.8371	75%	55.7%	33.1785	88%	39.2%
TC 3 (quarter-ellipse)	4.8624	63%	5.8216	75%	19.7%	5.9121	89.5%	1.6%
TC 4 (inverted quarter-ellipse)	4.6335	63%	5.1501	75%	11.1%	30.031	89.5%	483.1%
TC 5 (rectangular)	3.8706	63%	5.0196	75%	29.7%	5.3393	88.5%	6.4%
TC 6 (trapezoidal)	35.818	63%	43.6406	75%	21.8%	52.099	90%	19.4%
TC 7 (half-circle)	81.21	63%	93.66	75%	15.3%	130	90.5%	38.8%

It is possible to observe that in 32 of the 35 cases there is an increase in the Kurtosis function of the RMS characteristics from valve closure #4 (between 81% and 63% for each speed line), passing through closure #5 (between 90% and 75%) until reaching the surge (closure between 93% and 85%).

The application of Kurtosis for EA data in rotordynamics have been observed since the works of Rogers (1979) which present the detection of failure of rolling element bearings in mechanical machines even at low speeds. Other works also show the application of Kurtosis in rotating machines, such as Rush (1979), Lahdelma and Juuso (2011), Lee *et al.* (2018), Han *et al.* (2018) and Mousmoulis *et al.* (2019),

The EA analysis performed in this work indicates that the frequency range from 50 to 100 kHz is adequate to detect the pre-surge and surge in automotive turbochargers. This frequency range has been selected as well to observe cavitation in pumps (ALFAYEZ and MBA, 2005).

The values of the Kurtosis function of the RMS characteristic for the better seven band-pass filters for each TC at each speed line to compare the results with the 50-100 kHz band-pass filter are presented in the Figures 151 to 157 in Appendix D.

4.4. FINAL REMARKS

This experimental work provides results with two goals:

1. Performance classification of FRBs with different axial groove shapes of turbocharger.
2. EA procedure to detect pre-surge and surge in turbochargers.

In the analysis of turbocharger performance, two different approaches have been employed in this work:

- 1.1. Thermodynamic performance of TCs (compressor and turbine efficiency, maximum compressor compression ratio and maximum turbine expansion ratio).
- 1.2. Rotordynamic performance of TCs (synchronous and subsynchronous responses generated by the rotor-bearing system, under stationary and transient conditions).

Table 47 presents the final ranking of the final performance classification for the TCs, based on TD and RD results. Again, a 7-point Pugh score is used, with the a 3 to -3 points from 1st to 7th, respectively.

Table 47 – Final classification of bearing grooves.

Turbocharger (shape)	Final TD rank	Final RD rank	<u>Final TC score & rank</u>	
TC 2 (half-ellipse)	2 nd	3 rd	3	1st
TC 1 (triangular)	5 th	1 st	2	2nd
TC 5 (rectangular)	1 st	5 th	2	2nd
TC 3 (quarter-ellipse)	7 th	1 st	0	4th
TC 4 (inverted quarter-ellipse)	5 th	4 th	-1	5th
TC 6 (trapezoidal)	2 nd	7 th	-1	5th
TC 7 (half-circle)	4 th	6 th	-2	7th

For each result presented in this chapter, bibliography confirmation discussions have already been done in each section.

Considering all the tests performed, the main point to be presented is the clear division of two groups of bearings, with quite different behaviors. A first group is

composed of TCs with internal axial grooved SFRB that provide high performance and thermodynamic efficiency, which are rectangular, trapezoidal and half-ellipse shapes. In the second group, the triangular groove, quarter-ellipse and, again, the half-ellipse bearings, which present superior dynamic response (synchronous and subsynchronous vibrations) during its operation. It is also interesting to note that rectangular and trapezoidal shapes present the best performance results, but the worst in terms of vibratory response in permanent and transient conditions. Conversely, the quarter-ellipse shape has the best vibration response but the worst thermodynamic performance. The half-ellipse groove bearing is the only one to give good results in the TD and RD tests and, therefore, it is rated as the best.

5. CONCLUSION

This experimental study shows the differences in thermodynamic and rotordynamic behaviors of automotive turbochargers supported on semi floating journal bearings with different axial grooves. The influence of the bearing axial grooves on the thermodynamic efficiency and performance of turbocharger is evaluated by measuring pressure, temperature, and mass flow rate at several operating conditions. The dynamic response of turbocharger supported on bearings with different axial grooves is evaluated using vibrations signals.

The thermodynamic results show that the proper selection of the axial groove shape of semi floating journal bearings have strong influence in the thermodynamic performance and efficiency of the turbocharger compressor: the rectangular axial groove shape shows better thermodynamic performance, with the half-ellipse shows the better thermodynamic efficiency. The combined turbine-rotor performance and efficiency present slight differences between the different axial grooves shapes. Therefore, the axial groove shapes have more thermodynamic influence in the compressor analysis.

The rotordynamic results present different responses for steady-state and transient conditions. The frequency spectrum and rotor orbit analysis at constant speed indicates that triangular, half-ellipse and quarter-ellipse axial groove shapes always are ranked in top 3 position, while inverted quarter-ellipse and circle present the worst responses. However, in run-up and coast-down analysis, the half-ellipse became the worst shape, and the inverted quarter-ellipse became the better. Triangular and quarter-ellipse shapes maintain at top 3.

The acoustic emission procedure to detect pre-surge and surge conditions are based in several studies that present specific incipient characteristics of flow machines, such as cavitation in pumps. AE data are obtained in different valve closing positions and speeds conditions and treated using wavelet transforms and band-pass filters. Windowing of new treated data has the target to get one complete shaft revolution and get the characteristics of each revolution. The characteristic of each revolution is compared with the other revolutions of the same treated data and statistic functions present new values for analysis. The cross-correlation results between the acoustic emission data and the data obtained by accelerometers and proximity sensors did not indicate any superior or conclusive results. However, the Kurtosis statistical analysis of each RMS generated by each rotor revolution with specific threshold and 50 to 100 kHz bandpass filter indicated

that AE could be employed to determine the pre-surge and surge conditions in turbochargers. Pre-surge and surge events present frequencies within and near the frequency bands of the cavitation analysis of another research.

Two groups of axial grooves with different TD and RD behaviors can be formed. The first features high thermodynamic performance and efficiency, which are rectangular, trapezoidal and half-ellipse shapes. The second group present superior rotordynamic response in relation to synchronous and subsynchronous vibrations, which are triangular, quarter-ellipse and half-ellipse shapes.

The rectangular and trapezoidal shapes present the best thermodynamic results compared to the others, but the worst behavior in vibration response (synchronous and subsynchronous vibrations) at steady-state and transient conditions. The quarter-ellipse shape has the best vibration response but the worst thermodynamic performance. The half-ellipse groove bearing shows good results in both tests. In general, the work presents important subsidies for the selection of axial groove shapes in SFRB bearings for turbochargers according to the compressor inlet air flow and the turbocharger operating speed, and for different design conditions.

A limitation of the work refers to the small number of samples of bearings analyzed. For each type of SFRB, only one is manufactured in this work due to the choice of a more restricted metrological evaluation process to obtain the most similar geometric characteristics as possible between the bearings, not allowing to statistically analyze the behavior of each groove type. Because it is in a laboratory within a center with other experimental tests and equipment manufacturing, there is also a limitation in the methodology of obtaining acoustic emission measurements because there is not enough insulation, being necessary to carry out the work only when there are no other tests in the center.

Some improvements can be introduced on the test bench, including: 1) Increased heating value, for work with larger TCs; 2) Thermoacoustic isolation system, better isolating the system from the environment; 3) Creation of a unique vibratory response measurement system, introduced directly into the command center; 4) New sub-structure to install ICEs and test different TCs and TC conditions, for example, ICE using biofuels as ethanol.

Further experimental and numerical work can be carried out in the sequence, such as the study of other modifications in the grooves, such as groove width, number of grooves, their positioning, among others, as well as the study of interference of non-

cylindrical shapes of the inner and outer raceways of the SFRBs, use of RFRBs and comparison with SFRBs, hydrodynamic bearings with fixed and mobile geometry and gas bearings (GFB). The studies of GFBs for TCs has proven to be an important technology under study and with expressive results under certain operating conditions. Furthermore, a more thorough analysis of the same SFRB bearings with different groove shapes can be performed by modifying key bearing parameters such as L/D ratio, radial clearance, offset factor, preload factor, type of lubrication, among others. Numerical simulation works can be performed and compared with the experimental results presented here, as long as the different characteristics of the rotor behavior and lubrication are considered, correlated and interconnected in the simulations, as shown by several works. A new rotor test bench to test only the bearings at different load and speed conditions would be important to give information before the test in TC bench.

Acoustic emission studies can be performed using different lubrication conditions and their responses, as well as advancing the correlation analysis of pre-surge acoustic emission data with direct measurements such as compressor inlet and outlet pressure data.

The methodology used for the thermodynamic and rotordynamic analysis performed in this work provides very useful technical information about the performance and efficiency of turbochargers, as well as the vibration attenuation capacity of different bearings with different groove shapes under different airflows and speeds.

The comparative analysis of the performance of bearings of different axial grooves in a hydrodynamic lubrication regime clearly shows the importance of the proper selection of the axial groove shape for the support system of TCs operating with SFRBs and under different conditions. Considering that grooves in industry are normally produced by broaching, the change only takes place in the manufacturing of the tool with the shape and change the tool at CNC machining.

The work also brings a new methodology for detecting turbocharger pre-surge and surge conditions using analogous methodologies previously applied in flow machines for cavitation detection for example. A controlled speed system for TC based in AE data could be proposed in future developments.

Changes in the thermal and vibratory response of a turbocharger can be achieved by modifying the type of groove shape used and by using AE sensors with specific methodology, making the TC set presents better performance and efficiency, as well as safer dynamic operating conditions.

6. REFERENCES

- Abass, B. A., & Muneer, M. A. A. (2018). Static and Dynamic Performance of Journal Bearings lubricated With Nano-Lubricant. *Association of Arab Universities Journal of Engineering Sciences*, 25(2), 201-212.
- Abdelrhman, A. M., Hee, L. M., Leong, M. S., & Al-Obaidi, S. (2014). Condition monitoring of blade in turbomachinery: a review. *Advances in Mechanical Engineering*, 6, 210717.
- Acoustic Technology Group (2021). *AE Calibration and Simulators: Signal Source*. ATG Ltd. <https://atgndt.com/ae-calibration-and-simulators/calibration-signal-source/>
- Aghaali, H., Ångström, H. E., & Serrano, J. R. (2015). Evaluation of different heat transfer conditions on an automotive turbocharger. *International Journal of engine research*, 16(2), 137-151.
- Ahmadkhah, A., & Kakaee, A. H. (2021). Three-dimensional thermohydrodynamic investigation on the micro-groove textures in the main bearing of internal combustion engine for tribological performances. *Proceedings of the Institution of Mechanical Engineers, Part J: Journal of Engineering Tribology*, 235(4), 854-869.
- Alaviyoun, S. S., & Ziabasharhagh, M. (2020). Experimental thermal survey of automotive turbocharger. *International Journal of Engine Research*, 21(5), 766-780.
- Al-Dossary, S., Hamzah, R. R., & Mba, D. (2009). Observations of changes in acoustic emission waveform for varying seeded defect sizes in a rolling element bearing. *Applied acoustics*, 70(1), 58-81.
- Al-Dossary, S., Raja Hamzah, R. I., & Mba, D. (2006). Acoustic emission waveform changes for varying seeded defect sizes. In *Advanced Materials Research* (Vol. 13, pp. 427-432). Trans Tech Publications Ltd.
- Alexander, J., & Porpatham, E. (2021). Numerical and experimental analysis on the effects of turbocharged compressed bio-methane-fueled automotive spark-ignition engine. *Clean Technologies and Environmental Policy*, 1-18.
- Alexander, J., & Porpatham, E. (2021). Thermodynamic and experimental analysis of turbocharger for a downsized LPG fuelled automotive SI engine. *International Journal of Energy and Environmental Engineering*, 12(3), 383-399.
- Alfayez, L., & Mba, D. (2005). Detection of incipient cavitation and determination of the best efficiency point for centrifugal pumps using acoustic emission. *Proceedings of the Institution of Mechanical Engineers, Part E: Journal of process mechanical engineering*, 219(4), 327-344.
- Alford, J. S. (1965). Protecting turbomachinery from self-excited rotor whirl.

Al-Ghamd, A. M., & Mba, D. (2006). A comparative experimental study on the use of acoustic emission and vibration analysis for bearing defect identification and estimation of defect size. *Mechanical systems and signal processing*, 20(7), 1537-1571.

Alhashan, T., Addali, A., & Amaral Teixeira, J. (2016) Exploration of the possibility of acoustic emission technique in detection and diagnosis of bubble formation and collapse in valves. *IOSR Journal of Mechanical and Civil Engineering*, 13(6), pp. 32-40.

Ali, S. M., Hui, K. H., Hee, L. M., Leong, M. S., Abdelrhman, A. M., & Al-Obaidi, M. A. (2019). Observations of changes in acoustic emission parameters for varying corrosion defect in reciprocating compressor valves. *Ain Shams Engineering Journal*, 10(2), 253-265.

Ali, S. M., Hui, K. H., Hee, L. M., Leong, M. S., Abdelrhman, A. M., & Al-Obaidi, M. A. (2019). Observations of changes in acoustic emission parameters for varying corrosion defect in reciprocating compressor valves. *Ain Shams Engineering Journal*, 10(2), 253-265.

Allaire, P. E., & Flack, R. D. (1981). Design of journal bearings for rotating machinery. In *Proceedings of the 10th turbomachinery symposium*. Texas A&M University. Turbomachinery Laboratories.

Al-Obaidi, S. M. A., Leong, M. S., Hamzah, R. I., & Abdelrhman, A. M. (2012). A review of acoustic emission technique for machinery condition monitoring: defects detection & diagnostic. *Applied Mechanics and Materials*, 229, 1476-1480.

Alsaeed, A. A. (2005). *Dynamic stability evaluation of an automotive turbocharger rotor-bearing system* (Doctoral dissertation, Virginia Tech).

Alsaeed, A., Kirk, G., & Bashmal, S. (2014). Effects of radial aerodynamic forces on rotor-bearing dynamics of high-speed turbochargers. *Proceedings of the Institution of Mechanical Engineers, Part C: Journal of Mechanical Engineering Science*, 228(14), 2503-2519.

Amamou, A. (2022). Nonlinear stability analysis and numerical continuation of bifurcations of a rotor supported by floating ring bearings. *Proceedings of the Institution of Mechanical Engineers, Part C: Journal of Mechanical Engineering Science*, 236(5), 2172-2184.

Amamou, A., & Chouchane, M. (2011). Non-linear stability analysis of floating ring bearings using Hopf bifurcation theory. *Proceedings of the Institution of Mechanical Engineers, Part C: Journal of Mechanical Engineering Science*, 225(12), 2804-2818.

American Petrol Institute. (1996). *API Standard 684 - Tutorial on the API Standard Paragraphs Covering Rotor Dynamics and Balancing: An Introduction to Lateral Critical and Train Torsional Analysis and Rotor Balancing* (Standard No. API 684).

American Petrol Institute. (2014). *API Standard 670 - Machinery Protection Systems* (Standard No. API 670).

American Society for Testing and Materials. (2021). *ASTM Standard E976-15 – Standard Guide for Determining the Reproducibility of Acoustic Emission Sensor Response* (Standard E976-15:2021).

Ananthkrishnan, P., Egan, S., Archer, J., & Shipp, T. (2020, September). Maximum turbocharger efficiency for an engine operating at 50% brake thermal efficiency. In *14th International Conference on Turbochargers and Turbocharging* (pp. 191-203). CRC Press.

Araújo, K., Mahajan, D., Kerr, R., & da Silva, M. (2017). Global biofuels at the crossroads: an overview of technical, policy, and investment complexities in the sustainability of biofuel development. *Agriculture*, 7(4), 32.

Association Française des Ingénieurs em Appareils à Pression (2004), *Guide to good practice for acoustic emission (AE) testing of pressure equipment*, AFIAP - Sadave Éditeur.

Babak, V., Filonenko, S., & Kalita, V. (2006). Research of acoustic emission signals at destruction of graphite. *Aviation*, 10(1), 10-16.

Banerjee, D., Dehner, R., & Selamet, A. (2022). Turbulence Measurements at the Inlet of an Automotive Turbocharger Compressor Using Stereoscopic Particle Image Velocimetry. *Journal of Turbomachinery*, 144(1).

Barros, J. E. M. (2003). *Estudo de motores de combustão interna aplicando análise orientada a objetos* (Doctoral dissertation, Federal University of Minas Gerais).

Basri, H., & Yani, I. (2014) Oil Flow in Two Axial Groove Journal Bearing. In: *2014 International Conference on Mechanical Engineering and Automation (ICMEA 2014)*. Tianjin, China. 201-204

Bernhauser, L., Heinisch, M., Schörgenhumer, M., & Nader, M. (2017). The effect of non-circular bearing shapes in hydrodynamic journal bearings on the vibration behavior of turbocharger structures. *Lubricants*, 5(1), 6.

Biagio Turbos (2021). *Linha Projetos Específicos – AUT 1000*. MGFC Ltda. https://www.biagioturbos.com/produto_detalhes.asp?id=23

Bin, G. F., Huang, Y., Guo, S. P., Li, X. J., & Wang, G. (2018). Investigation of induced unbalance magnitude on dynamic characteristics of high-speed turbocharger with floating ring bearings. *Chinese Journal of Mechanical Engineering*, 31(1), 1-11.

Bin, G., Zhang, L., Yang, F., & Chen, A. (2021). The Influence of Ring-Speed Ratio Dynamic Change on Nonlinear Vibration Response of High-Speed Turbocharger Rotor System. *Shock and Vibration*, 2021.

Boczar, T., & Lorenc, M. (2006). Time-frequency analysis of the calibrating signals generated in the Hsu-Nielsen system. *Physics and chemistry of solid state*, 7(3), 585-588.

Boczar, T., & Lorenc, M. (2006). Time-frequency analysis of the calibrating signals generated in the Hsu-Nielsen system. *Physics and chemistry of solid state*, 7(3), 585-588.

Bonello, P., Brennan, M. J., & Holmes, R. (2002). Non-linear modelling of rotor dynamic systems with squeeze film dampers—an efficient integrated approach. *Journal of Sound and Vibration*, 249(4), 743-773.

Bontempo, R., Cardone, M., Manna, M., & Vorraro, G. (2015). Steady and unsteady experimental analysis of a turbocharger for automotive applications. *Energy Conversion and Management*, 99, 72-80.

Borghesani, P., Smith, W. A., Zhang, X., Feng, P., Antoni, J., & Peng, Z. (2018). A new statistical model for acoustic emission signals generated from sliding contact in machine elements. *Tribology International*, 127, 412-419.

Bote-Garcia, J. L., Mokhtari, N., & Gühmann, C. (2020, July). Wear monitoring of journal bearings with acoustic emission under different operating conditions. In *PHM Society European Conference* (Vol. 5, No. 1, pp. 8-8).

Boyaci, A., Seemann, W., & Proppe, C. (2007, December). On the dynamics of a nonlinear rotor-floating ring bearing system. In *PAMM: Proceedings in Applied Mathematics and Mechanics* (Vol. 7, No. 1, pp. 4050005-4050006). Berlin: WILEY-VCH Verlag.

Boyaci, A., Seemann, W., & Proppe, C. (2007, December). On the dynamics of a nonlinear rotor-floating ring bearing system. In *PAMM: Proceedings in Applied Mathematics and Mechanics* (Vol. 7, No. 1, pp. 4050005-4050006). Berlin: WILEY-VCH Verlag.

Boyce, M. P. (2010). *Handbook for cogeneration and combined cycle power plants – Second Edition*. ASME Press, New York, USA.

Brito, F. P., Miranda, A. S., & Fillon, M. (2016). Analysis of the effect of grooves in single and twin axial groove journal bearings under varying load direction. *Tribology International*, 103, 609-619.

Brito, F. P., Miranda, A. S., Bouyer, J., & Fillon, M. (2007). Experimental investigation of the influence of supply temperature and supply pressure on the performance of a two-axial groove hydrodynamic journal bearing. *ASME Journal of Tribology*, Vol. 129, N° 1, pp. 98-105.

Brito, F. P., Miranda, A. S., Claro, J. C. P., & Fillon, M. (2012). Experimental comparison of the performance of a journal bearing with a single and a twin axial groove configuration. *Tribology International*, 54, 1-8.

- Brito, F. P., Miranda, A. S., Claro, J. C. P., Teixeira, J. C., Costa, L., & Fillon, M. (2014). Thermohydrodynamic modelling of journal bearings under varying load angle and negative groove flow rate. *Proceedings of the Institution of Mechanical Engineers, Part J: Journal of Engineering Tribology*, 228(9), 955-973.
- Brown, R. D., Drummond, G., & Addison, P. S. (2000). Chaotic response of a short journal bearing. *Proceedings of the Institution of Mechanical Engineers, Part J: Journal of Engineering Tribology*, 214(4), 387-400.
- Brown, R. N. (1997). *Compressors: Selection and sizing*. Gulf Professional Publishing.
- Cao, J., Dousti, S., Allaire, P., & Dimond, T. (2017). Nonlinear transient modeling and design of turbocharger rotor/semi-floating bush bearing system. *Lubricants*, 5(2), 16.
- Chandrasekaran, L., Selvaraj, P. K., Vengala, P. R., & Arthanarisamy, S. D. (2021). Study of Turbocharger Fully Floating Hydrodynamic Bearing Oil Whirl Behavior— Test and Prediction. In *Proceedings of the 6th National Symposium on Rotor Dynamics* (pp. 329-339). Springer, Singapore.
- Chatterton, S., Dang, P. V., Pennacchi, P., De Luca, A., & Flumian, F. (2017). Experimental evidence of a two-axial groove hydrodynamic journal bearing under severe operation conditions. *Tribology International*, 109, 416-427.
- Chatterton, S., Dang, P. V., Pennacchi, P., De Luca, A., & Flumian, F. (2017). Experimental evidence of a two-axial groove hydrodynamic journal bearing under severe operation conditions. *Tribology International*, 109, 416-427.
- Chatzisavvas, I., Boyaci, A., Koutsovasilis, P., & Schweizer, B. (2015, September). Influence of the oil temperature of thrust bearings on the vibratory behavior of small turbochargers. In *International conference on engineering vibration*.
- Checucci, M., Becciani, M., Bellucci, J., Bianchini, A., Ferrara, G., Arnone, A., ... & Pini, N. (2018, June). An integrated design approach for turbocharger turbines based on the performance optimization in transitory conditions. In *Turbo Expo: Power for Land, Sea, and Air* (Vol. 51173, p. V008T26A022). American Society of Mechanical Engineers.
- Ciulli, E., Ferraro, R., Forte, P., Innocenti, A., & Nuti, M. (2021). Experimental Characterization of Large Turbomachinery Tilting Pad Journal Bearings. *Machines*, 9(11), 273.
- Conley, B., & Sadeghi, F. (2021). Experimental and Analytical Investigation of Turbocharger Whirl and Dynamics. *Tribology Transactions*, 64(2), 239-252.
- Conley, B., Sadeghi, F., Griffith, R. C., & McCormack, J. W. (2019). Experimental Investigation of the Dynamic Loads in a Ball Bearing Turbocharger. *Journal of Tribology*, 141(11), 111101.

Dai, H., Xiang, G., Wang, J., Guo, J., Wang, C., & Jia, H. (2022). Study on time-varying mixed lubrication performance of microgroove journal-thrust coupled bearing under water lubrication. *Industrial Lubrication and Tribology*.

Das, B. J., & Roy, L. (2018). Analysis and comparison of steady-state performance characteristics of two-axial groove and multilobe hydrodynamic bearings lubricated with non-Newtonian fluids. *Proceedings of the Institution of Mechanical Engineers, Part J: Journal of Engineering Tribology*, 232(12), 1581-1596.

Davis, R., & Inajima, T. (2021, November 13). Toyota CEO Defends Combustion Engines: 'The Enemy Is Carbon'. *Bloomberg*.
<https://www.bloomberg.com/news/articles/2021-11-13/japan-carmakers-showcase-carbon-neutral-fuels-in-road-race>

de Andrade, M. R., da Silva, V. L., & Beal, V. E. (2020) Application of the Pugh method for the selection of structural adhesives in precision instruments: a case study. *VI International Symposium on Innovation and Technology (SIINTEC)*. Salvador, Brazil. Federation of Industries of the State of Bahia.

Deligant, M., Podevin, P., & Descombes, G. (2012). Experimental identification of turbocharger mechanical friction losses. *Energy*, 39(1), 388-394.

Dhinakaran, R., Balamurugan, M., Seran, K., Gopalakrishnan, M., Vasudevan, R., & Swathi, C. L. (2017). Development of efficient compressors for turbochargers. In *ASME GT2017-64359, Proceedings of the turbo expo turbomachinery technical conference & exposition, June* (pp. 26-30).

Di Battista, D., Mauriello, M., & Cipollone, R. (2015). *Effects of an ORC based heat recovery system on the performances of a diesel engine* (No. 2015-01-1608). SAE Technical Paper.

Dimond, T. W., Sheth, P. N., Allaire, P. E., & He, M. (2009). Identification methods and test results for tilting pad and fixed geometry journal bearing dynamic coefficients—A review. *Shock and vibration*, 16(1), 13-43.

Dolatabadi, N., Rahmani, R., & Rahnejat, H. (2020). Prediction of acoustic emissions of turbocharger bearings.

Dousti, S., & Allaire, P. (2019). A thermohydrodynamic approach for single-film and double-film floating disk fixed thrust bearings verified with experiment. *Tribology International*, 140, 105858.

Dwivedi, V. K., & Pathak, P. (2021). Effect of axial groove location, length, and width ratio on bearing properties and stability. *Journal of Computational & Applied Research in Mechanical Engineering (JCARME)*, 10(2), 525-537.

Eftekharnjad, B., & Mba, D. (2009). Seeded fault detection on helical gears with acoustic emission. *Applied acoustics*, 70(4), 547-555.

Ehrich, F. (2004). Handbook of Rotordynamics, Florida.

Ehrich, F. F. (1972). Sum and difference frequencies in vibration of high speed rotating machinery. American Petrol Institute. (2014). *API Standard 617 - Axial and Centrifugal Compressors and Expandercompressors – Eighth Edition* (Standard No. API 617).

Evans, B. F., & Fulton, J. W. (2010). Wachel's Equation-Origin And Current Evaluation Of API 617 Rotor Stability Screening Criteria. In *Proceedings of the 39th Turbomachinery Symposium*. Texas A&M University. Turbomachinery Laboratories.

Fan, C. C., Syu, J. W., Pan, M. C., & Tsao, W. C. (2011). Study of start-up vibration response for oil whirl, oil whip and dry whip. *Mechanical Systems and Signal Processing*, 25(8), 3102-3115.

Faria, M. T. C., & Pimentel-Junior, G. L. (2019). On the crack propagation in rotating shafts supported by fluid film bearings using high-frequency acoustic emission analysis. *Arabian Journal for Science and Engineering*, 44(2), 1709-1712.

Feng, H., Jiang, S., & Ji, A. (2019). Investigations of the static and dynamic characteristics of water-lubricated hydrodynamic journal bearing considering turbulent, thermohydrodynamic and misaligned effects. *Tribology International*, 130, 245-260.

Figurella, N., Dehner, R., Selamet, A., Tallio, K., Miazgowicz, K., & Wade, R. (2014). Noise at the mid to high flow range of a turbocharger compressor. *Noise Control Engineering Journal*, 62(5), 306-312.

Filippov, A. V., Rubtsov, V. E., & Tarasov, S. Y. (2017). Acoustic emission study of surface deterioration in tribocontacting. *Applied Acoustics*, 117, 106-112.

Filsinger, D., Kuwata, G., & Ikeya, N. (2021). Tailored Centrifugal Turbomachinery for Electric Fuel Cell Turbocharger. *International Journal of Rotating Machinery*, 2021.

Fonseca, C. A., Santos, I. F., & Weber, H. I. (2018). Experimental comparison of the nonlinear dynamic behavior of a rigid rotor interacting with two types of different radial backup bearings: Ball & pinned. *Tribology International*, 119, 250-261.

Fowle, D., & Miles, D. (1975). Vibration Problems with High Pressure Centrifugal Compressors. *ASME Paper*, 75, 21-25.

Fritz, M., Burger, W., & Albers, A. (2001). Schadensfrüherkennung an geschmierten Gleitkontakten mittels Schallemissionsanalyse. *Tribologie Fachtagung*, 1, 30-1.

Furukawa, A., Ishizaka, K., & Watanabe, S. (2002). Flow measurement in helical inducer and estimate of fluctuating blade force in cavitation surge phenomena. *JSME International Journal Series B Fluids and Thermal Engineering*, 45(3), 672-677.

- Gadangi, R. K. (1995). *Transient rotordynamics with flexible shaft and flexible nonlinear hydrodynamic journal bearings with thermal effects* (Doctoral dissertation, Texas A&M University).
- Galindo, J., Serrano, J. R., Guardiola, C., & Cervelló, C. (2006). Surge limit definition in a specific test bench for the characterization of automotive turbochargers. *Experimental thermal and fluid science*, 30(5), 449-462.
- Galindo, J., Tiseira, A., Navarro, R., Tari, D., & Meano, C. M. (2017). Effect of the inlet geometry on performance, surge margin and noise emission of an automotive turbocharger compressor. *Applied Thermal Engineering*, 110, 875-882.
- Galindo, J., Tiseira, A., Navarro, R., Tari, D., & Meano, C. M. (2017). Effect of the inlet geometry on performance, surge margin and noise emission of an automotive turbocharger compressor. *Applied Thermal Engineering*, 110, 875-882.
- Gao, Z., Liu, S., Wang, H., Chen, M., & Wang, Z. (2017). Experimental investigation of characteristic frequency in compressor surge of a turbocharger. *Noise Control Engineering Journal*, 65(6), 611-617.
- Gharaibeh, K., & Costall, A. W. (2017, September). A Flow and Loading Coefficient-Based Compressor Map Interpolation Technique for Improved Accuracy of Turbocharged Engine Simulations. In *SAE 13th International Conference on Engines & Vehicles* (No. 2017-24-0023).
- Giakoumis, E. G. (2010). Lubricating oil effects on the transient performance of a turbocharged diesel engine. *Energy*, 35(2), 864-873.
- Golloch, R. (2005). Downsizing. *Downsizing bei Verbrennungsmotoren: Ein wirkungsvolles Konzept zur Kraftstoffverbrauchssenkung*, 67-146.
- Gonçalves Jr., A. A. (2002), *Apostila de Metrologia – Parte I – Laboratório de Metrologia e Automatização* (Undergraduate course in Mechanical Engineering, Federal University of Santa Catarina).
- Gong, J., Jin, Y., Liu, Z., Jiang, H., & Xiao, M. (2019). Study on influencing factors of lubrication performance of water-lubricated micro-groove bearing. *Tribology International*, 129, 390-397.
- Gong, J., Jin, Y., Liu, Z., Jiang, H., & Xiao, M. (2019). Study on influencing factors of lubrication performance of water-lubricated micro-groove bearing. *Tribology International*, 129, 390-397.
- Gooding, W. J., Meier, M. A., Gunter, E. J., & Key, N. L. (2020, September). Nonlinear Response and Stability of an Experimental Overhung Compressor Mounted With a Squeeze Film Damper. In *Turbo Expo: Power for Land, Sea, and Air* (Vol. 84225, p. V10BT29A016). American Society of Mechanical Engineers.

Groper, M., & Etsion, I. (2002). Reverse flow as a possible mechanism for cavitation pressure build-up in a submerged journal bearing. *J. Trib.*, *124*(2), 320-326.

Guan, C., Theotokatos, G., & Chen, H. (2015). Analysis of two stroke marine diesel engine operation including turbocharger cut-out by using a zero-dimensional model. *Energies*, *8*(6), 5738-5764.

Gunter, E. J. (2020). *Failure analysis of 2 liter engine turbochargers*. ResearchGate. https://www.researchgate.net/profile/Edgar-Gunter-2/publication/342515831_FAILURE_ANALYSIS_OF_2_LITER_ENGINE_TURBOCHARGERS/links/5ef9069892851c52d6050e78/FAILURE-ANALYSIS-OF-2-LITER-ENGINE-TURBOCHARGERS.pdf

Gunter, E. J., & Chen, W. J. (2005). Dynamic analysis of a turbocharger in floating bushing bearings. *ISCORMA-3, Cleveland, Ohio*, 19-23.

Guo, B. (2017). Optimal surface texture design of journal bearing with axial grooves. *International Journal of Heat and Technology*, *35*(2), 267-272.

Gürbüz, H., & Gönülaçar, Y. E. (2022). Experimental and statistical investigation of the effects of MQL, dry and wet machining on machinability and sustainability in turning of AISI 4140 steel. *Proceedings of the Institution of Mechanical Engineers, Part E: Journal of Process Mechanical Engineering*, 09544089221076243.

Han, H. S., Lee, C. N., Jeon, S. H., Lee, K. H., & Park, S. H. (2018). Development of an evaluation method to determine cavitation inception speed with aft hull vibration using kurtosis of the DEMON spectrum. *Ocean Engineering*, *152*, 167-180.

Han, H. S., Lee, C. N., Jeon, S. H., Lee, K. H., & Park, S. H. (2018). Development of an evaluation method to determine cavitation inception speed with aft hull vibration using kurtosis of the DEMON spectrum. *Ocean Engineering*, *152*, 167-180.

Hanriot, V.M., Troysi, F., Teixeira, J. A. G. S., Valle, R. M., & Sandoval, O. R.. (2019). Acoustic characterization of the noise generated by turbochargers. *Proceedings of COBEM 2019 – 25th Brazilian Congress of Mechanical Engineering*. Uberlandia, Brazil. Federal University of Uberlandia.

Hassan, A. S. (2007). Influence of the volute design parameters on the performance of a centrifugal compressor of an aircraft turbocharger. *Proceedings of the Institution of Mechanical Engineers, Part A: Journal of Power and Energy*, *221*(5), 695-704.

Hatakenaka, K., Tanaka, M., & Suzuki, K. (2002). A theoretical analysis of floating bush journal bearing with axial oil film rupture being considered. *J. Trib.*, *124*(3), 494-505.

Hatakenaka, K., Tanaka, M., & Suzuki, K. (2002). A theoretical analysis of floating bush journal bearing with axial oil film rupture being considered. *J. Trib.*, *124*(3), 494-505.

Heuer, T., Engels, B., & Wollscheid, P. (2005, January). Thermomechanical analysis of a turbocharger based on conjugate heat transfer. In *Turbo Expo: Power for Land, Sea, and Air* (Vol. 46997, pp. 829-836).

Heywood, J. B. (2018). *Internal combustion engine fundamentals*. McGraw-Hill Education.

Hodnett, M., Chow, R., & Zeqiri, B. (2004). High-frequency acoustic emissions generated by a 20 kHz sonochemical horn processor detected using a novel broadband acoustic sensor: a preliminary study. *Ultrasonics sonochemistry*, 11(6), 441-454.

Holmes, R., Brennan, M., & Gottrand, B. (2004, October). Vibration of an automotive turbocharger—a case study. In *Eighth International Conference on Vibrations in Rotating Machinery, 7-9 September 2004, University of Wales, Swansea, UK* (No. 2, p. 445). Professional Engineering Pub. Limited.

Holt, C., San Andre' s, L., Sahay, S., Tang, P., La Rue, G., & Gjika, K. (2005). Test response and nonlinear analysis of a turbocharger supported on floating ring bearings. *J. Vib. Acoust.*, 127(2), 107-115.

Holt, C., San Andre' s, L., Sahay, S., Tang, P., La Rue, G., & Gjika, K. (2005). Test response and nonlinear analysis of a turbocharger supported on floating ring bearings. *J. Vib. Acoust.*, 127(2), 107-115.

Holt, C., San Andres, L., Sahay, S., Tang, P., La Rue, G., & Gjika, K. (2003(a), January). Test response of a turbocharger supported on floating ring bearings: Part i—assessment of subsynchronous motions. In *International Design Engineering Technical Conferences and Computers and Information in Engineering Conference* (Vol. 37033, pp. 969-974).

Holt, C., San Andres, L., Sahay, S., Tang, P., La Rue, G., & Gjika, K. (2003(b), January). Test response of a turbocharger supported on floating ring bearings: Part ii—comparisons to nonlinear rotordynamic predictions. In *International Design Engineering Technical Conferences and Computers and Information in Engineering Conference* (Vol. 37033, pp. 975-980).

Hsu, N. N., & Breckenridge, F. R. (1981). Characterization and calibration of acoustic emission sensors. *Mater. Eval.*, 39, 60-68.

Huang, J., Li, Y., Jiang, B., & Cao, L. (2019). Analysis of measurement uncertainty of a surface acoustic wave micro-pressure sensor. *Measurement and Control*, 52(1-2), 116-121.

Iga, Y., Hashizume, K., & Yoshida, Y. (2011). Numerical analysis of three types of cavitation surge in cascade. *Journal of fluids engineering*, 133(7).

Inoue, T., & Ishida, Y. (2006). Chaotic vibration and internal resonance phenomena in rotor systems. *Journal of Vibration and Acoustics*, 128(2), 156-169.

Iwasaki, M., Ikeya, N., Marutani, Y., & Kitazawa, T. (1994). *Comparison of turbocharger performance between steady flow and pulsating flow on engines* (No. 940839). SAE Technical Paper.

Jääskeläinen, H. (2021, May 13). Multiple Compressors. *DieselNet Technology Guide*. https://dieselnet.com/tech/air_turbo_multi.php

Jain, A., Nueesch, T., Naegele, C., Lassus, P. M., & Onder, C. H. (2016). Modeling and control of a hybrid electric vehicle with an electrically assisted turbocharger. *IEEE transactions on vehicular technology*, 65(6), 4344-4358.

Jamaludin, N., Mba, D., & Bannister, R. H. (2001). Condition monitoring of slow-speed rolling element bearings using stress waves. *Proceedings of the Institution of Mechanical Engineers, Part E: Journal of Process Mechanical Engineering*, 215(4), 245-271.

Jarroux, C., Mahfoud, J., Dufour, R., Legrand, F., Defoy, B., & Alban, T. (2021). Investigations on the dynamic behaviour of an on-board rotor-AMB system with touchdown bearing contacts: modelling and experimentation. *Mechanical Systems and Signal Processing*, 159, 107787.

Jeddi, L., El Khelifi, M., & Bonneau, D. (2005). Thermohydrodynamic analysis for a hydrodynamic journal bearing groove. *Proceedings of the Institution of Mechanical Engineers, Part J: Journal of Engineering Tribology*, 219(4), 263-274.

Jemielniak, K. (2001). Some aspects of acoustic emission signal pre-processing. *Journal of Materials Processing Technology*, 109(3), 242-247.

Jie, H., Huaiyan, C., & Yun, C. (2011, August). Uncertainty evaluation using Monte Carlo method with MATLAB. In *IEEE 2011 10th International Conference on Electronic Measurement & Instruments* (Vol. 2, pp. 282-286). IEEE.

Jilakara, S., Vaithianathan, J. V., Natarajan, S., Ramakrishnan, V. R., Subash, G. P., Abraham, M., ... & Das, L. M. (2015). An experimental study of turbocharged hydrogen fuelled internal combustion engine. *SAE International Journal of Engines*, 8(1), 314-325.

Jin, D., Xiao, K., Xiang, G., Wang, Y., Wang, C., & Jia, H. (2021). A simulation model to comparative analysis the effect of texture bottom shape on wear and lubrication performances for micro-groove water lubricated bearings. *Surface Topography: Metrology and Properties*, 9(2), 025009.

Jolly, W. D. (1994). Investigation of acoustic emission coupling techniques: Southwest Research Inst., San Antonio (United States), N89-15683/0, NASA-CR-183541, 83 pp.(Sep. 1988). *NDT & E International*, 27(4), 219.

Joy, N. M., & Roy, L. (2016). Determination of optimum configuration among different configurations of two-axial groove hydrodynamic bearings. *Proceedings of*

the Institution of Mechanical Engineers, Part J: Journal of Engineering Tribology, 230(9), 1071-1091.

Kabral, R., & Ábom, M. (2018). Investigation of turbocharger compressor surge inception by means of an acoustic two-port model. *Journal of Sound and Vibration*, 412, 270-286.

Kadam, K. R., & Banwait, S. S. (2018). Performance characteristics of two-axial groove journal bearing for different groove angles. *Industrial Lubrication and Tribology*.

Katrašnik, T., Rodman, S., Trenc, F., Hribernik, A., & Medica, V. (2003). Improvement of the dynamic characteristic of an automotive engine by a turbocharger assisted by an electric motor. *J. Eng. Gas Turbines Power*, 125(2), 590-595.

Kaufmann, A. (2014). Using turbocharger maps in gas exchange simulation and engine control units. *Forschung im Ingenieurwesen*, 78(1), 45-57.

Keprt, J., & Benes, P. (2009). The determination of uncertainty in the calibration of acoustic emission sensors. *International Journal of Microstructure and Materials Properties*, 4(1), 85-103.

Kerth, J. (2003). *Experimental Rotordynamic Response of an Automotive Turbocharger with Floating Ring Bearings* (Doctoral dissertation, MS Thesis, Texas A&M University).

Kerviel, A., Pesyridis, A., Mohammed, A., & Chalet, D. (2018). An evaluation of turbocharging and supercharging options for high-efficiency fuel cell electric vehicles. *Applied Sciences*, 8(12), 2474.

Khonsari, M., & Booser, E. R. (2006). Parasitic Power Losses in Hydrodynamic Bearings. *Machinery Lubrication*. NORIA
<https://www.machinerylubrication.com/Read/862/parasitic-power-bearings>

Kim, H. S., Cho, M., & Song, S. J. (2003). Stability analysis of a turbine rotor system with Alford forces. *Journal of sound and vibration*, 1(260), 167-182.

Kim, Y. G., Lee, M. S., Cho, K. H., & Kim, U. K. (2017). Effects of a turbocharger cut out system on vibration characteristics of a propulsion shafting system and a large low speed marine diesel engine. *Journal of Mechanical Science and Technology*, 31(8), 3737-3745.

Kini, M. V., Pai, R. S., Rao, D. S., Shenoy, S., & Pai, R. (2009). Effect of groove location on the dynamic characteristics of multiple axial groove water lubricated journal bearing. *World Academy of Sci Engg and Tech*, 36, 738-742.

Kirk, R. G. (2014). Experimental evaluation of hydrodynamic bearings for a high speed turbocharger. *Journal of engineering for gas turbines and power*, 136(7).

Kirk, R. G., & Alsaeed, A. A. (2011). Induced unbalance as a method for improving the dynamic stability of high-speed turbochargers. *International Journal of Rotating Machinery*, 2011.

Kirk, R. G., Kornhauser, A. A., Sterling, J., & Alsaeed, A. (2010). Turbocharger on-engine experimental vibration testing. *Journal of Vibration and Control*, 16(3), 343-355.

Kitamura, T., Kameda, M., Watanabe, W., Horimoto, K., Akimoto, K., & Akahori, A. (2018, June). Measurement of unsteady pressure field in a turbocharger compressor using pressure-sensitive paint. In *Turbo Expo: Power for Land, Sea, and Air* (Vol. 51005, p. V02BT44A018). American Society of Mechanical Engineers.

Kolios, A., Mytilinou, V., Lozano-Minguez, E., & Salonitis, K. (2016). A comparative study of multiple-criteria decision-making methods under stochastic inputs. *Energies*, 9(7), 566.

Kopeliovich, D. (2015). Design of High Performance Bearings for Race Engines. *Engine Professional*. AERA <https://engineprofessional.com/2015EPQ2/>

Kosasih, P. B., & Tieu, A. K. (2004). An investigation into the thermal mixing in journal bearings. *Proceedings of the Institution of Mechanical Engineers, Part J: Journal of Engineering Tribology*, 218(5), 379-389.

Kozhukhov, Y. V., Lebedev, A. A., Chai, N. M., & Yablokov, A. M. (2020, November). Automatic centrifugal compressor pre-surge detection. In *AIP Conference Proceedings* (Vol. 2285, No. 1, p. 030047). AIP Publishing LLC.

Kumar, V., & Sharma, S. C. (2019). Effect of geometric shape of micro-grooves on the performance of textured hybrid thrust pad bearing. *Journal of the Brazilian Society of Mechanical Sciences and Engineering*, 41(11), 1-24.

Kumar, V., Sharma, S. C., & Narwat, K. (2019). Influence of micro-groove attributes on frictional power loss and load-carrying capacity of hybrid thrust bearing. *Industrial Lubrication and Tribology*.

Lahdelma, S., & Juuso, E. (2011). Signal processing and feature extraction by using real order derivatives and generalised norms. Part 1: Methodology. *International Journal of Condition Monitoring*, 1(2), 46-53.

Lamy, F., Takarli, M., Angellier, N., Dubois, F., & Pop, O. (2015). Acoustic emission technique for fracture analysis in wood materials. *International Journal of Fracture*, 192(1), 57-70.

Leahy, M., Mba, D., Cooper, P., Montgomery, A., & Owen, D. (2006). Detecting shaft-to-seal rubbing in power generation turbines with the Acoustic Emission technology.

- Leahy, M., Mba, D., Cooper, P., Montgomery, A., & Owen, D. (2006). Detecting shaft-to-seal rubbing in power generation turbines with the Acoustic Emission technology.
- Lee, I. B., & Hong, S. K. (2017). Effects of oil inlet pressure and temperature on the dynamic behaviors of a full-floating ring bearing supported turbocharger rotor. *The KSFM Journal of Fluid Machinery*, 20(2), 53-62.
- Lee, J. H., Kim, D. H., & Shin, Y. H. (2018). Hyperbolic localization of incipient tip vortex cavitation in marine propeller using spectral kurtosis. *Mechanical Systems and Signal Processing*, 110, 442-457.
- Lee, J. H., Kim, D. H., & Shin, Y. H. (2018, December). Localization of propeller tip vortex noise assisted by spectral kurtosis. In *INTER-NOISE and NOISE-CON Congress and Conference Proceedings* (Vol. 258, No. 3, pp. 4427-4436). Institute of Noise Control Engineering.
- Lee, J., Park, C., Kim, Y., Choi, Y., Bae, J., & Lim, B. (2019). Effect of turbocharger on performance and thermal efficiency of hydrogen-fueled spark ignition engine. *International journal of hydrogen energy*, 44(8), 4350-4360.
- Lee, S. G., Park, J. H., Yoo, K. B., Lee, S. K., & Hong, S. Y. (2006). Evaluation of internal leak in valve using acoustic emission method. In *Key Engineering Materials* (Vol. 326, pp. 661-664). Trans Tech Publications Ltd.
- Lee, Y. B., Park, D. J., & Sim, K. (2015). Rotordynamic performance measurements of an oil-free turbocharger supported on gas foil bearings and their comparisons to floating ring bearings. *International Journal of Fluid Machinery and Systems*, 8(1), 23-35.
- Li, B., Sun, J., Zhu, S., Fu, Y., Zhao, X., Wang, H., Teng, Q., Ren Y., Li, Y. & Zhu, G. (2019). Effect of the axial movement of misaligned journal on the performance of hydrodynamic lubrication journal bearing with rough surface. *Mechanics & Industry*, 20(4), 402.
- Li, S., Li, W., Ji, L., Shi, W., & Agarwal, R. K. (2021). Vortex Dynamics Analysis of Internal Flow Field of Mixed-Flow Pump under Alford Effect. *Water*, 13(24), 3575.
- Liang, F., Zhou, M., & Xu, Q. (2016). Effects of semi-floating ring bearing outer clearance on the subsynchronous oscillation of turbocharger rotor. *Chinese Journal of Mechanical Engineering*, 29(5), 901-910.
- Lifson, A., & Simmons, H. R. (1990). Vibration Monitoring Of Turbomachinery. In *Proceedings of the 19th Turbomachinery Symposium*. Texas A&M University. Turbomachinery Laboratories.
- Linhares, A. D., Faria, M. T. C., da Costa, A. R., & Martinez, C. B. (2011). Cavitation erosion tests in centrifugal pumps. *Proceedings of COBEM 2011 - 21st*

Brazilian Congress of Mechanical Engineering. Natal, Brazil. Federal University of Rio Grande do Norte.

Liu, A. X., & Zheng, X. Q. (2013). Methods of surge point judgment for compressor experiments. *Experimental Thermal and Fluid Science*, 51, 204-213.

Liu, X., & Chen, W. (2022). Structural Design and Optimization of Herringbone Grooved Journal Bearings Considering Turbulent. *Applied Sciences*, 12(1), 485.

López Hidalgo, M. A. (2014). *Estudio Teórico-Experimental de la Dinámica Rotacional de Turbocompresores de MCIA. Aplicación al Diagnóstico de Fallos* (Doctoral dissertation, Universitat Politècnica de València).

Lu, D., Theotokatos, G., Zhang, J., Zeng, H., & Cui, K. (2022). Parametric investigation of a large marine two-stroke diesel engine equipped with exhaust gas recirculation and turbocharger cut out systems. *Applied Thermal Engineering*, 200, 117654.

Lüddecke, B., Filsinger, D., & Ehrhard, J. (2012). On mixed flow turbines for automotive turbocharger applications. *International Journal of rotating machinery*, 2012.

Luo, Q. H., Hu, J. B., Sun, B. G., Liu, F. S., Wang, X., Li, C., & Bao, L. Z. (2019). Effect of equivalence ratios on the power, combustion stability and NO_x controlling strategy for the turbocharged hydrogen engine at low engine speeds. *international journal of hydrogen energy*, 44(31), 17095-17102.

Lycoming (2006). *Operator's Manual. Lycoming. TIO-540-AE2A Series*. Lycoming Engines.

Ma, J., Zhang, H., Lou, S., Chu, F., Shi, Z., Gu, F., & Ball, A. D. (2021). Analytical and experimental investigation of vibration characteristics induced by tribofilm-asperity interactions in hydrodynamic journal bearings. *Mechanical Systems and Signal Processing*, 150, 107227.

Malkawi, A., AlAdawy, A., Gadamsetty, R. K. V., & Lastra Melo, R. (2019, June). Compression Technology Selection for Downhole Application in Gas Wells. In *Turbo Expo: Power for Land, Sea, and Air* (Vol. 58721, p. V009T27A019). American Society of Mechanical Engineers.

Mallya, R., Shenoy, S. B., & Pai, R. (2017). Static characteristics of misaligned multiple axial groove water-lubricated bearing in the turbulent regime. *Proceedings of the Institution of Mechanical Engineers, Part J: Journal of Engineering Tribology*, 231(3), 385-398.

Mansouri, H., & Ommi, F. (2019). Performance prediction of aircraft gasoline turbocharged engine at high-altitudes. *Applied Thermal Engineering*, 156, 587-596.

- Mantelli, L., Ferrari, M. L., & Traverso, A. (2021). Dynamics and control of a turbocharged solid oxide fuel cell system. *Applied Thermal Engineering*, 191, 116862.
- Marelli, S., Misley, A., Silvestri, P., Capobianco, M., Taylor, A., & Canova, M. (2018). *Experimental Investigation on Surge Phenomena in an Automotive Turbocharger Compressor* (No. 2018-01-0976). SAE Technical Paper.
- Mba, D., & Hall, L. D. (2002). The transmission of acoustic emission across large-scale turbine rotors. *Ndt & E International*, 35(8), 529-539.
- Mba, D., Bannister, R. H., & Findlay, G. E. (1999(a)). Condition monitoring of low-speed rotating machinery using stress waves Part 1. *Proceedings of the Institution of Mechanical Engineers, Part E: Journal of Process Mechanical Engineering*, 213(3), 153-170.
- Mba, D., Bannister, R. H., & Findlay, G. E. (1999(b)). Condition monitoring of low-speed rotating machinery using stress waves Part 2. *Proceedings of the Institution of Mechanical Engineers, Part E: Journal of Process Mechanical Engineering*, 213(3), 171-185.
- McCarthy, D. M. C., Glavatskih, S. B., & Byheden, Å. (2009). Influence of oil type on the performance characteristics of a two-axial groove journal bearing. *Lubrication Science*, 21(9), 366-377.
- McGowan, R. C., Pieri, J. J., Szedlmayer, M. T., Kim, K., Clerkin, P. J., Kruger, K. M., Gondol, D. J., Kweon, C. B. M., Meininger, R. D., Gibson, J.A., Lindsey, M. R. & Musser, M. R. (2019). Experimental vibration analysis of an aircraft diesel engine turbocharger. In *AIAA Propulsion and Energy 2019 Forum* (p. 4008).
- Menon, S., Furman, A., & Krok, M. (2006, December). Detection of surge precursors in locomotive turbocharger. In *2006 IEEE International Conference on Industrial Technology* (pp. 3067-3071). IEEE.
- Michlmayr, G., Cohen, D., & Or, D. (2013). Shear-induced force fluctuations and acoustic emissions in granular material. *Journal of Geophysical Research: Solid Earth*, 118(12), 6086-6098.
- Miller, J. K. (2008). *Turbo: real world high-performance turbocharger systems*. CarTech Inc.
- Mitutoyo Sul Americana Ltda. (2019), *Mitutoyo – Catalog PG 405*. https://www.mitutoyo.com.br/download/catalogo geral/p2019/43_microscopios.pdf
- Mobley, R. K. (2001). *Plant engineer's handbook*. Elsevier.
- Mokhtari, N. (2020). *Überwachung hydrodynamischer Gleitlager basierend auf der Körperschallanalyse*. (Doctoral dissertation, Technische Universität Berlin, Germany).

- Mokhtari, N., & Gühmann, C. (2018). Classification of journal bearing friction states based on acoustic emission signals. *tm-Technisches Messen*, 85(6), 434-442.
- Mokhtari, N., Pelham, J. G., Nowoisky, S., Bote-Garcia, J. L., & Gühmann, C. (2020). Friction and wear monitoring methods for journal bearings of geared turbofans based on acoustic emission signals and machine learning. *Lubricants*, 8(3), 29.
- Mokhtari, N., Pelham, J. G., Nowoisky, S., Bote-Garcia, J. L., & Gühmann, C. (2020). Friction and wear monitoring methods for journal bearings of geared turbofans based on acoustic emission signals and machine learning. *Lubricants*, 8(3), 29.
- Moraal, P., & Kolmanovsky, I. (1999). *Turbocharger modeling for automotive control applications* (No. 1999-01-0908). SAE Technical Paper.
- Morgner, W.. *Schallemission - Schallillusion?* In: Vaupel lecture on the occasion of the DGZfP annual conference. 1997, pp. 1-29.
- Morhain, A., & Mba, D. (2003). Bearing defect diagnosis and acoustic emission. *Proceedings of the Institution of Mechanical Engineers, Part J: Journal of Engineering Tribology*, 217(4), 257-272.
- Mousmoulis, G., Yiakopoulos, C., Kassanos, I., Antoniadis, I., & Anagnostopoulos, J. (2019, December). Vibration and acoustic emission monitoring of a centrifugal pump under cavitating operating conditions. In *IOP Conference Series: Earth and Environmental Science* (Vol. 405, No. 1, p. 012003). IOP Publishing.
- Nguyen-Schäfer, H. (2013). *Aero and vibroacoustics of automotive turbochargers*. Springer Science & Business Media.
- Nguyen-Schäfer, H. (2015). *Rotordynamics of automotive turbochargers*. Cham, Switzerland: Springer International Publishing.
- Nicholas, J. C., & Kocur, J. A. (2005). Rotordynamic Design Of Centrifugal Compressors In Accordance With The New API Stability Specifications. In *Proceedings of the 34th Turbomachinery Symposium*. Texas A&M University. Turbomachinery Laboratories.
- Nossier, E. A., Omran, I. M., Abdel-Aziz, A. I., & Hennes, G. M. (2016) Evaluation of the Factors Affecting Turbocharger Service Life. *International Journal of Engineering Research & Technology*, 5(8), 43-46.
- Nowald, G., Boyaci, A., Schmoll, R., Koutsovasilis, P., Driot, N., & Schweizer, B. (2015, February). Influence of axial grooves in full-floating-ring bearings on the nonlinear oscillations of turbocharger rotors. In *SIRM 2015–11th International Conference on Vibrations in Rotating Machines, Magdeburg, Germany, February 23th–25th*.

- Nowoisky, I. S., Grzeszkowski, M., Mokhtari, N., Pelham, J. G., & Gühmann, C. (2020). Monitoring concept study for aerospace power gear box drive train. *Power*, 269, 286.
- Okudan, G. E., & Tauhid, S. (2008). Concept selection methods—a literature review from 1980 to 2008. *International Journal of Design Engineering*, 1(3), 243-277.
- Ozaki, M., Yoshida, T., Fujita, Y., Futae, T., Arai, T., & Yamada, Y. (2021). Development of Turbocharger for Next-generation Hybrid Electric Vehicles. *Mitsubishi Heavy Industries Technical Review*, 58(2), 1.
- Pai, R. S., & Pai, R. (2008). Stability of four-axial and six-axial grooved water-lubricated journal bearings under dynamic load. *Proceedings of the Institution of Mechanical Engineers, Part J: Journal of Engineering Tribology*, 222(5), 683-691.
- Patterson, S. (2014, March 21). GM Atlas 2900 Turbo Compressor Maps I. *Sumner's Home Page*. <http://1fatgmc.com/car/turbo-stuff/2900%20turbo%20compressor%20maps-1.html>
- Payri, F., Serrano, J. R., Olmeda, P., Paez, A., & Vidal, F. (2010, October). Experimental methodology to characterize mechanical losses in small turbochargers. In *Turbo Expo: Power for Land, Sea, and Air* (Vol. 44007, pp. 413-423).
- Peng, L., Zheng, H., & Shi, Z. (2021). Performance of Relative Clearance Ratio of Floating Ring Bearing for Turbocharger-Rotor System Stability. *Machines*, 9(11), 285.
- Peng, L., Zheng, H., & Shi, Z. (2021). Performance of Relative Clearance Ratio of Floating Ring Bearing for Turbocharger-Rotor System Stability. *Machines*, 9(11), 285.
- Perge, J., Hoepke, B., Uhlmann, T., Dohmen, J., & Lehmann, J. (2018). Turbocharger bearing friction measurement and simulation. In *Reibungsminimierung im Antriebsstrang 2015* (pp. 133-155). Springer Vieweg, Wiesbaden.
- Pesiridis, A., Salim, S. I. W., & Martinez-Botas, R. F. (2012, May). Turbocharger matching methodology for improved exhaust energy recovery. In *Proc. of the 10th Int. Conf. on Turbocharging and Turbochargers* (pp. 203-218).
- Pettinato, B. C., & DeChoudhury, P. (2003). Rotordynamic and bearing upgrade of a high-speed turbocharger. *J. Eng. Gas Turbines Power*, 125(1), 95-101.
- Physical Acoustics Corporation (2009), *AE Sensor calibration certificate – Sensor Name: S9208 – Sensor S/n: AG50* (Calibration chart, Physical Acoustics).
- Piancastelli, L., Frizziero, L., & Rocchi, I. (2012). Feasible optimum design of a turbocompound Diesel Brayton cycle for diesel-turbo-fan aircraft propulsion. *International Journal of Heat and Technology*, 30(2), 121-126.

Pimentel-Junior, G. L. S., Oliveira, F. B., & Faria, M. T. C. (2016). On the bump tests of cracked shafts using acoustic emission techniques. *Engineering*, 8(09), 572.

Pinkus, O. (1990). *Thermal aspects of fluid film tribology*. American Society of Mechanical Engineers.

Píšťek, V., Kučera, P., Fomin, O., & Lovska, A. (2020). Effective mistuning identification method of integrated bladed discs of marine engine turbochargers. *Journal of Marine Science and Engineering*, 8(5), 379.

Poddar, S., & Tandon, N. (2020). Study of oil starvation in journal bearing using acoustic emission and vibration measurement techniques. *Journal of Tribology*, 142(12).

Poddar, S., & Tandon, N. (2020). Study of oil starvation in journal bearing using acoustic emission and vibration measurement techniques. *Journal of Tribology*, 142(12).

Pugh, S. (1981, March). Concept selection: a method that works. In *Proceedings of the International conference on Engineering Design* (pp. 497-506).

Pugh, S. (1996) *Creative Innovative Products Using Total Design*, p.544, Addison-Wesley.

Rakopoulos, C. D., Giakoumis, E. G., & Michos, C. N. (2005). *Study of the transient behavior of turbocharged diesel engines including compressor surging using a linearized quasi-steady analysis* (pp. 37-52). Society of Automotive Engineers.

Rao, T. V. V. L. N., A Rani, A. M., Mohamed, N. M., Ya, H. H., Awang, M., & M Hashim, F. (2020). Static and stability analysis of partial slip texture multi-lobe journal bearings. *Proceedings of the Institution of Mechanical Engineers, Part J: Journal of Engineering Tribology*, 234(4), 567-587.

Ravaglioli, V., Cavina, N., Cerofolini, A., Corti, E., Moro, D., & Ponti, F. (2015). Automotive turbochargers power estimation based on speed fluctuation analysis. *Energy Procedia*, 82, 103-110.

Ren, G. (2020). A New Method to Calculate Water Film Stiffness and Damping for Water Lubricated Bearing with Multiple Axial Grooves. *Chinese Journal of Mechanical Engineering*, 33(1), 1-18.

Robbersmyr, K. G., Olsen, H., Karimi, H. R., & Tønder, K. (2014). Oil whip-induced wear in journal bearings. *The International Journal of Advanced Manufacturing Technology*, 73(5), 973-980.

Rogers, L. M. (1979). The application of vibration signature analysis and acoustic emission source location to on-line condition monitoring of anti-friction bearings. *Tribology international*, 12(2), 51-58.

Romero, C. C. (2004). *Contribución a la caracterización experimental y al modelado de turbinas de geometría variable en grupos de sobrealimentación* (Doctoral dissertation, PhD thesis. Universitat Politècnica de València).

Rotax (2019). *Operators Manual for Rotax engine type 914 series*. Rotax Aircraft Engines.

Roushenas, R., Razmi, A. R., Soltani, M., Torabi, M., Dusseault, M. B., & Nathwani, J. (2020). Thermo-environmental analysis of a novel cogeneration system based on solid oxide fuel cell (SOFC) and compressed air energy storage (CAES) coupled with turbocharger. *Applied Thermal Engineering*, 181, 115978.

Rowell, J., & Jaswal, I. (2017, August 18). Gas Turbine Uprates – Plant considerations and pitfalls. *Power Engineering*. <https://www.power-eng.com/gas/gas-turbine-uprates/#gref>

Roy, B., Roy, L., & Dey, S. (2021). Effect of Eccentricity and Surface Roughness on Probabilistic Performance of Two Axial Groove Bearing. *Journal of Engineering for Gas Turbines and Power*, 143(10).

Roy, L., & Kakoty, S. K. (2013). Optimum groove location of hydrodynamic journal bearing using genetic algorithm. *Advances in Tribology*, 2013.

Roy, L., & Majumdar, B. C. (2005). Effect of the location of axial groove on the steady state and dynamic characteristics of oil journal bearings. In *National conference on Machines and Mechanisms, (December (16-17). pages 261–268*.

Rubio, D., & Andrés, L. S. (2006). Bump-type foil bearing structural stiffness: experiments and predictions.

Rus, T., Dular, M., Širok, B., Hočevár, M., & Kern, I. (2007). An investigation of the relationship between acoustic emission, vibration, noise, and cavitation structures on a Kaplan turbine.

Rush, A. A. (1979). Kurtosis-crystal ball for maintenance engineers. *Iron and Steel International*, 52(1), 23.

Ryu, K., & Ashton, Z. (2016). Bump-type foil bearings and flexure pivot tilting pad bearings for oil-free automotive turbochargers: highlights in rotordynamic performance. *Journal of Engineering for Gas Turbines and Power*, 138(4).

Ryu, K., & Ashton, Z. (2017). Oil-free automotive turbochargers: drag friction and on-engine performance comparisons to oil-lubricated commercial turbochargers. *Journal of Engineering for Gas Turbines and Power*, 139(3).

Ryu, K., & Yi, H. (2018). Wire mesh dampers for semi-floating ring bearings in automotive turbochargers: measurements of structural stiffness and damping parameters. *Energies*, 11(4), 812.

- Sadegh, H., Mehdi, A. N., & Mehdi, A. (2016). Classification of acoustic emission signals generated from journal bearing at different lubrication conditions based on wavelet analysis in combination with artificial neural network and genetic algorithm. *Tribology International*, 95, 426-434.
- Sahu, K., & Sharma, S. C. (2019). A simulation study on the behavior of magnetorheological fluid on Herringbone-grooved hybrid slot-entry bearing. *Tribology Transactions*, 62(6), 1099-1118.
- San Andrés, L., & Kerth, J. (2004). Thermal effects on the performance of floating ring bearings for turbochargers. *Proceedings of the Institution of Mechanical Engineers, Part J: Journal of Engineering Tribology*, 218(5), 437-450.
- San Andrés, L., Barbarie, V., Bhattacharya, A., & Gjika, K. (2012). On the effect of thermal energy transport to the performance of (semi) floating ring bearing systems for automotive turbochargers. *Journal of Engineering for Gas Turbines and Power*, 134(10).
- San Andres, L., Rivadeneira, J. C., Gjika, K., Groves, C., & LaRue, G. (2007). Rotordynamics of small turbochargers supported on floating ring bearings—highlights in bearing analysis and experimental validation.
- San Andrés, L., Yu, F., & Gjika, K. (2018). On the Influence of Lubricant Supply Conditions and Bearing Configuration to the Performance of (Semi) Floating Ring Bearing Systems for Turbochargers. *Journal of Engineering for Gas Turbines and Power*, 140(3).
- Sanchez, P. K. (2019, October 29). Turbo Failure!. *Aviation Safety*. <https://www.aviationsafetymagazine.com/features/turbo-failure/>
- Sandoval, O. R. (2019). *Metodologias de caracterização de falhas no compressor centrífugo de turbocompressores automotivos* (Doctoral dissertation, Federal University of Minas Gerais).
- Sandoval, O. R., Machado, L. H. J., Caetano, B. C., Lara, I. F., & Molina, R. (2018, September). Influence of Temperature and Injection Pressure of Lubrication in the Vibration of an Automotive Turbocharger. In *International Conference on Rotor Dynamics* (pp. 388-397). Springer, Cham.
- Sause, M. G. (2011). Investigation of pencil-lead breaks as acoustic emission sources. *Journal of Acoustic Emission*, 29, 184-197.
- Sawicki, J. T., Sen, A. K., & Litak, G. (2009). Multiresolution wavelet analysis of the dynamics of a cracked rotor. *International Journal of Rotating Machinery*, 2009.
- Schlegel, V. (1984). Vibration Measurement and Monitoring. In *Dynamics of Rotors* (pp. 333-351). Springer, Vienna.

- Schwarz, J. B., & Andrews, D. N. (2014, October). Considerations for gas stand measurement of turbocharger performance. In *Proceedings 11th International Conference on Turbochargers and Turbocharging* (pp. 253-264).
- Schweizer, B. (2009). Oil whirl, oil whip and whirl/whip synchronization occurring in rotor systems with full-floating ring bearings. *Nonlinear Dynamics*, 57(4), 509-532.
- Schweizer, B. (2010). Dynamics and stability of turbocharger rotors. *Archive of Applied Mechanics*, 80(9), 1017-1043.
- Schweizer, B., & Sievert, M. (2009). Nonlinear oscillations of automotive turbocharger turbines. *Journal of Sound and Vibration*, 321(3-5), 955-975.
- Serrano, J. R., Guardiola, C., Dolz, V., Tiseira, A., & Cervelló, C. (2007). *Experimental study of the turbine inlet gas temperature influence on turbocharger performance* (No. 2007-01-1559). SAE Technical Paper.
- Serrano, J. R., Olmeda, P., Arnau, F. J., & Samala, V. (2020). A holistic methodology to correct heat transfer and bearing friction losses from hot turbocharger maps in order to obtain adiabatic efficiency of the turbomachinery. *International Journal of Engine Research*, 21(8), 1314-1335.
- Serrano, J. R., Olmeda, P., Arnau, F. J., Dombrovsky, A., & Smith, L. (2015). Turbocharger heat transfer and mechanical losses influence in predicting engines performance by using one-dimensional simulation codes. *Energy*, 86, 204-218.
- Serrano, J. R., Olmeda, P., Páez, A., & Vidal, F. (2010). An experimental procedure to determine heat transfer properties of turbochargers. *Measurement Science and Technology*, 21(3), 035109.
- Serrano, J. R., Olmeda, P., Tiseira, A., García-Cuevas, L. M., & Lefebvre, A. (2013(b)). Theoretical and experimental study of mechanical losses in automotive turbochargers. *Energy*, 55, 888-898.
- Serrano, J., Olmeda, P., Arnau, F., Reyes-Belmonte, M., & Lefebvre, A. (2013(a)). Importance of heat transfer phenomena in small turbochargers for passenger car applications. *SAE International Journal of Engines*, 6(2), 716-728.
- Seydel, J. (2006). Data envelopment analysis for decision support. *Industrial Management & Data Systems*, 106(1), 81-95.
- Sharma, S. C., & Tomar, A. K. (2021). Study on MR fluid hybrid hole-entry spherical journal bearing with micro-grooves. *International Journal of Mechanical Sciences*, 202, 106504.
- Sharma, S., Broatch, A., García-Tíscar, J., Allport, J. M., & Nickson, A. K. (2019). Acoustic characterisation of a small high-speed centrifugal compressor with casing treatment: An experimental study. *Aerospace Science and Technology*, 95, 105518.

Sharma, S., García-Tíscar, J., Allport, J. M., Jupp, M. L., & Nickson, A. K. (2018, June). Impact of impeller casing treatment on the acoustics of a small high speed centrifugal compressor. In *Turbo Expo: Power for Land, Sea, and Air* (Vol. 51005, p. V02BT43A010). American Society of Mechanical Engineers.

Shooroki, A. R., Rahmatabadi, A. D., & Mehrjardi, M. Z. (2021). Effect of using hybrid nano lubricant on the thermo-hydrodynamic performance of two lobe journal bearings. *Proceedings of the Institution of Mechanical Engineers, Part J: Journal of Engineering Tribology*, 13506501211053089.

Shoup, T. P., & Lawrence, J. (2016). *U.S. Patent No. 9,410,572*. Washington, DC: U.S. Patent and Trademark Office.

Sikorska, J. Z., & Mba, D. (2008). Challenges and obstacles in the application of acoustic emission to process machinery. *Proceedings of the Institution of Mechanical Engineers, Part E: Journal of Process Mechanical Engineering*, 222(1), 1-19.

Singh, A., & Gupta, T. C. (2020). Effect of rotating unbalance and engine excitations on the nonlinear dynamic response of turbocharger flexible rotor system supported on floating ring bearings. *Archive of Applied Mechanics*, 90(5), 1117-1134.

Singh, U., Roy, L., & Sahu, M. (2008). Steady-state thermo-hydrodynamic analysis of cylindrical fluid film journal bearing with an axial groove. *Tribology International*, 41(12), 1135-1144.

Sirakov, B., & Casey, M. (2013). Evaluation of heat transfer effects on turbocharger performance. *Journal of Turbomachinery*, 135(2).

Smolík, L., & Dyk, Š. (2020). Towards efficient and vibration-reducing full-floating ring bearings in turbochargers. *International Journal of Mechanical Sciences*, 175, 105516.

Society of Automotive Engineers. (1995). *SAE Standard J1723 - Supercharger Testing Standard* (Standard No. SAE J1723).

Society of Automotive Engineers. (2011). *SAE Standard J922 - Turbocharger Nomenclature and Terminology* (Standard No. SAE J922).

Society of Automotive Engineers. (2022). *SAE Standard J1826 - Turbocharger Gas Stand Test Code* (Standard No. SAE J1826).

Solaguren-Beascoa Fernández, M., Alegre Calderón, J. M., & Bravo Díez, P. M. (2009). Implementation in MATLAB of the adaptive Monte Carlo method for the evaluation of measurement uncertainties. *Accreditation and Quality Assurance*, 14(2), 95-106.

Storage, A. F., Wisler, D. C., Shin, H. W., Beacher, B. F., Ehrich, F. F., Spakovszky, Z. S., Martinez-Sanchez, M. & Song, S. J. (2001). Unsteady flow and whirl-inducing

- forces in axial-flow compressors: Part I—experiment. *J. Turbomach.*, 123(3), 433-445.
- Strogatz, S. H. (2018). *Nonlinear dynamics and chaos: with applications to physics, biology, chemistry, and engineering*. CRC press.
- Subbiah, R., & Littleton, J. E. (2018). *Rotor and Structural Dynamics of Turbomachinery*. Springer, Berlin.
- Subedi, G. (2020, September). *How to make correct decisions using a Pugh Matrix & Weighted Matrix* [Article]. LinkedIn. <https://www.linkedin.com/pulse/how-make-correct-decisions-using-pugh-matrix-weighted-gunjan-subedi/>
- Sun, P., Fang, X., Zhuang, F., Chen, C., Shang, H., Liu, Y., & Yang, B. (2021). Evaluation of applicability of empirical models of turbine performance to aircraft engine. *Aerospace Science and Technology*, 117, 106953.
- Sunil, P. (2012). Turbocharging and oil techniques in light motor vehicles. *Research Journal of Recent Sciences*, 1(1), 60-65.
- Takai, S., & Ishii, K. (2004, January). Modifying Pugh's design concept evaluation methods. In *International Design Engineering Technical Conferences and Computers and Information in Engineering Conference* (Vol. 46962, pp. 415-424).
- Technavio. (2021). *Industrial turbocharger market by end-user and geography - Forecast and Analysis 2021-2025*. Infnit Research Limited.
- Teixeira, J. A. G. S. (2020). *Desenvolvimento de modelagem matemática e observador experimental para cálculo em tempo real das características de funcionamento de compressores radiais de turbocompressores automotivos* (Master thesis, Federal University of Minas Gerais).
- Teng, C., & Homco, S. (2009). Investigation of compressor whoosh noise in automotive turbochargers. *SAE international journal of passenger cars-mechanical systems*, 2(2009-01-2053), 1345-1351.
- The American Society of Mechanical Engineers. (2019). ASME Standard PTC 19.1 – Test Uncertainty (Standard No. PTC 19.1:2019).
- Theobald, P., Zeqiri, B., & Avison, J. (2008). Couplants and their influence on AE sensor sensitivity. *Journal of acoustic emission*, 26, 91-97.
- Tian, J., Liu, L., Zhang, F., Ai, Y., Wang, R., & Fei, C. (2019). Multi-domain entropy-random forest method for the fusion diagnosis of inter-shaft bearing faults with acoustic emission signals. *Entropy*, 22(1), 57.
- Tian, L., Wakelin, M., Lancaster, C., & Lindsay, M. (2016). The effect of oil film instability on power losses prediction of a turbocharger rotor-fully floating ring bearing system. *Cummins Turbo Technologies: Huddersfield, UK*.

Tian, L., Wang, W. J., & Peng, Z. J. (2012). Effects of bearing outer clearance on the dynamic behaviours of the full floating ring bearing supported turbocharger rotor. *Mechanical Systems and Signal Processing*, 31, 155-175.

Tian, L., Wang, W. J., & Peng, Z. J. (2013). Nonlinear effects of unbalance in the rotor-floating ring bearing system of turbochargers. *Mechanical Systems and Signal Processing*, 34(1-2), 298-320.

Toutountzakis, T., Tan, C. K., & Mba, D. (2005). Application of acoustic emission to seeded gear fault detection. *Ndt & E International*, 38(1), 27-36.

Transparency Market Research (2021). *Industrial Turbocharger Market - Global Industry Analysis, Size, Share, Growth, Trends, and Forecast, 2021-2031*. TMR.

Unnþórsson, R. (2013). Hit detection and determination in AE bursts. *Acoustic emission-research and applications*, 1-20.

Urbański, B., & Przybyła, G. (2022, September). Hybrid drivetrain systems 48 V in rally cars. In *Powertrains, Fuels & Lubricants Conference & Exhibition* (p. 96).

Vahaviolos, S. J. (Ed.). (1999). *Acoustic emission: standards and technology update* (Vol. 1353). ASTM International.

Vance, J. M. (1991). *Rotordynamics of turbomachinery*. John Wiley & Sons.

Varbanets, R., & Karianskiy, S. (2012). Analyse of marine diesel engine performance. *Journal of Polish CIMAC*, 7(1), 269-276.

Venson, G. G.. (2007). *Desenvolvimento de um banco de ensaios e da metodologia experimental para o levantamento das características operacionais de turbocompressores utilizando gás quente* (Doctoral dissertation, Federal University of Minas Gerais).

Vergeynst, L. L., Sause, M. G., De Baerdemaeker, N. J., De Roo, L., & Steppe, K. (2016). Clustering reveals cavitation-related acoustic emission signals from dehydrating branches. *Tree physiology*, 36(6), 786-796.

Wachel, J. (1975). Nonsynchronous instability of centrifugal compressors. *ASME paper*, 75-pet-22.

Wagner, M. B., Younan, A., Allaire, P., & Cogill, R. (2010). Model reduction methods for rotor dynamic analysis: a survey and review. *International Journal of Rotating Machinery*, 2010.

Wang, W., He, Y., Zhao, J., Mao, J., Hu, Y., & Luo, J. (2020). Optimization of groove texture profile to improve hydrodynamic lubrication performance: Theory and experiments. *Friction*, 8(1), 83-94.

- Wen, H. B., Xia, Z. W., & Wang, K. L. (2013). Experimental research on the vibration and noise characteristics of the marine diesel engine turbocharger. In *Applied Mechanics and Materials* (Vol. 239, pp. 438-442). Trans Tech Publications Ltd.
- Westfall, C. (2015, July 21). Understanding Compressor Maps – Sizing A Turbocharger. *Engine Labs*. <https://www.enginelabs.com/engine-tech/power-adders/understanding-compressor-maps-sizing-a-turbocharger/>
- Wodtke, M., & Litwin, W. (2021). Water-lubricated stern tube bearing-experimental and theoretical investigations of thermal effects. *Tribology International*, *153*, 106608.
- Wohlrab, R. (1983). *Experimental determination of gap flow-conditioned forces at turbine stages and their effect on the running stability of simple rotors* (No. NASA-TM-77293).
- Xiang, G., Han, Y., Chen, R., Wang, J., Ni, X., & Xiao, K. (2020). A hydrodynamic lubrication model and comparative analysis for coupled microgroove journal-thrust bearings lubricated with water. *Proceedings of the Institution of Mechanical Engineers, Part J: Journal of Engineering Tribology*, *234*(11), 1755-1770.
- Xiang, G., Han, Y., Wang, J., Xiao, K., & Li, J. (2019). A transient hydrodynamic lubrication comparative analysis for misaligned micro-grooved bearing considering axial reciprocating movement of shaft. *Tribology International*, *132*, 11-23.
- Xie, Z., & Zhu, W. (2022). An investigation on the lubrication characteristics of floating ring bearing with consideration of multi-coupling factors. *Mechanical Systems and Signal Processing*, *162*, 108086.
- Xie, Z., Wang, X., & Zhu, W. (2022). Theoretical and experimental exploration into the fluid structure coupling dynamic behaviors towards water-lubricated bearing with axial asymmetric grooves. *Mechanical Systems and Signal Processing*, *168*, 108624.
- Xie, Z., Wang, X., & Zhu, W. (2022). Theoretical and experimental exploration into the fluid structure coupling dynamic behaviors towards water-lubricated bearing with axial asymmetric grooves. *Mechanical Systems and Signal Processing*, *168*, 108624.
- Xie, Z., Zhang, Y., Zhou, J., & Zhu, W. (2021). Theoretical and experimental research on the micro interface lubrication regime of water lubricated bearing. *Mechanical Systems and Signal Processing*, *151*, 107422.
- Xie, Z., Zhang, Y., Zhou, J., & Zhu, W. (2021). Theoretical and experimental research on the micro interface lubrication regime of water lubricated bearing. *Mechanical Systems and Signal Processing*, *151*, 107422.
- Xu, F., Sun, Y., Zhang, G., & Liu, Z. (2019). Effect of bump structural friction on the performance of bump foil bearing and rotor dynamic behavior: Experimental

- study. *Proceedings of the Institution of Mechanical Engineers, Part J: Journal of Engineering Tribology*, 233(5), 702-711.
- Xue, X., & Wang, T. (2019). Stall recognition for centrifugal compressors during speed transients. *Applied Thermal Engineering*, 153, 104-112.
- Yang, J., Gao, Y., Liu, Z., Zhao, C., Kang, T., Gu, L., & Xu, B. (2016). A method for modeling and analyzing the rotor dynamics of a locomotive turbocharger. *Nonlinear Dynamics*, 84(1), 287-293.
- Yathish, K., Binu, K. G., Shenoy, B. S., Rao, D. S., & Pai, R. (2014). Study of TiO₂ nanoparticles as lubricant additive in two-axial groove journal bearing. *International Journal of Mechanical, Aerospace, Industrial and Mechatronics Engineering*, 8(11), 1723-1729.
- Ying, G., Meng, G., & Jing, J. (2009). Turbocharger rotor dynamics with foundation excitation. *Archive of Applied Mechanics*, 79(4), 287-299.
- Ying, G., Meng, G., & Jing, J. (2009). Turbocharger rotor dynamics with foundation excitation. *Archive of Applied Mechanics*, 79(4), 287-299.
- Ylönen, M., Saarenrinne, P., Miettinen, J., Franc, J. P., Fivel, M. C., & Laakso, J. (2020). Estimation of Cavitation Pit Distributions by Acoustic Emission. *Journal of Hydraulic Engineering*, 146(2), 04019064.
- Yoshioka, T., & Fujiwara, T. (1982). A new acoustic emission source locating system for the study of rolling contact fatigue. *Wear*, 81(1), 183-186.
- Yoshioka, T., & Fujiwara, T. (1984). Application of acoustic emission technique to detection of rolling bearing failure. *American society of mechanical engineers*, 14(1), 55-76.
- Yu, Z., Xu, X., & Guo, X. (2011). Failure investigation of a locomotive turbocharger main shaft and bearing sleeve. *Journal of failure analysis and prevention*, 11(2), 167-174.
- Yu, Z., Xu, X., & Yu, H. (2015). Failure Analysis of the Related Components of a Locomotive Turbocharger. *Journal of Failure Analysis and Prevention*, 15(3), 407-416.
- Zeh, C., Willers, O., Hagemann, T., Schwarze, H., & Seume, J. R. (2020, September). Evaluation of the rotor temperature distribution of an automotive turbocharger under hot gas conditions including indirect experimental validation. In *Turbo Expo: Power for Land, Sea, and Air* (Vol. 84089, p. V02CT35A051). American Society of Mechanical Engineers.
- Zeidan, F. Y. (1989). *Cavitation effects on the performance of squeeze film damper bearings* (Doctoral dissertation, Texas A&M University).

Zeidan, F. Y., & Paquette, D. J. (1994). Application Of High Speed And High Performance Fluid Film Bearings In Rotating Machinery. In *Proceedings of the 23rd turbomachinery symposium*. Texas A&M University. Turbomachinery Laboratories.

Zeng, T., Upadhyay, D., Sun, H., & Zhu, G. G. (2016, July). Physics-based turbine power models for a Variable Geometry Turbocharger. In *2016 American Control Conference (ACC)* (pp. 5099-5104). IEEE.

Zhang, C., Men, R., Wang, Y., He, H., & Chen, W. (2019(a)). Experimental and numerical investigation on thermodynamic performance of full-floating ring bearings with circumferential oil groove. *Proceedings of the Institution of Mechanical Engineers, Part J: Journal of Engineering Tribology*, 233(8), 1182-1196.

Zhang, C., Wang, Y., Men, R., He, H., & Chen, W. (2019(b)). Dynamic behaviors of a high-speed turbocharger rotor on elliptical floating-ring bearings. *Proceedings of the Institution of Mechanical Engineers, Part J: Journal of Engineering Tribology*, 233(12), 1785-1799.

Zhang, C., Wang, Y., Men, R., He, H., & Chen, W. (2020). The effect of three-lobed bearing shapes in floating-ring bearings on the nonlinear oscillations of high-speed rotors. *Proceedings of the Institution of Mechanical Engineers, Part J: Journal of Engineering Tribology*, 234(5), 751-769.

Zhang, J., Li, N., Chen, Y., Zhai, J., Han, Q., & Hou, Z. (2022). A method of in-situ monitoring multiple parameters and blade condition of turbomachinery by using a single acoustic pressure sensor. *Mechanical Systems and Signal Processing*, 173, 109051.

Zheng, X., Sun, Z., Kawakubo, T., & Tamaki, H. (2017). Experimental investigation of surge and stall in a turbocharger centrifugal compressor with a vaned diffuser. *Experimental Thermal and Fluid Science*, 82, 493-506.

Zulhanafi, P., Syahrullail, S., & Ahmad, M. A. (2020). The tribological performance of hydrodynamic journal bearing using bio-based lubricant. *Tribology in Industry*, 42(2), 278.

APPENDIX A – Original and brand new fluid film bearings technical details of manufacturing and assembly

This appendix present some technical details of design, manufacturing and assembly of the original fluid film bearing used in the current BIAGIO AUT1000 Turbocharger.

Figure 119 shows the original journal bearings used in the BIAGIO AUT1000, with a lateral view (showing the external grooves for oil supply between the bearing inner part and the housing, and the internal lubrication hole) and an isometric view (showing the original axial grooves for oil supply between the bearing outer part and the shaft).

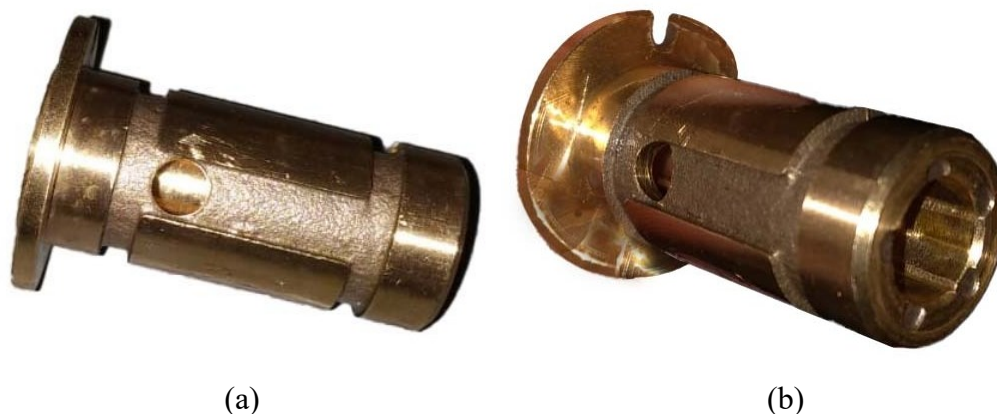


Figure 119 – (a) The fluid film journal bearing lateral view and (b) the isometric view.

The original journal bearing from AUT1000 uses a cast bearing model as initial base for a machining process with a CNC machining. During this process, the triangular internal axial is manufactured by broaching. This is the final process during the machining of cast bronze journal bearing and it produces five triangular axial grooves. Figure 120 displays the unprocessed cast bronze journal bearing and the journal bearing during the machining.

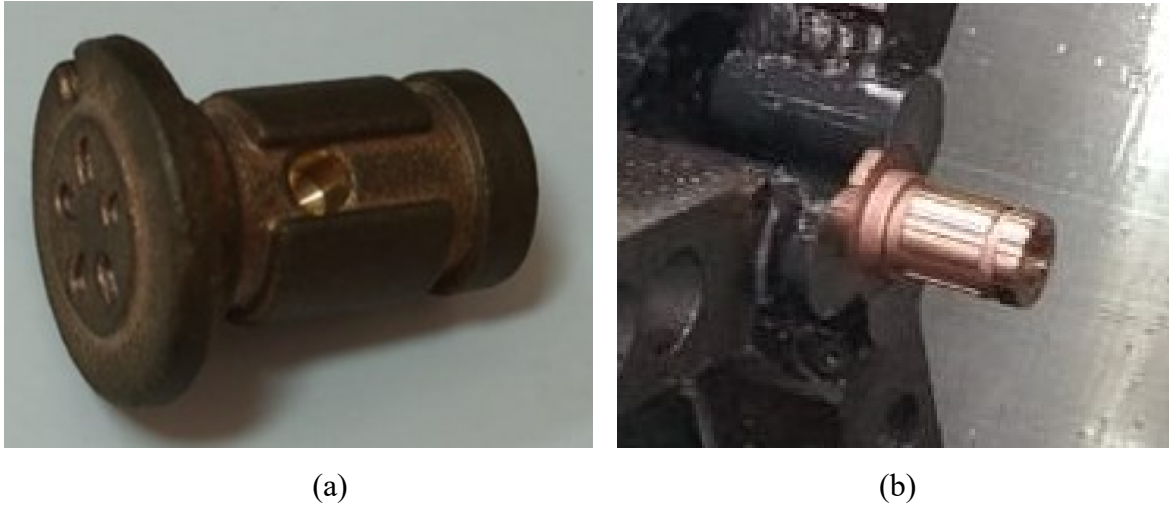


Figure 120 – cast bronze journal (a) before and (b) during the machining process

All the machining process are made in MGFC company as well, with a final tolerances check of various journal bearing dimensions. The Figure 121 shows some of the the metrology equipment, while Figure 122 and Table 48 present the tolerances allowed for a AUT100 journal bearing

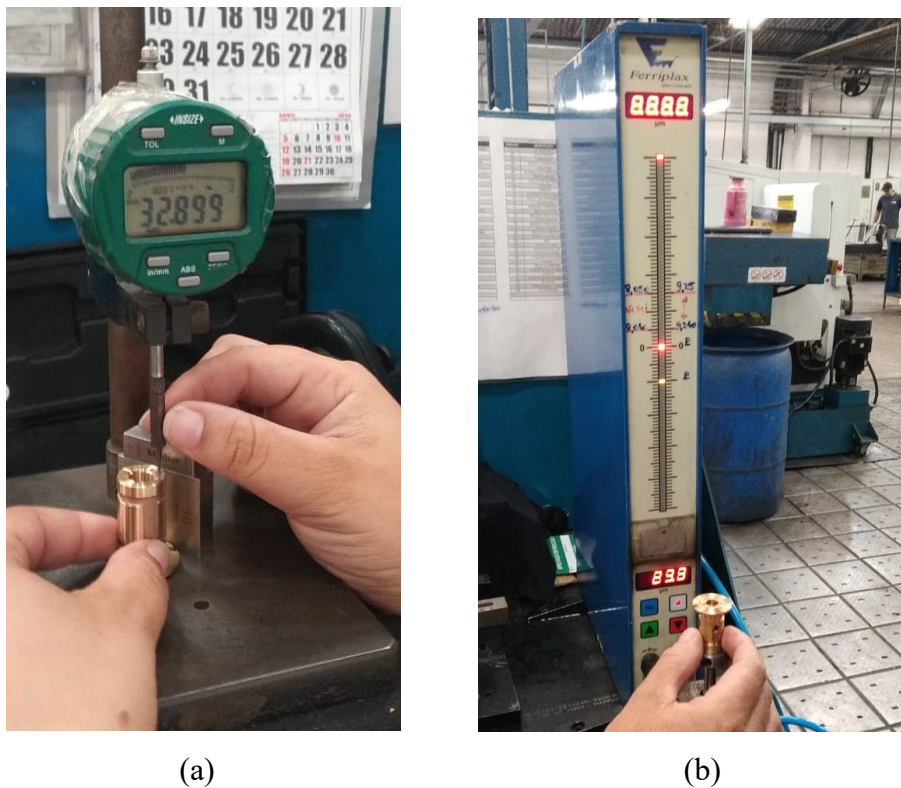


Figure 121 – Metrology verification of final AUT1000 journal bearing: (a) Full length of double bearing; and (b) Bearing internal diameter

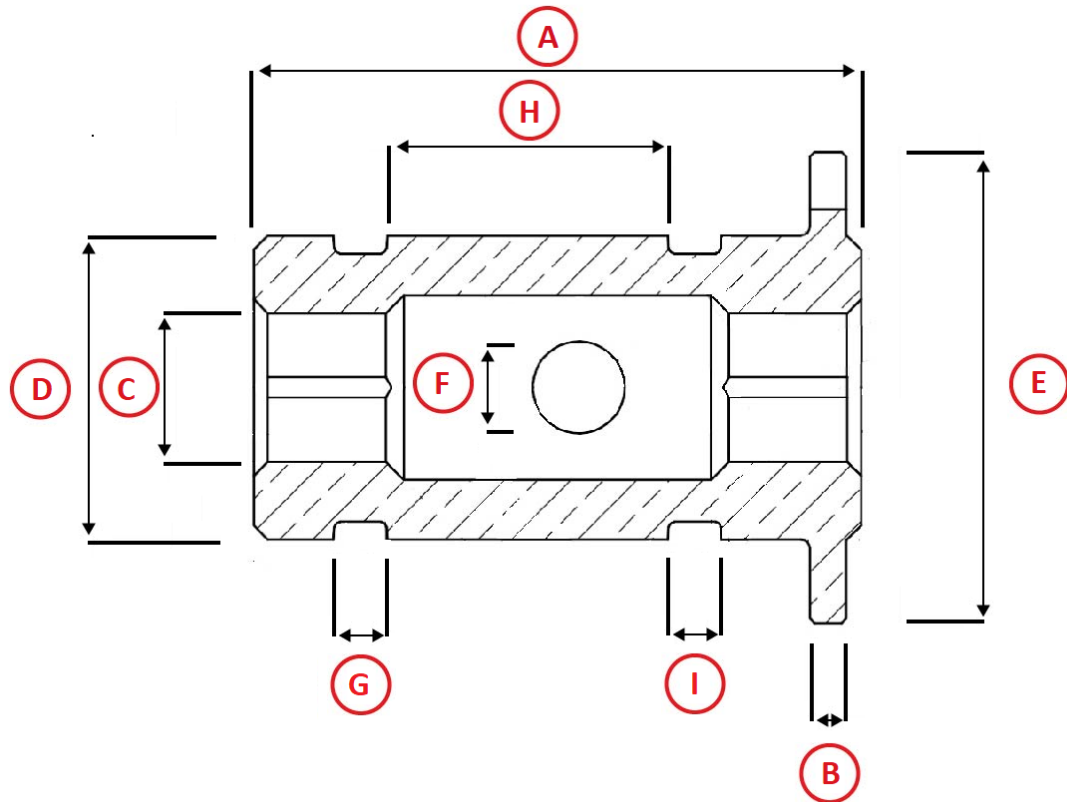


Figure 122 – Tolerances verified in AUT1000 journal bearing production

Table 48 – Dimensions and tolerances for AUT1000 journal bearing

Mark	Description	Dimension & Tolerance [mm]
A	Full length of double bearing	32.9 ± 0.01
B	Full thickness of axial support	1.97 ± 0.01
C	Bearing internal diameter (contact area)	8.045 ± 0.005
D	Bearing external diameter	16.44 (min) to 16.47 (max)
E	Diameter of axial support	25.5 ± 0.1
F	Diameter of internal lubrication hole	5.2 ± 0.25
G	Diameter of external rebound (opposite to axial support side)	14.2 ± 0.25
H	External length between rebounds	13.1 ± 0.1
I	Diameter of external rebound (same side of axial support)	14.2 ± 0.25

Dimensions measured at MGFC Ltd. for bearing approval are shown in Appendix B.

For the brand new bearings, a wire EDM machining is chose to manufacture the new groove shapes. Figure 123 shows 15 (fifteen) journal bearings (without axial grooves) manufactured. 11 (eleven) is approved after the factory metrological analysis. A stricter metrological analysis is performed and 7 (seven) are chosen to produce the axial grooves in the wire EDM machining.

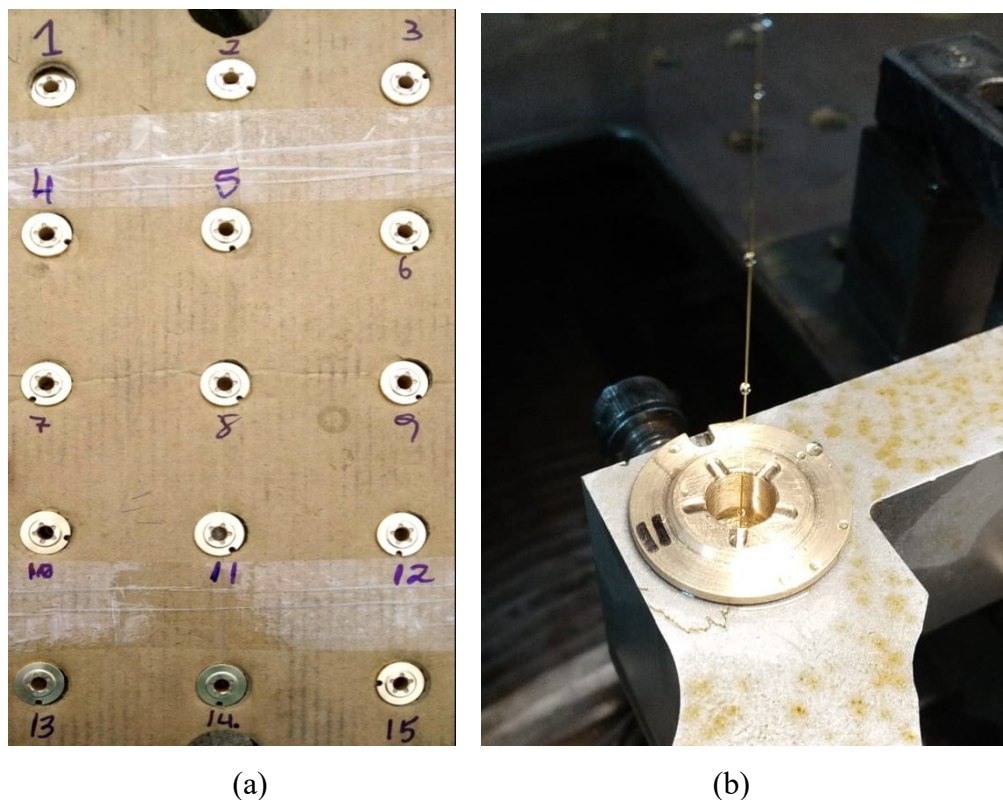


Figure 123 – (a) Journal bearings without axial grooves and (b) wire EDM machining manufacturing the different axial grooves shapes

The wire EDM uses CAD files with a CAM support to machining with precision the axial grooves. All the EDM is carried out at the Motoliga Ltd., located in Belo Horizonte, Minas Gerais, Brazil. Figure 124 shows the image during the machining.

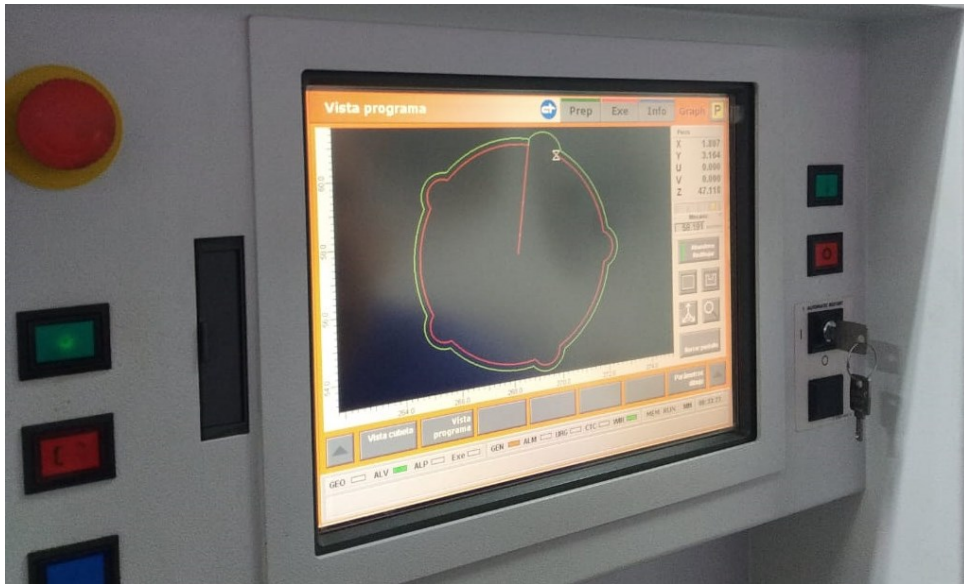









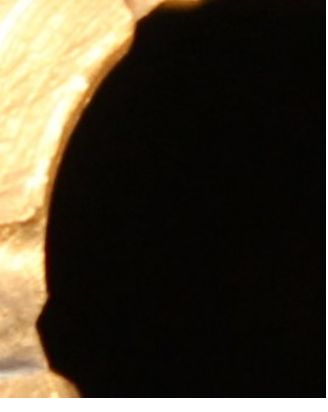



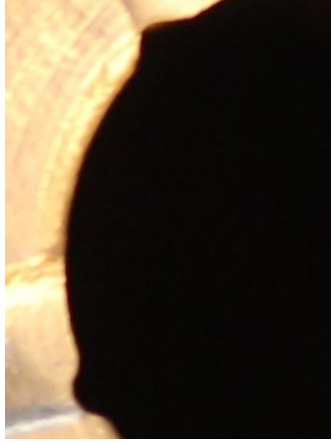

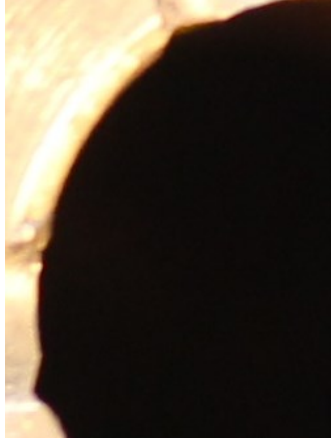
Figure 124 – On-time wire EDM machining during the process of axial groove production.

After the EDM machining, all journal bearings are cataloged. Table 49 present the real brand new journal bearing:

Table 49 – Final grooves of journal bearings and zoom at grooves

Groove shape	Final grooves	Groove zoom
Half-ellipse		

Groove shape	Final grooves	Groove zoom
Quarter-ellipse	 A top-down view of a brass-colored metal ring with a central hole and four radial spokes. A groove is cut into the ring's surface. The number '10' is handwritten in black ink on the left side of the ring.	 A close-up, high-contrast photograph of the groove's profile, showing a smooth, quarter-elliptical cross-section.
Inverted quarter-ellipse	 A top-down view of a brass-colored metal ring with a central hole and four radial spokes. A groove is cut into the ring's surface. The number '2' is handwritten in black ink on the left side of the ring.	 A close-up, high-contrast photograph of the groove's profile, showing an inverted quarter-elliptical cross-section.
Rectangular	 A top-down view of a brass-colored metal ring with a central hole and four radial spokes. A groove is cut into the ring's surface. The number '11' is handwritten in black ink on the left side of the ring.	 A close-up, high-contrast photograph of the groove's profile, showing a rectangular cross-section.
Trapezoidal	 A top-down view of a brass-colored metal ring with a central hole and four radial spokes. A groove is cut into the ring's surface. The number '12' is handwritten in black ink on the left side of the ring.	 A close-up, high-contrast photograph of the groove's profile, showing a trapezoidal cross-section.

Groove shape	Final grooves	Groove zoom
Circular		
Triangular		

As explained in Chapter 3, for a better logistics at the workbench tests, each brand new bearing are mounted at new rotor systems (Figure 125).



(a)



(b)

Figure 125 – Rotor-bearing at start (a) and at the end (b) of the assembly process

APPENDIX B – Metrological analysis of the brand new journal bearings

The metrological analysis of the bearings aims to verify the external and internal dimensions of the bearing, as well as each of the five grooves produced for each of the seven bearings produced in the metrological analysis considered in this study.

B.1. Metrological analysis of bearings externally and internally

After manufacturing each bearing, all are analyzed metrologically as described in section 3.3.1.

The apparatus for the internal and external dimensions of the bearing are property of MGFC Ltd., according to the factory's own standards, informed by it that all follow the necessary standards and are perfectly calibrated. Therefore, the data presented here are those informed by the factory and considered for the initial evaluation of the bearings.

This study considered a metrological analysis more restricted than the factory one to obtain the bearings closest to geometric characteristics, mainly in relation to the internal radius to produce the grooves (dimension B in Figure 121). This study considered a metrological analysis more restricted than the factory one to obtain the bearings closest to geometric characteristics, mainly in relation to the internal radius to manufacture the grooves (dimension B in Figure 126).

Figure 126 presents the dimensions analyzed and Table 50 shows for each of the fifteen bearings produced its dimensions and the seven chosen for manufacturing.

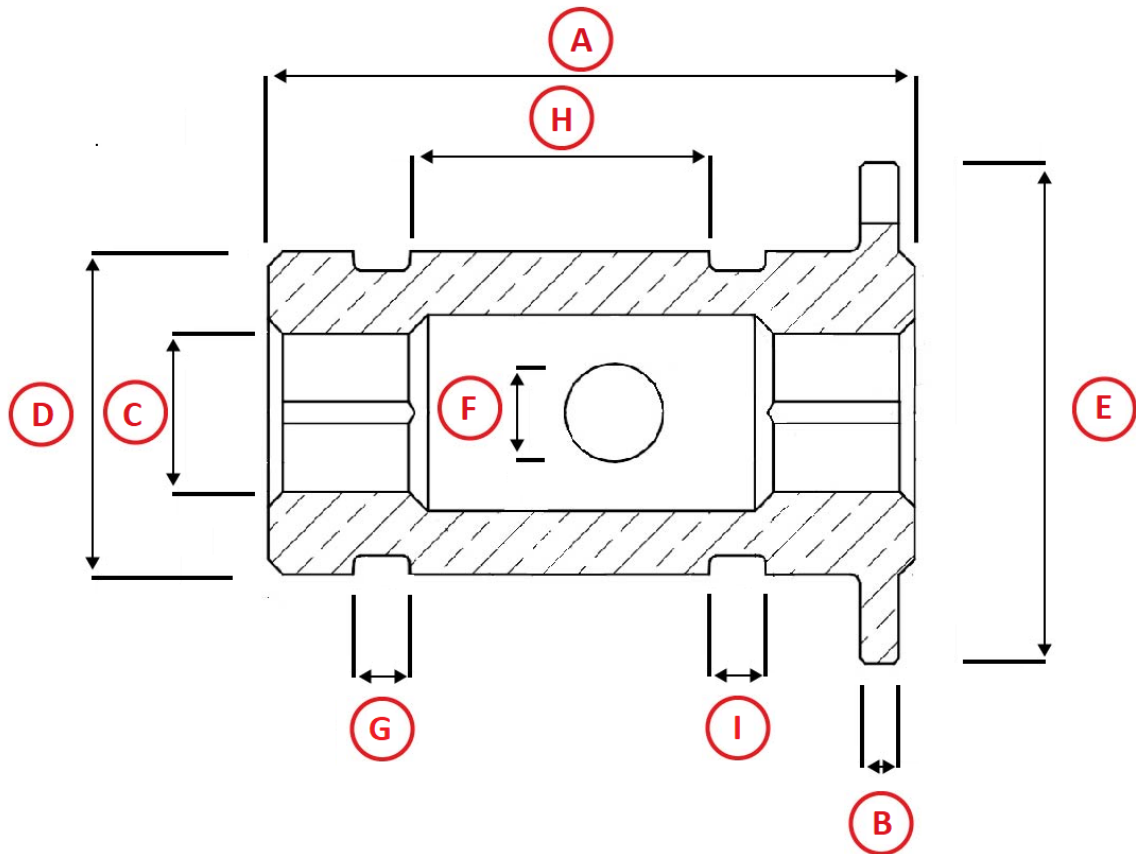


Figure 126 – Dimensions to be verified in AUT1000 journal bearing production

Table 50 – Geometric measures and tolerances of each bearing produced and verified by MGFC Ltd. (all measures in mm) – green (approved) and red (not approved)

Measures	A	B	C	D	E	F	G	H	I
Bearing	A	B	C	D	E	F	G	H	I
As designed	32.9	1.9	8.05	16.4	25.5	5.2	14.2	13.1	14.2
Tolerance	± 0.2	± 0.2	± 0.05	± 0.25	± 0.25	± 0.25	± 0.2	± 0.2	± 0.2
1	32.90	1.80	8.10	16.30	25.35	5.35	14.15	13.25	14.35
2	32.75	1.85	8.15	16.30	25.35	5.25	14.40	13.20	14.50
3	33.00	1.75	8.15	16.25	25.35	5.25	14.30	13.20	14.40
4	32.75	1.85	8.10	16.30	25.35	5.35	14.30	13.25	14.05
5	32.35	1.50	8.10	16.30	25.30	5.25	13.55	13.20	13.70
6	32.70	1.75	8.10	16.30	25.35	5.30	14.40	13.20	14.35
7	32.80	1.70	8.10	16.30	25.35	5.25	14.35	13.00	14.40
8	32.70	1.80	8.10	16.30	25.30	5.30	14.15	13.20	14.05
9	32.70	1.65	8.10	16.30	25.35	5.25	14.25	13.20	14.20
10	32.80	1.80	8.10	16.30	25.35	5.30	14.25	13.25	14.00
11	32.80	1.80	8.10	16.30	25.35	5.30	14.30	13.20	14.10

B.2. Experimental apparatus for metrological groove analysis

To analyze the dimensions of all grooves in each bearing, a measuring microscope from the Metrology Laboratory of the Federal University of Minas Gerais is used.

The Measuring Microscope “TM-505”, manufactured by Mitutoyo Sul Americana Ltd., shown in Figure 127 and Table 51 is used.

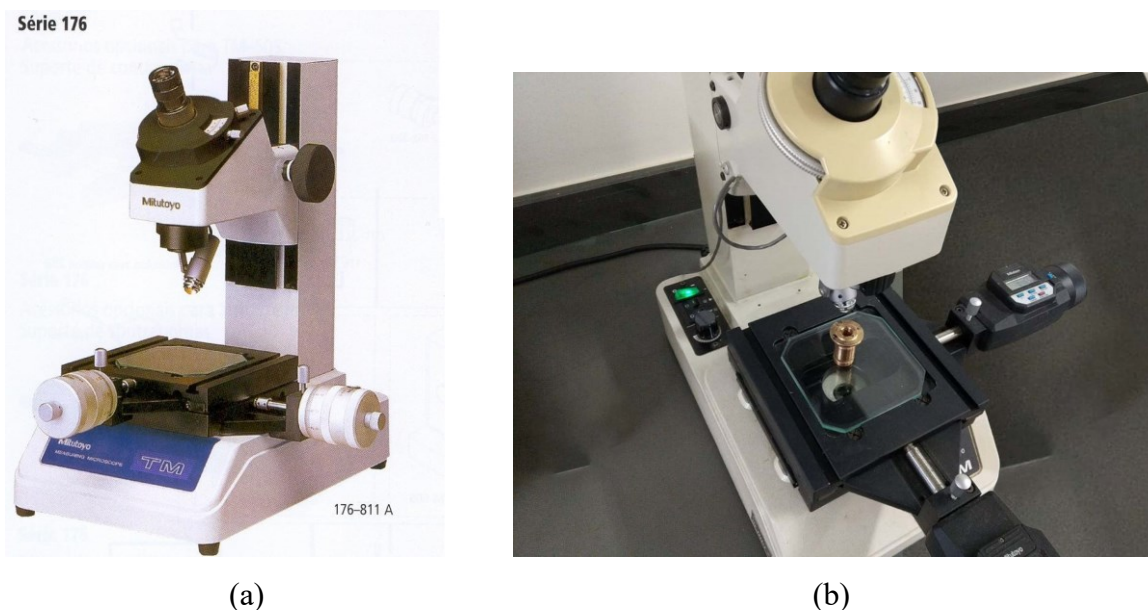


Figure 127 – Model TM-505 Measuring Microscope (MITUTOYO, 2019).

Table 51 – Main characteristics of the Measuring Microscope (MITUTOYO, 2019).

Manufacturer	Mitutoyo Sul Americana Ltd.
Model / P/N	TM-505 / 176-811 A
Maximum height of the piece	115 mm
Maximum piece weight	5 kg
Reading angle	360° (Graduation 6' Vernier)
Dimensions	210 mm x 333 mm x 391 mm
Weight	13.5 kg

The microscope slide table used with the measuring microscope is intended to guide the micrometer spindles to obtain the desired dimension, with characteristics presented in Table 52.

Table 52 – Characteristics of the microscope slide table used (MITUTOYO, 2019).

Manufacturer	Mitutoyo Sul Americana Ltd.
P/N	176-206
Capacidade geométrica (eixo X e Y)	50 mm x 50 mm

The characteristics of the set of lenses used (ocular and objective lens) are shown in Table 53.

Table 53 – Characteristics of the ocular and objective lens used (MITUTOYO, 2019).

Manufacturer	Mitutoyo Sul Americana Ltd.
P/N - ocular lens	176-116
Magnification - ocular lens	15 times
P/N – objective lens	176-137
Magnification – objective lens	10 times
Overall magnification	150 times
Field of view (FoV)	1.3 mm

The measurement system used consists of 2 micrometric digital heads, as shown in Figure 128. The characteristics of these heads are shown in Table 54.

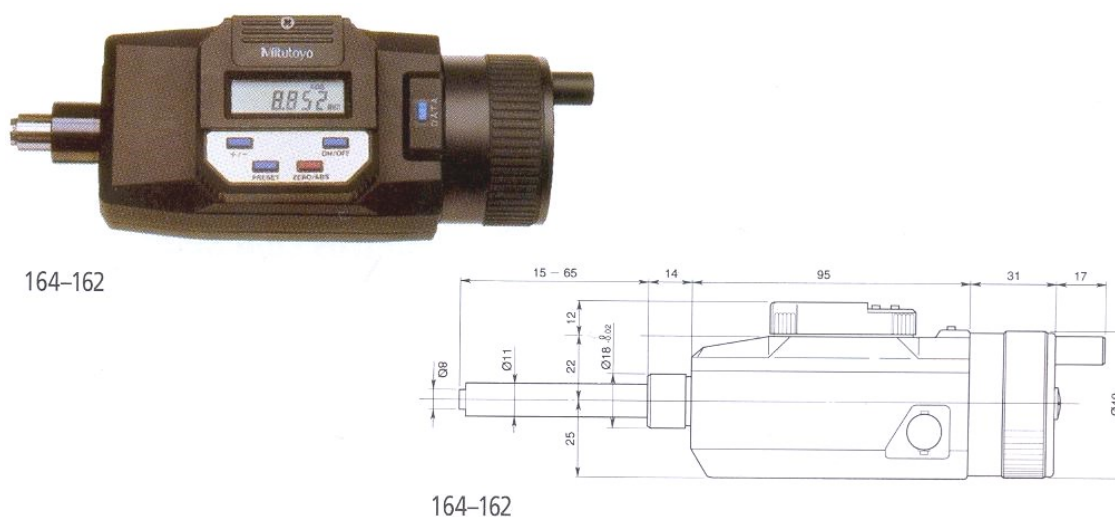


Figure 128 – Micrometric Head 164-162 (MITUTOYO, 2019).

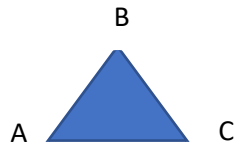
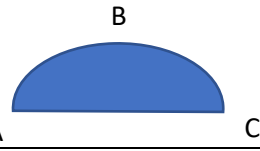
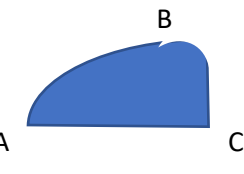
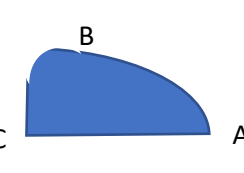
Table 54 – Characteristics of Digital Micrometric Heads (MITUTOYO, 2019).

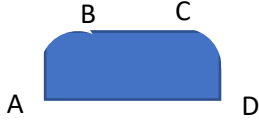
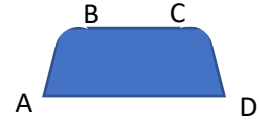
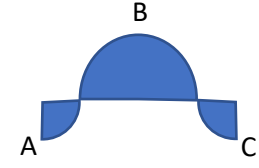
Manufacturer	Mitutoyo Sul Americana Ltda.
P/N	164-162
Capacity	0 mm to 50 mm
Resolution	0.001 mm
Accuracy	± 0.003 mm
Weight	500 g
Battery (P/N)	SR-44 (938882)

Before assembling the bearings on the rotor bench, they are all analyzed metrologically using the measuring microscope to check the groove shapes.

For each type of groove, some reference points are chosen to be measured, presented in Table 55, which are the main geometric characteristics. All grooves have three referential points, except rectangular and trapezoidal, that have four. All reference points are explained, mainly due to the radius of the wire EDM. All reference drawings show the points where the radius of the wire directly interferes with the manufacture of the groove.

Table 55 – Reference points and details for the metrological analysis

Turbocharger (bearing axial groove shape)	Reference Points	Details
TC 1 (triangular)		<ul style="list-style-type: none"> - Wire radius interference: Point B; - Points A and C measured from the detection of the exit from the bearing perimeter and entry into the groove; - Point B: Maximum height
TC 2 (half- ellipse)		<ul style="list-style-type: none"> - Points A and C measured from the detection of the exit from the bearing perimeter and entry into the groove; - Point B: Maximum height
TC 3 (quarter- ellipse)		<ul style="list-style-type: none"> - Wire radius interference: Point B; - Points A and C measured from the detection of the exit from the bearing perimeter and entry into the groove; - Point B: Maximum shape height before start the wire radius;
TC 4 (inverted quarter-ellipse)		<ul style="list-style-type: none"> - Wire radius interference: Point B; - Points A and C measured from the detection of the exit from the bearing perimeter and entry into the groove; - Point B: Maximum shape height before start the wire radius;

Groove	Reference Points	Details
TC 5 (rectangular)		<ul style="list-style-type: none"> - Wire radius interference: Points B and C; - Points A and D measured from the detection of the exit from the bearing perimeter and entry into the groove; - Points B and C: Maximum shape height before start the wire radius;
TC 6 (trapezoidal)		<ul style="list-style-type: none"> - Wire radius interference: Points B and C; - Points A and D measured from the detection of the exit from the bearing perimeter and entry into the groove; - Points B and C: Maximum shape height before start the wire radius;
TC 7 (half-circle)		<ul style="list-style-type: none"> - Points A and C measured from the detection of the exit from the bearing perimeter and entry into the groove; - Point B: Maximum height

Five measurements are taken of each reference points for each groove for each of the 7 bearings used. Figure 129 presents a schematic drawing showing the groove count, always the outer cut portion of the SFRB bearing clamping pin.

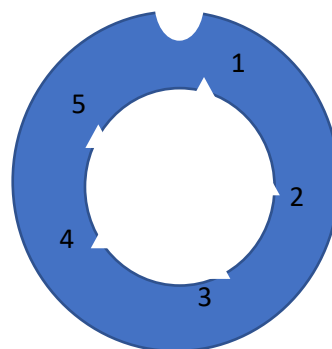


Figure 129 – Schematic drawing with the reference number of each groove.

With the reference points, it is possible to obtain the two main characteristics for this work:

1. the perimeter projection (width) of each groove: 1.090 mm (as designed);
and
2. the area of each groove: 0.171 mm² (as designed) which are shown in Tables 56 to 62, showing the measurements of grooves 1 to 5 of each groove shape.

Table 56 – Theoretical and manufactures measures for TC 1 (triangular groove).

Groove	Measures	1	2	3	4	5
# 1	Width (mm)	1.048	1.181	1.097	1.182	1.196
	Area (mm ²)	0.164	0.165	0.163	0.157	0.160
# 2	Width (mm)	1.138	1.198	1.201	1.220	1.216
	Area (mm ²)	0.178	0.183	0.181	0.163	0.192
# 3	Width (mm)	1.116	1.221	1.068	1.132	1.105
	Area (mm ²)	0.173	0.159	0.178	0.184	0.178
# 4	Width (mm)	1.066	1.066	1.071	1.218	1.053
	Area (mm ²)	0.169	0.178	0.187	0.173	0.160
# 5	Width (mm)	1.066	1.171	1.078	1.227	1.069
	Area (mm ²)	0.168	0.188	0.168	0.185	0.170

Table 57 – Theoretical and manufactures measures for TC 2 (half-ellipse groove).

Groove	Measures	1	2	3	4	5
# 1	Width (mm)	1.061	1.181	1.097	1.182	1.196
	Area (mm ²)	0.189	0.163	0.156	0.164	0.166
# 2	Width (mm)	1.271	1.198	1.201	1.220	1.216
	Area (mm ²)	0.211	0.158	0.175	0.178	0.181
# 3	Width (mm)	1.372	1.221	1.068	1.132	1.105
	Area (mm ²)	0.210	0.160	0.166	0.192	0.157
# 4	Width (mm)	1.077	1.066	1.071	1.218	1.053
	Area (mm ²)	0.175	0.192	0.188	0.183	0.186
# 5	Width (mm)	1.116	1.077	1.185	1.103	1.148
	Area (mm ²)	0.174	0.189	0.172	0.162	0.170

Table 58 – Theoretical and manufactures measures for TC 3 (quarter-ellipse groove).

Groove	Measures	1	2	3	4	5
# 1	Width (mm)	1.106	1.203	1.211	1.202	1.062
	Area (mm ²)	0.164	0.177	0.180	0.192	0.187
# 2	Width (mm)	1.241	1.052	1.080	1.094	1.146
	Area (mm ²)	0.226	0.170	0.161	0.192	0.165

Groove	Measures	1	2	3	4	5
# 3	Width (mm)	1.278	1.144	1.110	1.190	1.099
	Area (mm ²)	0.225	0.185	0.190	0.184	0.167
# 4	Width (mm)	1.049	1.217	1.115	1.114	1.114
	Area (mm ²)	0.165	0.155	0.168	0.166	0.191
# 5	Width (mm)	1.102	1.087	1.115	1.187	1.075
	Area (mm ²)	0.159	0.178	0.163	0.178	0.159

Table 59 – Theoretical and manufactures measures for TC 4 (inverted quarter groove).

Groove	Measures	1	2	3	4	5
# 1	Width (mm)	1.086	1.056	1.178	1.069	1.110
	Area (mm ²)	0.166	0.155	0.190	0.171	0.177
# 2	Width (mm)	1.093	1.072	1.074	1.045	1.099
	Area (mm ²)	0.195	0.187	0.190	0.170	0.159
# 3	Width (mm)	1.100	1.201	1.083	1.112	1.169
	Area (mm ²)	0.167	0.165	0.154	0.161	0.184
# 4	Width (mm)	1.098	1.218	1.147	1.099	1.136
	Area (mm ²)	0.159	0.165	0.174	0.187	0.185
# 5	Width (mm)	1.201	1.052	1.126	1.079	1.193
	Area (mm ²)	0.191	0.171	0.188	0.170	0.182

Table 60 – Theoretical and manufactures measures for TC 5 (rectangular groove).

Groove	Measures	1	2	3	4	5
# 1	Width (mm)	1.095	1.189	1.199	1.202	1.161
	Area (mm ²)	0.164	0.155	0.175	0.181	0.182
# 2	Width (mm)	1.207	1.151	1.175	1.050	1.111
	Area (mm ²)	0.201	0.163	0.171	0.171	0.188
# 3	Width (mm)	1.212	1.134	1.057	1.078	1.183
	Area (mm ²)	0.198	0.159	0.174	0.166	0.173
# 4	Width (mm)	1.062	1.210	1.055	1.207	1.194
	Area (mm ²)	0.147	0.179	0.170	0.179	0.174
# 5	Width (mm)	1.031	1.052	1.084	1.048	1.154
	Area (mm ²)	0.153	0.189	0.163	0.181	0.178

Table 61 – Theoretical and manufactures measures for TC 6 (trapezoidal groove).

Groove	Measures	1	2	3	4	5
# 1	Width (mm)	1.210	1.210	1.189	1.111	1.232
	Area (mm ²)	0.192	0.173	0.161	0.154	0.171
# 2	Width (mm)	1.191	1.212	1.066	1.144	1.113
	Area (mm ²)	0.190	0.180	0.171	0.164	0.190
# 3	Width (mm)	1.054	1.197	1.081	1.204	1.063
	Area (mm ²)	0.161	0.187	0.154	0.189	0.192
# 4	Width (mm)	1.047	1.158	1.052	1.203	1.152
	Area (mm ²)	0.139	0.181	0.166	0.175	0.175
# 5	Width (mm)	1.072	1.159	1.169	1.106	1.196
	Area (mm ²)	0.143	0.153	0.190	0.178	0.192

Table 62 – Theoretical and manufactures measures for TC 7 (half-circle groove).

Groove	Measures	1	2	3	4	5
# 1	Width (mm)	1.086	1.219	1.160	1.075	1.183
	Area (mm ²)	0.171	0.182	0.180	0.163	0.167
# 2	Width (mm)	1.222	1.211	1.131	1.187	1.089
	Area (mm ²)	0.180	0.177	0.173	0.168	0.174
# 3	Width (mm)	1.117	1.165	1.175	1.192	1.183
	Area (mm ²)	0.195	0.188	0.162	0.153	0.178
# 4	Width (mm)	1.011	1.086	1.158	1.207	1.108
	Area (mm ²)	0.133	0.174	0.164	0.186	0.175
# 5	Width (mm)	1.100	1.165	1.203	1.092	1.078
	Area (mm ²)	0.173	0.185	0.185	0.179	0.180

Systematic Errors are not compensated in the measurement system, and the maximum error is used to estimate the final measurement value (GONÇALVES Jr., 2002).

The sources of uncertainty considered are:

- Repeatability: The uncertainty component of repeatability is typically random, there are no associated systematic components. In this case, the experimental standard deviation of the random variable x , represented by s , is used. The determination

of s is made from n values independently obtained for the variable x , i.e., x_k (for $k = 1, 2, \dots$):

$$s(x) = \sqrt{\frac{\sum_{k=1}^n (x_k - \bar{x})^2}{n-1}} \quad (\text{A.1})$$

Next, the experimental standard deviation of the mean of the measured m_n measurements must be estimated, which is an estimate of the associated standard uncertainty u :

$$u(x) = \frac{s(x)}{\sqrt{m_n}} \quad (\text{A.2})$$

- Parallax due to observation through the ocular lens: When observing the groove reference points through the eyepiece (ocular lens), the position of the observer is extremely important. If the observer's head is tilted too severely, a parallax error may occur when observing the boundary surface. Therefore, careful observation is very well evaluated. Even so, it is considered a random error within the limit of $\pm 0,003$ mm.

- Resolution: The Mitutoyo catalog, the manufacturer of the micrometric head, informs that the maximum error is ± 0.003 mm. However, in addition to the random error of the head, there is an error in relation to the guide table, which cannot be considered without any error in its displacement. Thus, a random error of ± 0.005 mm for the guide head assembly is considered.

The sources of uncertainty are summarized in Table 63.

Table 63 – Uncertainty sources and random effects.

Uncertainty sources	Random effects				
	Gross Value	Type of Distribution	Divider	u	ν
1 - Repeatability (5 times)	each value	normal	1	each value	4
2 – Parallax due to observation through the eye lens	0.003 mm	uniforme	2.236068	0,0013 mm	∞
3 – Resolution	0.005 mm	uniforme	2.236068	0,0022 mm	∞

From the respective values of the random effects obtained, the calculation must be performed to compose the combined standard uncertainty. The combined standard uncertainty (u_c) of the various sources of uncertainty can be estimated from the standard uncertainties of each source of uncertainty by:

$$u_c = \sqrt{u_1^2 + u_2^2 + \dots + u_p^2} \quad (\text{A.3})$$

where: - u_1, u_2, \dots, u_p represent the standard uncertainties of each of the p sources of uncertainty; and

- u_c represents the combined standard uncertainty.

When standard uncertainties from various sources of uncertainty are considered to estimate the combined standard uncertainty, the number of degrees of freedom resulting from the combined standard uncertainty must be estimated.

The number of effective degrees of freedom (ν_{ef}) is the number of degrees of freedom associated with the standard uncertainty. Gonçalves Jr. (2002) recommends using the Welch-Satterthwaite equation to estimate the number of effective degrees of freedom:

$$\frac{u_c^4}{\nu_{ef}} = \frac{u_1^4}{\nu_1} + \frac{u_2^4}{\nu_2} + \dots + \frac{u_p^4}{\nu_p} \quad (\text{A.4})$$

where: - u_c is the combined standard uncertainty;

- u_1, u_2, \dots, u_p are the standard uncertainties of each of the p sources of uncertainty;

- $\nu_1, \nu_2, \dots, \nu_p$ are the number of degrees of freedom of each of the p sources of uncertainty;

The combined standard uncertainty, estimated through equation (A.4), corresponds to the standard deviation resulting from the combined action of the various sources of uncertainty considered.

In engineering applications, it is common to work with 95% confidence levels. To reach this level, the combined standard uncertainty u_c , which corresponds to just one standard deviation, must be multiplied by a numerical coefficient, the Student coefficient. This coefficient is called the *coverage factor*, commonly represented by the symbol k_{95} when the 95% confidence level is used. (GONÇALVES Jr., 2002).

The *expanded uncertainty* ($U_{95\%}$) corresponds to the range of values that frame the uncertainty with a confidence level of approximately 95%. is estimated by:

$$U_{95\%} = k_{95\%} \cdot u_c \quad (\text{A.5})$$

where: $k_{95\%}$ is the coverage factor for the 95% confidence level.

To obtain this value, use Table 64.

Table 64 – Values for the coverage factor ($k_{95\%}$) for a 95% confidence level as a function of the number of effective degrees of freedom (v_{ef}).

v_{ef}	1	2	3	4	5	6	7	8	10	12	14	16
$k_{95\%}$	12.71	4.30	3.18	2.78	2.57	2.45	2.39	2.31	2.23	2.18	2.14	2.12
v_{ef}	18	20	25	30	35	40	45	50	60	80	100	∞
$k_{95\%}$	2.10	2.09	2.06	2.04	2.03	2.02	2.01	2.01	2.01	2.00	2.00	2.00

Tables 65 to 71 present the final values of the measurements of the dimensions of the designed grooves considering all sources of uncertainty.

Table 65 – Geometric Parameters of each groove for TC 1 (triangular groove).

Groove	Measures	Mean	Experimental Standard Deviation	Combined Standard Uncertainty	Effective degrees-of-freedom	$k_{95\%}$	Expanded Uncertainty $U_{95\%}$
# 1	Width (mm)	1.141	0.058	0.026	4	2.78	0.073
	Area (mm ²)	0.162	0.003	0.003	93	2.00	0.006
# 2	Width (mm)	1.195	0.030	0.013	4	2.78	0.037
	Area (mm ²)	0.179	0.009	0.005	7	2.39	0.012
# 3	Width (mm)	1.128	0.051	0.023	4	2.78	0.064
	Area (mm ²)	0.174	0.008	0.005	8	2.31	0.011
# 4	Width (mm)	1.095	0.062	0.028	4	2.78	0.077
	Area (mm ²)	0.173	0.009	0.005	8	2.31	0.011
# 5	Width (mm)	1.122	0.065	0.029	4	2.78	0.081
	Area (mm ²)	0.176	0.009	0.005	8	2.31	0.011

Table 66 – Geometric Parameters of each groove for TC 2 (half-ellipse groove).

Groove	Measures	Mean	Experimental Standard Deviation	Combined Standard Uncertainty	Effective degrees-of-freedom	k _{95%}	Expanded Uncertainty U _{95%}
# 1	Width (mm)	1.143	0.054	0.024	4	2.78	0.068
	Area (mm ²)	0.168	0.011	0.006	6	2.45	0.014
# 2	Width (mm)	1.221	0.026	0.012	4	2.78	0.033
	Area (mm ²)	0.181	0.017	0.008	5	2.57	0.021
# 3	Width (mm)	1.180	0.080	0.036	4	2.78	0.099
	Area (mm ²)	0.177	0.021	0.010	5	2.57	0.025
# 4	Width (mm)	1.097	0.061	0.027	4	2.78	0.076
	Area (mm ²)	0.185	0.006	0.004	16	2.12	0.008
# 5	Width (mm)	1.126	0.037	0.017	4	2.78	0.047
	Area (mm ²)	0.173	0.009	0.005	8	2.31	0.011

Table 67 – Geometric Parameters of each groove for TC 3 (quarter-ellipse groove).

Groove	Measures	Mean	Experimental Standard Deviation	Combined Standard Uncertainty	Effective degrees-of-freedom	k _{95%}	Expanded Uncertainty U _{95%}
# 1	Width (mm)	1.157	0.061	0.027	4	2.78	0.076
	Area (mm ²)	0.180	0.010	0.005	7	2.39	0.010
# 2	Width (mm)	1.123	0.067	0.030	4	2.78	0.083
	Area (mm ²)	0.183	0.024	0.011	4	2.39	0.025
# 3	Width (mm)	1.164	0.065	0.029	4	2.78	0.081
	Area (mm ²)	0.190	0.019	0.009	5	2.57	0.023
# 4	Width (mm)	1.122	0.054	0.024	4	2.78	0.067
	Area (mm ²)	0.169	0.012	0.006	6	2.45	0.014
# 5	Width (mm)	1.113	0.039	0.018	4	2.78	0.049
	Area (mm ²)	0.167	0.009	0.005	8	2.31	0.011

Table 68 – Geometric Parameters of each groove for TC 4 (inverted quarter-ellipse groove).

Groove	Measures	Mean	Experimental Standard Deviation	Combined Standard Uncertainty	Effective degrees-of-freedom	k _{95%}	Expanded Uncertainty U _{95%}
# 1	Width (mm)	1.100	0.043	0.019	4	2.78	0.054
	Area (mm ²)	0.172	0.012	0.006	6	2.45	0.014
# 2	Width (mm)	1.077	0.019	0.009	5	2.57	0.023
	Area (mm ²)	0.180	0.014	0.007	6	2.45	0.016
# 3	Width (mm)	1.133	0.045	0.020	4	2.78	0.056
	Area (mm ²)	0.166	0.010	0.005	7	2.31	0.012
# 4	Width (mm)	1.140	0.044	0.020	4	2.78	0.055
	Area (mm ²)	0.174	0.011	0.006	6	2.45	0.014
# 5	Width (mm)	1.130	0.060	0.027	4	2.78	0.074
	Area (mm ²)	0.180	0.009	0.005	8	2.31	0.011

Table 69 – Geometric Parameters of each groove for TC 5 (rectangular groove).

Groove	Measures	Mean	Experimental Standard Deviation	Combined Standard Uncertainty	Effective degrees-of-freedom	k _{95%}	Expanded Uncertainty U _{95%}
# 1	Width (mm)	1.169	0.040	0.018	4	2.78	0.050
	Area (mm ²)	0.171	0.010	0.005	7	2.39	0.011
# 2	Width (mm)	1.139	0.054	0.024	4	2.78	0.068
	Area (mm ²)	0.179	0.014	0.007	5	2.57	0.017
# 3	Width (mm)	1.133	0.059	0.027	4	2.78	0.074
	Area (mm ²)	0.174	0.013	0.006	6	2.45	0.016
# 4	Width (mm)	1.146	0.071	0.032	4	2.78	0.089
	Area (mm ²)	0.170	0.012	0.006	6	2.45	0.014
# 5	Width (mm)	1.074	0.044	0.020	4	2.78	0.055
	Area (mm ²)	0.173	0.013	0.006	6	2.45	0.016

Table 70 – Geometric Parameters of each groove for TC 6 (trapezoidal groove).

Groove	Measures	Mean	Experimental Standard Deviation	Combined Standard Uncertainty	Effective degrees-of-freedom	k _{95%}	Expanded Uncertainty U _{95%}
# 1	Width (mm)	1.190	0.042	0.019	4	2.78	0.053
	Area (mm ²)	0.170	0.013	0.006	6	2.45	0.015
# 2	Width (mm)	1.145	0.053	0.024	4	2.78	0.066
	Area (mm ²)	0.179	0.010	0.005	7	2.39	0.013
# 3	Width (mm)	1.120	0.066	0.030	4	2.78	0.083
	Area (mm ²)	0.177	0.016	0.008	5	2.57	0.019
# 4	Width (mm)	1.122	0.062	0.028	4	2.78	0.078
	Area (mm ²)	0.167	0.015	0.007	5	2.57	0.018
# 5	Width (mm)	1.140	0.045	0.020	4	2.78	0.056
	Area (mm ²)	0.171	0.020	0.009	5	2.57	0.024

Table 71 – Geometric Parameters of each groove for TC 7 (half-circle groove).

Groove	Measures	Mean	Experimental Standard Deviation	Combined Standard Uncertainty	Effective degrees-of-freedom	k _{95%}	Expanded Uncertainty U _{95%}
# 1	Width (mm)	1.145	0.056	0.025	4	2.78	0.070
	Area (mm ²)	0.173	0.007	0.004	10	2.23	0.009
# 2	Width (mm)	1.168	0.050	0.023	4	2.78	0.063
	Area (mm ²)	0.174	0.004	0.003	36	2.04	0.006
# 3	Width (mm)	1.166	0.026	0.012	4	2.78	0.033
	Area (mm ²)	0.175	0.016	0.007	5	2.57	0.019
# 4	Width (mm)	1.114	0.066	0.030	4	2.78	0.083
	Area (mm ²)	0.166	0.018	0.008	5	2.57	0.022
# 5	Width (mm)	1.128	0.048	0.022	4	2.78	0.060
	Area (mm ²)	0.180	0.004	0.003	28	2.05	0.007

The expanded uncertainty target for this work is the width is less than 0.1 mm and area less than 0.025 mm². To achieve this target, 5 measurements are necessary, as described in the tables above.

APPENDIX C – Steady-state frequency spectra

In this appendix, all the frequency spectra obtained for each valve closing position are presented (six positions, from fully open to surge condition), in the five different speed lines.

In this classification, the figures are divided between each of the seven turbos and in the three directions with fixed accelerometers.

Figures 130, 131 and 132 each show the 30 frequency spectra for the x (horizontal radial), y (vertical radial) and z (axial) axes, respectively, for TC 1, totalizing 90 frequency spectra.

Figures 133, 134 and 135 are presented in the same way as the previous one, for TC 2.

In the same way, there is always a group of 3 figures, until reaching Figures 148, 149 and 150 for TC 7.

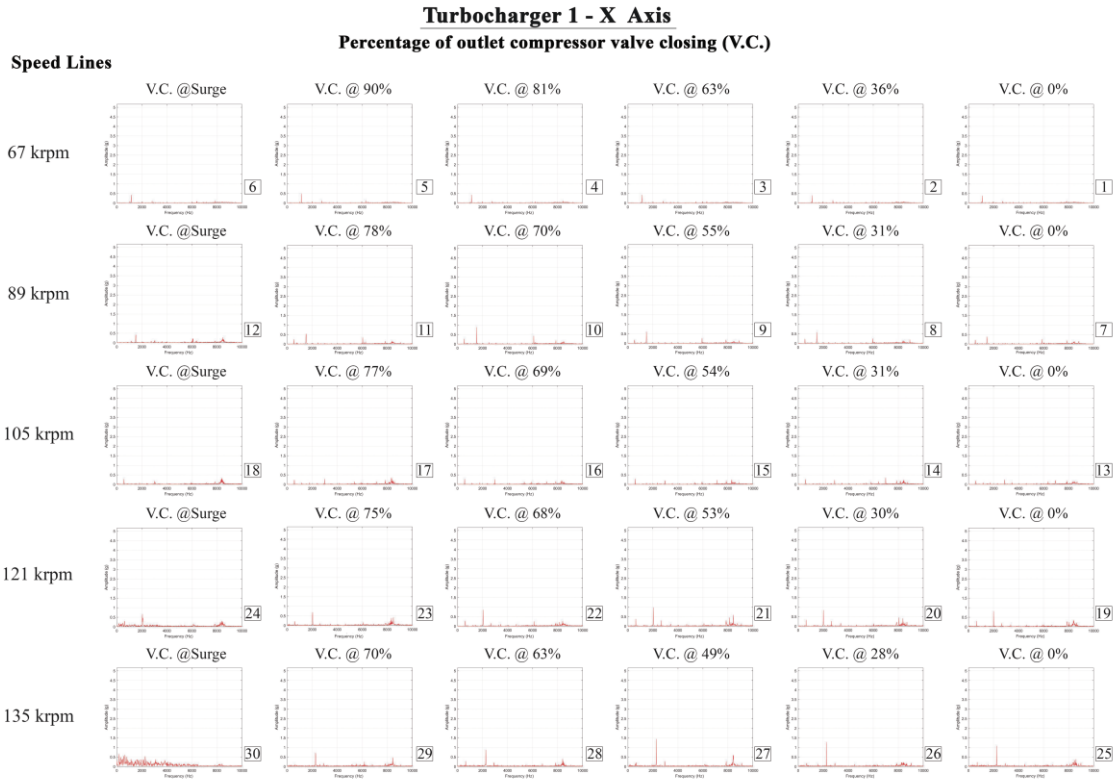


Figure 130 – Frequency spectra for the x axis (horizontal radial) for TC 1

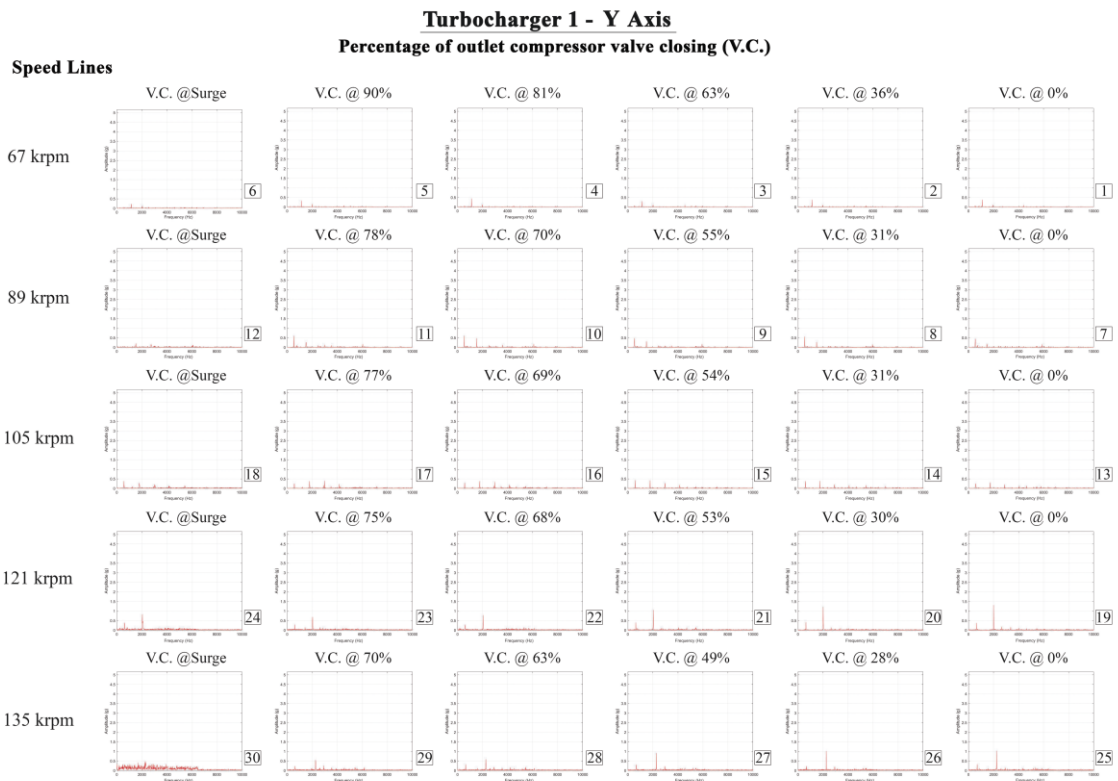


Figure 131 – Frequency spectra for the y axis (vertical radial) for TC 1

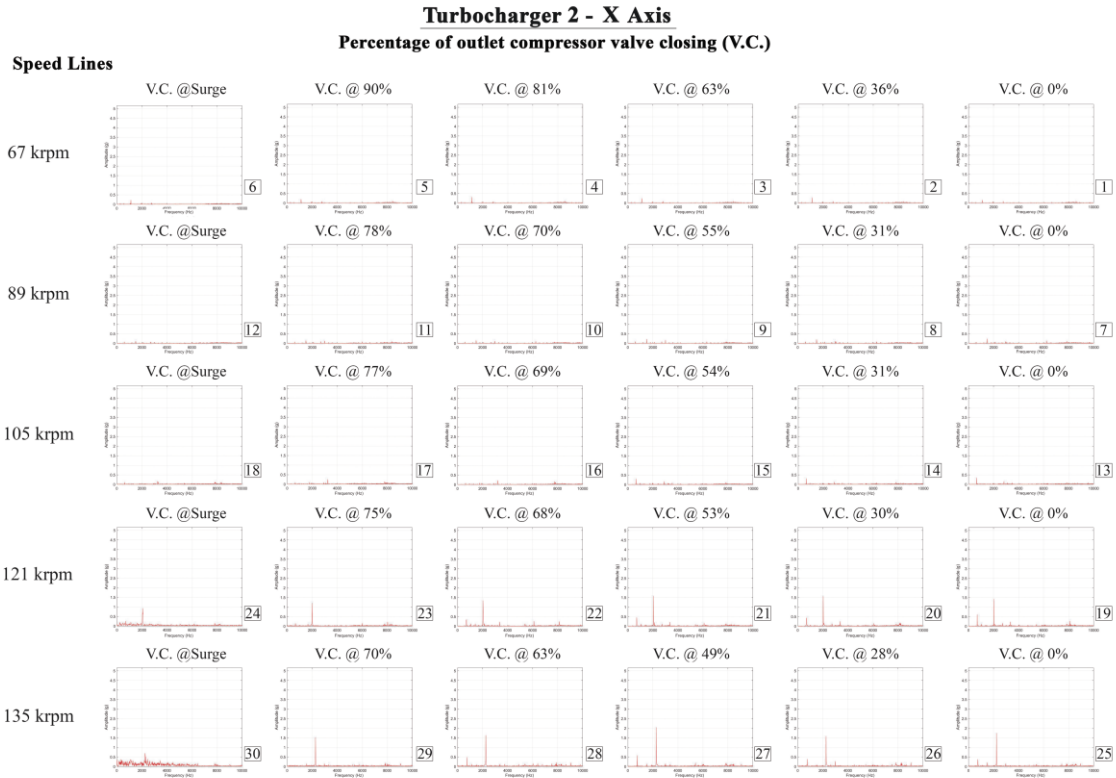


Figure 132 – Frequency spectra for the z axis (axial) for TC 1

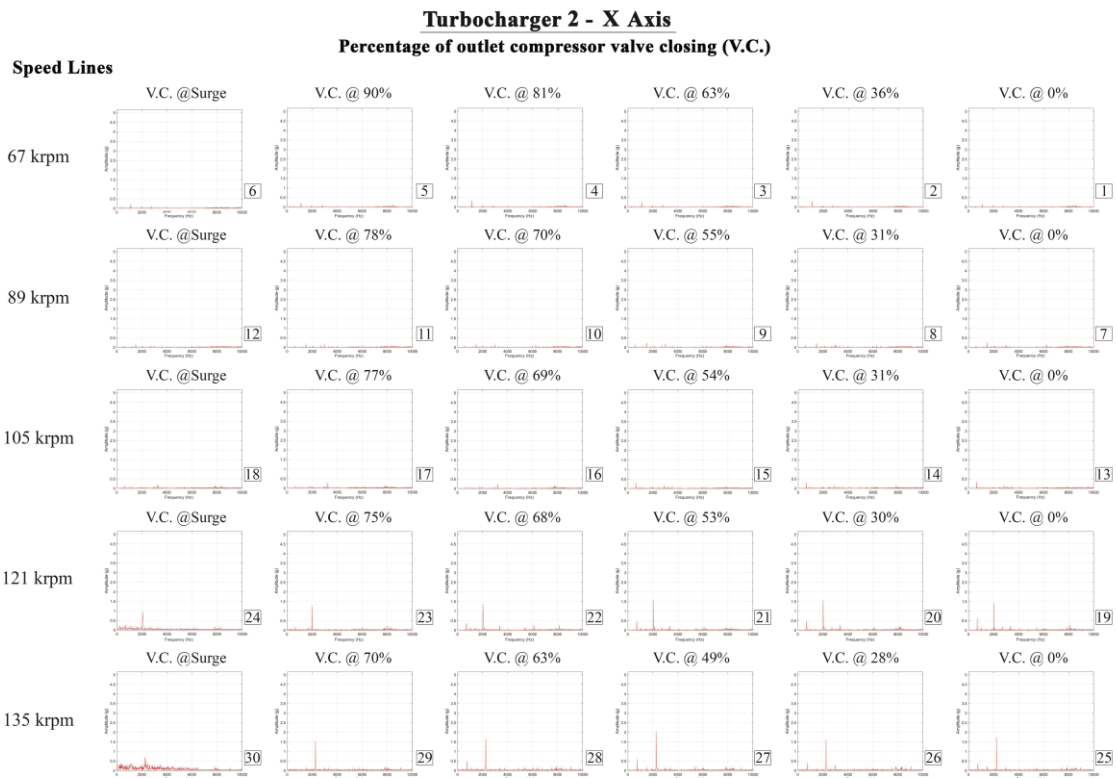


Figure 133 – Frequency spectra for the x axis (horizontal radial) for TC 2

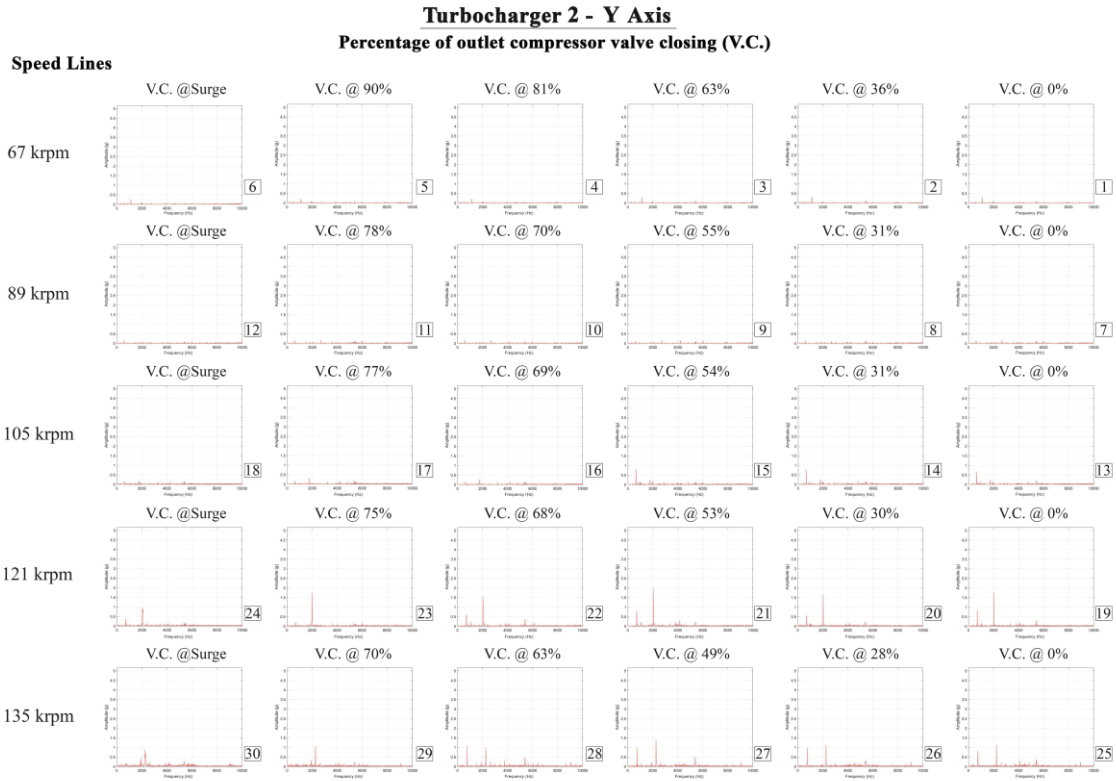


Figure 134 – Frequency spectra for the y axis (vertical radial) for TC 2

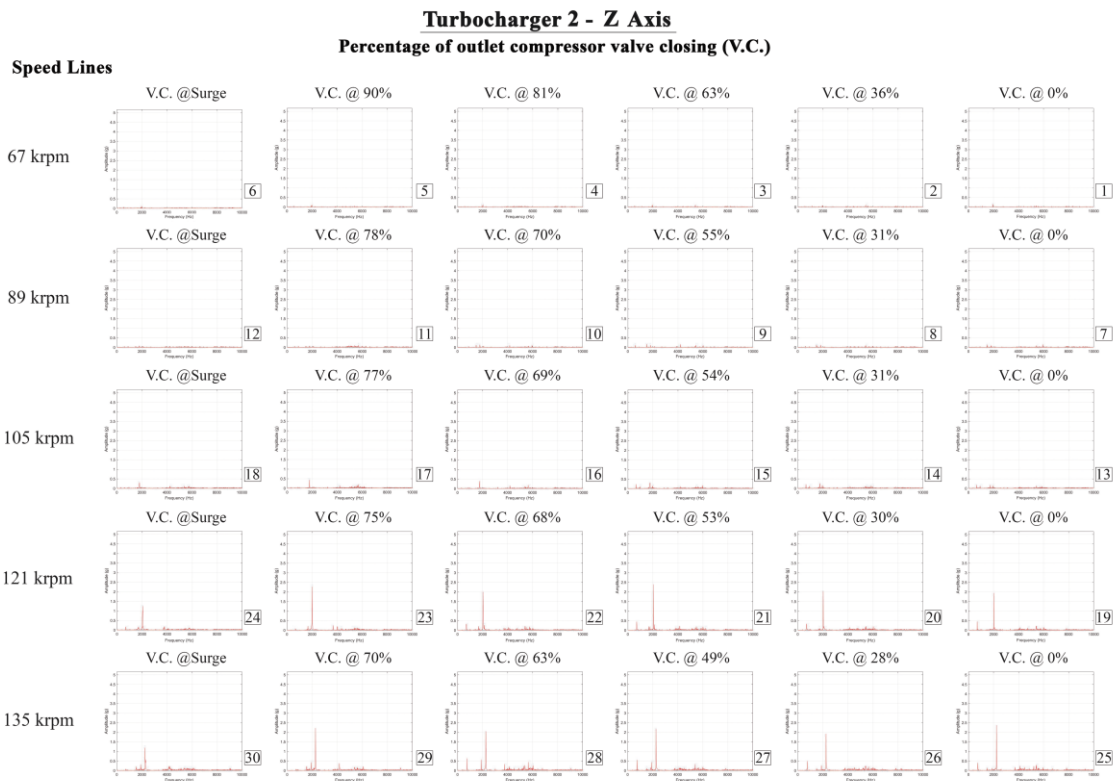


Figure 135 – Frequency spectra for the z axis (axial) for TC 2

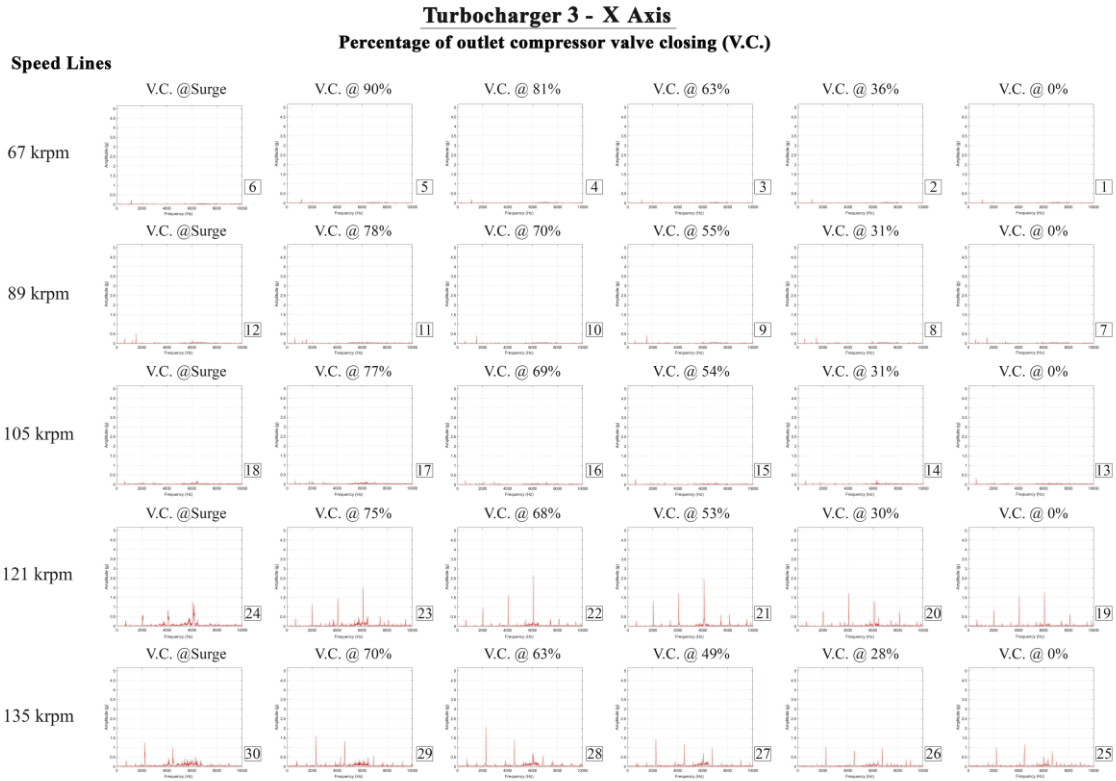


Figure 136 – Frequency spectra for the x axis (horizontal radial) for TC 3

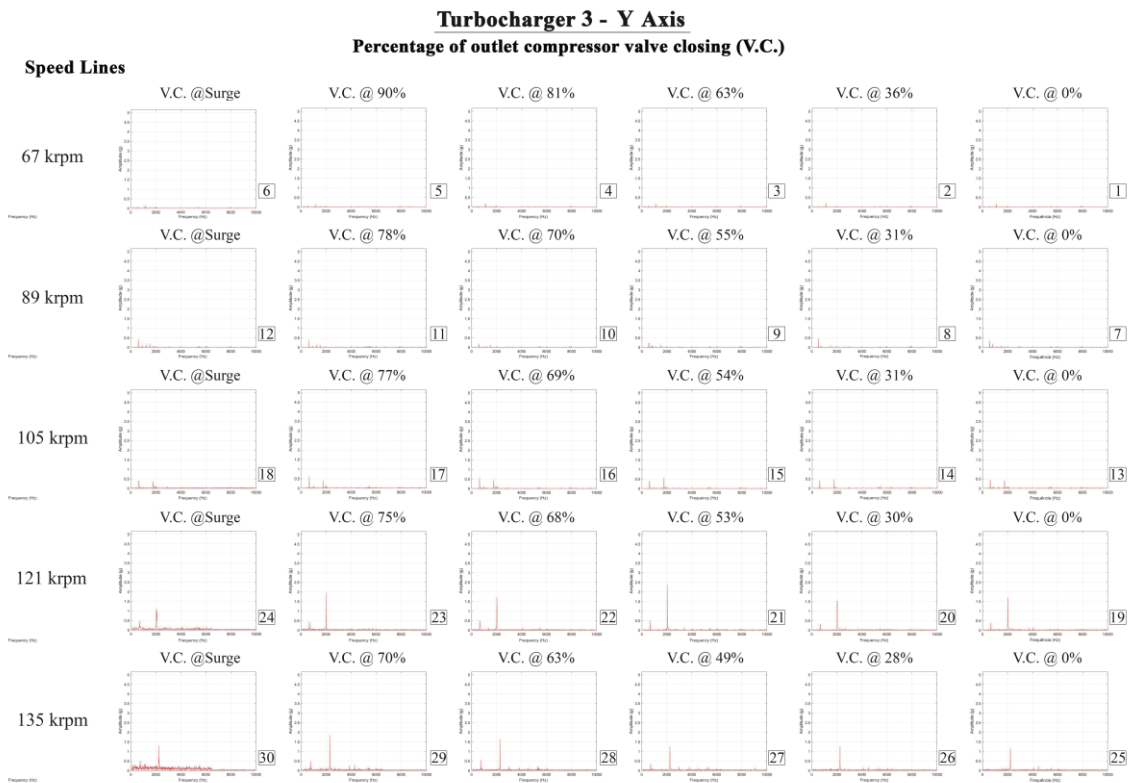


Figure 137 – Frequency spectra for the y axis (vertical radial) for TC 3

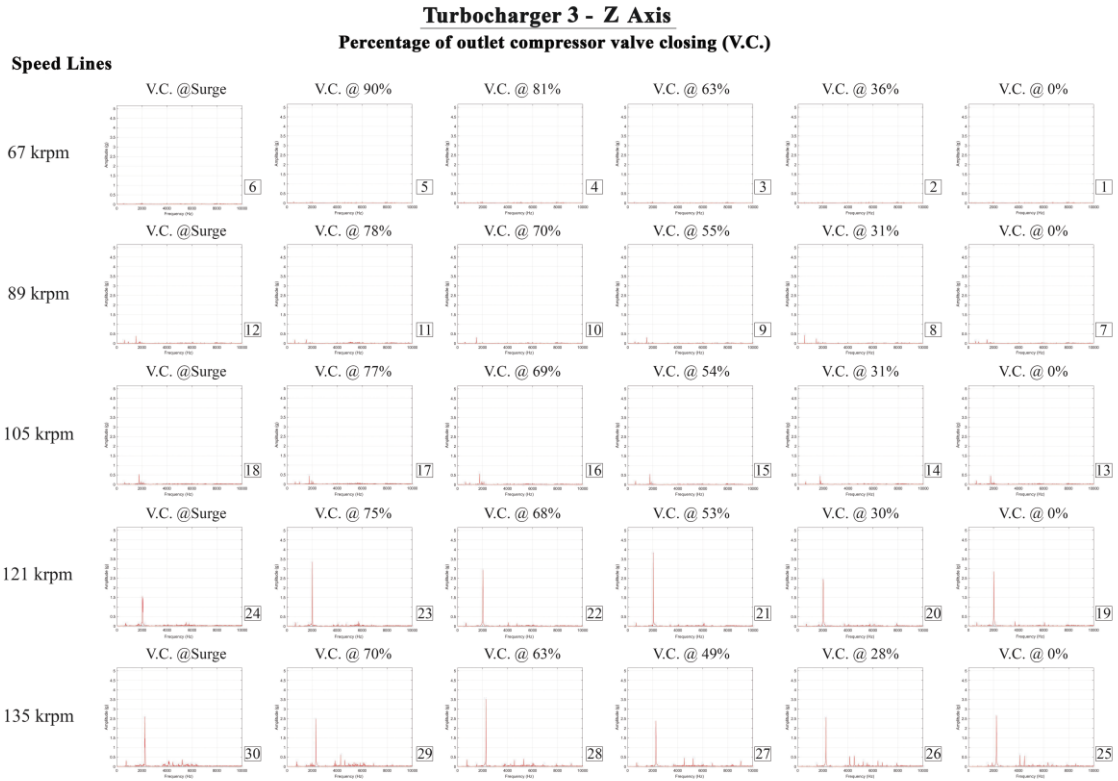


Figure 138 – Frequency spectra for the z axis (axial) for TC 3

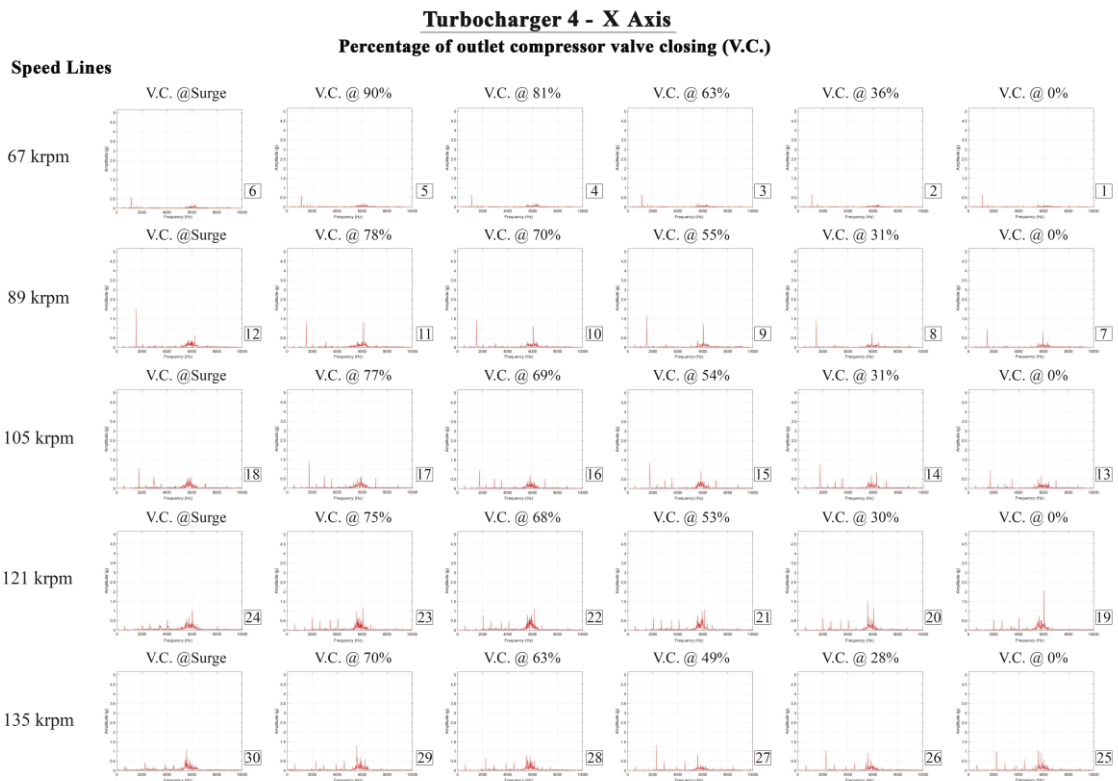


Figure 139 – Frequency spectra for the x axis (horizontal radial) for TC 4

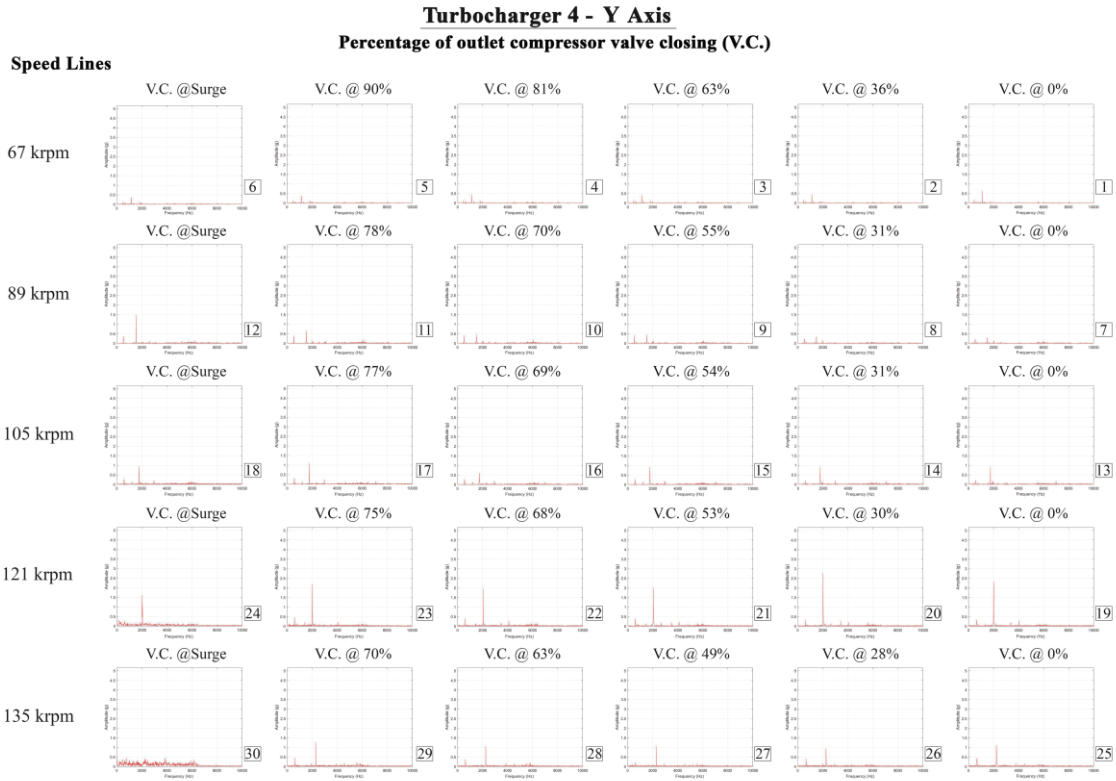


Figure 140 – Frequency spectra for the y axis (vertical radial) for TC 4

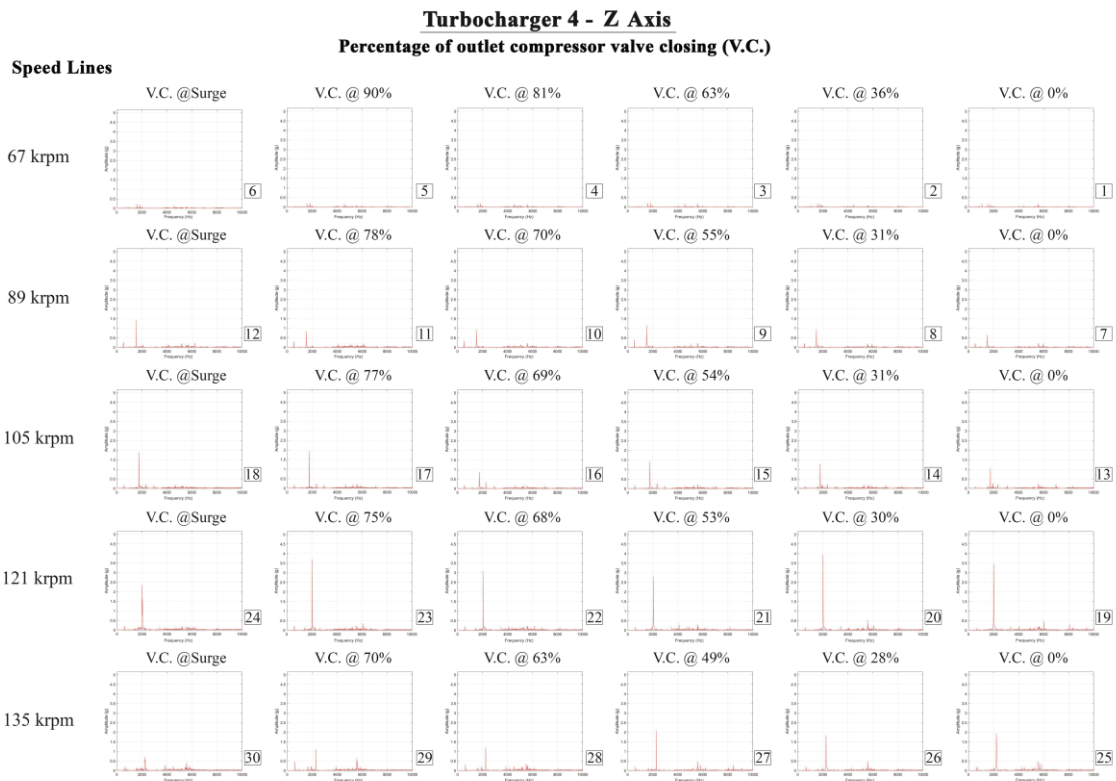


Figure 141 – Frequency spectra for the z axis (axial) for TC 4

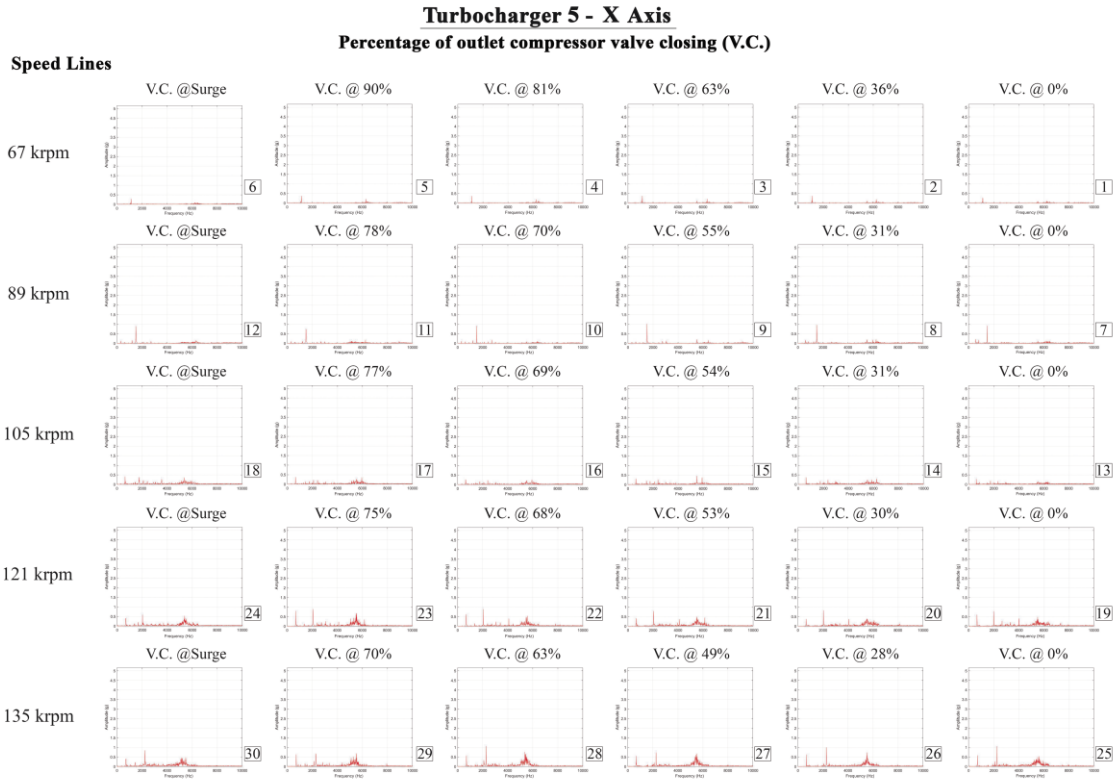


Figure 142 – Frequency spectra for the x axis (horizontal radial) for TC 5

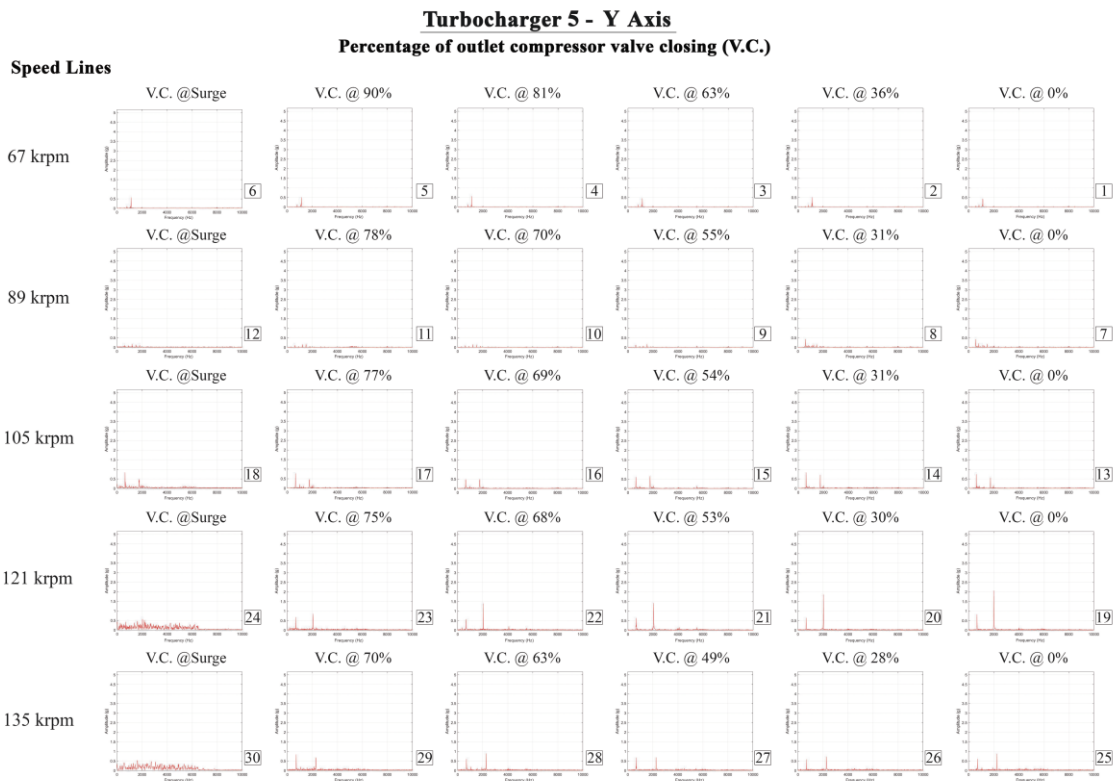


Figure 143 – Frequency spectra for the y axis (vertical radial) for TC 5

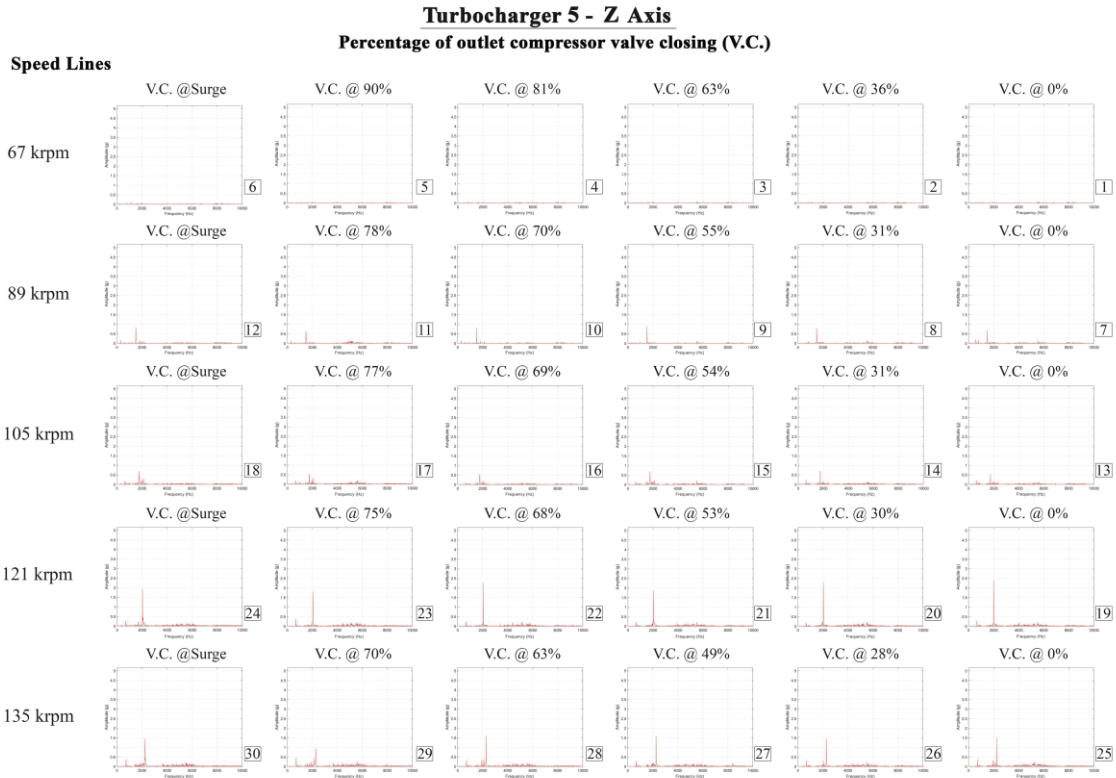


Figure 144 – Frequency spectra for the z axis (axial) for TC 5

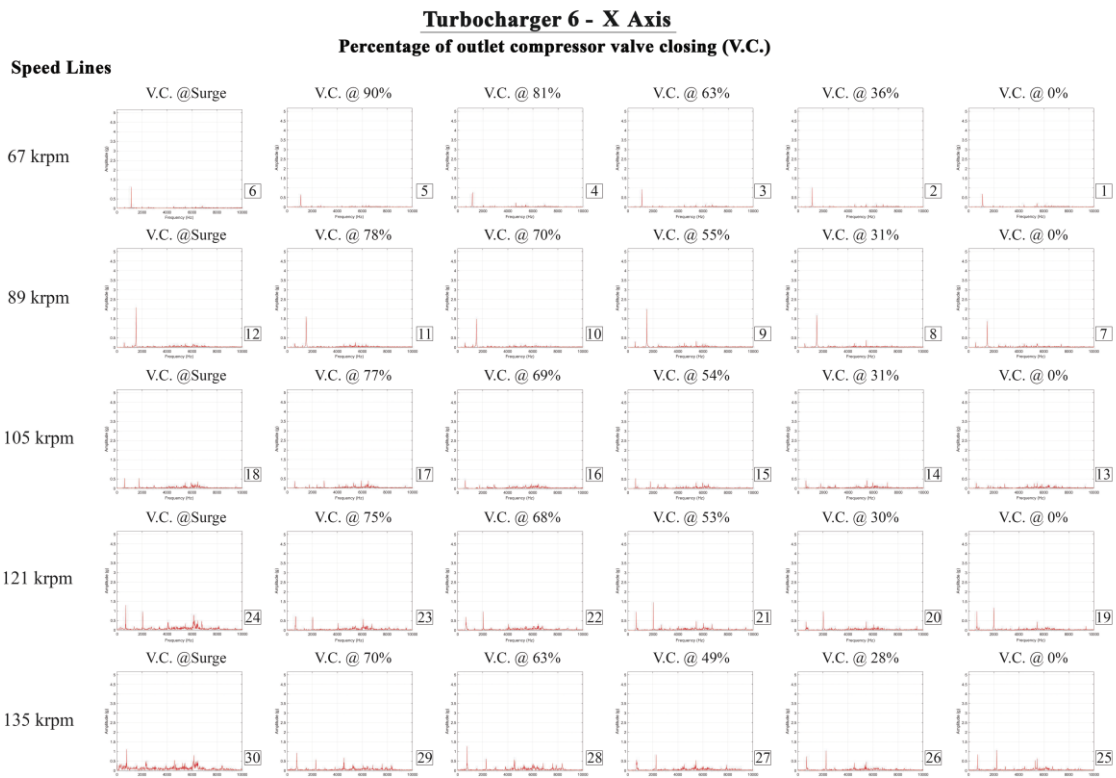


Figure 145 – Frequency spectra for the x axis (horizontal radial) for TC 6

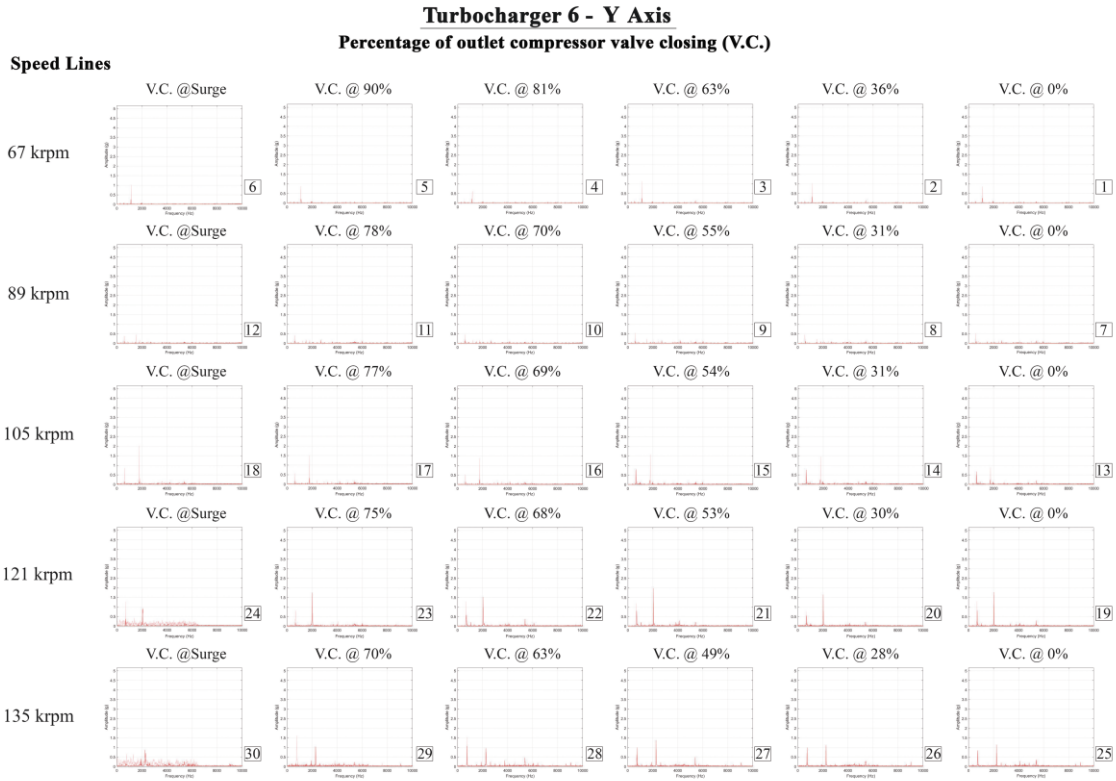


Figure 146 – Frequency spectra for the y axis (vertical radial) for TC 6

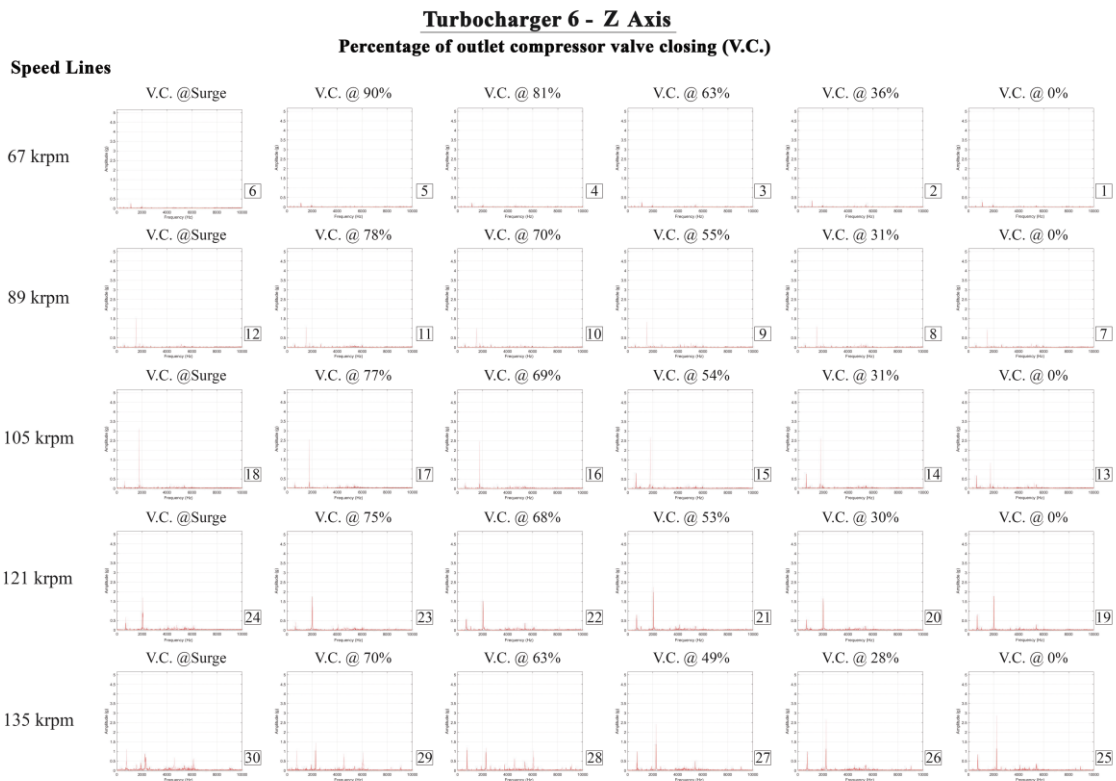


Figure 147 – Frequency spectra for the z axis (axial) for TC 6

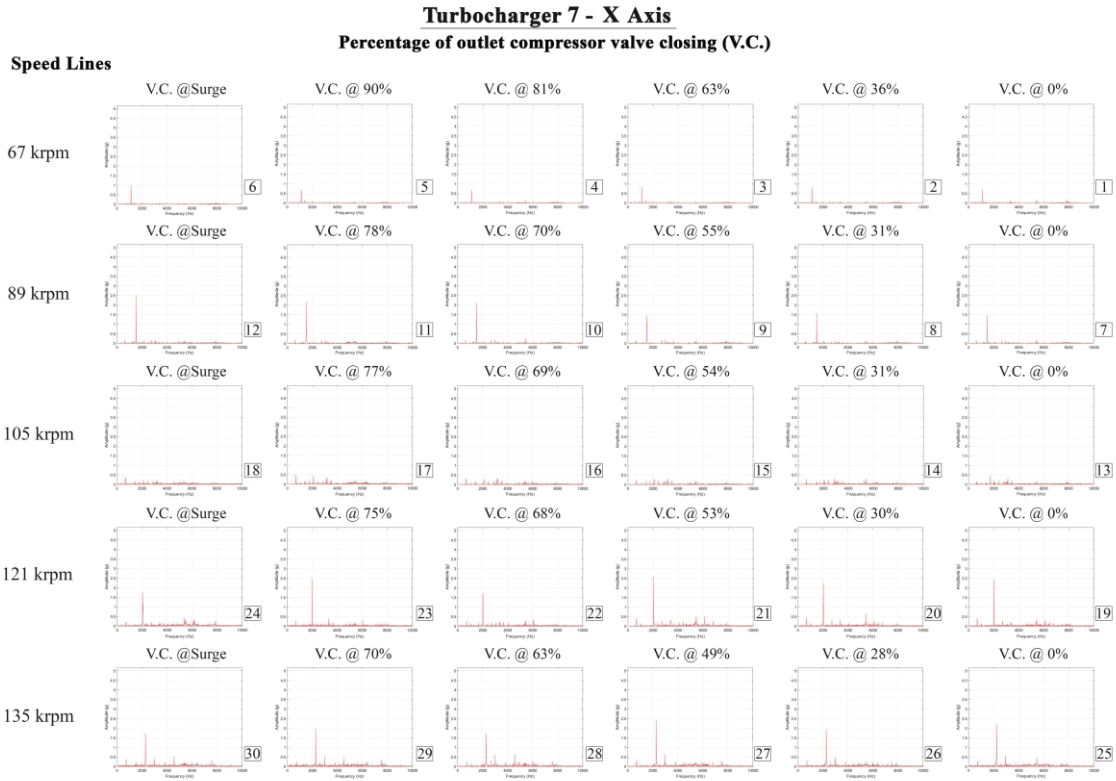


Figure 148 – Frequency spectra for the x axis (horizontal radial) for TC 7

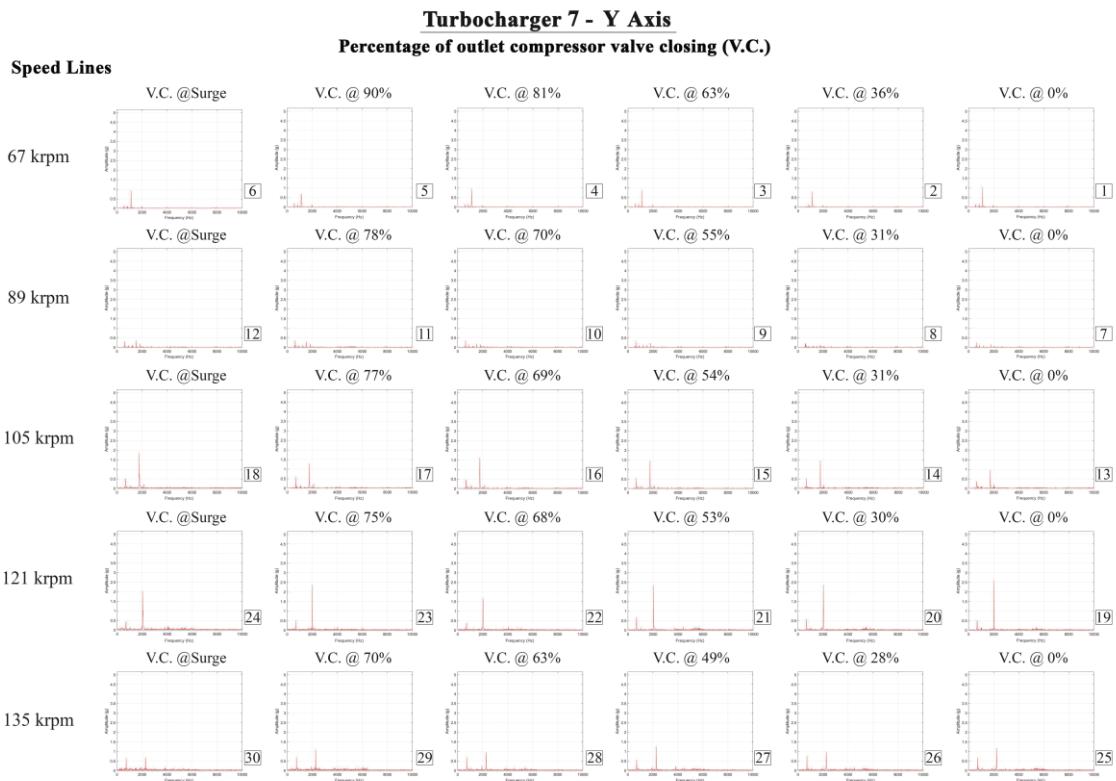


Figure 149 – Frequency spectra for the y axis (vertical radial) for TC 7

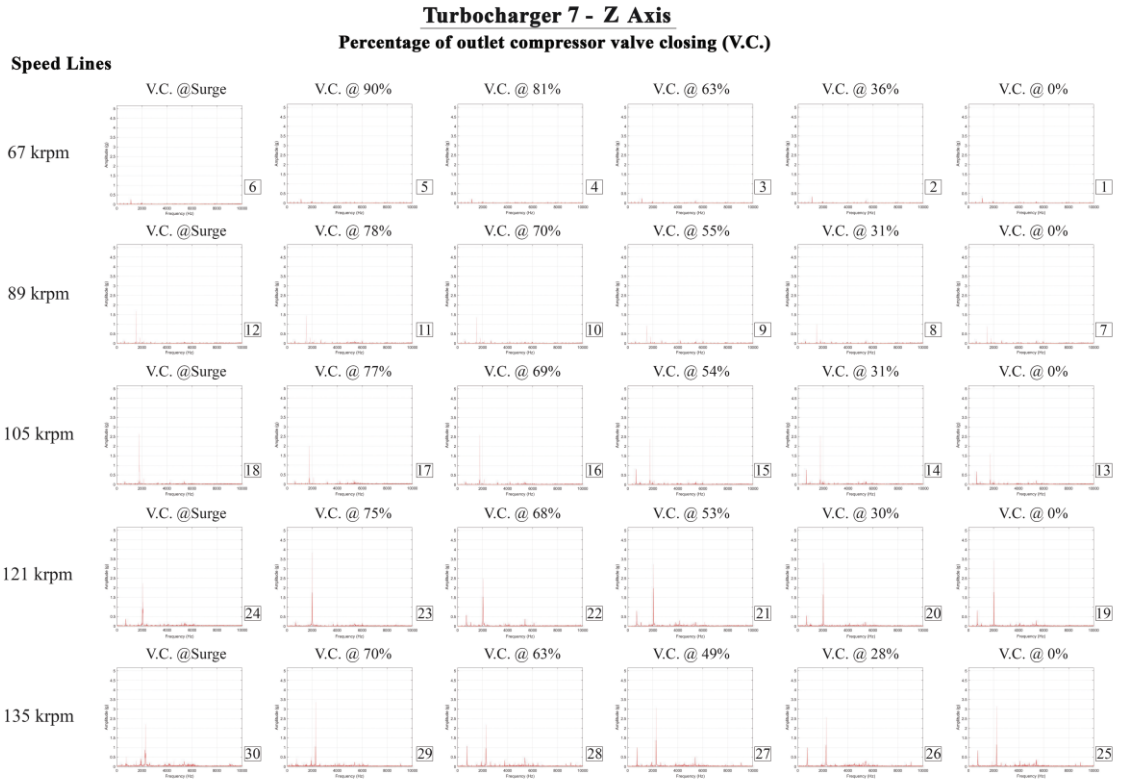


Figure 150 – Frequency spectra for the z axis (axial) for TC 7

APPENDIX D – Kurtosis graphs for each turbocharger

Appendix D presents in more detail the Kurtosis plots obtained for each RMS measured for each shaft revolution.

In each figure, 5 graphs are presented, each one presenting a speed line and each graph presents the seven filters used for analysis: band-pass filter between 50 and 100 kHz (used as a reference in this work), band-pass filter between 80 and 160 kHz, 100 kHz high-pass filter, band-pass filter between 100 and 300 kHz, 300 kHz high-pass filter, band-pass filter between 300 and 700 kHz, 700 kHz high-pass filter. These filters are chose for presenting the best analysis data.

Figures 151 to 157 present the graphs for TC 1 to TC 7, respectively.

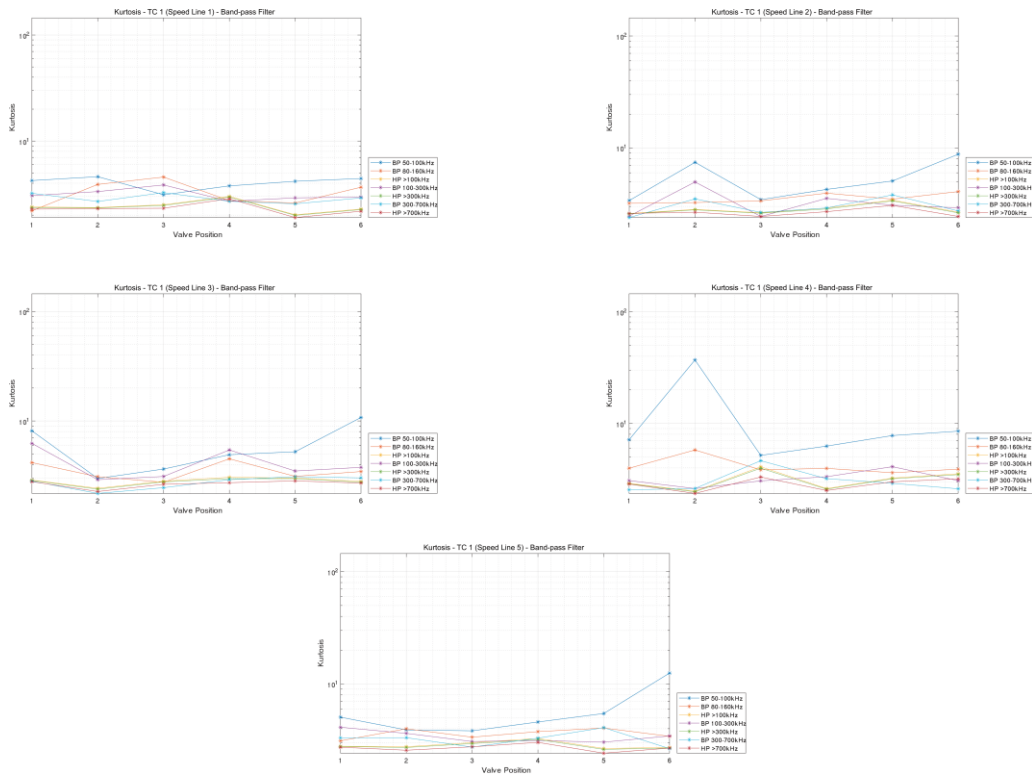


Figure 151 – Kurtosis of filtered AE data from TC 1 speed lines 1 to 5.

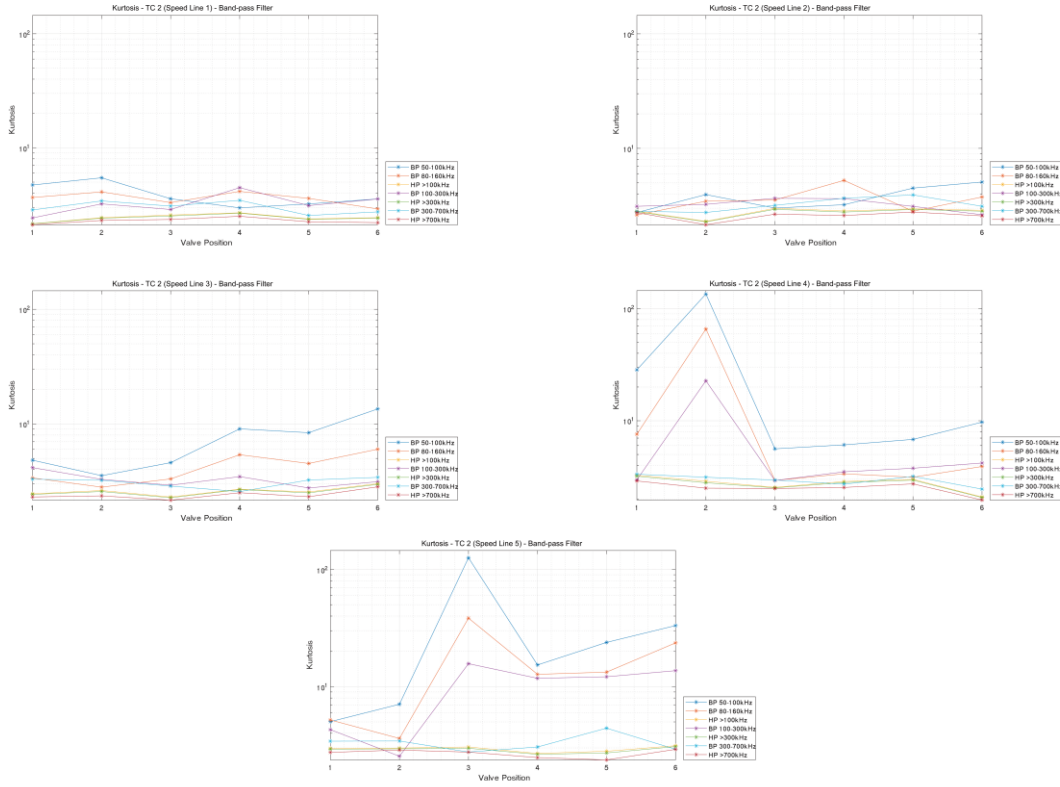


Figure 152 – Kurtosis of filtered AE data from TC 2 speed lines 1 to 5.

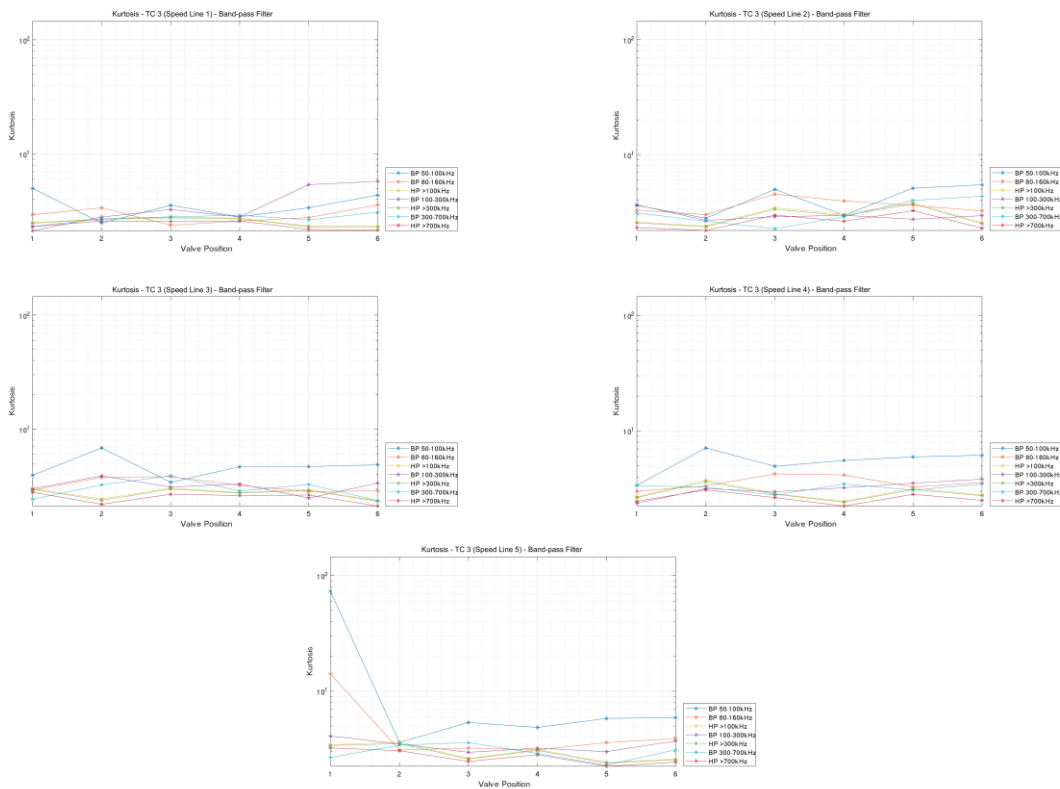


Figure 153 – Kurtosis of filtered AE data from TC 3 speed lines 1 to 5.

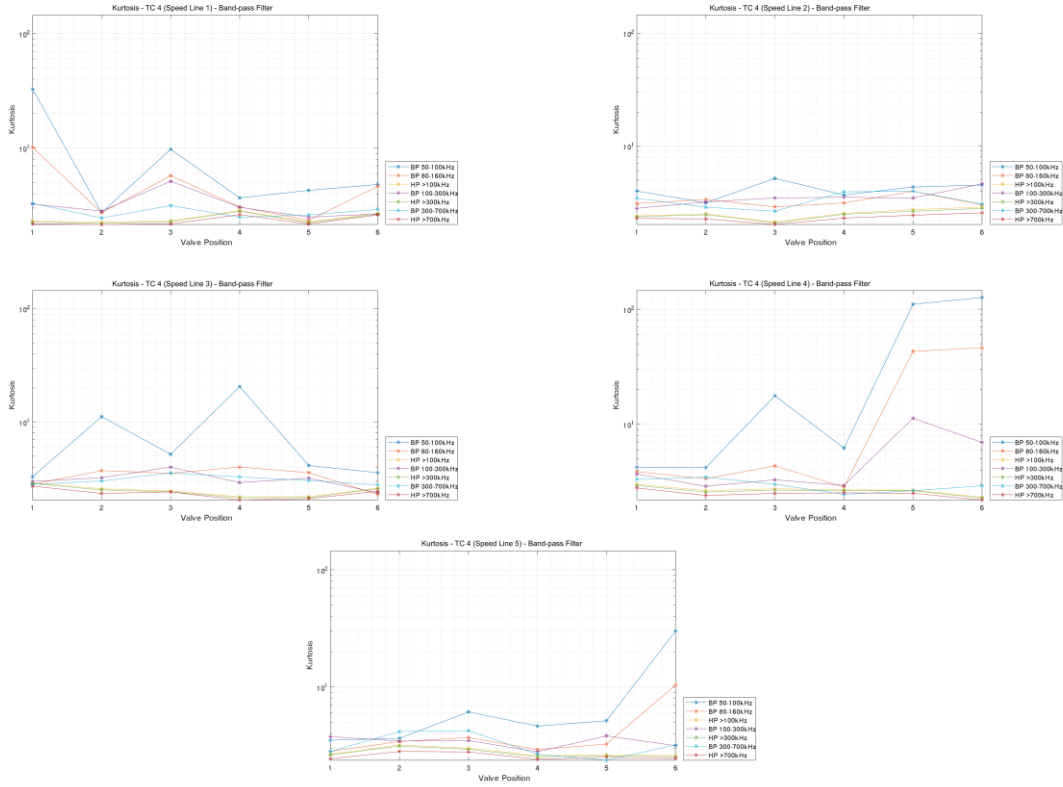


Figure 154 – Kurtosis of filtered AE data from TC 4 speed lines 1 to 5.

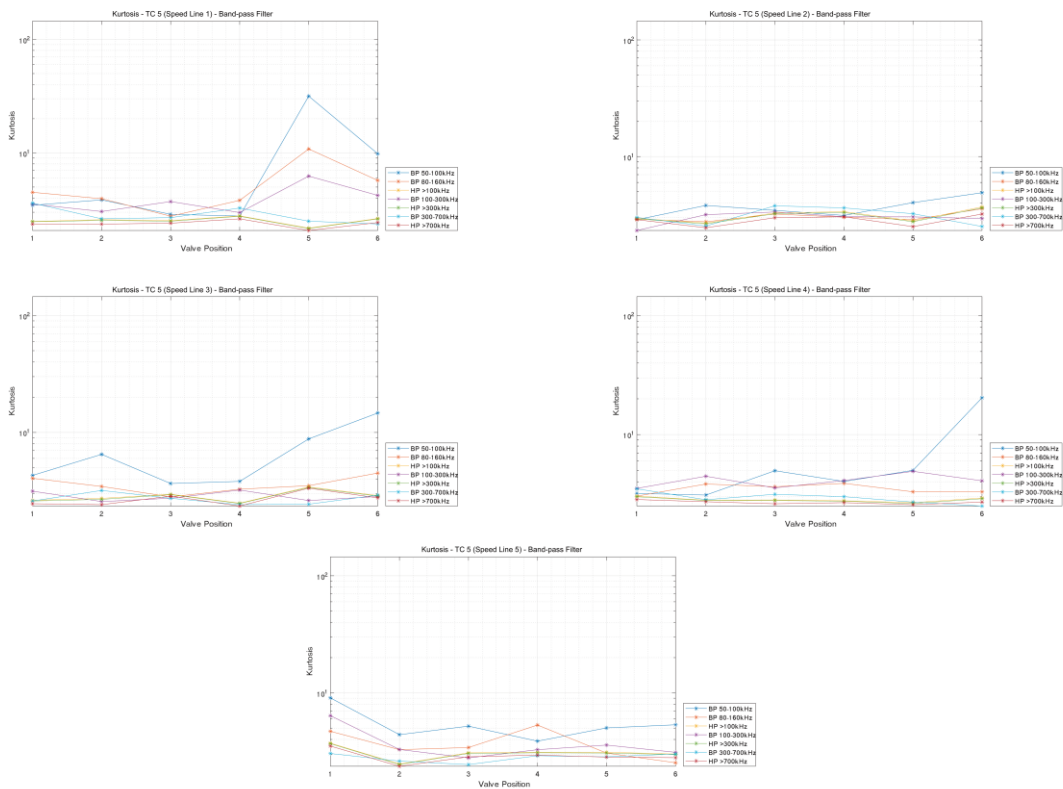


Figure 155 – Kurtosis of filtered AE data from TC 5 speed lines 1 to 5.

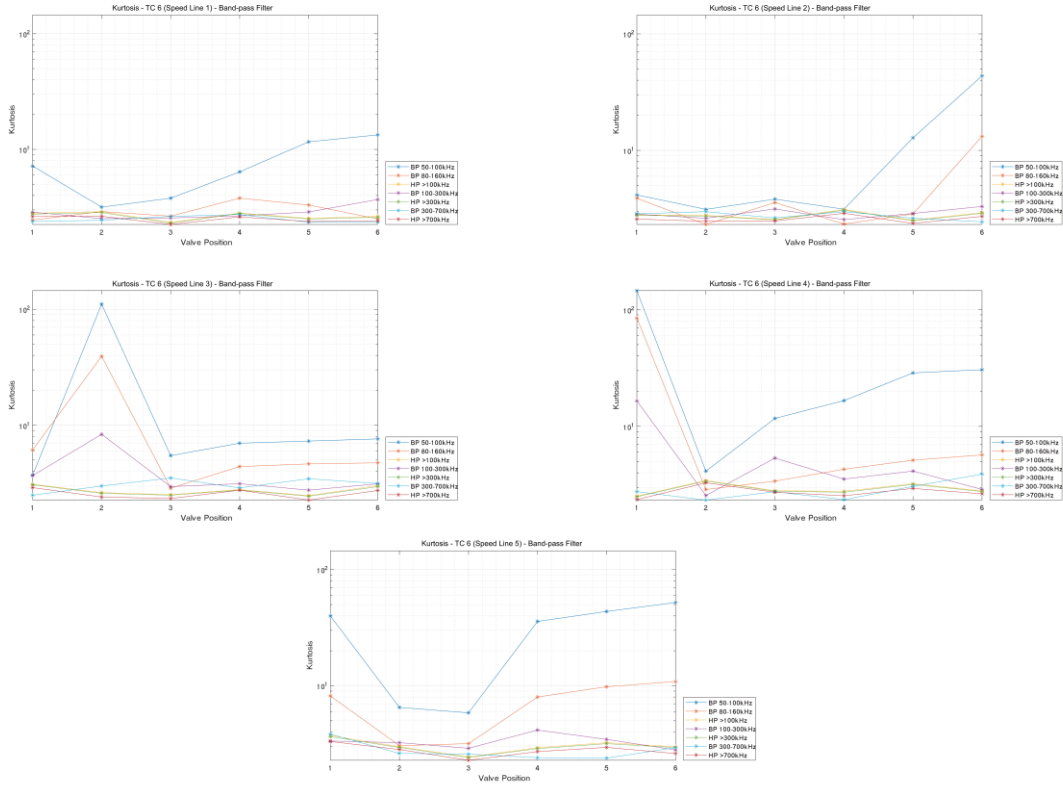


Figure 156 – Kurtosis of filtered AE data from TC 6 speed lines 1 to 5.

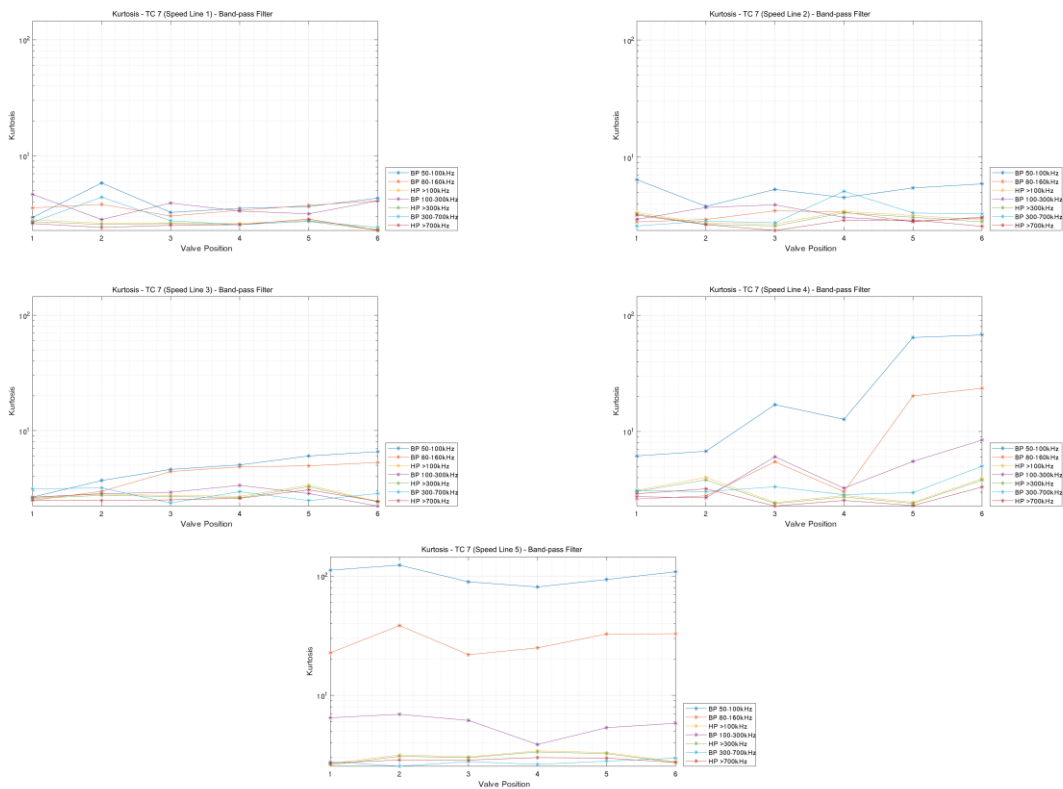


Figure 157 – Kurtosis of filtered AE data from TC 7 speed lines 1 to 5.